Complex Metal Oxides for Photocatalytic Applications

by

Tanya M. Breault

A dissertation submitted in partial fulfillment
of the requirements for the degree of
Doctor of Philosophy
(Chemistry)
in the University of Michigan
2013

Doctoral Committee:
- Assistant Professor Bart M. Bartlett, chair
- Professor Richard M. Laine
- Assistant Professor Stephen Maldonado
- Professor Vincent L. Pecoraro
- Associate Professor Jamie D. Phillips

Dedication

To my family, who has encouraged and supported me every step of the way

Acknowledgments

I would like to first thank my research advisor, Bart Bartlett, for giving me the opportunity to work in his lab for the past five years. I appreciate your guidance and support throughout all stages of research. I particularly admire your enthusiasm for science. He has created a fun work environment that fosters both creative and critical thinking. Your constructive criticism is much appreciated and has made me a better scientist. Thank you, Bart.

Thank you to my committee members: Rick, Stephen, Vince, and Jamie. I am grateful for your feedback and suggestions throughout all stages of my research.

There are several influential people I am grateful for prior to starting work at Michigan. My passion and enthusiasm for science cultivated from freshman high school chemistry class under the guidance of Mr. Furey. I am grateful he shared his love of chemistry and inspired me to learn and grow as a chemist as a freshman in high school. A special thanks to Prof. Kimberly Schandel for encouraging me to double major in chemistry and math. I also thank Prof. James Hauri and all the time he spent helping me in various classes. His energy is contagious and much appreciated. A special thanks to Prof. Brian Niece, for which my love of inorganic chemistry is attributed. I am forever grateful for his dedication to teaching and curriculum development efforts. Thanks to Allen Bruehl at the ASC. His genuine disposition and passion for helping everyone is unbridled.. The world needs more people like him. I'd also like to thank Nancy Kerner for being a wonderful chemistry lecturer and role-model for educators. I've enjoyed working with you and developing coursework.

I am grateful for the many members of the Bartlett Lab who have offered support over the years. Thank you to Sarah Simmons for the early days we spent together ordering chemicals and setting up lab. I miss our daily Wizard of Oz trivia even thought I was never very good at it. Thanks to Dave Yancey, Andrea Geyer, Ryan Bradstreet, Michael Holland, Aaron Goodman, and Brendan Liddle for creating an enjoyable work environment when the lab was few in numbers. Thank you to Joe Yourey for being a great desk mate. Your creative and curious nature towards science will afford you great success in future endeavors. All the best to you. Thanks to Emily Nelson for being a great friend and running inspiration. I enjoyed working early mornings with you. Good luck in the future and find something that truly makes you happy. To the rest of the current lab members: Jimmy Brancho, Xiaoguang Hao, Ben Klepser, Bruce Kraay, Charles Lhermitte, Kayla Pyper, and undergrads- good luck with your chemistry and future endeavors.

There are several people outside of the Bartlett Lab for which I am grateful for their friendship- it’s been fun over the years. A special thanks to Alaina DeToma- the past 6 months would have been unbearable without someone to share the misery of thesis writing and job hunting with. Thank you for lending an ear and offering advice. Best of luck to you! To everyone else, in particular Shilpa Gadwal, Melissa Zastrow, Gary Jensen, Lauren Goodrich, Sameer Phadke, David Chow, Junsi Gu, Sabrina Peczonczyk, Laura Pfund, Jeremy Feldblyum, Ahleah, Rohr, Joey Braymer, Daniel Miller, Chelsea Huff, Shana Santos, and Alana Canfield, thank you all for your friendship.

There are many staff members who have been most helpful over the years and deserve gratitude for keeping the department and building running smoothly. Margarita Bekiares, Jon Boyd, Ed Radwan, Tracy Stevenson, and Antek Wong-Foy- thank you for your hard work and dedication to your jobs.

A very special thank you to my best friend, Elizabeth Fortino. While we have only been able to spend a few days together over the past few years- our phone calls and letters to each other have made this process endurable. You are a forever friend and I am very lucky to know you. I am extremely proud of all of your accomplishments.

A special thanks to Cameron Moore. I would not have been able to get through the past few years without your constant support and encouragement. Your love and passion for chemistry is truly inspiring and I wish you nothing but the best in all that you do. I am a better person for knowing you. Thanks for making tacos. I love you.

My family has been a constant support system throughout my life, for which I am eternally grateful. Mom and Dad- your constant love and support throughout this whole process has not gone without notice. Thank you for the weekly cards and thoughtful care packages. I love you both very much. To Tara and Zach- thanks for visiting and daily face time sessions that were often the highlight of my day. I hope to teach Ellie and Mallory lots of math and science in the years to come! Trish- our visits were fun, Go Blue! Finally, a thanks to Grampa for all the chats while walking home and for trying to understand water splitting. A true inspiration and role-model at the young age of 91. To all other family member, Aunt Kathy, Aunt Debbie, the Ducharmes, the Niemczyks, the Robinsons, and the Morins- your support is, and always will be, much appreciated.

Table of Contents

List of Figures

List of Tables

List of Appendices

List of Abbreviations

2-MOE	2-methoxyethanol
BE	binding energy (eV)
BET	Brunauer-Emmett-Teller model
C	concentration of methylene blue dye at a time, t
C_0	initial bulk concentration of dye
C_e	liquid phase dye concentration at equilibrium (mg/L)
CB	conduction band
E^o	thermodynamic potential
E_g	band gap (eV)
EDX	energy dispersive x-ray spectroscopy
EPR	electron paramagnetic resonance spectroscopy
F^+-center	electron trapped on an oxygen vacancy
FTO	fluorine-tin-oxide
F(R)	Kubelka-Munk equation
$k_{40\ ppm\ MB}$	rate constant for methylene blue dye degradation (h^{-1})
K_L	sorption equilibrium constant (L/mg)
KP_i	potassium phosphate buffer
LC/MS	liquid chromatography/mass spectrometry
LMB	leucomethylene blue
m	mass of adsorbent (g)
MB	methylene blue
N_{ph}	solar flux density
OEC	oxygen evolving complex
Pheo	pheophytin
PSI	photosystem I
PSII	photosystem II
Q	plastoquinone
QH_2	plastoquinol
N_i	interstitial nitrogen
N_S	substitutional nitrogen
NHE	normal hydrogen electrode
q_e	adsorption capacity of dye (mg/g)
q_m	q_e for a complete monolayer of dye (mg/g)
SEM	scanning electron microscopy
t	time (h)
V	volume of dye solution
VB	valence band
XPS	X-ray photoelectron spectroscopy
XRD	X-ray diffraction

Abstract

Synthesizing narrow band gap semiconductors that absorb longer wavelengths of the solar spectrum ($\lambda \leq 550$ nm) is an active research area focusing on using sunlight and a photocatalyst for water splitting to evolve hydrogen gas as a renewable form of energy. Harnessing the energy of sunlight through electron transfer is useful for environmental remediation since industrial effluents often contain a significant concentration of organic dyes that require degradation. In this thesis, a variety of compounds are synthesized via a facile sol-gel approach in order to produce visible light harvesting compounds. The major contribution of the work outlined in this thesis details the composition, structure, absorption, and mechanism of dye degradation for a co-incorporated system, TiO_2:(Nb,N).

A series of co-incorporated compounds, TiO_2:(Nb,N), possessing the anatase structure have been prepared by a sol-gel technique. This technique allows us to synthesize mono-alloyed compositions, $Ti_{1-(5x/4)}Nb_xO_2$, which are converted to co-incorporated forms by annealing under flowing ammonia to afford $Ti_{1-(5x/4)}Nb_xO_{2-y-\delta}N_y$, referred to as NbN-*x*. We prepare the composition-dependent series and fully characterize the surface and bulk properties. High mole-percent niobium compositions exhibit the fastest rate constants for methylene blue dye degradation, 0.779 h^{-1} for NbN-25. This composition possesses maximum nitrogen incorporation, ~ 2 mole percent, with minimal Ti^{3+}. NbN-25 is active towards visible light ($\lambda \leq 515$ nm) water oxidation when loaded with 1 wt. % RuO_2 in the presence of an electron acceptor.

Visible light absorbing metal oxide titanates have been prepared and structurally characterized. Modified sol-gel processes were used to alloy various metal oxide phases—

titania, perovskite, and Ruddlesden-Popper. Thin films of TiO_2:Mn and $SrTiO_3$:Mn were prepared by spin casting precursor sols and annealing in air, affording phase pure compositions determined by X-ray diffraction and ICP analysis. Both phases absorb light into the visible part of the solar spectrum ($\lambda \leq 500$ nm); however, the presence of Mn^{3+} results in capacitive behavior that limits the use of the photoanodes towards water oxidation. Ruddlesden-Popper powders, $K_2La_2Ti_{3-x}Fe_xO_3$, absorb visible light to ~ 515 nm, and electrodes were prepared to examine the photoelectrochemistry.

Chapter 1. Introduction

1.1 Global energy demands

Worldwide energy consumption is projected to double by mid-century due to population and economic growth. Global energy demands could be met from fossil fuel sources; however the cumulative nature of CO_2 emissions presents immense environmental concerns.[1] An important scientific challenge of the 21st century targets addressing the world's energy demands by using clean, renewable energy. This will require scientists to develop innovative approaches towards creating carbon-neutral fuels. The United States' current energy consumption is dominated by non-renewable sources: petroleum, coal, and natural gas (81 %), shown in Figure 1.1.[2] Renewable energy (9 %) offers the promise of providing alternative fuel sources; however, employment of each renewable energy source is not a simple endeavor, with ongoing research occurring in all areas.[3–7] Solar energy is by far the largest useable source available— the sun delivers enough energy in a single day to meet global demands for years to come. The main challenge remains in finding efficient ways to harvest and store solar energy, which is currently an active area of research worldwide.

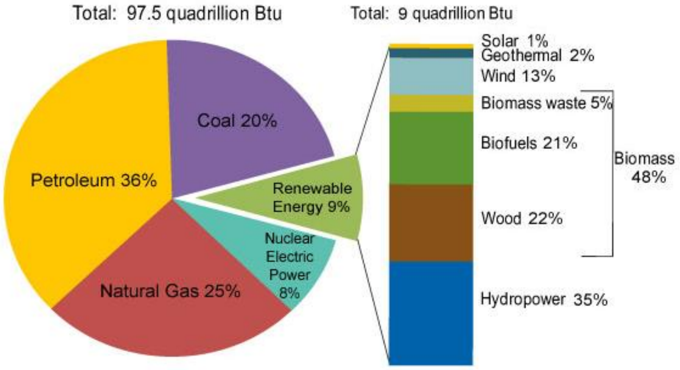

Figure 1.1 U.S. Energy Consumption by source.

1.2 Solar energy storage through water splitting

Due to the intermittency issues related to many of the renewable energy sources available, energy conversion and subsequent storage becomes a key component for research and development in these areas. For example, the sun only shines for a certain number of hours each day in a specific location. Efficiently harnessing, converting, and storing solar energy becomes an extremely important process in order to use solar energy as a viable alternative energy source. In recent years increased interest in the direct conversion of solar energy to chemical fuels has motivated research groups worldwide. An attractive scheme for this purpose involves the overall water splitting into hydrogen and oxygen, for which research draws inspiration from nature.

Natural photosynthesis is able to achieve solar to fuel conversion through use of solar energy, water, and carbon dioxide. Photosynthesis produces oxygen that is released into the atmosphere and hydrogen that combines with carbon dioxide to produce organic molecules and sugars.[8] The two primary light processes, requiring absorption of four photons each, occur at photosystem II (PSII) and photosystem I (PSI) through a series of electron transfer events. A photon absorbed by PSII generates $P680^+$, which is a very strong oxidizing agent. This step drives the water splitting reaction and reduction of pheophytin (Pheo) to plastoquinone (Q) and plastoquinol (QH_2). The oxygen evolving catalyst (OEC) in PSII serves as an electron donor, mediated by tyrosine, to $P680^+$. The OEC contains a multi-metallic core, $CaMn_4O_x$, which facilitates the multielectron nature of the water oxidation half reaction. The multielectron nature of manganese in the OEC core forms the motivation for synthetic targets discussed in Chapter 4. Once PSI absorbs light, a strong reducing species is formed, NAPDH, which reduces CO_2 to organic molecules and sugars. [9–12]

Overall water splitting and the production of carbohydrates from CO_2 and water can be summarized in the following two equations respectively:

$$2H_2O \rightarrow 2H_2 + O_2 \qquad (1)$$

$$2nCO_2 + 2nH_2O + h\nu \rightarrow 2(CH_2O)_n + 2nO_2 \qquad (2),$$

where various carbohydrates can result. The efficiency of photosynthesis is quite low— 1-2% for the best scenarios. However, this low efficiency is enough for global sustainability.[13] Research has focused on mimicking photosynthesis, referred to as artificial photosynthesis, achieved through targeting the overall water splitting reaction. The common component between photosynthesis and artificial photosynthesis involves the water oxidation half reaction.

Overall water splitting is comprised of the following two half reactions:

$$4H^+ + 4e^- \rightarrow 2H_2 \qquad (3)$$

$$O_2 + 4H^+ + 4e^- \rightarrow H_2O \qquad (4),$$

where protons are reduced to form hydrogen gas (equation 3), and water is oxidized to form oxygen gas (equation 4). The water oxidation reaction is much more complex than the reduction reaction, requiring four electrons and four protons. The overall reaction (equation 1) is thermodynamically uphill, requiring 474 kJ • mol^{-1} for the $4e^-$ process. In addition to the large positive free energy associated with the water oxidation half reaction, there is typically an overpotential of ~ 600 mV needed to overcome slow kinetics. Photocatalysts, either homogeneous or heterogeneous in nature, provide a means to drive overall water splitting in the forward direction. Light provides the free energy *and* allows the reaction to occur from an excited state with a lower activation barrier. In both homo- and heterogeneous systems, reliance on late transition metals and low conversion efficiencies have limited large scale application of water splitting systems to date.

Heterogeneous photochemical water splitting was introduced by Fujishima and Honda in 1976 when they first reported the utility of a rutile TiO_2 wafer as a photoelectrode capable of water splitting under UV irradiation.[14] In the presence of Fe^{3+}, a few mA of current flowed (~ 1 cm^2 electrode area), equating to a quantum efficiency of 0.1. Following this initial discovery, significant worldwide research efforts have focused on improving the efficiency of semiconductor systems— either through modifying band gaps of well studied wide band gap semiconductors, such as TiO_2, or through targeting novel photocatalyst compositions with narrow band gaps. In either approach, basic requirements for semiconductor photocatalyst dictate the utility of a semiconductor for photocatalytic applications, as is outlined in the next Section.

1.3 Fundamental requirements for a semiconductor photocatalyst

The photocatalytic properties of a semiconductor depend strongly on the electronics of the band structure. In an ideal semiconductor photocatalytic process, as illustrated in Figure 1.2, absorption of light higher in energy than the semiconductor's band gap creates an electron/hole pair, where electrons are excited from the valence band (VB) to the conduction-band (CB), thus creating holes in the VB.

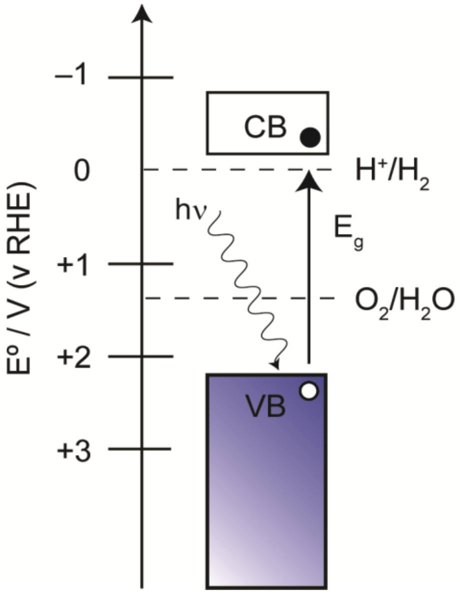

Figure 1.2 Ideal band structure for a semiconductor water splitting photocatalyst.

Four fundamental requirements for an efficient semiconductor photocatalyst are necessary for photocatalytic water splitting to proceed efficiently. First, in order to maximize absorbing longer wavelengths of the solar spectrum, the band gap should be ~ 2 eV, which corresponds to absorption of wavelengths less than ~ 620 nm and accounts for any associated overpotential. Traditionally, many wide band gap semiconductors, such as TiO_2[14] and $SrTiO_3$[15], have been explored as water splitting photocatalysts; however, their efficiencies are limited by their band gaps (≥ 3.0 eV), which corresponds to UV light absorption only.[16]

The drawback for UV active catalysts relates to the solar flux density, N_{ph}, in the UV and visible regions of the solar spectrum, shown in Figure 1.3. The solar spectrum is comprised of 2 % UV light ($\lambda < 400$ nm, $N_{ph} = 8.4 \times 10^{19}$ m^{-2} s^{-1}) compared to 47 % visible light ($400 < \lambda < 800$ nm, $N_{ph} = 1.6 \times 10^{21}$ m^{-2} s^{-1}) highlighted in grey in Figure 1.3. Approaches to modifying semiconductors to absorb longer wavelengths of light has been the subject of much research in order to maximize efficiency by absorbing light throughout the solar spectrum. Modifying semiconductors is nontrivial and will be discussed at greater detail in the next several sections.

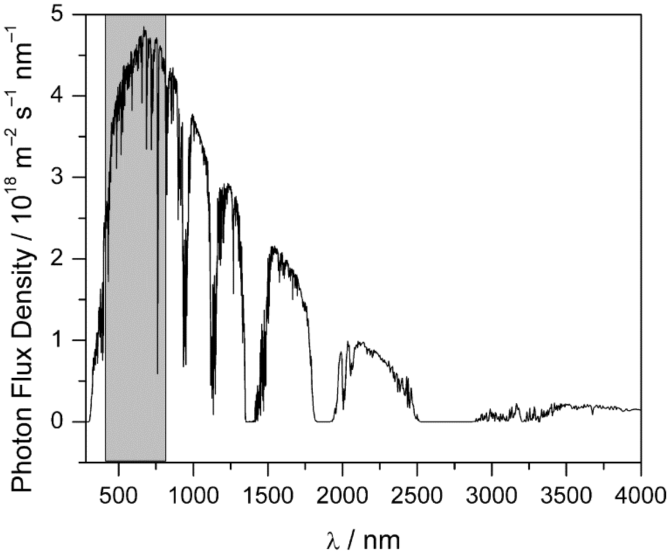

Figure 1.3 Photon flux density at various wavelengths of the solar spectrum.

Second, when targeting *overall water splitting* the band edge energies should straddle the water splitting half reactions, as illustrated in Figure 1.2. Upon irradiating a semiconductor and creating electron/hole pairs, the electrons and holes must be at sufficient energies in order for both half reactions to occur. The CB should be at an energy more negative than the proton reduction potential (0 V vs. NHE under standard conditions), and the VB energy should be more positive than the water oxidation potential (1.23 V vs. NHE under standard conditions) in order for overall water splitting to occur on a single semiconductor. In this thesis, the focus of our research is on the water oxidation half reaction, which requires the VB to be more positive than the water oxidation half reaction.

Furthermore, upon irradiating the photocatalyst, generating charge-carriers that subsequently migrate to surface reaction sites must occur rapidly with respect to recombination in the bulk of the material. Highly crystalline materials are attractive for suppressing recombination occurring at defect sites and grain boundaries simply because fewer defects exist. For example, metal oxides often contain oxygen vacancy defects, denoted as $\square_O^{\bullet\bullet}$ in Kröger-Vink notation, in order to achieve charge neutrality; however these sites can trap electrons and decrease photoactivity (Chapter 2).

Finally, the material must be chemically stable in the presence of reactive, oxidizing species. There are many attractive candidates with narrow band gaps for the overall water splitting reaction; however, the stability of some compounds, such as CdS and WO_3, limits their wide scale use. The degradation of these catalysts is caused by photogenerated holes degrading the compound in addition to oxidizing water. For example, metal oxides are targeted due to their abundance, affordability, and robustness. Efforts to target narrow band-gap metal oxides have focused on nitrogen substitution (N^{3-}) for oxygen (O^{2-}), resulting in oxynitride compounds.[17] Substitutional nitrogen can be decomposed by photogenerated holes as follows:

$$2N^{3-} + 6h^{+} \rightarrow N_{2(g)}, \qquad (6)$$

which evolves nitrogen gas. In this situation the compound is not stable for long irradiation periods— requiring modifying the semiconductor further (such as forming heterojunctions) or developing novel narrow band gap semiconductors. Furthermore, strict synthetic control over nitrogen content is difficult since most approaches rely on ammonolysis, which involves flowing ammonia at high temperatures over semiconductor particles. This process may only nitride the surface of the semiconductor, whereas bulk nitridation is desired. Designing alternative synthetic routes is a separate topic and will be discussed in Chapter 6.

1.4 Lattice and electronic structure of TiO_2

TiO_2 exhibits three different lattice phases: rutile, anatase, and brookite. Rutile and anatase are commonly used in photocatalysis, with anatase typically showing a higher photocatalytic activity due to higher electron mobility.[18] A third phase, brookite, is metastable and has not been highlighted in the literature as often. The structure of rutile and anatase is comprised of chains of TiO_6 octahedra, where each Ti^{4+} is surrounded by an octahedron of six O^{2-} ions. For rutile, there is a slight orthorhombic distortion to this octahedron. In anatase the symmetry is lowered due to significant distortion. The Ti—Ti distances in anatase are longer (3.79 Å and 3.04 Å vs. 3.57 Å and 2.96 Å in rutile) and the Ti—O distances are shorter (1.934 Å and 1.980 Å vs. 1.949 Å and 1.980 Å in rutile). Anatase has four edge and four corner sharing octahedra, shown in Figure 1.4a. The rutile structure, however, has two octahedra that share edge oxygen atoms and eight that share corner oxygen atoms, shown in Figure 1.4b. These differences account for different mass densities and electronic band structures between the two forms.[19]

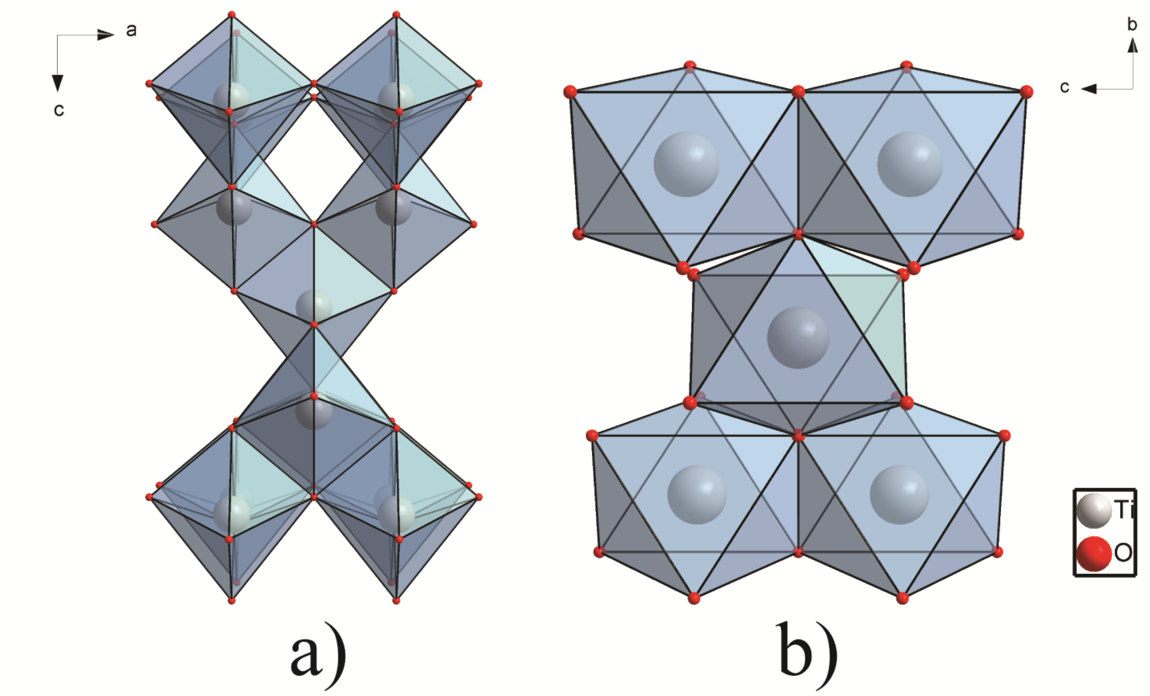

Figure 1.4 Crystal structures of a) anatase and b) rutile phase TiO_2.

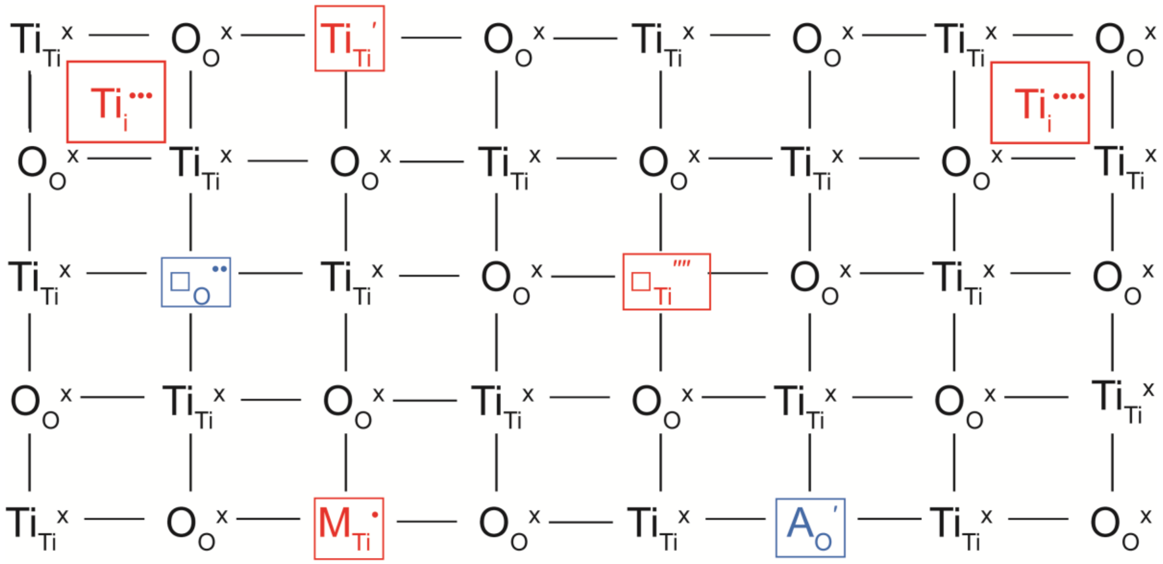

Figure 1.5 Schematic representation of point defects present in TiO_2 (adapted from ref. 20)

Table 1.1 Kröger-Vink notation and meanings.

Kröger-Vink notation	meaning
Ti_{Ti}^{x}	Ti^{4+} on titanium site
Ti_{Ti}'	Ti^{3+} on titanium site
O_{O}^{x}	O^{2-} ion on oxygen site
$\square_{Ti}''''$	Ti^{4+} vacancy
$Ti_{i}^{\bullet\bullet\bullet}$	Ti^{3+} interstitial ion
$Ti_{i}^{\bullet\bullet\bullet\bullet}$	Ti^{4+} interstitial ion
$\square_{O}^{\bullet\bullet}$	O^{2-} vacancy
$M_{Ti}^{\bullet}$	M^{5+} cation on Ti^{4+} site
A_{O}'	A^{3-} anion on O^{2-} site

Both rutile and anatase have filled valence bands comprised of O(2p) orbitals and empty conduction bands composed of Ti(3d), (4s) and (4p) orbitals. The lower portion of the conduction band is primarily Ti(3d) orbitals. It is important to note that TiO_2 is a nonstoichiometric compound that is commonly represented by the formula TiO_{2-x}, where x represents nonstoichiometry. The intrinsic ionic defects in undoped TiO_2 include oxygen vacancies, titanium interstitials, and/or titanium vacancies, illustrated in Figure 1.5 using Kröger-Vink notation to describe point defects, explained in Table 1.1.

Discussing the defect structure of TiO_2 is important in relation to the electronic structure, for point defects result in mid gap trap states (Section 1.5, Figure 1.6) that can either help or hinder photocatalysis (Chapter 2). Furthermore, oxygen vacancies result in an *n*-type material due to the concomitant formation of Ti^{3+} that results from charge compensation. Kröger-Vink notation is discussed throughout this thesis, since the majority of the work is focused on substituting aliovalent ions (Nb^{5+}) for Ti^{4+} in TiO_2. Possible charge mechanisms for Nb^{5+} substitution for Ti^{4+} is discussed in Chapter 2.

1.5 Band-gap engineering

This section highlights three approaches to modifying existing wide band gap semiconductors in order for the materials to absorb longer wavelengths of light— cation doping, anion doping, and co-incorporating. In the following sections, examples will only focus on modifying titanium dioxide, as it closely relates to the majority of the work presented throughout this thesis (Chapters 2 and 3). Figure 1.6 illustrates results that may arise when modifying TiO_2 with donors and/or acceptor ions and will be referenced in the following sections. In defect free TiO_2 the VB is comprised of O(2p) orbitals while the CB is composed of Ti(3d) orbitals.

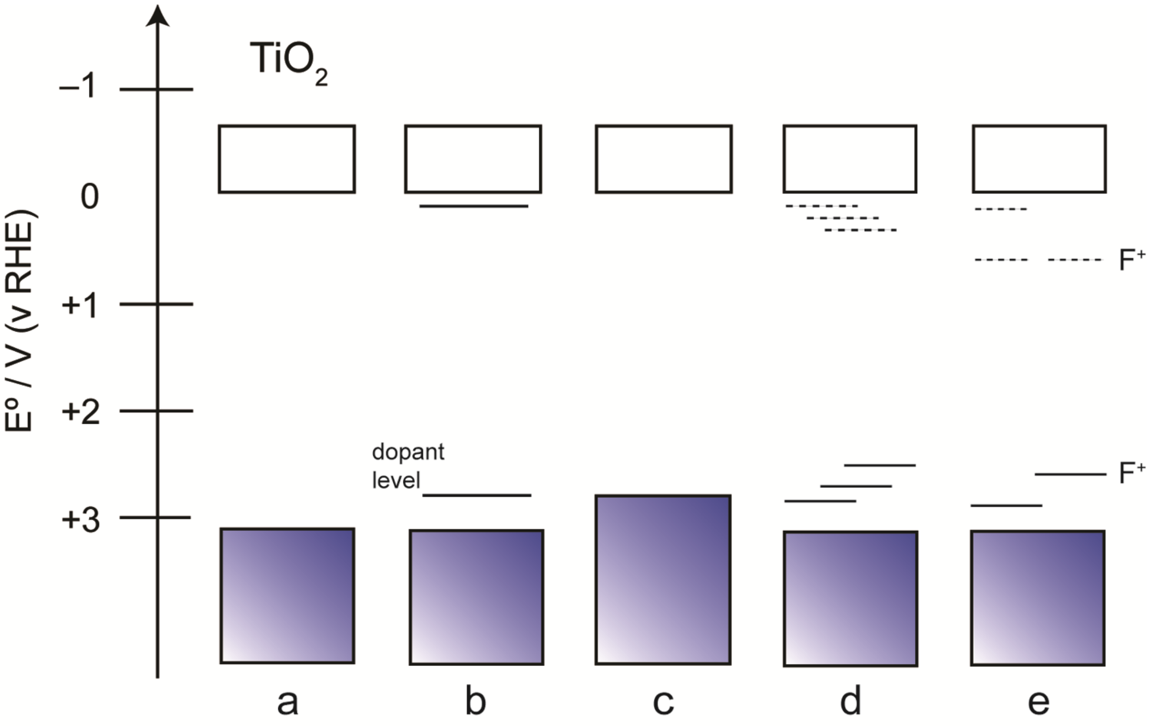

Figure 1.6 Various band structures resulting from introducing donor and/or acceptor ions in TiO_2: a) pristine TiO_2, b) localized dopant levels near CB and VB, c) localized dopant levels, arising from $\square_{O}^{\bullet}$ (F^+) and Ti^{3+} near the VB, and d) effective hybridization of O(2p) and N(2p) at the VB.

1.5.1 Cation doping

An approach to target narrow band gap semiconductors ($E_g < 3.0$ eV) relies on introducing metal cations via direct substitution for titanium on the crystal lattice site. However, in many cases, introducing transition metal dopants results in limited photocatalytic activity due to localized trap states near the VB or CB, illustrated in Figure 1.6b. Studies involving 3*d* metals incorporated in TiO_2 for photocatalytic applications in the past few years alone include the following examples: V,[21–26] Cr,[27–30] Mn,[31–35] Fe,[36–42] Co,[43–45] Ni,[46,47] Cu,[48–50] and Zn.[51–54] Research has not been limited to first row transition metals— 4d[55–58] and 5d[59–61] transition metal doping in TiO_2 has also been experimentally synthesized. Photocatalytic enhancement (~ 6-fold) has been observed for Ru-doped TiO_2 nanotubes compared to undoped TiO_2.[62] While some improvement in the photocatalytic activity of cation doped TiO_2 is reported, significant photocatalytic enhancement is limited by the defect-rich structures, motivating researchers to find alternative routes for modified TiO_2.

In all instances, substituting an aliovalent M^{n+} (M = transition metal, n = integer $\neq +4$) for Ti^{4+} in TiO_2 ($Ti_{1-x}M_xO_2$) requires charge compensation to preserve the principle of electroneutrality, which occurs in the form of interstitial cations/anions and/or cation/anion vacancies. Defect sites, Ti^{3+} and/or color centers, F^+ (electrons trapped on oxygen vacancies), contribute to the bathochromic shift in the absorption spectra for many of the complex metal oxide compositions. For example, incorporating Nb^{5+} for Ti^{4+} in TiO_2 has been the focus of experimental research for years due to improved conductivity properties.[63] The correct formula; however, depends upon the experimentally determined oxidation state of each cation in the structure. $Ti_{1-(5x/4)}Nb_xO_2$ would indicate complete Nb^{5+} substitution. Alternative charge compensation mechanisms for substituting Nb^{5+} for Ti^{4+} are discussed in Section 2.3.2.

1.5.2 Anion doping

In lieu of substituting a cation for titanium in TiO_2, another approach focuses on substituting an anion for oxygen in the titania sublattice. In 2001 Asahi and co-workers reported the oxidation of TiN to produce N-doped TiO_2, which was visible light active towards dye degradation.[64] This report opened the field for anion-doping to produce visible light active photocatalysts. Since then, reports on anion doping in TiO_2 include B-,[65] C-,[66] N-,[64,67] P-,[68–70] and S- doping,[71] along with various combinations of co-anion doping.[72–77] The motivation for anion doping in TiO_2 is to incorporate a less electronegative element than oxygen such that the orbital energy is higher and results in effective hybridization between O(2p) and N(2p) orbitals in the valence band. Incorporating nitrogen, which is less electronegative than oxygen (3.0 *vs.* 3.5 eV respectively), raises the VB and results in a lower band gap material (Figure 1.6d). Anion-doping creates localized dopant levels (Figure 1.6c) which act as trap states and limit photoactivity. However, N-doping in TiO_2 has led to enhanced photoactivity, resulting from interaction between the N dopant and Ti^{3+} that lead to increased IPCE values at wavelengths ≤ 550 nm.[78]

1.5.3 Co-alloying

The following question arises: How do we overcome these defect-rich structures that result from cation and anion doping? One recently explored approach to circumvent these issues is co-alloying with a donor-acceptor pair. The distinction between doping and alloying from the perspective of electronic structure must be discussed. To dope means to add localized states such that the Fermi level shifts in energy, but band edges remain unchanged (Figure 1.6b). To alloy means to alter the band edges, effectively hybridizing (O(2p) and N(2p) for instance) to form a new band with wider dispersion (Figure 1.6d). Calculations demonstrate that the band structure of anatase can be engineered to prepare visible light photocatalysts for water splitting. [79]

Research efforts both computationally[80–86] and experimentally have focused on numerous co-alloying pairs in TiO_2: (Nb,N),[87,88] (Ta,N),[89] (Mo,N),[90] (W,N),[91–93] and (W,C).[94] For the nitrogen examples, the photocatalytic activity increases (typically measured by the rate of organic dye degradation) compared to the TiO_2; however, charge compensation by the action of only the donor and acceptor pairs is not achieved, resulting in *co-incorporated* compositions with localized N(2p) levels just above the valence band. A real research challenge lies in synthetic control over donor-acceptor pairs as well as targeting specific donor-acceptor compositions to result in the greatest photoactivity.

1.6 Outline and scope of this thesis

This thesis is structured around the synthesis, characterization, and photocatalytic activity of narrow band gap complex metal oxides for photocatalytic applications— specifically degradation of methylene blue dye (Chapter 2) and water oxidation (Chapters 3 and 4). Chapter 4 will highlight various synthetic strategies and complex metal oxide structures that we have targeted for water oxidation photocatalysts, with specific focus on the challenges associated with our targets.

Chapter 2 highlights a facile sol-gel route for synthesizing a novel co-incorporated system, TiO_2:(Nb,N). The co-incorporated system will be discussed in great detail— its preparation, structure, composition, and electronic structure, as well as fundamental understanding of surface and bulk properties that contribute to the function of this compound as a photocatalyst. In particular, emphasis is placed on tuning the absorption spectrum through compositional control and examining the resulting reactivity and mechanism of methylene blue dye degradation.

Following the studies in Chapter 2, using the compound $Ti_{1-(5x/4)}Nb_xO_{2-y-\delta}N_y$, denoted NbN-25 throughout, to photocatalytically oxidize water will be the focus of Chapter 3. The necessity of a co-catalyst (RuO_2) and sacrificial electron acceptor (IO_3^-) in order to drive the water oxidation half reaction will be discussed, complete with optimizing co-catalyst weight percent loading and cut-on experiments to measure the rate of oxygen evolution at various wavelengths.

Chapter 4 highlights synthetic efforts for thin films and powders of various structure types for photocatalytic applications— titania, perovskites, and layered perovskites. We report their syntheses, characterization, and electrochemistry of either thin film or powdered films of these structure types, highlighting the potential new science and limitations to the compositions we targeted.

Chapter 5 presents collaborative efforts pursued with Professor Rudy Luck at Michigan Technological University, with specific focus on the magnetism of dinuclear cobalt complexes. Chapter 6 will offer insight into non-hydrolytic sol-gel routes for incorporating nitrogen into titanium dioxide, a new approach for constructing powdered electrodes, and new synthetic targets for over water splitting photocatalysts.

Following the main thesis, there are appendices containing supporting data pertinent to certain chapters. Appendix A contains physical characterization results that complement the story told in Chapters 2 and 3, while Appendix B includes data for Chapter 4. The appendix figures are appropriately referenced in each chapter.

1.7 References

1 Lewis, N. L.; Nocera, D. G. Proc. Natl. Acad. Sci. U.S.A **2006**, *103*, 15729-15735.

2 Energy Information Administration; U.S. Department of Energy, www.eia.doe.gov (accessed December 2012).

3 Turner, J. A. *Science*, **1999**, *285*, 687-689.

4 Reece, S. Y.; Hamel, J. A.; Sung, K.; Jarvi, T. D.; Esswein, A. J.; Pijpers, J. J. H.; Nocera, D. G. *Science* **2011**, *334*, 645-648.

5 O'Regan, B.; Grätzel, M. *Nature*, **2001**, *353*, 737-740.

6 Osterloh, F. E. *Chem. Soc. Rev.* **2012**, doi: 10.1039/c2cs35266d.

7 Details on renewable energy sources are available from the National Renewable Energy Laboratory (NREL), http://www.nrel.gov/ceb.html.

8 Barber, J. *Chem. Soc. Rev*, **2009**, *38*, 185–196.

9 Najafpour, M. M.; *Plant Biosyst*. **2006**, *140*, 163-170.

10 McEvoy, J. P.; Brudvig, G. W. *Chem. Rev*. **2006**, *106*, 4455-4483.

11 Yano, J.; Yachandra, V. K. *Inorg. Chem.* **2008**, *47*, 1711-1726.

12 Najafpour, M. M. *Origins Life Evol. Biosphere* **2009**, *39*, 151-163.

13 Cook, T. R.; Dogutan, D. K.; Reece, S. Y.; Surendranath, Y.; Teets, T. S.; Nocera, D. G. *Chem. Rev.* **2010**, *110*, 6474-6502.

14 Fujishima, A.; Honda, K. *Nature* **1972**, *238*, 37-38.

15 Wrighton, M. S.; Ellis, A. B.; Wolczanski, P. T.; Morse, D. L.; Abrahamson, H. B.; Ginley, D. S. *J. Am. Chem. Soc.* **1976**, *98*, 2774-2779.

16 Osterloh, F. E. *Chem. Soc. Rev.* **2013**, *42*, 2294-2320.

17 Maeda, K.; Domen, K. *J. Phys. Chem. C* **2007**, *111*, 7851-7861.

18 Tang, H.; Prasad, K.; Sanjinès, R.; Schmid, P. E.; Lévy, F. *J. Appl. Phys.* **1994**, *75*, 2042-2047.

19 Linsebigler, A. L.; Lu, G.; Yates, J. T. *Chem. Rev.* **1995**, *95*, 735-758.

20 Kubacka, A.; Fernández-García, M.; Colón, G. *Chem. Rev.* **2012**, *112*, 1555-1614.

21 Islam, M. M.; Bredow, T.; Gerson, A. *Chem. Phys. Chem.* **2011**, *12*, 3467-3473.

22 Chang, S-M.; Liu, W-S. *App. Cat. B: Environ.* **2011**, *101*, 333-342.

23 Hoang, L. H.; Hai, P. V.; Hanh, P. V.; Nguyen, H. H.; Chen, X-B.; Yang, I-S. *Mater. Lett.* **2011**, *65*, 3047-3050.

24 Cimieri, I.; Pelman, H.; Nursen, A.; Geens, J.; Lambert, S. D.; Heinrichs, B.; Poelman, D. *J. Sol-Gel Sci. and Technol.* **2012**, *63*, 526-536.

25 Lin, W-C.; Lin, Y-J. *Environ. Eng. Sci.* **2012**, *29*, 447-452.

26 Khakpash, N.; Simchi, A.; Jafari, T. *J. Mater. Sci. Mater. in Electron.* **2012**, *23*, 659-667.

27 Jaimy, K. B.; Gosh, S.; Sankar, S.; Warrier, K. G. K. *Mater. Res. Bull.* **2011**, *46*, 914-921.

28 Peng, Y-H,; Huang, G-F.; Huang, W-Q. *Adv. Powder Technol.* **2012**, *23*, 8-12.

29 Wang, L.; Egerton, T. A. *Adv. Mater. Res.* **2012**, 502-506.

30 Xie, Y.; Huang, N.; You, S.; Liu, Y.; Sebo, B.; Liang, L.; Fang, X.; Liu, W.; Guo, S.; Zhao, X-Z. *J. Power Sources* **2013**, *224*, 168-173.

31 Ni, Y.; Zhu, Y.; Ma, X. *Dalton Trans.* **2011**, *40*, 3689-3694.

32 Deng, Q. R.; Xia, X. H.; Guo, M. L.; Gao, Y.; Shao, G. *Mater. Lett.* **2011**, *65*, 2051-2054.

33 Liu, S.; Guo, E.; Yin, L. *J. Mater. Chem.* **2012**, *22*, 5031-5041.

34 Pereira, A. L. J.; Gracia, L.; Beltran, A.; Lisboa-Filho, P. N.; da Silva, J. H. D.; Andres, J. *J. Phys. Chem. C* **2012**, *116*, 8753-8762.

35 Shahmoradi, B.; Negahdar, M; Maleki, A. *Environ. Eng. Sci.* **2012**, *29*, 1032-1037.

36 Wu, Q.; Ouyang, J.; Xie, K.; Sun, L.; Wang, M.; Lin, C. *J. Hazard. Mater.* **2012**, *199*, 410-417.

37 Yu, S.; Yun, H. J.; Lee, D. M.; Yi, J. *J. Mater. Chem.* **2012**, *22*, 12629-12635.

38 He, M.; Li, D.; Jiang, D.; Chen, M. *J. S. S. Chem.* **2012**, *192*, 139-143.

39 Delekar, S. D.; Yaday, H. M.; Achary, S. N.; Meena, S. S.; Pawar, S. H. *Appl. Surf. Sci.* **2012**, *263*, 536-545.

40 Li, J-Q.; Wang, D-F.; Guo, Z-Y.; Zhu, Z-F. *Appl. Surf. Sci.* **2012**, *263*, 382-388.

41 Su, R.; Bechstein, R.; Kibsgaard, J.; Vang, R. T.; Besenbacher, F. *J. Mater. Chem.* **2012**, *22*, 23755-23758.

42 Dukes, F. M.; Iuppa, E.; Meyer, B.; Shultz, M. J. *Langmuir* **2012**, *28*, 16933-16940.

43 Le, T. T.; Akhtar, M. S.; Park, D. M.; Lee, J. C.; Yang, O-B. *Appl. Catal. B.: Environ.* **2012**, *111*, 397-401.

44 Ganesh, I.; Gupta, A. K.; Kumar, P. P.; Chandra Sekhar, P. S.; Radha, K.; Padmanabham, G.; Sundararajan, G. *Mater. Chem. and Phys.* **2012**, *135*, 220-234.

45 Hamal, D. B.; Klabunde, K. J. *J. Phys. Chem. C* **2011**, *115*, 17359–17367.

46 Mercado, C.; Seeley, Z.; Bandyopadhyay, A.; Bose, S.; McHale, J. L. *ACS Appl. Mater. & Inter.* **2011**, *3*, 2281-2288.

47 Singn, D.; Singh, N.; Sharma, S. D.; Kant, C.; Sharma, C. P.; Pandey, R. R.; Saini, K. K. *J. Sol-Gel Sci. and Technol.* **2011**, *58*, 269-276.

48 Lin, W-C.; Yang, W-D. *Adv. Mater. Res.* **2012**, *391*, 728-731.

49 Zhang, M.; Li, L.; Meng, X. *Adv. Mater. Res.* **2011**, *197*, 1028-1031.

50 Yonghong, Ni.; Zhu, Y. *Dalton Trans.* **2011**, *40*, 3689-3694.

51 Huang, F.; Li, Q.; Thorogood, G. J.; Cheng, Y-B.; Caruso, R. A. *J. Mater. Chem.* **2012**, *22*, 17128-17132.

52 Chauhan, R.; Kumar, A.; Chaudhary, R. P. *J. Sol-Gel Sci. and Technol.* **2012**, *61*, 585-591.

53 Liu, Q.; Zhou, Y.; Duan, Y.; Lin, Y. *Appl. Mech. and Mater.* **2011**, *66*, 224-228.

54 Zhao, D. F.; Lu, H. D.; Tian, C. *Adv. Mater. Res.* **2011**, *239*, 3090-3095.

55 Yang, Min.; Jha, H.; Liu, N.; Schmuki, P. *J. Mater. Chem.* **2011**, *21*, 15205-15208.

56 Das, C.; Roy, P.; Yang, M.; Jha, H.; Schmuki, P. *Nanoscale*, **2011**, *3,* 3094-3096.

57 Luo, S-Y.; Yan, B-X.; Shen, J. *Thin Solid Films*, **2012**, *522*, 361-365.

58 Gutierrez, C.; Salvador, P. *J. Electroanal. Chem. and Inter. Electrochem.* **1985**, *187*, 139-150.

59 Choi, W.; Termin, A.; Hoffman, M. R. *J. Phys. Chem.* **1994**, *98*, 13669-13679.

60 Choi, J-H.; Kwon, S-H.; Jeong, Y-K.; Kim, I.; Kim, K-H. *J. Electrochem. Soc.* **2011**, *158*, B749-753.

61 Liu, S.; Guo, E.; Yin, L. *J. Mater. Chem.* **2012**, *22*, 5031-5041.

62 Roy, P.; Das, C.; Lee, K.; Hahn, R.; Ruff, T.; Moll, M.; Schmuki, P. *J. Am. Chem. Soc.* **2011**, *133*, 5629-5631.

63 Furubayashi, Y.; Hitosugi, T.; Yamamoto, Y.; Inaba, K.; Kinoda, G.; Hirose, Y.; Shimada, T.; Hasegawa, T. *Appl. Phys. Lett.* **2005**, *86*, 252101.

64 Asahi, R.; Morikawa, T.; Ohwaki, T.; Aoki, K.; Taga, Y. *Science* **2001**, *293*, 269-271.

65 Zheng, J.; Liu, Z.; Liu, X.; Yan, X.; Li, D.; Chu, W. *J. Alloys Comp.* **2011**, *509*, 3771-3776.

66 Cheng, C.; Sun, Y. *App. Surf. Sci.* **2012**, *263*, 273-276.

67 Zhang, J.; Wu, Y.; Xing, M.; Leghari, S. A. K.; Sajjad, S. *Energy Environ. Sci.* **2010**, *3*, 715-726.

68 Gopal, N. O.; Lo, H-H.; Ke, T-F.; Lee, C-H.; Chou, C-C.; Wu, J-D.; Sheu, S-C.; K, S-C. *J. Phys. Chem. C* **2012**, *116*, 16191-16197.

69 Peng, Y.; He, J.; Liu, Q.; Xun, Z.; Yan, W.; Pan, Z.; Wu, Y.; Liang, S.; Cheng, W.; Wei, S. *J. Phys. Chem. C* **2011**, *115*, 8184-8188.

70 Li, F.; Jiang, Y.; Xia, M.; Sun, M.; Xue, B.; Liu, D.; Zhang, X. *J. Phys. Chem. C*, **2009**, *113*, 18134-18141.

71 Xu, P.; Xu, T.; Lu, J.; Gao, S.; Hosmane, N. S.; Huang, B.; Dai, Y.; Wang, Y. *Energy Environ. Sci.* **2010**, *3*, 1128-1134.

72 Liu, G.; Yin, L-C.; Wang, J.; Niu, P.; Zhen, C.; Xie, Y.; Cheng, H-M. *Energy Environ. Sci.* **2012**, *5*, 9603-9610.

73 Xu, Q. C.; Zhang, Y.; He, Z.; Joachim, S. C.; Tan, L. T. T. Y. *J. Nano. Res.* **2012**, *14*, 1042/1-12.

74 Zhou, X.; Jin, B.; Zhang, S.; Wang, H.; Yu, H.; Peng, F. *Electrochem. Comm.* **2012**, *19*, 127-130.

75 Tian, H.; Hu, L.; Zhang, C.; Mo, L.; Li, W.; Sheng, J.; Dai, S. *J. Mater. Chem.* **2012**, *22*, 9123-9130.

76 Xing, M-Y.; Li, W-K.; Wu, Y-M.; Zhang, J-L.; Gong, X-Q. *J. Phys. Chem. C* **2011**, *115*, 7858-7865.

77 Etacheri, V.; Seery, M. K.; Hinder, S. J.; Pillai, S. C. *Inorg. Chem.* **2012**, *51*, 7164-7173.

78 Hoang, S.; Berglund, S. P.; Hahn, N. T.; Bard, A. J.; Mullins, C. B. *J. Am. Chem. Soc.* **2012**, *134*, 3659-3662.

79 Li, Y-F.; Xu, D.; Oh, J. I.; Shen, W.; Li, X.; Yu, Y. *ACS Catal.* **2012**, *2*, 391-398.

80 Gai, Y.; Li, J.; Li S.; Xia, J.; Wei, S. *Phys. Rev. Lett.* **2009**, *102*, 036402/1-3.

81 Yin, W.-J.; Tang, H.; Wei, S.-H.; Al-Jassim, M. M.; Turner, J.; Yan, Y. *Phys. Rev. B* **2010**, *82*, 045106/1-6.

82 Wang, P.; Liu, Z.; Lin, F.; Zhou, G.; Wu, J.; Duan, W.; Gu, B.; Zhang, B. *Phys. Rev. B*, **2010**, *82*, 193103.

83 Ma, X.; Wu, Y.; Lu, Y.; Xu, J.; Wang, Y. ; Zhu, Y. *J. Phys. Chem. C* **2011**, *115*, 16963-16969.

84 Yin, W. -J; Wei, S.; Al-Jassim, M. M.; Yan, Y. *Phys. Rev. Lett.* **2011**, *106*, 066801/1-4.

85 Márquez, A.M.; Plata, J. J.; Ortega, Y.; Sanz, J. F. *J. Phys. Chem. C* **2012**, *116*, 18759-18767.

86 Çelik, V.; Mete, E.; *Phys. Rev. B.* **2012**, 205112.

87 Cottineau, T.; Béalu, N.; Gross, P-A.; Pronkin, S. N.; Keller, N.; Savinova, E. R.; Keller, V. *J. Mater. Chem. A* **2013**, *1*, 2151-2160.

88 Breault, T. M.; Bartlett, B. M. *J. Phys. Chem. C* **2012**, *116*, 5986-5994.

89 Hoang, S. H.; Guo, S.; Mullins, C. B. *J. Phys. Chem. C* **2012**, *116*, 23283-23290.

90 Li, M.; Zhang, J.; Zhang, U. *Catal. Comm.* **2012**, *19*, 175-179.

91 Li, M.; Zhang, J.; Zhang, Y. *Chem. Phys. Lett.* **2012**, *527*, 63-66.

92 Marquez, A. M.; Plata, J. J.; Ortega, Y.; Sanz, J. F.; Colon, G.; Kubacka, A.; Fernandez-Garcia, M. *J. Phys. Chem. C* **2012**, *116*, 18759-18767.

93 Thind, S.; Wu, G.; Tian, M.; Chen, A. *Nanotechnol.* **2012**, *23*, 475706/1-8.

94 Neville, E. M.; Mattle, M. J.; Loughrey, D.; Rajesh, B.; Rahman, M.; MacElroy, J. M. D.; Sullivan, J. A.; Thampi, K. R. *J. Phys. Chem. C* **2012**, *116*, 16511-16521.

Chapter 2. Development of Novel Co-incorporated Compounds for Dye Degradation

Portions of this chapter have been published:
Breault, T. M.; Bartlett, B. M. *J. Phys. Chem. C* **2012**, *116*, 5986-5994. Reprinted with permission. Copyright 2012 American Chemical Society.
Figures: 2.1, 2.2, 2.3, 2.4; Table: 2.1

Breault, T. M.; Bartlett, B. M. *J. Phys. Chem. C* **2013**, *in revision*.
Figures: 2.8, 2.9, 2.10, 2.12, 2.13, 2.14

2.1 Introduction

Of the design strategies for targeting narrow band gap semiconductors outlined in Chapter 1, co-alloying in TiO_2 is the least explored area, with recent interest, both computationally[1–7] and experimentally[8–27], emerging over the past several years. Through co-alloying, it is predicted that isoelectronic 4d (Nb^{5+} or Mo^{6+}) and 5d (Ta^{5+} or W^{6+}) cations residing on the titanium crystallographic sites result in orbital mixing with the d^0 Ti 3d conduction band, and charge-compensating anions such as N^{3-} or P^{3-} residing on the oxygen sites results in orbital mixing at the top of the valence band. This gives rise to overall lower band-gap materials with suitable band edges for chemical reactions requiring active oxygen species, such as organic dye degradation.

One such promising combination from recent computational work is TiO_2:(Nb,N) in a high mole-percent regime (12.5% oxygen is replaced by nitrogen in the anion lattice, with 25% niobium replacing titanium on the cation sublattice to compensate the charge), where the band-gap is predicted to be ~ 2.50 eV.[28] In addition, recent calculations on Nb- and C- co-incorporated TiO_2 demonstrate that the conduction-band edge is unchanged in the altered composition;[29] thus providing motivation for experimentally investigating co-incorporated Nb- and N- in TiO_2. Furthermore, previous studies showed that the anatase structure is found to be more active toward the photocatalytic degradation of dyes than is rutile based on electron mobility.[30]

We chose to begin our photocatalytic studies by degrading an organic dye, which can undergo electron transfer processes from the photoexcited semiconductor to generate highly reactive radicals that facilitate the degradation process. For the dye itself, we chose methylene blue (MB), a potentially hazardous, water soluble pollutant common in dying cotton, wood, and silk. Its decomposition in water using semiconductor photocatalysts has been explored,[31–33] and dye degradation using TiO_2 and its doped/alloyed derivatives was recently reviewed.[34] The two key aspects to consider for enhancing catalytic activity are 1) tuning the composition to lower the band-gap and delocalize charge carriers, and 2) increasing the surface area for faster dye adsorption in the dark, both of which will be discussed in this chapter.

The work presented in this chapter develops a facile sol-gel approach for synthesizing a series of novel *co-incorporated* compounds, with the general composition TiO_2:(Nb,N). We investigate the composition dependence on both niobium incorporation and the effect of annealing under flowing ammonia for various time periods. In order to probe the structure-function relationship of these compounds, we describe the composition, probe the electronic structure at the surface and bulk, and present photocatalytic activity for MB degradation.

2.2 Experimental

2.2.1 Materials and general procedures

Reagent grade chemicals were obtained from Aldrich or Strem. Titanium(IV) butoxide (Aldrich) and niobium(V) chloride (Strem) were stored and weighed in a nitrogen filled glove box (Vacuum Atmospheres Nexus II). 2-methoxyethanol (2-MOE) (Aldrich) was distilled prior to use. Sol-gel reactions were carried out in custom made 4 mL quartz crucibles. An MTI box furnace was used to anneal gels under air. An MTI tube furnace, fitted with a PurityPlus Stainless Steel Flowmeter, was used to anneal powders under flowing oxygen or anhydrous ammonia. The commercial P-25 TiO_2 (80% anatase, 20% rutile, BET area, 50 m^2/g) supplied by Degussa Corporation was used for comparison. Millipore water (18.2 MΩ) was used for all experiments.

2.2.2 Synthesis of TiO_2:(Nb,N) and congeners

Oxide precursors were prepared by a sol-gel route. In a typical synthesis, 0.181 g of niobium(V) chloride and 0.68 mL of titanium(IV) butoxide were dissolved in a 1:3 mole ratio in 2 mL of 2-methoxyethanol and stirred until transparent and colorless. The colorless and transparent solution was allowed to stir at room temperature overnight before annealing in quartz crucibles in an MTI box furnace at 500 °C for 12 hours, with 2 hour heating and cooling periods. The obtained white powders (~ 100-250 mg) were then annealed in a tube furnace under flowing ammonia (110 mL/min) for 4 hours and subsequently cooled under flowing N_2 for 6 hours. Yield: 0.245 g (100% based on starting 25% Nb).

TiO_2, TiO_2:Nb, and TiO_2:N were similarly prepared according to the procedure outlined above. Briefly, TiO_2 was synthesized by dissolving 0.68 mL titanium(IV) butoxide in 2 mL of 2-MOE and annealing under air at 500 °C for 12 hours. TiO_2:N was prepared by taking the as prepared TiO_2 and annealing under flowing NH_3 (110 mL/min) for 4 hours, with cooling under nitrogen. We emphasize that TiO_2:N denotes the synthetic approach of annealing under ammonia and does not indicate the presence of substitutional nitrogen incorporation, *vide infra*.

2.2.3 Synthesis of TiO_2:(Nb,N)-1, -2, and -3

TiO_2:(Nb,N)-**1**, was synthesized by annealing the TiO_2:Nb precursor sol under air followed by nitridation under ammonia. TiO_2:(Nb,N)-**2** was generated by heating the as synthesized compound (TiO_2:(Nb,N)-**1**) to 500 ºC under flowing O_2 at a rate of ~110 mL/min for 5 hours in the tube furnace. Finally, annealing the TiO_2:Nb precursor sol described in Section 2.2.2 in flowing O_2 for 12 h, followed by ammonia at 500 °C for 4 h generated the compound TiO_2:(Nb,N)-**3**.

2.2.4 Synthesis of NbN-*x* and NbN-25-*z*

The desired mole ratio of niobium(V) chloride and titanium(IV) butoxide was dissolved in 2 mL of 2-MOE and annealed at 500 °C for 12 hours. Target compounds include 1, 5, 10, 15, 20, 25, and 30 % niobium incorporation for titanium. All compounds were subjected to identical nitridation treatments, in which the isolated niobium-alloyed compound was annealed at 500 °C under flowing NH_3 for 4 hours. Compounds are herein identified as NbN-*x*, where *x* represents the target mole-percent of niobium (*e.g.* NbN-1 is 1% Nb in TiO_2, annealed under NH_3, 4 hours).

Furthermore, we held the temperature and ammonia flow rate constant, 500 °C and 110 mL/min respectively, and varied nitridation time for one alloyed composition, Nb-25. Dwell periods of 0, 1, 2, 3, 4, 5, and 6-hour dwell periods were used, and resulting compounds are denoted as NbN-25-*z*, where *z* is the dwell time.

2.2.5 Physical methods

X-ray diffraction patterns were recorded on a Bruker D8 Advance diffractometer equipped with a graphite monochromator, a Lynx-Eye detector, and parallel beam optics using Cu-Kα radiation ($\lambda = 1.54184$ Å). Patterns were collected using a 0.6 mm incidence slit, with a step size and scan rate of 0.05°/step and 2 s/step respectively. Tungsten powder was used as an internal standard for all refined x-ray diffraction patterns. Phases were identified as anatase TiO_2 (JCPDF 71-1166) using MDI Jade version 5.0. Observed TiO_2 Bragg reflections were compared to those calculated from the single crystal X-ray structure.[35]

UV-Vis spectra were recorded using an Agilent-Cary 5000 spectrophotometer equipped with a Praying Mantis diffuse reflectance accessory. Spectra were recorded in reflectance mode and transformed mathematically into the normalized Kubelka-Munk function, $F(R) = (1-R)^2/2R$. Tauc plots were generated using this function. X-ray photoelectron spectra were recorded on a Kratos XPS (8 mA, 14 keV, Monochromatic Al). Samples were secured to the transfer bar via copper tape and were subsequently pumped overnight under high vacuum to 1×10^{-9} torr. All peaks were calibrated to C(1s) at 284.5 eV, which is attributed to adventitious carbon. The XPS data were fit using CasaXPS program.

Scanning electron microscopy (SEM) images and energy dispersive X-ray (EDX) spectra were obtained using an FEI Nova Nanolab SEM/FIB with an accelerating voltage of 10 kV and 15 kV respectively. Nb_2O_5 and TiO_2 were used as standards for EDX spectra. Electron paramagnetic resonance (EPR) spectra were recorded on a Brüker X-band frequency (9.3 GHz) EMX spectrometer at 298, 77 K, and 4 K. The microwave power and frequency were 20.51 mW and 9.28 GHz, respectively with modulation amplitude of 1.00 G at 100 KHz.

The nitrogen sorption isotherms were obtained at 77 K using a Quantachrome Instrument (Boynton Beach, Florida U.S.A.). Ultrahigh purity N_2 (99.999%) was purchased from Cryogenic Gases. The surface areas were determined by the Brunauer-Emmett-Teller (BET) model using multiple points. IR spectra were collected on a Bruker alpha-P ATR instrument. LC/MS analyses were performed on a Micromass LCT time-of-flight mass spectrometer.

2.2.6 Adsorption isotherms

Isotherm experiments were performed using a constant mass of TiO_2 sample (10 mg in 10 mL) and adding regular aliquots of 500 mg/L methylene blue (MB) every 30 minutes. The adsorption capacity (q_e, mg/g) was obtained by $q_e = \frac{(C_0 - C_e)V}{m}$, where C_0 is the initial dye concentration in the liquid phase (mg/L), C_e is the liquid phase dye concentration at equilibrium (mg/L), V is the volume of dye solution used (L), and m is the mass of adsorbent used (g). Kinetic studies on the adsorption of methylene blue were carried out in the dark to determine the dark adsorption equilibria.

2.2.7 Photodegradation of methylene blue

Methylene blue dye photodegradation measurements were performed using a custom-built Pyrex glass cell fitted with a quartz viewing window. A Newport-Oriel 150 W Xe arc lamp, focusing lens, and an AM1.5G filter were used to simulate solar irradiation. An ice bath was used to maintain the temperature at ~ 25 °C. 50 mg of photocatalyst was dispersed in 50 mL of 40 ppm methylene blue solution and was allowed to equilibrate in the dark for 3 hours prior to irradiation. The degradation was monitored spectrophotometrically by taking two 3 mL aliquots every 30 minutes, centrifuging them for 10 min at 3500 rpm, and monitoring the absorbance at 665 nm. The aliquots were returned to the cell after absorbance measurements were recorded.

2.3 Results and discussion

2.3.1 Structure and characterization of TiO_2:(Nb,N) under ambient conditions

The co-incorporated compound TiO_2:(Nb,N)-**1** was prepared via sol-gel processing. We synthesized the control compounds TiO_2, TiO_2:N, and TiO_2:Nb via the same process for comparison. We emphasize that each compound in this series was not optimized for each individual composition, rather each compound was subjected to the same treatment for comparison purposes. We compare all of the physical properties and rates of dye degradation (*vide infra*) for all of the compounds in this study directly in Table 2.1 and highlight specific results in this section. Notably, all of the compounds synthesized in this study crystallize in the anatase form (Figure A.1). Important to the phase purity of our material, we note that the infinite-time temperature for the anatase to rutile phase transition under atmospheric pressure occurs at a higher temperature, 610 ºC,[36] than the 500 ºC annealing temperature employed in our reaction. Accordingly, anatase is the only phase present in the X-ray diffraction analysis. We expect to see a larger *d*-spacing as the larger niobium inserts on the 4a Wyckoff site. Indeed, the *d*-spacing increases from 3.515 Å in TiO_2 to 3.542 Å with added niobium. The digestion of these compounds was not achieved for elemental analysis, so we used energy dispersive X-ray (EDX) spectroscopy to analyze the chemical composition of the compounds containing Ti and Nb. The Ti:Nb mole ratio was 2.9 for TiO_2:Nb and 3.3 for TiO_2:(Nb,N), which well agrees with the targeted Ti:Nb ratio of 3 (Figure A.2).

Table 2.1 Lattice parameters, band gap, surface area, particle size, dye adsorbance, first order rate constants for anatase-structured congeners.

	P-25	TiO_2	TiO_2:N	TiO_2:Nb	TiO_2:(Nb,N)-**1**	TiO_2:(Nb,N)-**2**	TiO_2:(Nb,N)-**3**
a / Å	—	3.7830	3.7834	3.8219	3.8168	3.8151	3.8167
c / Å	—	9.5089	9.5157	9.5273	9.5288	9.5304	9.5490
E_g / eV	3.20	2.97	2.90	3.05	2.01	2.44	2.29
SA / $m^2 \bullet g^{-1}$	54	2	41	68	63	52	47
Particle size / nm	21	1500	40	20	20	20	20
N_s/N_i by XPS	—	—	—	—	0.593	0.220	0.176
q_e / mg • g^{-1}	—[a]	0	0	21	36	32	33
$k_{40\text{ ppm MB}}/h^{-1}$	0.561	0.155	0.0556	0.366	1.203	0.234	0.439

[a] Dye adsorbance was not experimentally determined due to the low density of the P-25 TiO_2, which required both centrifugation and filtration for absorbance readings, which made it difficult to construct adsorption isotherms.

Nitrogen sorption isotherms reveal that despite very similar preparative methods, the alloyed materials generated from the sol-gel synthesis show dramatically different surface area and porosity than their TiO_2 analogue (Figure A.3). The surface area of anatase TiO_2 is low, only 2 m^2/g. However, all of the alloyed compounds have surface areas in the range 41–68 m^2/g, similar to that of commercial P-25 (50 m^2/g). Moreover, hysteresis is observed in the sorption isotherms of the alloyed compounds, indicating mesoporosity, which is useful for catalysis if substrate can be adsorbed into the pores without blocking the absorbance of our nanoparticles. MB absorbs at 665 nm, which does not compete for light absorption with catalyst.

The stark contrast between the porosity of TiO_2 and its congeners prepared under ambient conditions by sol-gel processing is substantiated by the particle morphology observed in the SEM images of Figure 2.1. TiO_2 forms a dense structure that appears ordered in the 1–10 μm size domain. However, all of the alloyed compositions form uniform 20–40 nm particles. Before annealing, all solutions from the sol-gel preparation are transparent and colorless, suggesting that morphology differences arise from the incorporation of Nb and/or annealing under ammonia flow.[37] Mesoporous TiO_2:Nb prepared via the sol-gel route also resulted in 20 nm particles.

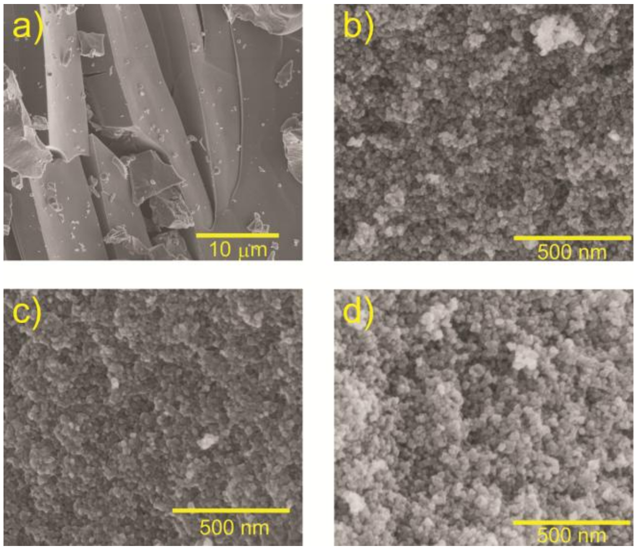

Figure 2.1 SEM images of a) TiO_2, b) TiO_2:Nb, c) TiO_2:N, and d) TiO_2:(Nb,N)-**1**.

Figure 2.2 shows the electronic absorption data for our compounds. TiO_2 shows an absorption edge of ~ 430 nm. The singly-incorporated compounds show little change in their absorption spectra, with edges of 400 and 440 nm for the niobium and nitrogen samples, respectively. However, the co-incorporated compound absorbs out to ~ 580 nm, with two distinct bands observed. The indirect band gaps, E_g, are determined by extrapolating the linear part of the $(F(R)hv)^{0.5}$ curve versus the photon energy hv to $(F(R)hv)^{0.5} = 0$, shown in the inset of Figure 2.2.

The 150 nm bathochromic shift in the co-incorporated compound can be adequately described by introducing localized states. The increase in band gap reduction can be attributed to the increase in alloy concentration, specifically inclusion of N content. It is shown theoretically that the incorporated N would result in a localized N(2p) bands positioned just above the VB, which would decrease the band gap and enhance absorption at longer wavelengths, which is what we observe in our UV-Vis spectrum. TiO_2:(Nb,N)-**1** has the smallest band gap (2.0 eV) of all prepared samples in this study, and shows the highest nitrogen incorporation as substitutional nitrogen ($N_s/N_i = 0.593$ by analyzing the XP spectra, *vide infra*). This suggests that N(2p) levels are localized above the O(2p) orbitals and are responsible for the orange color we observe.

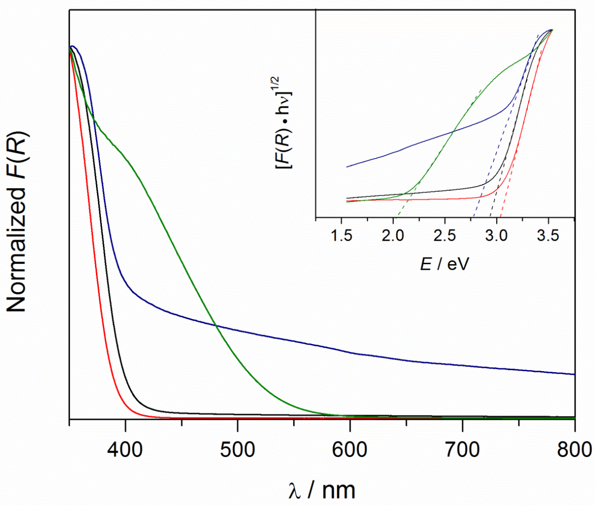

Figure 2.2 UV-Vis Diffuse reflectance spectra of TiO_2 (black), TiO_2:Nb (red), TiO_2:N (blue), and TiO_2:(Nb,N)-**1** (green). **Inset**. Tauc plots for each compound showing indirect band gaps.

To gain insight into the composition of these compounds at the surface, we used X-ray photoelectron spectroscopy (XPS) (Figures A.4-A.9). The XP spectrum of the co-incorporated TiO_2:(Nb,N)-**1** compound is shown in Figure 2.3. The XP spectra of Ti(2p) in the co-incorporated composition and in all samples show peaks at ~ 458.6 eV and 464.0 eV, consistent with the standard $2p_{3/2}$ and $2p_{1/2}$ binding energies for Ti^{4+} in anatase.[38] These energies are also consistent for Ti(2p) peak binding energies in the TiO_2:Nb compounds, which excludes charge-transfer at the surface. The binding energies of Nb $3d_{5/2}$ and $3d_{3/2}$ are ~206.9 and 209.6 eV respectively (2.7 eV spin-orbit splitting), consistent with the standard values of Nb^{5+} in Nb_2O_5.[39,40] Figure 2.3b shows Nb $3d_{5/2}$ and $3d_{3/2}$ shoulders, suggestive of two different Nb environments on the surface (Nb-N and Nb-O linkages) of the co-incorporated sample, but still consistent with a Nb^{5+} formal oxidation state. The XP spectrum of O(1s) in Figure 2.3c shows a dominant peak at 530.0 eV with a shoulder at 530.7 eV, characteristic of metal oxo- and surface hydroxo, respectively, consistent with IR data (Figure A.10 and Table A.1).

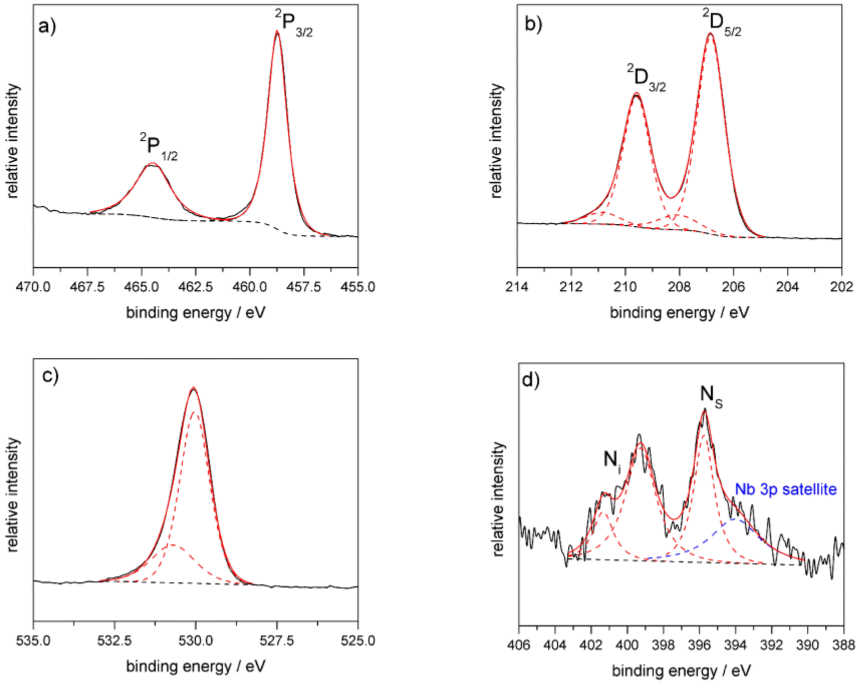

Figure 2.3 XP spectra of the TiO2(Nb,N)-1 co-incorporated sample are: a) Ti(2p), b) Nb(3d), c) O(1s), and d) N(1s).

XPS is a surface-sensitive technique and not necessarily indicative of the bulk composition. Therefore, low temperature electron paramagnetic resonance (EPR) spectroscopy, shown in Figure 2.4, sheds insight into the electronic structure of sol-gel synthesized anatase materials. We note that several hundred milligrams of material was placed in the EPR tube in order to observe a signal, indicating that the signal arises from small impurities. At 4 K, TiO_2:(Nb,N)-**1** exhibits anisotropic resonances at $g_{//} = 1.980$ and $g_{\perp} = 1.942$, which has been shown to correspond to bulk Ti^{3+}.[41–43] This spectral assignment is in accord with our XPS data: some Ti^{3+} is present in the bulk with only Ti^{4+} at the surface. A minor feature can be observed at $g = 2.000$, indicative of an electron trapped on an oxygen vacancy (an F^+-center)[44–48]. Moreover, XPS is not sensitive to oxygen concentration, so any vacancies are imperceptible by this technique. For the EPR of the co-incorporated sample, we note that with the $I = 9/2$ nucleus of ^{93}Nb, 10 hyperfine lines should be observed in the spectrum.[49,50] However, the hyperfine splitting at 4.4 K and 9.3 GHz is not resolved, common to other reports.[51]

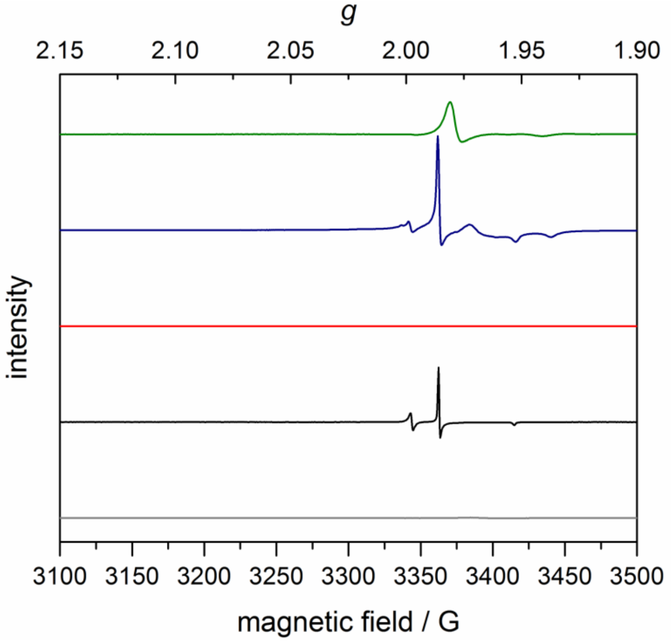

Figure 2.4 EPR spectra recorded at 4 K. From bottom to top, samples are: Degussa P-25 (gray), TiO_2 (black), TiO_2:Nb (red), TiO_2:N (blue), and TiO_2:(Nb,N)-**1** (green).

An important question that we must address is: What is the location and chemical nature of nitrogen in the titania lattice? To answer this, we return to our XPS data shown above. It is important to note that the goal of co-incorporating donor acceptor pairs in TiO_2 is the presence of substitutional nitrogen (nitrogen replacing oxygen atoms on the anion sublattice), such that charge compensation between Nb^{5+} and N^{3-} can occur. The N(1s) XP spectrum for TiO_2:(Nb,N)-**1** in Figure 2.3d reveals three deconvoluted peaks at binding energies of 401.8, 399.4, and 396.0 eV. The peak observed at 394.0 eV corresponds to the Nb(3p) satellite peak.[31] In the XP spectra of oxidized titanium nitride, it has been shown previously that the N(1s) peaks at higher binding energy are assigned to interstitial nitrogen (N_i), and the additional peak at 396.0 eV to atomic β–N states, or substitutional nitrogen (N_s).[52]

All of our samples include these two higher binding energy N(1s) peaks, however, only the co-incorporated sample includes the peak at 396.0 eV (Figure A.9). This suggests that in the co-incorporated TiO_2:(Nb,N)-**1** compound, nitrogen has been substitutionally incorporated into the TiO_2 structure in the form of N–Ti–N bonds, most likely diamagnetic N^{3-} since we see no paramagnetic signals that would coincide with a N^{2-} incorporation in our EPR studies. This result also explains our observation of two different chemical environments for Nb—those having Ti–O nearest-neighbors and those having Ti–N nearest neighbors. The ratio of N_s/N_i for this compound is 0.593, which is significantly greater than the TiO_2:(Nb,N)-**2** or TiO_2:(Nb,N)-**3** compounds (Table 2.1).

The following sections will focus on the TiO_2:(Nb,N)-**1** composition as that material shows the greatest catalytic activity. Full characterization of each composition has been performed, and the results of these experiments will be revealed throughout the next sections and in Appendix A to support the conclusions gleaned from the data presented on TiO_2:(Nb,N).

2.3.2 Effect of annealing under oxygen on structure and composition

The assertion that electrons are trapped on oxygen vacancies with bulk Ti^{3+} being present as impurities in our sol-gel synthesized TiO_2, TiO_2:N, and the co-incorporated composition, TiO_2:(Nb,N)-**1**, can be tested directly by reacting the compound with O_2 (Figure A.11). Therefore, we generated new compositions (noted as TiO_2:(Nb,N)-**2** for the co-incorporated material) by heating the synthesized compounds to 500 ºC under flowing O_2 at a rate of ~110 mL/min for 5 hours in the tube furnace (Figure A.12). The resulting materials are EPR silent (Figure A.13), therefore we surmise the following equilibrium is critical in equation 1:

$$3Ti^{4+} + 2O_O^{\times} \rightleftharpoons 3Ti^{3+} + \square_O^{\bullet\bullet} + \square_O^{\bullet} + O_2(g) \qquad (1)$$

$$Ti^{4+} + 2O_O^{\times} \rightarrow \square_{Ti}^{''''} + 4\square_O^{\bullet\bullet} + TiO_2 \qquad (2)$$

where $\square_O^{\bullet}$ and $\square_O^{\bullet\bullet}$ represent an F^+-center and an oxygen vacancy respectively in Kröger-Vink notation. The equilibrium shown in equation 1 has a strong O_2 partial pressure dependence, and in a control experiment in which the starting sol was annealed under N_2, no TiO_2 results (data not shown). Here, after annealing TiO_2:(Nb,N)-**1** in O_2, the equilibrium lies far to the left, and no Ti^{3+} remains in the EPR spectrum, although the minor F^+-center feature remains, albeit as an extremely broad, low intensity signal. The XP spectra show Ti^{4+} and Nb^{5+} as formal oxidation states (Figures A.14-A.17). Equation 2 shows an alternative mechanism for charge compensation, presence of cation ($\square_{Ti}^{''''}$) and anion vacancies ($\square_O^{\bullet\bullet}$), and would result in an EPR silent TiO_2:(Nb,N)-**1** species, which is not observed. In addition to annealing the synthesized solid TiO_2:(Nb,N)-**1** in O_2 to generate TiO_2:(Nb,N)-**2**, we show that we can achieve the exact same result from annealing the TiO_2:Nb precursor sol in flowing O_2 for 12 h, followed by ammonia at 500 °C for 4 h to generate compound TiO_2:(Nb,N)-**3**, which is also EPR silent.

Then, in the case of adding only niobium to the lattice, charge compensation can be rationalized by the following reactions:

$$Nb_2O_5 \rightarrow 2Nb_{Ti}^{\bullet} + 4O_O^{\times} + O_i^{''} \tag{3}$$

$$2Nb_2O_5 \rightarrow 4Nb_{Ti}^{\bullet} + \square_{Ti}^{''''} + 10O_O^{\times} \tag{4}$$

$$Nb_2O_5 \rightarrow 2Nb_{Ti}^{\bullet} + 2e^{-} + 4O_O^{\times} + 1/2O_2 \tag{5}$$

Equation 3 represents Nb^{5+} substituting for Ti^{4+}, which leads to introduction of interstitial oxygen ($O_i^{''}$).[53] Equation 4 introduces titanium vacancies, $\square_{Ti}^{''''}$.[54] Equation 5 results in free electrons, which can then go on to reduce Ti^{4+} to Ti^{3+}.[55] Based on our EPR silence, we cannot distinguish between equations 3 and 4; however, equation 5 can be ruled out as a possible charge compensation mechanism because it would contain an EPR active signal, Ti^{3+}.

2.3.3 Photocatalytic activity

Combining the electronic absorption data and porosity, we hypothesize that the co-incorporated TiO_2:(Nb,N)-**1** anatase compound should degrade MB dye at the fastest rate under the action of visible light since its band gap is lowest and the compound contains reactive Ti^{3+} species. MB concentration was monitored in the bulk solution every 30 minutes until adsorption/desorption equilibrium was reached, thus generating adsorption isotherms for various concentrations of dye. The theoretical Langmuir isotherm assumes that adsorption occurs at specific homogenous sites within the adsorbent and the capacity of the adsorbent is finite. The Langmuir equation is as follows: $q_e = \frac{K_L q_m C_e}{1 + K_L C_e}$, where C_e is the equilibrium concentration (mg/L); q_e is the amount of dye adsorbed at equilibrium (mg/g); q_m is q_e for a complete monolayer (mg/g), which gives maximum adsorption capacity of the adsorbent; and K_L is the sorption equilibrium constant (L/mg).

A signature of complete coverage of dye to the adsorbent surface is a plateau in the isotherm, observed in Figure 2.5. As shown in Figure 2.5, TiO_2:(Nb,N)-**1** and TiO_2:Nb show q_e = 36 and 21 respectively. However, TiO_2 and TiO_2:N prepared in the same manner show minimal dye adsorption at any concentration and result in negligible dye adsorbance. Notably, TiO_2:N has a significantly higher surface area that is on par with the other alloyed compounds. In Figure 2.5 the niobium incorporated compositions TiO_2:(Nb,N)-**1**, TiO_2:(Nb,N)-**2**, TiO_2:(Nb,N)-**3**, show q_e = 36, 32, and 33 respectively. Therefore, we conclude that dye adsorption is not simply a function of having high surface area (all compounds also have similar surface area and morphology, Figure A.18). Rather, the chemical composition plays a significant role and suggests that perhaps methylene blue binds most strongly to the niobium sites in these materials. Furthermore, compounds **1**, **2**, and **3** absorb visible light, with variance in the absorbance at 450 nm probably due to defect structure arising from various nitrogen incorporation, substitutional and interstitial, in each of the three compounds (Table 2.1, Figure A.19).

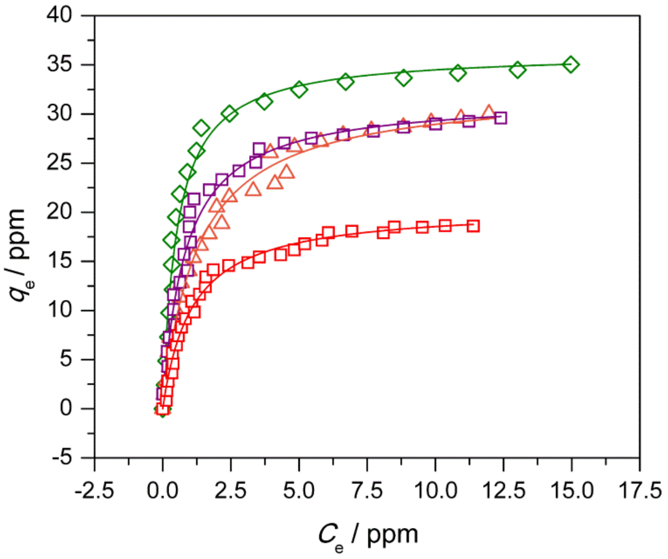

Figure 2.5 Langmuir isotherms for the adsorption of MB on TiO_2:(Nb,N)-**1** (◊), TiO_2:(Nb,N)-**2** (□),TiO_2:(Nb,N)-**3** (△), and TiO_2:Nb (□). Catalyst–MB dosage = 0.010 g/ 10 mL, equilibration time = 30 min.

Based on the adsorption studies, the starting concentration of MB for all of the degradation experiments was chosen to be 40 ppm, such that the concentration of MB in solution after equilibrium could be easily monitored for the compound that adsorbs the most dye. For comparison, photocatalytic degradation of MB over commercial Degussa P-25 was also performed under the same conditions. Three hours of dark adsorption/desorption of MB on the catalyst surface was allowed before kinetic studies occurred. In the dark, no significant changes in MB concentration for any compound were observed (Figure A.20-21).

Figure 2.6 shows that after two hours of irradiation of visible light (AM1.5G incident radiation at 550 mW/cm^2), TiO_2:(Nb,N)-**1** degrades 93% of MB, compared to just 74% for anatase TiO_2 prepared using the same sol-gel processing and 62% for commercial grade P25. Furthermore, Figure 2.7 compares the degradation profiles for the compositions prepared under different atmospheric conditions. Again, TiO_2:(Nb,N)-**1** degrades 93% of MB after two hours compared to just 40 and 57% for TiO_2:(Nb,N)-**2** and TiO_2:(Nb,N)-**3** compounds respectively.

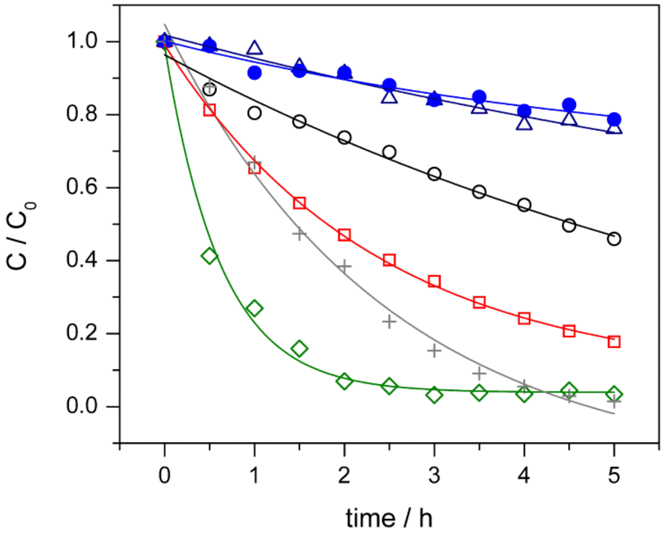

Figure 2.6 Degradation profile of MB under filtered 150 W Xe irradiation: control 40 ppm MB (●), TiO_2:N (Δ), TiO_2 (○), TiO_2:Nb (□), Degussa P-25 (+), and TiO_2:(Nb,N)-**1** (◊). Degradation was monitored by UV-Vis spectrophotometry, taking the ratio of the absorbance at 665 nm compared to the initial absorbance of a 40 ppm MB solution.

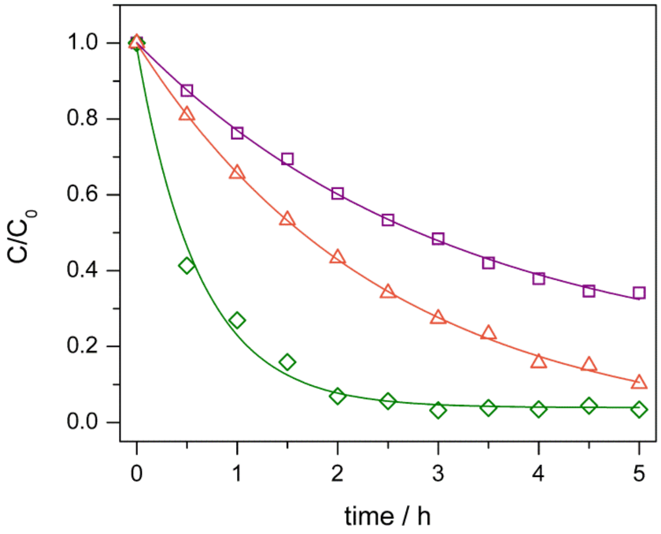

Figure 2.7 Degradation profile of MB under filtered 150 W Xe irradiation: TiO_2:(Nb,N)-**1** (green), TiO_2:(Nb,N)-**2** (violet), and TiO_2:(Nb,N)-**3** (orange). Degradation was monitored by UV-Vis spectrophotometry, taking the ratio of the absorbance at 665 nm compared to the initial absorbance of a 40 ppm MB solution.

The photodegradation kinetics of MB on the different compounds can be described as pseudo-first order, given by the Langmuir-Hinshelwood expression, $-\ln\left(\frac{C}{C_0}\right) kt$, where C_0 is the initial concentration of MB, C is the concentration of MB at time t, and k is the limiting rate constant of the reaction (Figure A.22). TiO_2:(Nb,N)-**1** degrades MB at the fastest rate of 0.0201 min^{-1} (1.203 h^{-1}), in support of our hypothesis. The pseudo-first-order rate constant for each catalyst is provided in Table 2.1. There is one report of preparing Nb-doped anatase nanoparticles using urea or ammonia in a hydrothermal synthesis.[56] However, in this report, the absorption spectrum is not significantly changed from that of pure anatase TiO_2 and the pseudo-first-order rate constant is smaller, 0.53 h^{-1} *vs*. 1.203 h^{-1}, using UV-ray black light.

Physical parameters that affect the kinetics of dye degradation include mass of catalyst, wavelength of irradiated light, initial dye concentration, and temperature.[57] Since physical parameters vary for each experimental set up, direct comparisons are difficult to make. However, we do want to compare the utility of our approach to other recently reported results. A nanosheet solid solution of $Bi_2Mo_{0.25}W_{0.75}O_6$ exhibits a first order rate of 0.774 h^{-1} with a catalyst loading of 100 mg catalyst in 100 mL of 10 ppm MB solution under visible light irradiation from a 300 W Xe lamp.[58] We note that we observe higher catalyst turnover using higher concentration of MB dye, half the incident light intensity, and solar simulation.

2.3.4 Composition-dependence of TiO_2:(Nb,N)-*x* compounds

Following our previous studies on TiO_2:(Nb,N), we raised several questions: 1) Is the high mole-percent regime ideal for the closest donor acceptor match? 2) Can we tune the band gap by varying the donor mole-percent? 3) Is the substitutional nitrogen incorporation dependant on mole-percent niobium? 4) Is Ti^{3+} the active site for increased activity? We address these questions in the following sections.

We expand upon our previous study of the TiO_2:(Nb,N) co-incorporated system in order to elucidate the role that each component (Nb and N) plays in determining the band-gap energy and the rate of dye degradation. We present a series of (Nb,N) compounds ranging in mole-percent of the donor element, which is straightforwardly dictated by our sol-gel precursors; the sol is annealed in air to form the niobium alloyed compound. Target compounds included 1, 5, 10, 15, 20, 25, and 30 % niobium incorporation for titanium in the anatase structure to give the compound $Ti_{1-(5x/4)}Nb_xO_2$. Then, all compounds are subjected to the same nitridation treatment, in which the isolated niobium-alloyed compound is annealed at 500 °C under flowing ammonia for 4 hours to give $Ti_{1-(5x/4)}Nb_xO_{2-y-\delta}N_y$. In this compound, y represents the total mole-percent of nitrogen in the compound and δ is the formation of oxygen vacancies to reach charge compensation. Compounds are herein identified as NbN-*x*, where *x* represents the target mole-percent of niobium in the compound (*e.g.* NbN-1 is 1% Nb in TiO_2, annealed under NH_3 for 4 hours).

Figure 2.8a shows X-ray diffraction patterns for all co-incorporated samples in our new composition-dependent series; all compounds crystallize in the anatase structure. As discussed in Chapter 1, anatase was chosen as the target phase for all compounds in this series due to its higher electron mobility compared to rutile. Furthermore, all compounds are annealed at the same temperature to target anatase phase for comparative purposes. As shown in Figure 2.8b there is a shift to lower 2θ angles for the (*101*) Bragg reflection as the niobium incorporation is increased from 1 to 30 mole-percent. Rietveld refinement was performed using tungsten as an internal standard in order to obtain accurate lattice parameters. We note that there is a linear increase in the a cell parameter, although the c parameter remains constant (Figure A.23). These results are in accord with Vegard's Law.[59] Due to the difficulty of digesting these compounds for elemental analysis, we turned to EDX spectroscopy to determine the relative ratios of Ti/Nb in the compounds; we find good agreement between experimental values and the targeted ratios (Figure A.24, Table A.2).

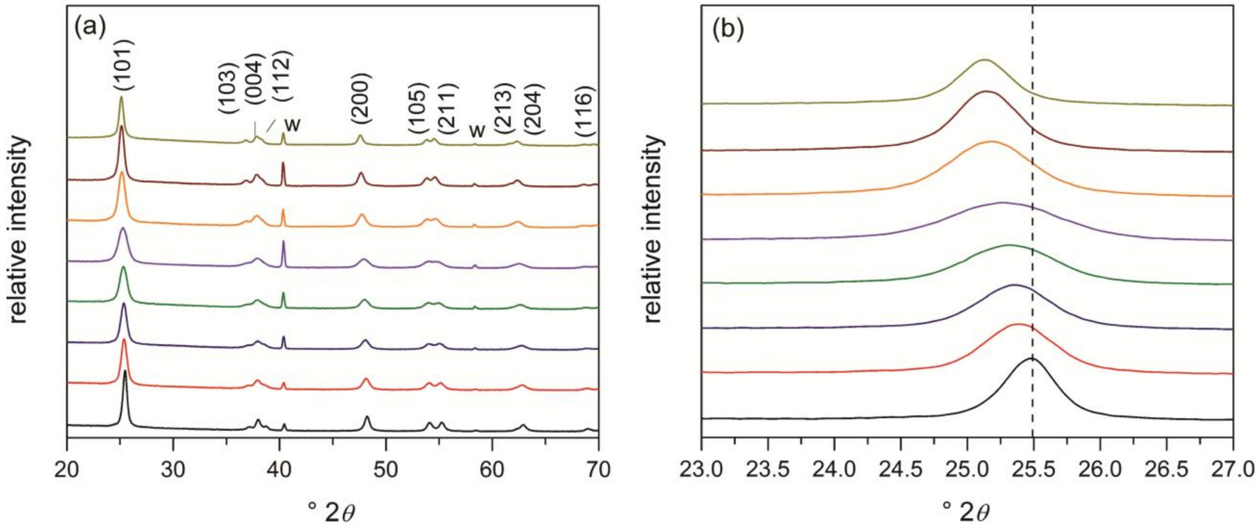

Figure 2.8 X-ray diffraction patterns of NbN-*x* compounds from bottom to top 0, 1, 5, 10, 15, 20, 25, and 30 (a) full range and (b) (*101*) peak.

Next, we investigated the optical absorption properties of our co-incorporated series. The normalized reflectance data for the series of TiO_2:(Nb,N) compounds is shown in Figure 2.9, with corresponding indirect band-gap values listed in Table 2.2. Anatase TiO_2 has an absorption band edge at 410 nm, and through incorporation of both Nb and N, this edge shifts to longer wavelengths—out to 525 nm (2.36 eV). In general, there is an inverse relationship between the mole-percent niobium and the band gap; the band-gap energy ranges from 2.37 eV (x = 1) to 2.20 eV (x = 30), Figure A.25. *It is noted that without the nitridation treatment, all compounds display a band-gap energy of ~ 3.1 eV*, and it is known that incorporating niobium into TiO_2 results in a wider band-gap material (Figure A.26).[60–62] However, there is no report of tuning the band gap by co-incorporating niobium and nitrogen into the anatase structure in order to decrease the band gap. By varying the mole-percent of niobium in TiO_2 and subjecting the compounds to similar ammonia treatments, we assume that the resulting change in band-gap energy is due to the increased solubility of nitrogen as niobium incorporation is increased. This observation has been reported in the literature for other N-F codoping into TiO_2.[63] The increase in substitutional nitrogen will result in faster rates of methylene blue dye degradation.

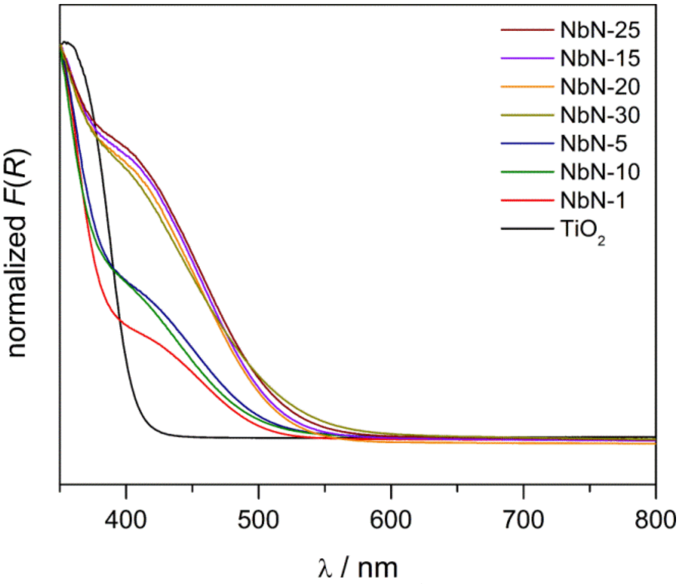

Figure 2.9 Diffuse reflectance UV-Vis spectroscopy of NbN-x compounds.

Table 2.2 Indirect band gap, dye adsorbed, and methylene blue dye degradation rate constants.

% Nb	E_g / eV	q_e / mg • g^{-1}	$k_{40\text{ ppm MB}}$ / h^{-1}
1	2.37	17	0.115
5	2.37	22	0.146
10	2.36	32	0.250
15	2.26	36	0.444
20	2.24	30	0.516
25	2.21	34	0.779
30	2.20	33	0.759

The surface chemical environments of the constituent elements in the co-incorporated series are probed by XP spectroscopy (Figure A.27). As we have previously reported, Nb exists as Nb^{5+}, with $3d_{5/2}$ and $3d_{3/2}$ binding energies at ~207.0 and 209.0 eV respectively.[64] Then, Saha and Tomkins report that Ti^{4+} found in pure titania has a Ti(2p) binding energy of 459.4 eV.[52] For all members of the NbN-*x* series, we observe a shift of the Ti(2p) peak to lower binding energy for all compounds. NbN-1 has the lowest Ti(2p) binding energy (458.3 eV), while NbN-30 has the highest binding energy (458.8 eV) for the series. A decrease in the Ti(2p) binding energy is indicative of a lowering of the valence state from Ti^{4+} to Ti^{3+} as a result of N^{3-} substituting for O^{2-}, which causes an increase in the electron density around the Ti atom.[65,66] The values we observe are consistent with a formal Ti oxidation state intermediate between +3 and +4. We note a shift to lower binding energy compared to Ti^{4+} in pure titania,[67] and we observe a similar trend for the O(1s) peak (Table A.3). These results suggest that increasing the mole-percent of niobium allows for better charge compensation of the N^{3-} substitution, although we stress that in our previous work, elemental analysis shows that only 2 mole-percent total nitrogen is achieved regardless of the niobium mole fraction.[68]

The trend we observe with the Ti(2p) peak shifting to higher binding energy with less Ti^{3+} present at high mole-percent niobium can be supported with EPR spectra recorded at 4 K (Figure A.28). A strong Ti^{3+} signal is present ($g_{//}$ = 1.980 and $g_{\perp}$ = 1.942) at low mole-percents of niobium[69–71]; however, above NbN-15, all compounds exhibit an extremely weak Ti^{3+} signal not visible on the same scale as the lower *x* NbN-*x* compounds. We note that we used 130 mg of pure sample for each measurement *(i.e.*—not NbN-*x* embedded in a diamagnetic host matrix), so all signals observed are trace impurities.

XPS analysis highlights the distinct chemical environments of nitrogen incorporation in the co-incorporated series. The XP spectra for the N(1s) peak is illustrated in Figure 2.10a. All samples exhibit peaks centered around 400.0 eV, which are attributed to interstitial nitrogen in the form of N—O—Ti bonds.[72–74] The line at 396.0 eV is the reference line for substitutional nitrogen (N_S) in TiN, which creates N—Ti—N environments.[75] The intensity of the peak increases with increasing niobium incorporation. Figure 2.10b shows the ratio of the deconvoluted area of the XPS peak at 396.0 eV to the total N(1s) area as a function of the target % niobium incorporated into TiO_2. We observe a linear relationship between substitutional nitrogen and incorporated niobium. We do not observe this trend when we plot the ratio of the deconvoluted area of the N_i XPS peak at 400.0 eV to the total N(1s) area as a function of the target % niobium (Figure A.29). This result is also consistent with the decrease in band gap with increasing niobium content, suggesting that high mole-percent niobium allows for increased solubility of nitrogen (N_S). Furthermore, EPR results support this concept: the Ti^{3+} signal decreases with increases mole-percent niobium. This observation also provides evidence for greater charge compensation between niobium and nitrogen at high mole-percents niobium, resulting in less Ti^{3+}.

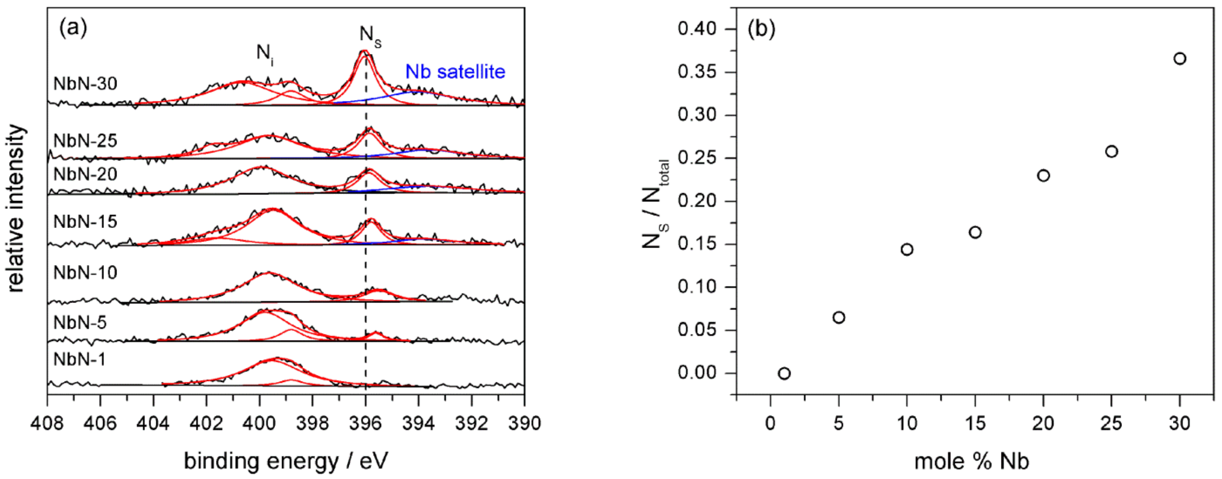

Figure 2.10 a) XP spectra for N1s peak, N_i and N_S represent chemisorbed and substituional nitrogen respectively, with a vertical line at 396 eV; b) Deconvoluted area of N_S (396 eV) / total N(1s) area *vs*. target mole % Nb substituting for Ti in TiO_2.

MB degradation is performed in order to probe the photocatalytic activity of these compounds. After three hours of stirring 50 mg of NbN-*x* catalyst dispersed in a 50 mL aqueous solution of 40 ppm MB dye in the dark to allow for adsorption/desorption equilibrium, each compound was irradiated using a 150 W Xe lamp fitted with an AM1.5G simulating solar filter. After three hours of dark equilibration, the concentration of dye adsorbed to the catalyst is consistent for 10 % and greater substitution of niobium for titanium (Table 2.2), such that any differences in degradation rate are not attributable to variations in the surface coverage of the dye. Figure 2.11a shows the degradation profiles for each of the NbN-*x* compounds when irradiated for 3 hours. The relative concentrations of MB dye were fit by the first-order rate Langmuir-Hinshelwood expression, rate = $-\ln(C/C_0)kt$, where C_0 is the initial concentration of MB, C is the concentration of MB at time t, and k is the limiting rate constant of the reaction. Data were fit over the entire 3 h of irradiation. We note that as the mole-percent of niobium increases, the rate of dye degradation also increases ($k_{40\text{ ppm MB, max}}$ ~ 0.779 h^{-1}), as depicted in Figure 2.11b (Figure A.30 for plot of $\ln(C/C_0)$ *vs*. t). The fastest degradation rates also correspond to the compounds with the smallest band-gap values by UV-vis spectroscopy, the weakest Ti^{3+} signals in the EPR spectra, and the greatest substitutional nitrogen by XPS analysis. We propose that in addition to having larger band gaps, Ti^{3+} sites can act as charge recombination centers for small *x* and decrease the rate of dye degradation for low mole-percent niobium incorporation compounds.

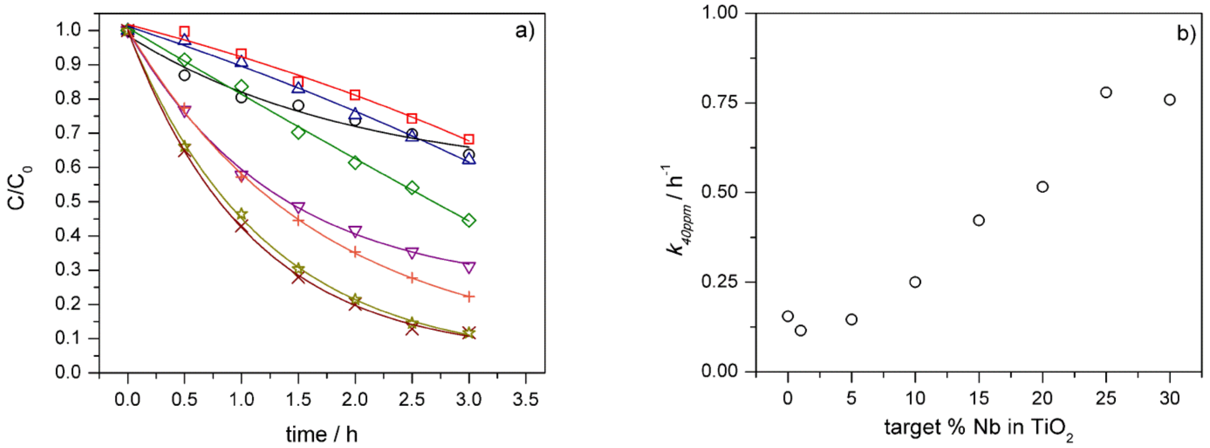

Figure 2.11 a) MB degradation profiles for NbN-*x* compounds: NbN-0 (○), NbN-1 (□), NbN-5 (△), NbN-10 (◇), NbN-15 (▽), NbN-20 (+), NbN-25 (×), and NbN-30 (☆). b) first-order rate constant, *k vs*. targeted mole % Nb in NbN compounds.

2.3.5 Synthesis and characterization of NbN-25-*z* compounds

We next investigated the relationship between nitridation time and rate of MB degradation in our champion NbN-25 compound, which degrades MB dye seven times faster than does TiO_2 and almost twice as fast as P-25 (Figure A.31). We held the temperature and ammonia flow rate constant, 500 °C and 110 mL/min respectively, and varied nitridation time for the Nb-25 compounds, resulting in Nb-25 (*z* = 0), 1, 2, 3, 4, 5, and 6-hour dwell periods, denoted NbN-25-*z*, where *z* is the dwell time. Regardless of nitridation time, all compounds maintain the anatase structure (Figure A.32); however, the optical properties change based on the dwell time, shown in Figure 2.12 with corresponding Tauc plots in Figure A.33. For *z* = 1, the band-gap energy is 2.45 eV; for *z* = 6, the band gap decreases to 2.25 eV (Table A.4).

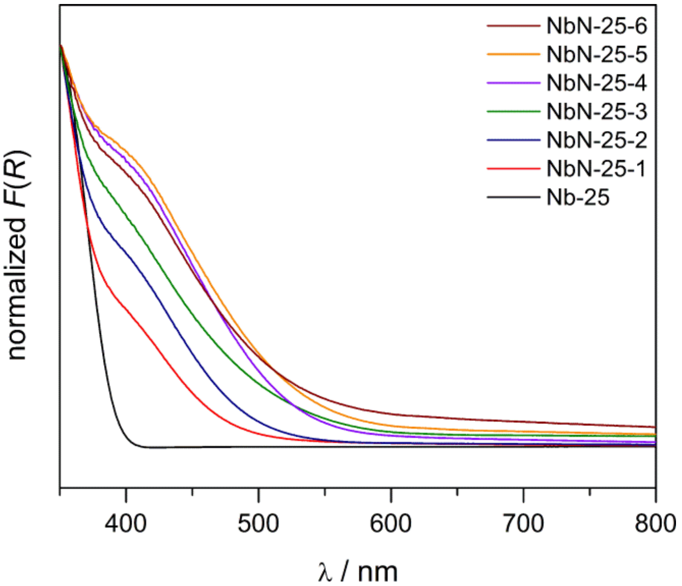

Figure 2.12 Diffuse reflectance of NbN-25-*z* annealed under ammonia for varying dwell times.

Then, using approximately 100 mg of each pure sample, trace Ti^{3+} impurities can be detected by EPR spectroscopy (Figure A.34). Deconvolution of the N(1s) spectra for these compounds reveal no differences in the area of the substitutional nitrogen divided by the total N 1s area, in contrast to what we observed when varying the niobium mole percent (Figure A.35). This result indicates that 2 mole % of substitutional nitrogen is the maximum achievable at 25 mole % of niobium. We do not observe a shift in the Ti(2p) binding energy (Table A.5).

We then probe the effect of annealing time for the NbN-25-*z* compounds on the rate of methylene blue degradation using a constant starting concentration, C_0 = 40 ppm. The degradation profiles of MB degradation are comparable, (Figure A.36), and we perform the UV-Vis absorption kinetics experiments in independent triplicates, with each data point and error bar representing the mean and standard deviation respectively. As shown in Figure 2.13, the rate constant for dye degradation is nearly independent of annealing time. We do note that in all cases, a nearly three-fold increase in rate is observed upon nitridation (z = 0 has no added nitrogen), signifying that nitrogen substitution is critical for photocatalytic degradation of MB. A maximum rate, $k = 0.779\ h^{-1}$, is observed for NbN-25-4.

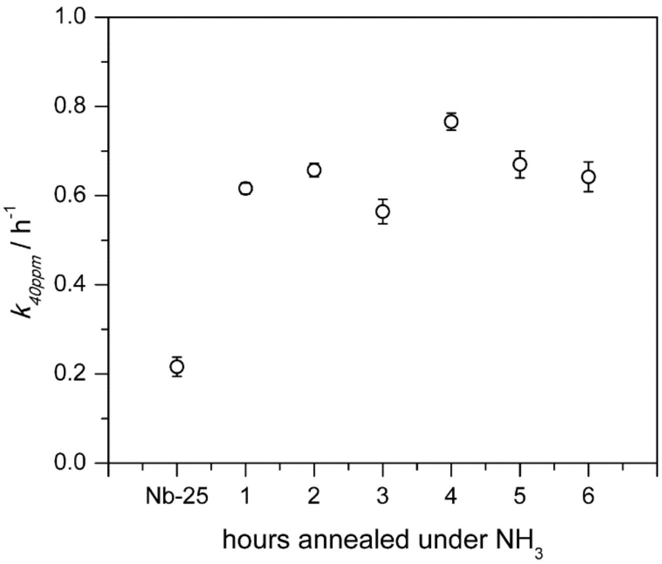

Figure 2.13 First-order rate constant *vs*. nitridation time under flowing NH_3 for NbN-25-*z* compounds.

2.4 Photocatalytic mechanism of MB dye degradation

The decoloration of MB can be attributed to two competing reactions: degradation (degradation) or photobleaching. The final products of complete degradation are described by the reaction:

$$C_{16}H_{18}N_3SCl + 25/2\ O_2 \rightarrow HCl + H_2SO_4 + 3HNO_3 + 16CO_2 + 6H_2O \qquad (6)$$

An alternative mechanism to the irreversible degradation of MB in equation 1 is the simple photobleaching of MB, which is reversible. MB is deep blue in color (ε = 63,000 M^{-1} cm^{-1} at λ_{max} = 665 nm), and can be reduced by two electrons to colorless leucomethylene blue (LMB) shown in Scheme 1.

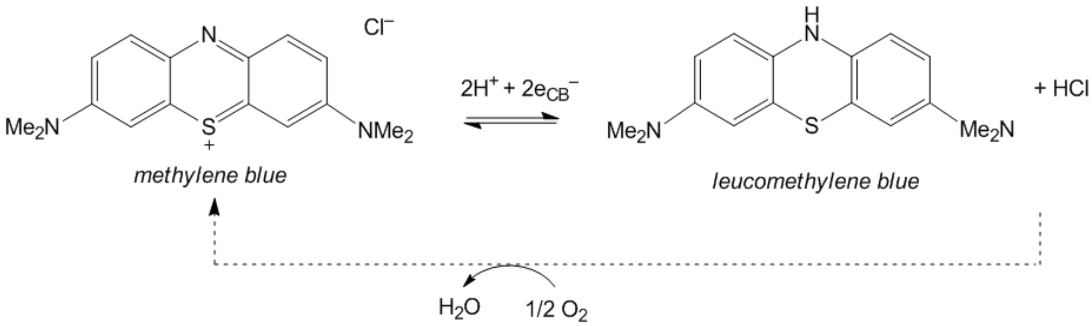

Scheme 1.

Since both degradation and photobleaching result in decoloration of MB, it is important to distinguish between the two mechanistic pathways. Following three hours of irradiation under ambient conditions, the photodegradation intermediate products of MB (*m/z* = 284.06) in our NbN-25-4 experiment and a MB control experiment were identified using LC/MS analysis. Demethylation products include: azure B (*m/z* = 270.05), azure A (*m/z* = 256.04), azure C (*m/z* = 241.04), and thionine (*m/z* = 226.91); ring breaking products include: 4-((hydroxymethyl)(methyl)amino)benzene-1,2-diol (*m/z* = 167.08), benzenesulfonic acid (*m/z* = 158.93), and dimethylaniline (*m/z* = 123.07) (Figure A.37 and Table A.6). These results suggest that the degradation pathway is favored over photobleaching.

In order to confirm that the photobleaching of MB is not a competing pathway, we performed a MB dye degradation study by continually purging the solution with nitrogen gas throughout the entire experiment. After three hours of irradiation, the rate for NbN-25-4 was ~ 2.5 times slower than in the presence of oxygen (k = 0.318 *vs*. 0.779 h^{-1}). If MB is reduced to LMB under anaerobic conditions, the process should be reversible upon reintroducing oxygen into the system. This result is not what we observe: after bubbling oxygen through the cell for ninety minutes following the nitrogen purged reaction, there is no change in the absorption spectrum (Figure A.38), suggesting that the reversible reduction of MB to LMB is not a competing reaction for degrading MB.[76] However, we also note that we do not observe a noticeable pH change in our reaction, suggesting that degradation is incomplete as it written in equation 4 after only 3 hours of irradiation.

NbN-25-4 exhibits an optical gap of ~ 2.2 eV, which poses the question: what reactive species are responsible in degrading MB? Photogenerated electron/hole pairs typically produce superoxide and hydroxyl radicals respectively. The formation of superoxide and hydroxyl radicals has been experimentally determined by using radical quenchers.[77–79] Iodide, I^-, is a scavenger for valence band h^+ and $OH^\bullet$.[80] Adding KI (2 mM), which is high enough concentration to deliver constant I^- to the surface of the photocatalyst, to 40 ppm MB dye stirred with NbN-25-4 inhibits degradation (43 % degradation after 1 hour, Figure A.39), indicating that $OH^\bullet$ is a species contributing to MB degradation. On the other hand, adding benzoquinone (BQ) as an effective $O_2^{\bullet-}$ scavenger has also been well documented.[81] Adding BQ (2 mM) results in completely suppressing MB degradation for the first hour of irradiation. However, degradation does proceed for the remaining 2 hours of irradiation. When a higher concentration of BQ is employed (20 mM), dye degradation is suppressed for only 30 min, followed by rapid degradation (Figure A.39). Presumably the *in situ* formation of peroxide species (confirmed by a peroxide test) accelerates dye degradation, which is documented in the literature.[82,83] Notably, in a separate experiment, adding 20 mM H_2O_2 to NbN-25-4 in 40 ppm MB results in 70% degradation after 1 hour (Figure A.40) compared to only 55 % in the absence of H_2O_2. Furthermore, in the absence of oxygen, MB degradation (62 % degradation after 3 hours) is retarded, presumably due to the lack of superoxide formation. Adding the $\bullet OH$ scavenger (2 mM KI) in the absence of oxygen results in a further decrease in MB degradation rate (56 % degradation after 3 hours). These results suggest that both oxidants $O_2^{\bullet-}$ and $\bullet OH$ are involved in the initial degradation of MB on NbN-25-4. The degradation process is complex, as illustrated in Figure 2.14, where many oxidizing species are conceivable. Furthermore, using a 455 nm cut-on filter results in MB degradation (Figure A.41), shows that *visible* light excitation creates a catalytically active species, showing that indeed, the longer wavelengths contribute to the degradation process.

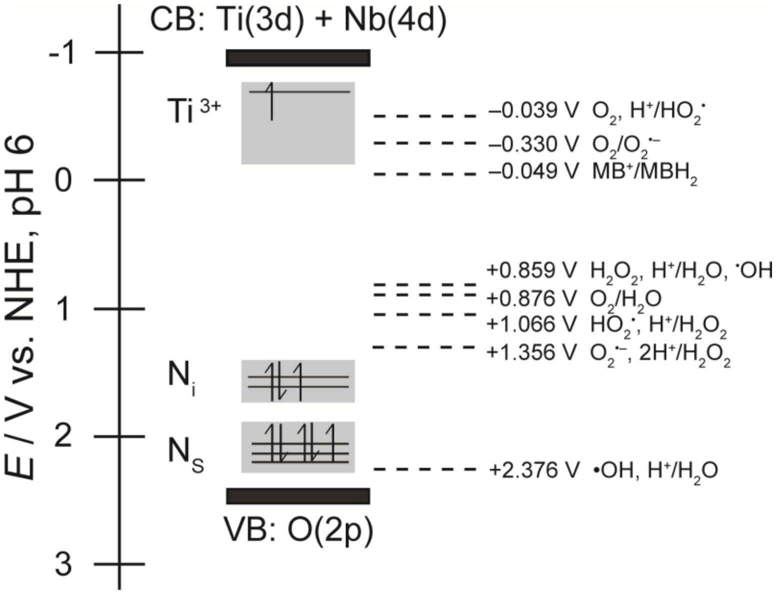

Figure 2.14 Energy diagram (pH 6) including reduction potentials for species involved in MB degradation by NbN-25-4. Band edges for NbN-25-4 are approximated based on band gap and DFT calculated positions for Ti^{3+}, N_i, and N_S from refs. 63 and 84.

We present a photocatalytic mechanism for our co-incorporated compound NbN-25-4. One well known possible mechanism for the photocatalytic degradation of methylene blue can be summarized as follows:

$$\text{NbN-25-4} + h\nu \rightarrow e^- + h^+ \tag{7}$$

$$O_2 + e^- \rightarrow O_2^{\bullet -} \tag{8}$$

$$OH^-_{(\text{surface})} + h^+ \rightarrow \bullet OH \tag{9}$$

$$\text{MB} + O_2^{\bullet -} + \bullet OH \rightarrow \text{degradation products} \tag{10}$$

where first an electron/hole pair is created upon irradiating NbN-25-4 (equation 7). These free carriers combine with O_2 and surface OH^- (equations 8 and 9) to yield the active oxygen species $O_2^{\bullet -}$ and •OH. Finally, in the presence of MB dye, these radical yield the degradation products (equation 10). NbN-25-4 absorbs ~ 550 nm (2.2 eV), therefore we hypothesize that our N(2p) levels are close in energy to the hydroxyl radical potential (E (H_2O/•OH) = 2.37 eV) such that the photoinduced holes can react with surface hydroxyl species to form hydroxyl radicals.[85–87]

However, the O(2p) levels are low enough in energy for the photoinduced holes to oxidize either H_2O or surface OH^- to •OH that reacts with MB dye (equation 4), also contributing to the degradation process.

Our peroxide results suggest a possible alternate pathway involves forming H_2O_2 from $O_2^{\bullet-}$ according to the following set of reactions:

$$O_2^{\bullet-} + H^+ \rightarrow HO_2^{\bullet} \tag{11}$$

$$HO_2^{\bullet} + H^+ \rightarrow H_2O_2 \tag{12}$$

$$H_2O_2 + h\nu \rightarrow 2\ {\bullet}OH \tag{13}$$

$$\text{MB} + 2\ {\bullet}OH \rightarrow \text{degradation products} \tag{14}$$

where the superoxide radical reacts with a proton (the pH of the solution is 6) to form the hydroperoxy radical (equation 11), which then goes on to react with another proton to generate hydrogen peroxide (equation 12). Under illumination, hydrogen peroxide decomposes to form two hydroxyl radicals (equation 13), which subsequently oxidize MB to give the observed degradation products (equation 14).

In order for the reactions 7 – 10 (and 11 – 14) to lead to dye degradation, generating photoinduced electron/ hole pairs that separate and migrate to surface reaction sites is crucial. Introducing Nb^{5+} in the sol-gel reaction results in the following charge compensation possibility, adopted from Baumard and Tani:[88]

$$Nb_2O_5 \rightarrow 2Nb_{Ti}^{\bullet} + 2e^- + 4O_O^{\times} + \tfrac{1}{2}O_2 \tag{15}$$

$$2e^- + 2Ti_{Ti}^{\times} \rightarrow 2\ Ti_{Ti}' \tag{16}$$

The free electrons formed in equation 15 can reduce Ti^{4+} to Ti^{3+} (equation 16) which act as recombination centers that slow the rate of dye degradation. We observe that at low mole-percent niobium donor incorporation (1 – 5%), a stronger Ti^{3+} EPR signal is observed, and there is less *substitutional* nitrogen at the surface in the co-incorporated samples, observed by integrating the N(1s) peaks in the XP spectra. Conversely, at high mole-percent niobium (10 – 30%), the Ti^{3+} signal is extremely weak, and there is more substitutional nitrogen. The relationship between Ti^{3+} and substitutional nitrogen could act in concert to decreases electron-hole recombination, thereby yielding a faster rate of dye degradation. Of course, we must also consider that the band gap shrinks with increasing substitutional nitrogen and mole-percent niobium. In this case, generating more electron-hole pairs under solar irradiation would also contribute to a faster dye degradation rate. Since active oxygen species are required to carry out MB dye degradation, current efforts focus on using NbN-*x* as a water oxidation photocatalyst.

2.5 Conclusions

In this chapter we report the sol-gel synthesis of a series of anatase-phase compositions of TiO_2 that have been alloyed with niobium and nitrogen for the first time. The co-incorporated compound, TiO_2:(Nb,N)-**1**, shows a bathochromic shift of 150 nm, resulting in an indirect band gap of 2.2 eV. Co-incorporating produces 20 nm particles and a higher surface area compared to the undoped analogue. We also observe evidence for F^+-centers in the compound. To further understand the electronic structure both at the surface and in bulk, we have prepared the co-incorporated phase in two different methods: one in which we anneal the compound in oxygen to fill in oxygen vacancies and oxidize Ti^{3+} to Ti^{4+}, TiO_2:(Nb,N)-**2**; the other in which we synthesize the compound under oxygen (instead of air) and anneal in ammonia, TiO_2:(Nb,N)-**3**. All of compositions outperform the TiO_2 analogue, with the originally prepared co-incorporated composition TiO_2:(Nb,N)-**1** showing a 7-fold increase in MB dye degradation rate (1.203 h^{-1}) over the TiO_2.

In Section 2.3.4, we aim to understand the composition-dependence of our co-incorporated compound and report the synthesis of a series of NbN-*x* compounds with varying mole-percent of niobium substituting for titanium (*x* ranges from 1 to 30). All compounds show a decreased band gap of ~2.3 eV. XP spectra show the presence of substitutional nitrogen, which increases in intensity with increasing mole-percent niobium. All compounds photocatalytically degrade methylene blue dye, with a maximum rate constant of 0.779 h^{-1} for NbN-25. This represents a six-fold increase in rate compared to lower mole-percent NbN-*x* compounds. We identify the demethylation and ring-breaking products in the photodegradation of MB dye, suggesting a plausible mechanistic pathway involves electron transfer processes to form reactive radicals species. Chapter 2 presented a study on dye degradation, but we aim to extend these studies further and reveal the utility of these compounds as water oxidation photocatalysts, the topic of Chapter 3.

2.6 References

1 Gai, Y.; Li, J.; Li S.; Xia, J.; Wei, S. *Phys. Rev. Lett.* **2009**, *102*, 036402/1-3.

2 Yin, W.-J.; Tang, H.; Wei, S.-H.; Al-Jassim, M. M.; Turner, J.; Yan, Y. *Phys. Rev. B* **2010**, *82*, 045106/1-6.

3 Wang, P.; Liu, Z.; Lin, F.; Zhou, G.; Wu, J.; Duan, W.; Gu, B.; Zhang, B. *Phys. Rev. B*, **2010**, *82*, 193103.

4 Ma, X.; Wu, Y.; Lu, Y.; Xu, J.; Wang, Y. ; Zhu, Y. *J. Phys. Chem. C* **2011**, *115*, 16963-16969.

5 Yin, W. -J; Wei, S.; Al-Jassim, M. M.; Yan, Y. *Phys. Rev. Lett.* **2011**, *106*, 066801/1-4.

6 Márquez, A.M.; Plata, J. J.; Ortega, Y.; Sanz, J. F. *J. Phys. Chem. C* **2012**, *116*, 18759-18767.

7 Çelik, V.; Mete, E.; *Phys. Rev. B.* **2012**, 205112.

8 Li, D.; Haneda, H.; Hishita, S.; Ohashi, N. *Chem. Mater.* **2005**, *17*, 2596-2602.

9 In, S.; Orlov, A.; Berg, R.; Garcia, F.; Jimenez, S. P.; Tikhov, M. S.; Wright, D. W.; Lambert,R. M. *J. Am. Chem. Soc.* **2007**, *129*, 13790-13791.

10 Shi, J. W.; Zheng, J. T.; Hu, Y.; Zhao, Y. C. *Mater. Chem. Phys.* **2007**, *106*, 24-249.

11 He, Z.; Xu, X.; Song, S.; Xie, L.; Tu, J.; Chen, J.; Yan, B. *J. Phys. Chem. C* **2008**, *112*,16431-16437.

12 Xu, J. H.; Li, J.; Dai, W.; Cao, Y.; Li, H.; Fan, K. *Appl. Catal. B: Environ.* **2008**, *79*, 72-80.

13 Liu, G.; Zhao, Y.; Sun, C.; Lu, G. Q.; Cheng, H. M. *Angew. Chem., Int. Ed.* **2008**, *47*, 4516-4520.

14 Ling, Q.; Sun, J.; Zhou, Q. *Appl. Surf. Sci.* **2008**, *254*, 3236-3241.

15 Song, S.; Tu, J.; Xu, L.; Xu, X.; He, Z.; Qiu, J.; Ni, J.; Chen, J. *Chemosphere* **2008**, *73*, 1401-1406.

16 Liu, G.; Sun, C.; Cheng, L.; Jin, Y.; Lu, H.; Wang, L.; Smith, S. C.; Lu, G. Q.; Cheng, H. M. *J. Phys. Chem. C* **2009**, *113*, 12317-12324.

17 Shi, J. W. *Chem. Eng. J* **2009**, *151*, 241-246.

18 Tan, K.; Zhang, H.; Xie, C.; Zheng, H.; Gu, Y.; Zhang, W. F. *Catal. Commun.* **2010**, *11*, 331-335.

19 Wang, E.; He, T.; Zhao, L.; Chen, Y.; Cao, Y. *J. Mater. Chem.* **2011**, *21*, 144-150.

20 Kuvarega, A. T.; Krause, R. W. M.; Mamba, B. B. *J. Phys. Chem.C* **2011**, *115*, 22110-22120.

21 Jaiswal, R.; Patel, N.; Kothari, D.C.; Miotello, A. *Appl. Cat. B.* **2012**, *126*, 47-54.

22 Zhang, J.; Xi, J.; Ji, Z. *J. Mater. Chem.* **2012**, *22*, 17700-17708.

23 Cottineau, T.; Béalu, N.; Gross, P-A.; Pronkin, S. N.; Keller, N.; Savinova, E. R.; Keller, V. *J. Mater. Chem. A* **2012**, Accepted manuscript, doi: 10.1039/C2TA00922F.

24 Hoang, S. H.; Guo, S.; Mullins, C. B. *J. Phys. Chem. C* **2012**, *116*, 23283-23290.

25 Li, X. *Int. J. Elec. Sci.* **2012**, *7*, 11519.

26 Fisher, M. B.; Keane, D. A.; Fernández-Ibáñez, P.; Colreavy, J.; Hinder, S. J.; McGuigan, K. G.; Pillai, S. C. *App. Catal. B. Environ.* **2013**, *7*, 8-13.

27 Gao, B.; Luo, X.; Fu, H.; Lin, B.; Chen, Y.; Gu, Z. *Mater. Res. Bull.* **2013**, *2,* 587-594.

28 Yin, W.-J.; Tang, H.; Wei, S.-H.; Al-Jassim, M. M.; Turner, J.; Yan, Y. *Phys. Rev. B* **2010**, *82*, 045106/1-6.

29 Ma, X.; Wu, Y.; Lu, Y.; Xu, J.; Wang, Y. ; Zhu, Y. *J. Phys. Chem. C* **2011**, *115*, 16963-16969.

30 Tayade, R. J. ; Surolia, P. K. ; Kulkarni, R. G. ; Jasra, R. V. *Sci. Technol. Adv. Mater.* **2007**, *8*, 455.

31 Matthews, R. W. *J. Chem. Soc., Faraday Trans. 1* **1989**, *85*, 1291-1302.

32 Reeves, P.; Ohlhausen, R.; Sloan, D.; Pamplin, K.; Scoggins, T.; Clark, C.; Hutchingson, B.; Green D. *Solar Energy* **1992**, *48*, 413-420.

33 Lakshmi, S.; Renganathan, R.; Fujita, S. *J. Photochem. Photobiol. A* **1995**. *88*, 163-167.

34 Teh, C. M.; Mohamed, A. R. *J. Alloys. Compd.* **2011**, *509*, 1648-1660.

35 Klein, S.; Weitze, H. J. *J. Appl. Crystallogr.* **1975**, *8*, 54-59.

36 Rao, C. N. R. *Can. J. Chem.* **1961**, *39*, 498-500.

37 Wang, Y.; Smarsly, B. M.; Djerdj, I. *Chem. Mater.* **2010**, *22*, 6624-6631.

38 Sen, S. K.; Riga, J.; Verbist, J. *Chem. Phys. Lett.* **1976**, *39*, 560-564.

39 Wagner, C. D.; Riggs, W. M.; Davis, L. E.; Moulder, J. F.; Mullenberg, G. E. Handbook of X-ray Photoelectron Spectroscopy, Perkin-Elmer, Eden Prairie, **1979**.

40 Bahl, N. K. *J. Phys. Chem. Solids* **1975**, *36*, 485-491.

41 Hirano, M.; Ichihashi, Y. *J. Mater. Sci.* **2009**, *44*, 6135-6143.

42 Khomenko, V. M.; Langer, K.; Rager, H.; Fett, A. *Phys. Chem. Mineral.* **1998**, *25*, 338-346.

43 Deshpande, A.; Madras, G.; Gupta, N. M. *Mater. Chem. Phys.* **2011**, *126*, 546-554.

44 Cornaz, P. F.; Van Hooff, J. H. C.; Pluijm, F. J.; Schuit, G. C. A. *Discuss. Faraday Soc.* **1966**, *41*, 290-304.

45 Sun, Y.; Egawa, T.; Zhang, L.; Yao, X. *J. Mat. Sci. Lett.* **2003**, *22*, 799-802.

46 Serwicka, E. *Colloids and Surfaces* **1985**, *13*, 287-293.

47 Sun, Y.; Egawa, T.; Shao, C.; Zhang, L.; Yao, X. *J. Phys. Chem. Sol.* **2004**, *75*, 1793-1797.

48 Reyes-Garcia, E. A.; Sun, Y.; Reyes-Gil, K. R.; Raftery, D. *SS. Nuc. Mag. Res.* **2009**, *35*, 74-81.

49 Chester, P. F. *J. Appl. Phys.* **1961**, *32*, 866-868.

50 Zimmermann, P. H. *Phys. Rev. B.* **1973**, *8*, 3917-3928.

51 Kiwi, J.; Suss, J. T.; Szapiro, S. *Chem. Phys. Lett.* **1984**, *106*, 135-138.

52 Saha, N.; Tompkins, H. *J. Appl. Phys.* **1992**, *7*, 3072.

53 Zhang, C.; Ikeda, M.; Uchikoshi, T.; Li, J.; Watanabe, T.; Ishigaki, T. *J. Mater. Res.* **2011**, *26*, 658-670.

54 Ruiz, A. M.; Dezanneau, G.; Arbiol, J.; Cornet, A.; Morante, J. R. *Chem. Mater*. **2004**, *16*, 862-871.

55 Baumard, J. F.; Tani, E. *J. Chem. Phys.* **1977**, *67*, 857-860.

56 Hirano, M.; Matsushima, K. *J. Am . Ceram. Soc.* **2006**, *89*, 110-117.

57 Herrmann, J. M. *Catal. Today* **1999**, *53*, 115-129.

58 Zhou, L.; Yu, M; Yang, J.; Wang, Y.; Yu, C. *J. Phys. Chem. C* **2010**, *114*, 18812-18818.

59 Vegard, L.; Hauge, T. *Zeitschrift für Physik* **1927**, *42*, 1-14.

60 Zhao, L.; Zhao, X.; Liu, J.; Zhang, A.; Wang, D.; Wei, B. *J. Sol-Gel Sci. Technol*. **2010**, *53*, 475-479.

61 Emeline, A.V.; Furubayashi, Y.; Zhang, X.; Jin, M.; Murakami, T.; Fujishima, A. *J. Phys. Chem. B.* **2005**, *109*, 24441-24444.

62 Nikolay, T.; Larina, L.; Shevaleevskiy, O.; Ahn, B.T. *Energy Environ. Sci.* **2011**, *4*, 1480-1486.

63 Di Valentin, C.; Finazzi, E.; Pacchioni, G. *Chem. Mater.* **2008**, *20*, 3706–3714.

64 Atuchin, V. V.; Kalabin, I. E.; Kesler, V. G.; Pervukhina, N. K. *J. Elec. Spec. and Rel. Phen.* **2005**, *142*, 129-134.

65 Etacheri, V.; Seery, M. K.; Hinder, S. J.; Pillai, S. C. *Chem. Mater.* **2010**, *22*, 3843-3853.

66 Cong, Y.; Zhang, J. Z.; Chen, F.; Anpo, M. *J. Phys. Chem. C* **2007**, *111*, 6976.

67 Chen, H.; Nambu, A.; Wen, W.; Graciani, J.; Zhong, Z.; Hanson, J.; Fujita, E.; Rodriguez, J. A. *J. Phys. Chem C* **2007**, *111*, 1366-1372.

68 Breault, T. M.; Bartlett, B. M. *J. Phys. Chem. C* **2012**, *116*, 5986–5994.

69 Hirano, M.; Ichihashi, Y. *J. Mater. Sci.* **2009**, *44*, 6135–6143.

70 Khomenko, V. M.; Langer, K.; Rager, H.; Fett, A. *Phy. Chem. Mineral.* **1998**, *25*, 338–346.

71 Deshpande, A.; Madra, G.; Gupta, N. M. *Mater. Chem. Phys.* **2011,** *126*, 546–554.

72 Chen, X.; Burda, C. *J. Phys. Chem. B* **2004**, *108*, 15446–15449.

73 Sato, S.; Nakamura, R.; Abe, S. *Appl. Cat. A: Gen.* **2005**, *284*, 131–137.

74 Napoli, F. N.; Chiesa, M.; Livraghi, S.; Giamello, E.; Agnoli, S.; Granozzie, G.; Pacchioni, G. Valentin, C. D. *Chem. Phys. Lett.* **2009**, *477*, 135–138.

75 Asahi, R.; Morikawa, T.; Ohwaki, T.; Aoki, K.; Taga, Y. *Science* **2001**, *293*, 269-271.

76 Mills, A.; Wang, J. *J. Photochem. and Photobiol. A: Chem.* **1999**, *127*, 123–134.

77 Li, F-. T.; Zhao, Y.; Hao, Y-. J.; Wang, X-. J.; Liu, R-. H.; Zhao, D-. S.; Chen, D-. S. *J. Hazard. Mater.* **2012**, *239*, 118–127.

78 Mohapatra, L.; Parida, K.; Satpathy, M. *J. Phys. Chem. C* **2012**, *116*, 13063–13070.

79 Yang, Y.; Zhang, G.; Yu, S.; Shen, X. *Chem. Eng. Jour.* **2010**, *162*, 171–177.

80 Li, G.; Qu, J.; Zhang, X.; Liu, H.; Liu, H. *J. Mol. Catal. A: Chem.* **2006**, *259*, 238–244.

81 Ilan, Y. A.; Czapski, G.; Meisel, D. T. *Biochem.et Biophys. Acta.* **1976**, *430*, 209–224.

82 Andronic, L.; Isac, L.; Duta, A. *J. Photochem. Photobio. A: Chem.* **2011**, *221*, 30–37.

83 Shang, M.; Wang, W.; Sun, S.; Ren, J.; Zhou, L.; Zhang, L. *J. Phys. Chem. C* **2009**, *113*, 20228–20233.

84 Di Valentin, C.; Pacchioni, G. *J. Phys. Chem. C* **2009**, *113*, 20543-20552.

85 Rauf, M. A.; Ashraf, S. S. *Chem. Eng. Journal* **2009**, *151*, 10–18.

86 Pian, X-. T.; Lin, B-. Z.; Chen, Y-. L.; Kuang, J-. D.; Zhang, K-. Z.; Fu, L-. M. *J. Phys. Chem. C* **2011**, *115*, 6531–6539.

87 Chen, X.; Mao, S. S. *Chem. Rev.* **2007**, *107*, 2891–2959.

88 Baumard, J. F.; Tani, E. *J. Chem. Phys.* **1977**, 67, 857–860.

Chapter 3. Water Oxidation using Co-catalyst Loaded NbN-25

Portions of this chapter have been submitted for publication:
Breault, T. M.; Bartlett, B. M. **2013**, *submitted.*
Figures: 3.2, 3.3, 3.4, 3.5, 3.6, 3.7, 3.8, 3.9, 3.10

3.1 Introduction

Chapter 1 provided motivation for the pursuit of renewable energy sources, specifically targeting solar energy storage and conversion through carbon-neutral fuel cycles. Chapter 2 provided a comprehensive study on the synthesis, physical characterization, and photocatalytic degradation of methylene blue for a composition-dependent series of (Nb,N) co-incorporated anatase TiO_2 compounds, $Ti_{1-(5x/4)}Nb_xO_{2-y-\delta}N_y$. The mechanism of MB degradation was examined and suggests good electron transfer capabilities for these photocatalysts. From these investigations, we elucidated the role that defect structure played in photocatalysis and chose to focus this chapter on the highest performing compound, 25 mole-percent niobium, denoted as NbN-2. This compound had maximum substitutional nitrogen and minimal Ti^{3+} present, resulting in exhibiting the fastest rate constant for dye degradation presumably due to better charge compensation and few defect sites.

It is known that the water splitting rate for a given photocatalyst can be remarkably improved through loading a co-catalyst, typically in the form of nanoparticles, illustrated in Figure 3.1. Figure 3.1 in an illustration of an ideal, visible-light harvesting photocatalyst loaded with appropriate dual co-catalysts for each half reaction, PtO_x for reducing protons and RuO_2 for water oxidation. Co-catalysts facilitate charge transfer at the surface by trapping photogenerated electrons or holes, and transferring them in multi-electron steps. For the proton half reaction, PtO_x[1] is a co-catalyst typically used, not of particular interest for this chapter because we focus on the water oxidation half reaction. Recent progress on earth-abundant water oxidation co-catalysts loaded onto photocatalysts include CoP_i, [2–5] CoO_x,[6,7] and NiO_x[8,9]; however, noble metal oxides, such as RuO_2[10–13] and IrO_2,[14–18] have been found to be the most efficient water oxidation catalysts. Dual co-catalyst loading has also been successfully employed. [7,19,20]

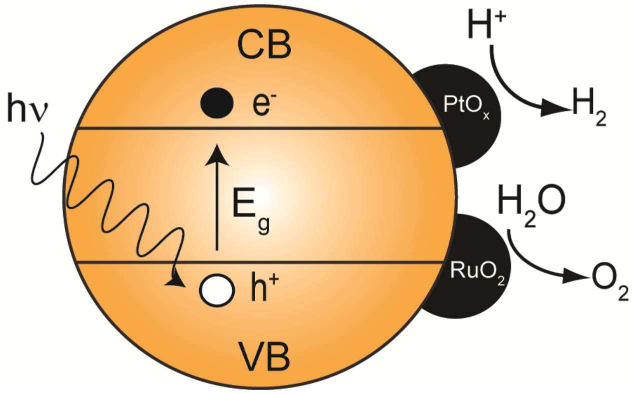

Figure 3.1 Proposed mechanism for photocatalytic water oxidation using a visible light harvesting semiconductor modified with RuO_2 and/or PtO_x under visible light irradiation.

The two half reactions (equations 1 and 2) of overall water splitting (equation 3) are expressed in the following reactions:

$$4H^+ + 4e^- \rightarrow 2H_2 \qquad E^o_{cathodic} = 0V - 0.0591\ V\ (pH)\ (NHE) \qquad (1)$$

$$O_2 + 4H^+ + 4e^- \rightarrow H_2O \qquad E^o_{anodic} = 1.23V - 0.0591\ V\ (pH)\ (NHE) \qquad (2)$$

$$2H_2O \rightarrow 2H_2 + O_2 \qquad E^o_{overall} = -1.23V - 0.0591\ V\ (pH)\ (NHE) \qquad (3),$$

where protons are reduced to form hydrogen gas (equation 1), and water is oxidized to form oxygen gas (equation 2). The overall reaction (equation 3) is thermodynamically uphill, requiring 474 kJ • mol^{-1} for the 4e$^-$ process. The water oxidation reaction is kinetically slower, requiring four proton-coupled-electron transfer steps. The slow kinetics is typified by an overpotential of ~ 600 mV associated with the reaction. Using co-catalysts should improve this overpotential and result in faster rates for our nanoparticles.

Electron donors or acceptors are added in order to study either the proton reduction or water oxidation half reactions separately. Adding an electron acceptor ensures that the overall reaction has a lower overpotential. Two commonly used electron acceptors for studying the water oxidation half reaction are reduction of silver, Ag^+/Ag^0,6,[7, 21–26] or iodate, IO_3^-/I^-,[13,27–30] according to the following reactions:

$$Ag^+ + e^- \rightarrow Ag^0 \qquad (E^o = 0.799 \text{ V vs. NHE}) \qquad (4)$$

$$IO_3^- + 6H^+ + 6e^- \rightarrow I^- + 3H_2O \qquad (E^o = 1.087 \text{ V vs. NHE}) \qquad (5)$$

In equation 4, Ag^+/Ag^0 decreases the driving force, but plates metallic silver onto the surface of the photocatalyst, limiting light absorption by the particles and decreases oxygen evolution over time. In equation 5 reducing IO_3^- to I^- is multi-electron, but significantly decreases the driving force for the overall reaction. Through using a co-catalyst and electron acceptor, finding a suitable water oxidation photocatalyst to couple with a suitable proton reduction photocatalyst can result in a Z-scheme set-up, where each half reaction is performed on separate photocatalysts. This allows for suitable hydrogen and oxygen evolving photocatalysts that are optimized for each half reaction rather than a single particle responsible for overall water splitting. In this chapter, we aim to study the ability of a co-incorporated compound, NbN-25, as a water oxidation photocatalyst using a co-catalyst and electron acceptor.

3.2 Experimental

3.2.1 Materials and general procedures

Co-incorporated compounds were prepared according to the synthetic procedure outline in Chapter 2.[31] Reagent grade chemicals were obtained from Sigma Aldrich and Strem. $RuCl_3•3H_2O$ (Strem) and $NaIO_3$ (Sigma Aldrich) were used as received without further purification. An MTI box furnace was used to anneal the powders loaded with co-catalyst in scintillation vials in air. House-supplied nitrogen, passed through a Drierite™ drying unit, was used to purge solutions and cell headspace. Millipore water (18.2 MΩ) was used for all experiments.

3.2.2 Preparation of co-catalyst loaded compounds

A stock solution of 1 mg/mL $RuCl_3$ was prepared by dissolving the appropriate amount of $RuCl_3•3H_2O$ in Millipore water and stirring at room temperature for 20 minutes. The appropriate concentration of stock solution was then added to approximately 100 mg of the photocatalyst ($Ti_{1-(5x/4)}Nb_xO_{2-y-\delta}N_y$, TiO_2:(Nb,N) at 25 mole percent Nb, denoted as NbN-25) to achieve various loading weight percents (0.5 – 2 wt%). The solutions were stirred vigorously at 100 °C until all of the water evaporated. The subsequent co-catalyst loaded powder was annealed in air at 350 °C for 1 hour, with 20 min heating and cooling stages. Powders were ground with a mortar and pestle prior to testing for photocatalytic water oxidation.

3.2.3 Physical methods

X-ray diffraction patterns were recorded on a Bruker D8 Advance diffractometer equipped with a graphite monochromator, a Lynx-Eye detector, and parallel beam optics using Cu-Kα radiation (λ = 1.54184 Å). Patterns were collected using a 0.6 mm incidence slit, with a step size and scan rate of 0.05º/step and 2 s/step respectively. Phases were identified as RuO_2 (JCPDF 70-2662) using MDI Jade version 5.0.

UV-Vis spectra were recorded using an Agilent-Cary 5000 spectrophotometer equipped with a Praying Mantis diffuse reflectance accessory. Spectra were recorded in reflectance mode, using $BaSO_4$ as the background material. The reflectance data were transformed mathematically into the Kubelka-Munk function, $F(R) = (1-R)^2/2R$.

X-ray photoelectron spectra were recorded on a Kratos XPS (8 mA, 14 keV, Monochromatic Al). Powder samples were secured to the transfer bar with copper tape and were pumped overnight under high vacuum to 1×10^{-9} torr. The XPS data were fit using the CasaXPS program, with all peaks calibrated to C(1s) at 284.5 eV.

High resolution transmission electron microscopy was performed on a JEOL 3011 high resolution electron microscope. HRTEM samples were prepared by sonicating a dispersion of NbN-25 powder in acetone and drop casting the suspension onto a Cu grid with an ultra-thin holy carbon film (Ted Pella™).

3.2.4 Water oxidation set-up

The water oxidation reaction was performed in a custom built Pyrex cell with a quartz window. 50 mg of NbN-25 loaded with RuO_2 was suspended in 30 mL of 1 mM $NaIO_3$ (headspace of 34 mL, 64 mL total volume). The photocatalyst and solution were stirred vigorously and purged with nitrogen for 1 hour. A fluorescence probe (FOSSPOR Ocean Optics Inc.) was calibrated at 20.9 % O_2 and 0 % O_2 before use. Once the solution was purged and the probe equilibrated at 0 % O_2, the cell was irradiated for three hours using a Newport-Oriel 150 W Xe arc lamp fitted with a water filter to remove IR light and appropriate cut-on filters ($\lambda >$ 295, 415, 455, 515 nm), specified throughout this chapter. The temperature fluctuated by ~3 °C throughout the three hour experiment. The ideal gas law was used to calculate the number of moles of O_2 produced, using the measured volume of the head space, temperature recorded by the NeoFox probe, and partial pressure of O_2 recorded with the fluorescence probe. Henry's law was used to account for dissolved O_2.

3.3 Results and discussion

Chapter 2 discussed the synthesis and physical characterization of a co-incorporated powder, $Ti_{1-(5x/4)}Nb_xO_{2-y-\delta}N_y$, abbreviated NbN-25, (25 mole percent niobium incorporation in TiO_2 annealed under flowing NH_3), which showed excellent photocatalytic activity for the degradation of MB dye.[31,32] We hypothesized that NbN-25 would perform visible light water oxidation due to its small band gap (~ 2.2 eV) and ability to generate active oxygen species in aqueous solution. We recognize that dye degradation and water oxidation proceed via different mechanisms; however, the photodegradation of MB dye provides a starting place for electron transfer chemistry, where finding new materials capable of performing photocatalytic redox reactions is important. Herein we examine the process of performing water oxidation on a single particle surface, using co-catalysts for increased rates.

3.3.1 Characterizing the co-catalyst loaded co-incorporated compound

An impregnation technique was used to load a desired quantity of RuO_2 co-catalyst (0.5-2 wt %) onto the co-incorporated compound, followed by annealing in air at 350 °C for 1 hour. The low annealing temperature and dwell time of 350 °C for 1 hour were selected in order to maintain substitutional nitrogen at the surface of the co-incorporated compound, which is confirmed by X-ray photoelectron spectroscopy to be present before and after annealing in air, shown in Figure 3.2. This result suggests that 350 °C is a low enough temperature in order to maintain substitutional nitrogen within the anatase structure.

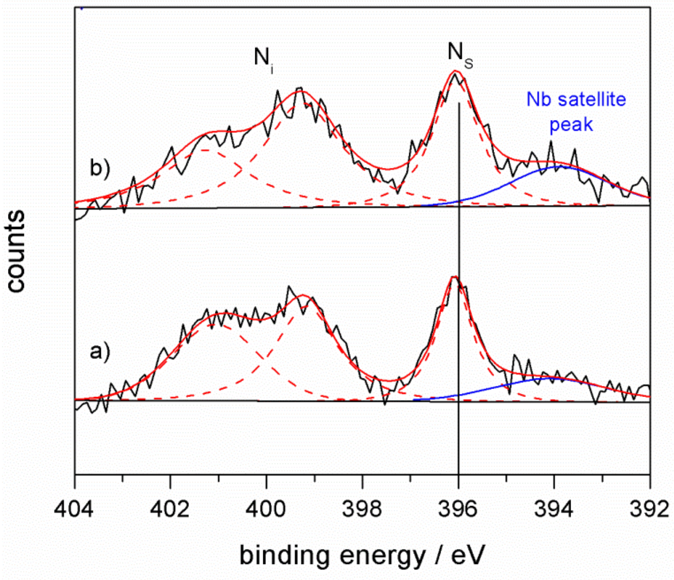

Figure 3.2 XP spectra of NbN-25 loaded with 1 wt% RuO_2 a) before and b) after annealing at 350 °C for 1 hour in air.

At low weight percent loading of RuO_2, the co-catalyst is not detected by X-ray diffraction (Figure A.42). To verify the formation of RuO_2, a control experiment shows that annealing an aqueous solution of $RuCl_3{\bullet}3H_2O$ in air at 350 °C for 1 hour forms polycrystalline RuO_2, confirmed by powder XRD (Figure A.43). High resolution transmission electron microscopy (HRTEM) is used in order to probe the crystallinity and formation of crystalline NbN-25 and RuO_2 nanoparticles. HRTEM images are presented in Figure 3.3. NbN-25 nanoparticles are shown to have particle diameters ranging from 10 – 20 nm in Figure 3.3a, with a histogram representing the range of particle diameters shown in Figure 3.4. The particles are homogenous, but slightly agglomerated. The NbN-25 (*101*) planes are highlighted in Figure 3.3b, assigned by their *d*-spacing value of 0.35 nm. Figure 3.3c and d are representative images for 1 wt% RuO_2 loading, with *d*-spacing for (*101*) of 0.35 nm, and (*110*) RuO_2 of 0.32 nm.

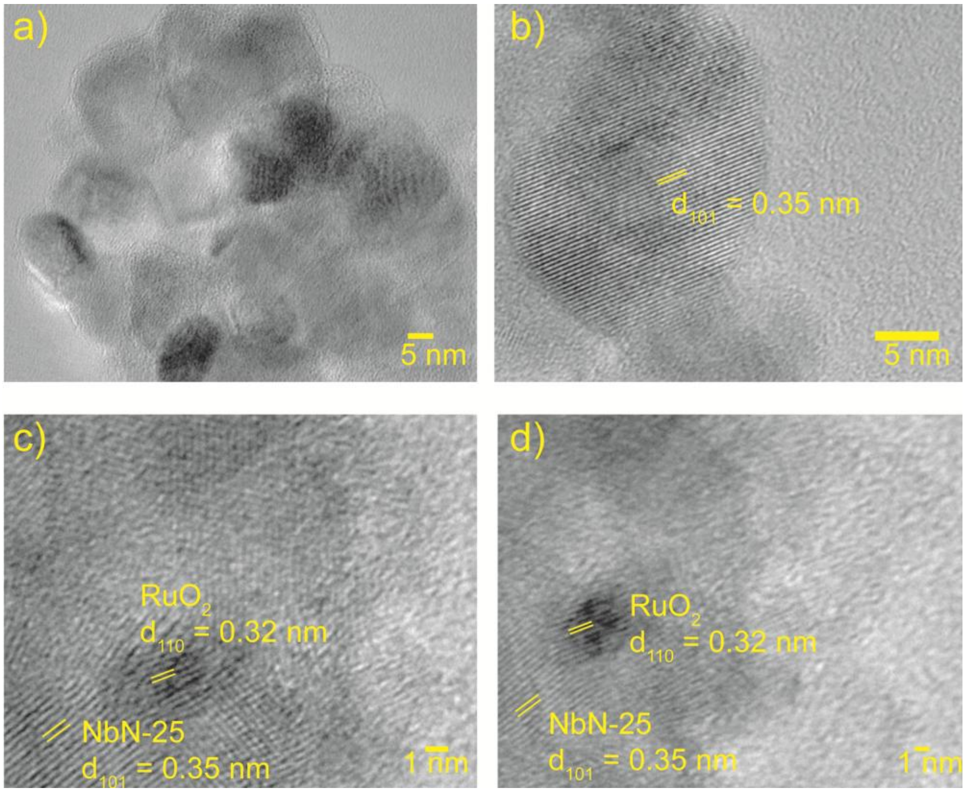

Figure 3.3 TEM images of a) dispersed NbN-25 nanoparticles, b) NbN-25 d_{101} spacing, c) and d) 1 wt% RuO_2 loaded NbN-25.

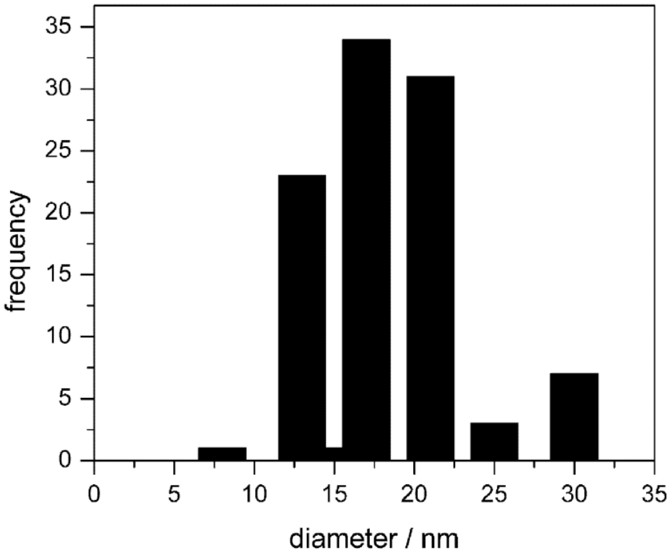

Figure 3.4 Histogram of the particle diameter for 100 nanoparticles of NbN-25.

Furthermore, important to photocatalysis, diffuse reflectance UV-Vis spectroscopy, shown in Figure 3.5, shows that loading NbN-25 with 1 wt% RuO_2 does not significantly interfere with the absorption band of the photocatalyst. NbN-25 particles without RuO_2 co-catalyst absorbs light at $\lambda \leq 525$ nm, depicted in Figure 3.5a. We observe the absorption band of NbN-25 loaded with 1 wt% RuO_2 unchanged to ~ 500 nm, shown in Figure 3.5b, with slight baseline absorption for $\lambda > 500$nm. The baseline absorption from 500 – 800 nm is due to the presence of RuO_2. At higher weight percent loading, 2 wt% RuO_2, significant baseline absorption is observed and could interfere with the absorption by the photocatalyst at all wavelengths, shown in Figure 3.5c. The difference in absorption at various weight percent loading of RuO_2 has implications for water oxidation, *vide infra*.

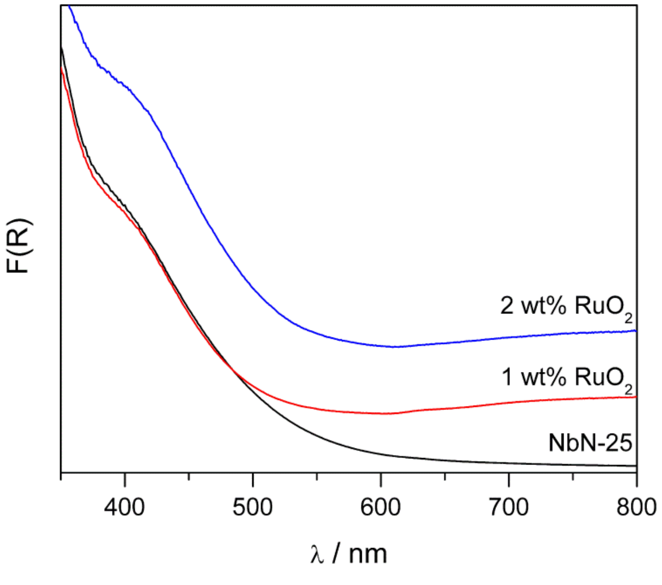

Figure 3.5 Diffuse reflectance spectroscopy for a) bare NbN-25, b) 1 wt % RuO_2 loaded NbN-25, and c) 2 wt % RuO_2 loaded NbN-25.

3.3.2 Water oxidation

The water oxidation performance of NbN-25 and RuO_2 loaded NbN-25 compound was examined in the presence of a sacrificial electron acceptor, IO_3^-, as follows:

$$2IO_3^- + 12H^+ + 12e^- \rightarrow 2I^- + 6H_2O \qquad (E^o = 1.087 \text{ V vs. NHE}) \qquad (6)$$

$$6H_2O \rightarrow 12H^+ + 12e^- + 3O_2 \qquad (E^o = 1.23 \text{ V vs. NHE}) \qquad (7)$$

$$2IO_3^- \rightarrow 2I^- + 3O_2 \qquad (E^o = -0.143 \text{ V vs. NHE}) \qquad (8),$$

where IO_3^- is reduced to I^- (equation 6) and water is oxidized to oxygen (equation 7), to yield the overall reaction displayed in equation 8. As discussed in Section 3.1, iodate was chosen as the electron acceptor over silver ions in order to avoid plating a metallic material on the particles. A test reaction involving reducing Ag^+/Ag^0 was conducted; however, oxygen evolution over the course of 3 hours was not observed due to the immediate plating of silver particles throughout the entire cell, resulting in black powders. Using silver as an electron acceptor has been reported in the literature with the caveat that slower kinetics over time are due to forming metallic Ag.[33]

NbN-25 was tested as a water oxidation photocatalyst in aqueous 1 mM $NaIO_3$ under simulated solar irradiation (AM1.5G). Without added RuO_2, no oxygen is evolved after three hours of illumination, even when the irradiance is increased to ~ 600 nmW/cm^2 (6-times that of the high noon solar flux). Previous work in methylene blue dye degradation shows that oxidation products, such as benzenesulfonic acid and dimethylaniline derived from •OH, an active oxygen species, are formed upon irradiating NbN-25 in 40 ppm MB solution. The process of forming hydroxyl radicals hints that hole transfer for water oxidation could be slow, and a co-catalyst that can carry out multi-electron chemistry, such as RuO_2, may assist in storing photogenerated holes. Under 6-sun illumination of a 1 mM $NaIO_3$ solution with 1 wt% RuO_2 loaded onto NbN-25, 16 μmol O_2 are observed after 3 hours of irradiation, illustrated in Figure 3.6.

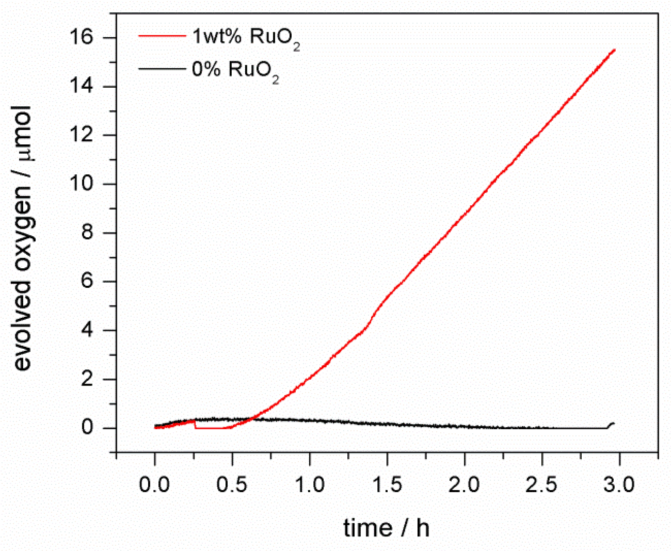

Figure 3.6 Oxygen evolution from NbN-25 with (red) and without (black) the presence of a co-catalyst RuO_2. Reaction conditions: 50 mg loaded powder, 30 mL of 1 mM $NaIO_3$, 150 W Xe lamp fitted with an AM 1.5 global filter, ~ 600 mW/cm^2.

The oxygen evolution reaction depends strongly on the percentage of co-catalyst loading of RuO_2 at 350 °C. The water oxidation activity improves with increasing loading percent of co-catalyst, reaching a maximum water oxidation rate of ~ 7 μmol•h^{-1} at 1 wt% RuO_2, shown in Figure 3.7. At 1 wt% RuO_2 loading, the oxygen evolution rate was significantly enhanced compared to bare NbN-25 (~ 7 *vs*. 0 μmol•h^{-1}), which did not evolve any oxygen under the reaction conditions. We hypothesize that loading higher percents of RuO_2 (> 1%) results in poor light absorption by NbN-25 particles due to the presence of RuO_2 coverage on the surface of the nanoparticles. The absorption spectrum of 2 wt% co-catalyst loaded NbN-25 is shown in Figure 3.5c, where there is significant baseline absorption at all wavelengths of light due to RuO_2 coverage. At 1 wt% RuO_2 loading, the absorption edge at 500 nm is not altered; however, there is slight baseline absorption > 500 nm. We used the optimized co-catalyst loading percent, 1 wt% RuO_2, for the remainder of the experiments presented in this chapter.

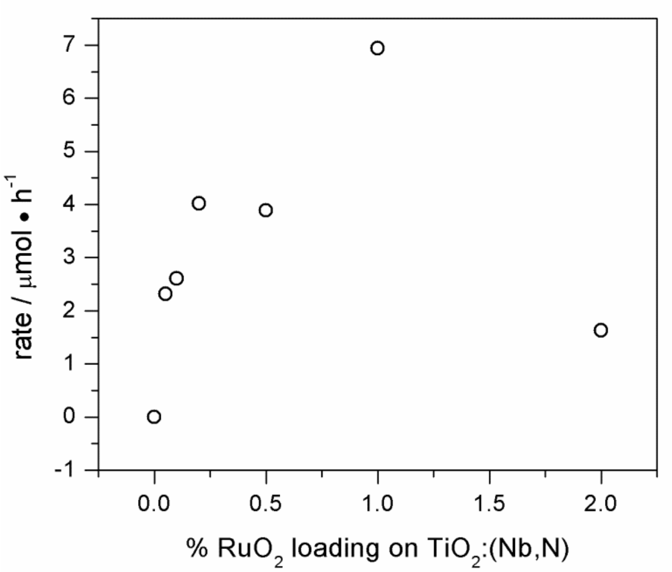

Figure 3.7 Optimization of RuO_2 wt% on NbN-25, annealed at 350 °C for 1 hour. Reaction conditions: 50 mg loaded powder, 30 mL of 1 mM $NaIO_3$, 150 W Xe lamp fitted with an AM 1.5 global filter.

Furthermore, the stability of nitrogen containing compounds is questionable under highly oxidizing conditions, such as water oxidation. In some photocatalytic reactions that employ (oxy)nitride photocatalysts, substitutional nitrogen can be decomposed by photogenerated holes according to the reaction:

$$2N^{3-} + 6h^{+} \rightarrow N_{2(g)} \qquad (9),$$

which liberates nitrogen gas. Nitrogen gas is often detected via gas chromatography techniques performed in conjunction with detecting oxygen and/or hydrogen when irradiating photocatalysts. While we have not performed this in situ experiment ourselves, we should be cognizant of the stability issues related to (oxy)nitrides. To begin to address this notion, we have used XP spectroscopy to compare the substitutional nitrogen present in NbN-25 before and after illumination. Substitutional nitrogen is present before and after exposure to the oxidizing conditions, confirmed by XP spectroscopy shown in Figure 3.8. The unchanging features in the XPS results suggest that our compounds do not degrade by this mechanism under our operating conditions.

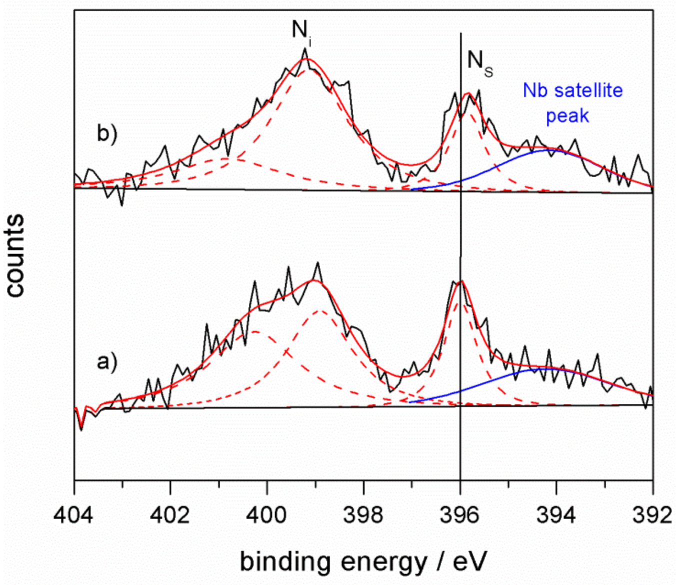

Figure 3.8 XP spectra of TiO_2:(Nb,N) loaded with 1 wt% RuO_2 a) before and b) after 3h irradiation.

3.3.3 Oxygen evolution using cut-on filters

Important to photocatalysis, we next investigated the visible light response of this compound by using a 150 W Xe lamp fitted with a water filter to eliminate IR light that can cause fluctuating temperatures that occur upon illumination (T = 23 °C ± 3 °C). The reaction conditions included 50 mg of 1 wt% RuO_2 loaded photcatalyst in 30 mL of N_2-purged 1 mM $NaIO_3$ solution in an air tight cell. The cut-on filters used to probe oxygen evolution at longer wavelengths included $\lambda \geq 295$, 400, 455 and 515 nm. The irradiance for each experiment was kept constant at ~ 640 mW/cm^2.

Figure 3.9 shows that oxygen evolution depends on the incident wavelength of light, with total μmols oxygen evolved after three hours of illumination (red circles) trending quite well with the diffuse reflectance absorption edge of this compound (black line). Maximum oxygen is evolved (~ 33 μmol) when UV light is included ($\lambda \geq 295$); however, measureable oxygen is also observed when UV light is excluded: $\lambda \geq 455$ nm, ~ 12 μmol oxygen and $\lambda \geq 515$ nm, ~ 8 μmol oxygen. Oxygen detection at longer wavelengths of light suggests that the N-based impurity levels formed above the O(2p) valence band by introducing Nb^{5+} and N^{3-} (discussed in detail in Section 2.4) are contributing to the photocatalytic activity of this co-incorporated compound for water oxidation. These results are consistent with using a cut-on filter for MB degradation by the same compound, which also resulted in degradation of methylene blue dye (Figure A.41).

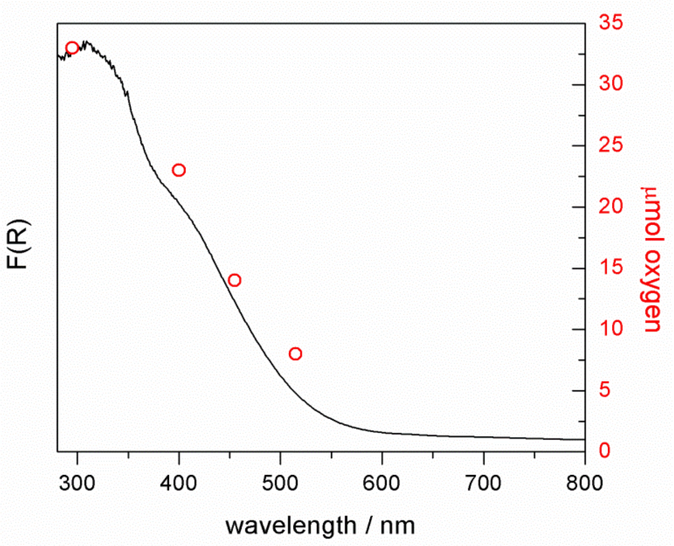

Figure 3.9 Dependence of O_2 evolution after three hours of irradiation with cut-on wavelengths for NbN-25 loaded with 1wt% RuO_2. The diffuse reflectance spectra of NbN-25 is also shown. Reaction conditions: 50 mg catalyst, 1 mM $NaIO_3$, 150 W Xe lamp, water filter, ~ 640 mW/cm^2.

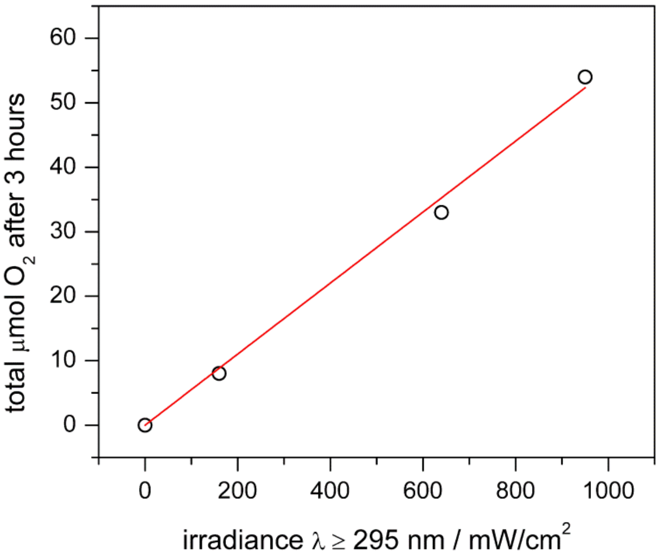

Figure 3.10 µmol O_2 vs. powder density for NbN-25 loaded with 1 wt% RuO_2. Reaction conditions: 50 mg catalyst, 1 mM $NaIO_3$, 150 W Xe lamp, water filter, ~ 640 mW/cm^2.

Using a single cut-on filter ($\lambda \geq 295$ nm) at various irradiance results in a linear relationship between the total μmol of O_2 produced after 3 hours and the power density. This preliminary result suggests that photogenerated holes are oxidizing water effectively, and photogenerated electrons are reducing iodate. Constructing photoanodes (Chapter 6) to relate light intensity to photocurrent density will reveal more information regarding interfacial kinetics and recombination rates. Furthermore, incident photon to current efficiencies and quantum yields at various wavelengths can be calculated.[34] For defect-rich co-incorporated compositions such as NbN-25, the role of defect structure can be exploited through the above mentioned experiments.

3.4 Future directions and perspective

Initial experiments using NbN-25 as a visible light responsive photocatalyst have produced promising results, evident through the cut-on experiments discussed in the previous section. We have developed a novel co-incorporated composition that is a *visible light* photocatalyst for water oxidation at $\lambda \leq 515$ nm. As discussed in Chapter 2, NbN-25 includes ~ 2 mole-percent total nitrogen and the lowest EPR signal for Ti^{3+}. The synergistic effect between Ti^{3+} and N impurity levels may lead to a smaller band gap of ~ 2.2 eV. NbN-25 is a superior photocatalyst for MB degradation compared to low mole-percent co-incorporated compositions that possess less surface substitutional nitrogen and more Ti^{3+}. We have tested some lower co-incorporated compositions loaded with 1 wt% RuO_2 as water oxidation photocatalysts, but do not observe a trend in photoactivity (Figure A.44). In all cases, 1 wt% RuO_2 results in enhanced photoactivity for water oxidation compared to non-loaded samples.

What are the future directions for this co-incorporated compound? A good starting point would be varying the co-catalyst as well as the co-catalyst loading technique. As discussed in the introduction of this chapter, numerous co-catalysts have been successfully incorporated with photocatalysts to result in enhanced water oxidation. No work has been done to co-catalyst load NbN-25 with CoO_x or IrO_x electrocatalysts; however, for other photocatalysts, the specific choice of co-catalyst affects the water oxidation photoactivity.[6] The loading method is also an important factor, so exploring the photodeposition of RuO_2, CoP_i, and IrO_x and the affect it has on water oxidation rates would shed insight on the role each water oxidation catalyst plays. Photodeposition relies on irradiating NbN-25 and creating an electron/hole pair that participates in the reduction of soluble co-catalyst species, ultimately depositing the desired co-catalyst on the active surface of the photocatalyst. This technique could be advantageous if the time of deposition is precisely controlled such that the desired co-catalyst is loaded only at photoactive spots. We hypothesize the resulting rates of water oxidation will increase based on good contact between photocatalyst and water oxidation catalyst.

To increase the efficiency of this system, dual co-catalyst loading is another option to consider. There are many instances of enhanced photocatalytic water oxidation when co-catalysts for each half reaction are used in concert (PtO_x and RuO_2 for instance).[29,30,35,36] The dual co-catalyst loading will be a key experiment to explore; however, challenges with annealing temperature being low enough to maintain substitutional nitrogen will be the limiting factor for good crystallinity of co-catalysts, thus possibly limiting the overall efficiency for water oxidation. Examining the role of PtO_x loading for hydrogen production should also be explored, for the CB minimum should lie more negative that the proton reduction potential, providing possibility of these compounds also acting as proton reduction photocatalysts. This experiment will require GC/MS headspace analysis, which can be performed by a future student in collaboration with a laboratory with this equipment.

Finally, Chapter 6 discusses future directions on a new synthetic approaches for making (oxy)nitride type materials. This synthetic direction is important for two reasons: 1) synthetic control over substitutional nitrogen could allow for better donor/acceptor match, decreasing defect impurities that may be acting as trap states above the valence band, and 2) an innovative approach could afford new morphologies and/or particle sizes, which could positively enhance photocatalytic activity. Also discussed in Chapter 6 is constructing photoanodes with good ohmic contact in order to elucidate the electronic structure of this composition (and other future co-incorporated compositions). Impedance spectroscopy will be important in order to experimentally determine the conduction band energy level. With well contacted photoanodes in hand, co-catalyst loading and necking treatments can be performed to optimize the performance of these electrodes as water oxidation photoanodes.

3.5 Conclusions

In conclusion, this chapter highlights the *visible light* water oxidation activity for a co-incorporated compound, NbN-25, in an aqueous $NaIO_3$ solution. NbN-25 was modified with RuO_2 via an impregnation technique, which resulted in polycrystalline co-catalyst loaded compounds. Adding a co-catalyst was necessary in order to evolve oxygen, and water oxidation activity depended on the co-catalyst weight percent loading. At 1 wt% RuO_2 loading, 16 μmol of oxygen was detected after three hours of illumination, which was the superior performing photocatalyst reported in this chapter. Most importantly NbN-25 was able to oxidize water under visible light irradiation, at $\lambda \leq 455$ and 515 nm, corresponding to the absorption edge of the compound.

3.6 References

1 Sabio, E. M.; Chamousis, R. L.; Browing, N. D.; Osterloh, F. E. *J. Phys. Chem. C* **2012**, *116*, 3161-3170.

2 Zhong, D. K.; Gamelin, D. R. *J. Am. Chem. Soc.* **2010**, *132*, 4202-4207.

3 Seabold, J. A.; Choi, K-. S. *Chem. Mater.* **2011**, *23*, 1105-1112.

4 Bledowski, M.; Wang, L.; Ramakrishnan, A.; Bétard, A.; Khavryuchenko, O. V.; Beranek, R. *Chem. Phys. Chem.* **2012**, *13*, 3018-3024.

5 Wang, D.; Li, R.; Zhu, J.; Shi, J.; Han, J.; Zong, X.; Li, C. *J. Phys. Chem. C* **2012**, *116*, 5082-5089.

6 Ma, S. S. K.; Hisatomi, T.; Maeda, K.; Moriya, Y.; Domen, K. *J. Am. Chem. Soc.* **2012**, *134*, 19993-19996.

7 Zhang, F.; Yamakata, A.; Maeda, K.; Moriya, Y.; Takata, T.; Kubota, J.; Teshima, K.; Oishi, S.; Domen, K. *J. Am. Chem. Soc.* **2012**, *134*, 8348-8351.

8 Townsend, T. K.; Browning, N. D.; Osterloh, F. E. *Energy Environ. Sci.* **2012**, *5*, 9543-9550.

9 Miseki, Y.; Kato, H.; Kudo, A. *Energy Environ. Sci.* **2009**, *2*, 306-314.

10 Sato, J.; Saito, N.; Yamada, Y.; Maeda, K.; Takata, T.; Kondo, J. N.; Hara, M.; Kobayashi, J.; Domen, K.; Inoue, Y. *J. Am. Chem. Soc.* **2005**, *127*, 4150-4151.

11 Kadowaki, H.; Saito, N.; Nishiyama, H.; Kobayashi, H.; Shimodaira, Y.; Inoue, Y. *J. Phys. Chem. C* **2007**, *111*, 439-444.

12 Inoue, Y. *Energy Environ. Sci.* **2009**, *2*, 364-386.

13 Maeda, K.; Abe, R.; Domen, K.; *J. Phys. Chem. C* **2011**, *115*, 3057-3064.

14 Meekins, B. H.; Kamat, P. V. *J. Phys. Chem. Lett.* **2011**, *2*, 2304-2310.

15 Suzuki, T.; Hisatomi, T.; Teramura, K.; Shimodaira, Y.; Kobayashi, H.; Domen, K. *Phys. Chem. Chem. Phys.* **2012**, *14*, 15475-15481.

16 Hoertz, P. G.; Kim, Y-L.; Youngblood, W. J.; Mallouk, T. E. *J. Phys. Chem. B* **2007**, *111*, 6845-6856.

17 Frame, F. A.; Townsend, T. K.; Chamousis, R. L.; Sabio, E. M.; Dittrich, T.; Browning, N. D.; Osterloh, F. E. *J. Am. Chem. Soc.* **2011**, *133*, 7264-7267.

18 Lee, Y.; Suntivich, J.; May, K. J.; Perry, E. E.; Shao-Horn, Y. *J. Phs.. Chem. Lett.* **2012**, *3*, 399-404.

19 Ma, S. S. K.; Maeda, K.; Abe, R.; Domen, K. *Energy Environ. Sci.* **2012**, *5*, 8390-8397.

20 Zhang, F.; Maeda, K.; Takata, T.; Domen, K. *Chem. Commun.* **2010**, *46*, 7313-7315.

21 Kudo, A.; Omori, K.; Kato, H. *J. Am. Chem. Soc.* **1999**, *121*, 11459-11467,

22 Kasahara, A.; Nukumizu, K.; Hitoki, G.; Takata, T.; Kondo, J. N.; Hara, M.; Kobayashi, H.; Domen, K. *J. Phys. Chem. A* **2002**, *106*, 6750-6753.

23 Kasahara, A.; Mukumizu, K.; Hitoki, G.; Takata, T.; Kondo, J. N.; Hara, M.; Kobayashi, H.; Domen, K. *J. Phys. Chem. B* **2003**, *107*, 791-797.

24 Siritanaratkul, B.; Maeda, K.; Hisatomi, T.; Domen, K. *Chem. Sus. Chem.* **2011**, *4*, 74-78.

25 Maeda, K.; Domen, K. *Angew. Chem. Int. Ed.* **2012**, *51*, 1-6.

26 Hitoki, G.; Takata, T.; Kondo, J.; Hara, M.; Kobayashi, H.; Domen, K. *Chem. Commun.* **2002**, 1698-1699.

27 Abe, R.; Sayama, K.; Sugihara, H. *J. Phys. Chem. B* **2005**, *109*, 16052-16061.

28 Abe, R.; Higashi, M; Domen, K. *Chem. Sus. Chem.* **2011**, *4*, 228-237.

29 Wang, D.; LI, R.; Zhu, J.; Shi, J.; Han, J.; Zong, X.; Li, C. *J. Phys. Chem. C* **2012**, *116*, 5082-5089.

30 Ma, S. S. K.; Maeda, K.; Abe, R.; Domen, K. *Energy Environ. Sci.* **2012**, *5*, 8390-8397.

31 Breault, T. M.; Bartlett, B. M. *J. Phys. Chem. C* **2012**, *116*, 5986-5994.

32 Breault, T. M.; Bartlett, B. M. *J. Phys. Chem. C* **2013**, *in revision*.

33 Maeda, K.; Shimodaira, Y.; Lee, B.; Teramura, K.; Lu, D.; Kobayashi, H.; Domen, K. *J. Phys. Chem. C* **2007**, *111*, 18264-18270.

34 Wang, H.; Lindgren, T.; He, J.; Hagfeldt, A.; Lindquist, S-. E. *J. Phys. Chem. B* **2000**, *104*, 5686-5696.

35 Lin, F.; Zhang, Y.; Wang, L.; Zhang, Y.; Wang, D.; Yang, M.; Yang, J.; Zhang, B.; Jiang, Z.; Li, C. *Appl. Cat. B: Environ.* **2012**, *127*, 363-370.

36 Lin, F.; Wang, D.; Jiang, Z.; Ma, Y.; Li, J.; Li, R.; Li, C. *Energy Environ. Sci.* **2012**, *5*, 6400-6406.

Chapter 4. Sol-Gel Synthesis of Complex, Visible Light Absorbing Titanates

4.1 Introduction

Chapters 2 and 3 focus on a co-incorporated photocatalyst, TiO_2:(Nb,N), and applications for dye degradation and water oxidation respectively. Chapter 4 shifts focus to visible light harvesting complex titanates that we have targeted with similar electronic structures (Chapter 1, filled O(2p) valence bands and empty Ti(3d) conduction bands). This chapter discusses two common synthetic approaches for obtaining complex metal oxides— solid-state and sol-gel chemistry, emphasizing the advantages of the latter. The focus of this chapter is on chemically modifying three different structure types— titania (TiO_2), perovskite ($SrTiO_3$), and Ruddlesden-Popper ($K_2La_2Ti_3O_{10}$) phases, illustrated in Figure 4.1, such that they absorb longer wavelengths of light. Research on each of these phases originated over forty years ago, with each phase performing as a UV photocatalyst towards water splitting.[1–3] Research efforts focus on modifying these host structures to enhance photocatalysis, with many review articles[4–11]

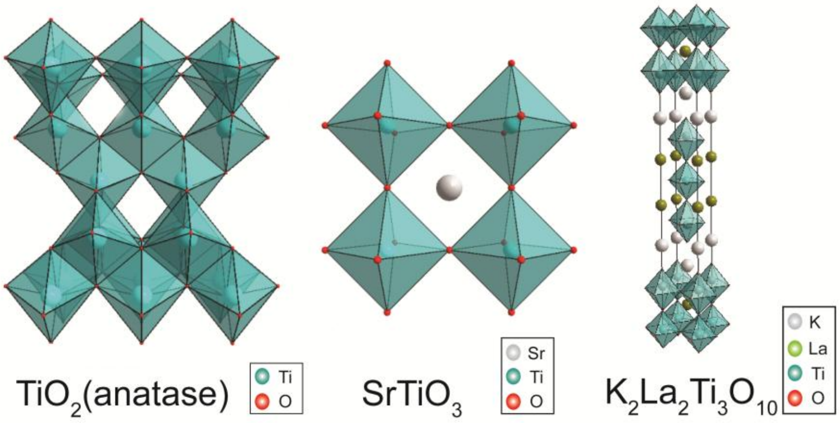

Figure 4.1 From left to right, titania, perovskite, and Ruddlesden-Popper structures.

Solids can be synthesized using a wide range of techniques, which provides a strong foundation for solid-state inorganic chemistry.[12] Researchers are motivated to design new compounds to meet the changing needs of society, so taking advantage of these techniques is critical for future development. Synthetic approaches include, but are not limited to, solid-state, sol-gel, hydrothermal, solvothermal, molten salt, combustion, ablation, and co-precipitation syntheses. Two approaches that we have successfully used to synthesize novel target compounds are highlighted in this chapter.

Traditional high-temperature "heat and beat" reactions are used to combine two or more solid precursors to produce a single phase compound. This technique requires grinding metal oxide and/or carbonate precursors and annealing at very high temperatures (≥ 800 °C) under various atmospheres (ambient, nitrogen, argon, vacuum). Often times, this process requires intermittent grinding and annealing steps, resulting in week-long heating schemes to yield phase pure products. Furthermore, solid-state reactions often result in large particles that aggregate together. For catalysis, high surface area compounds are desirable in order to increase the number of reaction sites, so producing large aggregates would be unfavorable. Regardless, this technique has been successful in synthesizing many phase pure compounds and was a starting point in our laboratory. One major drawback of solid state synthesis is that reactants are not mixed on the atomic scale, which can limit homogeneity. This chapter focuses on sol-gel syntheses, which afford synthetic control when targeting mono- or co-incorporated compositions.

In contrast to solid-state chemistry, *chimie douce* (soft chemistry) relies on low temperature reactions to produce phases of interest. In the sol-gel process, a solution of molecular precursors, containing stoichiometric concentrations of metal cations, is converted by a chemical reaction into a sol or a gel, which upon annealing, gives a solid material. This process allows the production of single or multicomponent materials with high purity, novel compositions, tailored nanostructures, and potentially greater chemical homogeneity at lower temperature.[13] The chemistry of sol-gel processing is based on hydrolysis and polycondensation of metal alkoxides, leading to the formation of an extended network.[14] Varying compositions, such as TiO_2:Mn, $SrTiO_3$:Mn, and $K_2La_2Ti_3O_{10}$:Fe discussed in this chapter, are obtained based on the chemical conditions under which such compounds are synthesized.[15]

The hydrolysis ratio and the nature of the alkoxy groups are important factors influencing the relative rates of hydrolysis and condensation reactions. Alkoxy groups are hard π-donor ligands, so they are able to stabilize the highest oxidation number of the metal.[16] Metal alkoxide monomers are hydrolyzed to first form a hydroxo-alkoxide species, such as $Ti(OR)_3(OH)$, depicted in equation 1. This titanium complex can either be further hydrolyzed or undergo condensation with formation of oxo (oxolation) or hydroxo (hydroxolation) bridges in independent kinetic regimes, equations 2 and 3.[17]

$$\mathrm{Ti{-}OR} + \mathrm{H_2O} \rightarrow \mathrm{Ti{-}OH} + \mathrm{ROH} \qquad (1)$$

$$\mathrm{Ti{-}OH} + \mathrm{OR{-}Ti} \rightarrow \mathrm{Ti{-}O{-}Ti} + \mathrm{ROH} \qquad (2)$$

$$\mathrm{Ti{-}OH} + \mathrm{OH{-}Ti} \rightarrow \mathrm{Ti{-}O{-}Ti} + \mathrm{H_2O} \qquad (3)$$

The goal of this chapter is to discuss the synthesis and characterization of new crystalline mixed metal oxides and their performance as water oxidation photoanodes. More specifically, we aim to produce *visible light harvesting titanates that absorb wavelengths into the visible portion of the solar spectrum*, as discussed in Chapter 1. Special attention is placed on the chemical nature of the surfaces of these compositions by using X-ray photoelectron spectroscopy. Specific targets include alloying metal cations into TiO_2, $SrTiO_3$, and $K_2La_2Ti_3O_{10}$, all well studied wide band-gap semiconductors, with transition metal cations (Mn^{4+}, Fe^{3+}, and Nb^{5+}), as we examine the water oxidation half reaction through constructing photoanodes. Our goal with these compositions is to synthesize light harvesting titanates capable of photocatalytic water oxidation, for which we utilize linear sweep voltammetry under solar simulated irradiation as our benchmark. To date, many compounds are studied under basic conditions; however, we aim to target compounds that evolve oxygen under neutral conditions, with the ultimate hope that they can be employed with two limitless sources; natural seawater and solar irradiation.

4.2 Experimental

4.2.1 Materials and general procedures

Reagent grade chemicals were obtained from Aldrich or Strem and used without purification unless specified. Potassium carbonate, lanthanum nitrate, titanium (IV) butoxide, titanium (IV) isopropoxide, strontium acetate, manganese (III) acetylacetonate, citric acid, acetic acid, methanol, and ethylene glycol were obtained from Aldrich. Ruthenium (III) chloride trihydrate and niobium(V) chloride was obtained from Strem. 2-methoxyethanol (2-MOE) (Aldrich) was distilled over sodium prior to use. Sol-gel reactions were carried out in custom made 4 mL quartz crucibles. An MTI box furnace was used to anneal gels and films under air. An MTI tube furnace was used to anneal films (placed in alumina crucibles) under flowing nitrogen (house-N_2). Millipore water (18.2 MΩ) was used for all experiments. Buffered electrolytes (0.1 M) were made from stock solutions of monobasic and dibasic potassium phosphate (Aldrich) solutions. Fluorinated tin oxide (FTO) was purchased from Pilkington Glass (TEC 15) and cut into 1 cm x 4 cm strips. The pre-cut slides were sonicated in ethanol and acetone (20 min each) and dried in air prior to use.

4.2.2 Synthesis of TiO_2:Mn

A sol-gel process was used to synthesize thin films of TiO_2:Mn. We used a similar sol-gel synthesis as reported in Chapter 2. In a typical synthesis for doping 5 mole-percent manganese, the appropriate mole-ratio of titanium(IV) butoxide (0.5 mL) and manganese (III) acetylacetonate (0.0273 g) were stirred in 1.75 mL of 2-methoxyethanol and 0.25 mL of acetic acid at room temperature. Meanwhile, FTO slides were cleaned via ultrasonication for 20 min in first ethanol and then acetone baths. A desired area (~ 1 cm^2) was left exposed at one end of the FTO slide, with the remaining surface masked with electrical tape. Five drops of the solution were spin coated onto the FTO slides at 2000 rpm for 20 sec. Films were annealed at various temperatures (500-650 °C) and under various atmospheres (atmospheric, nitrogen), specified throughout the appropriate section.

4.2.3 Synthesis of $SrTiO_3$:Mn

A modified sol-gel process[18] was carried out using acetic acid, 2-methoxyethanol, strontium acetate, manganese (III) acetylacetonate, and titanium(IV) butoxide. In a typical synthesis for 20 mole-percent manganese doped $SrTiO_3$, 0.250 g of strontium acetate was dissolved in 1.25 mL acetic acid at 80 °C with vigorous stirring to promote dissolution. Once dissolved, the metal salt (0.129 g of manganese acac) was added in the appropriate mole-ratio and allowed to stir until dissolved. Adding 0.25 mL of 2-methoxyethanol increased the viscosity of the solution, allowing for improved wettability for spin coating purposes. Titanium(IV) butoxide was added in the correct molar ratio (0.31 mL), and the solutions were allowed to stir for several hours until becoming orange/brown in color. The solutions were centrifuged at 3000 rpm for 10 min prior to use. Five drops of the solution were spin coated onto FTO slides at 2000 rpm for 20 sec. Films were annealed at 600°C for 4 hours.

4.2.4 Synthesis of $K_2La_2Ti_3O_{10}$

$K_2La_2Ti_3O_{10}$, and alloyed analogs, were prepared using the Pechini method to target RP phase compounds.[19] 6.5 mL methanol and 4.5 mL ethylene glycol were added to a beaker and allowed to stir in air at room temperature. 2.62 mmol $Ti(O^iPr)_4$ (0.8 mL) was added, along with 20 mmol of chelating agent, citric acid (3.850 g). 2.41 mmol K_2CO_3 (0.333 g) was slowly added and allowed to dissolve, requiring about 1 hour of stirring. 1.88 mmol $La(NO_3)•6H_2O$ (0.815 g) was added, along with $NbCl_5$ (0.21 mmol, 0.058 g) (or $FeCl_3$) to target an alloyed composition. The resulting resin was annealed at 375 °C for 4 hours and 900 °C for 2 hours. If noted, substitutional nitrogen was attempted to be incorporated into the system by including monoethanolamine in the precursors during the sol-gel process.

4.2.5 Physical methods

X-ray diffraction patterns were recorded on a Bruker D8 Advance diffractometer equipped with a graphite monochromator, a Lynx-Eye detector, and parallel beam optics using Cu-Kα radiation (λ = 1.54184 Å). Patterns were collected using a 0.6 mm incidence slit, with a step size and scan rate of 0.05°/step and 2 s/step respectively.

UV-Vis spectra of powders were recorded using an Agilent-Cary 5000 spectrophotometer equipped with a Praying Mantis diffuse reflectance accessory. Spectra were recorded in reflectance mode, using $BaSO_4$ as the background material. UV-Vis spectra of thin films were recorded using an internal diffuse reflectance sphere, using a Teflon disk and bare FTO slide as the background material.

X-ray photoelectron spectra were recorded on a Kratos XPS (8 mA, 14 keV, Monochromatic Al). Samples were secured to the transfer bar with copper tape and were pumped overnight under high vacuum to 1×10^{-9} torr. The XPS data were fit using the CasaXPS program, with all peaks calibrated to C(1s) at 284.5 eV. Scanning electron microscopy (SEM) images and energy dispersive X-ray (EDX) spectra were obtained using an FEI Nova Nanolab SEM/FIB with an accelerating voltage of 10 kV and 15 kV respectively.

Current-voltage, *j-V*, curves were generated using a custom built, airtight three electrode cell with a quartz window, Ag/AgCl reference electrode, and Pt wire counter electrode. Contact to the photoanode was made via silver paint and a metal clip. Measurements were performed in 0.1 M KP_i buffered at pH 7 unless otherwise noted. Photocurrent was measured using a 150 W Xe lamp filtered by an AM1.5G filter. The power output of the optical bundle was ~ 300 mW/cm^2 (3 suns), so values were adjusted appropriately to correspond to 1 sun simulation (100 mW/cm^2).

4.2.6 Film preparation

Sol-gel thin films were prepared using a Laurell 400B Model Spin Processor. An FTO slide was masked with electrical tape at one end and five drops of solution were deposited onto the substrate (~ 1 cm^2). The slide was spin coated for a desired time (typically about 20 sec) at a certain speed (typically 2,000 rpm). Sol-gel thin films were allowed to dry in air before annealing under the specified conditions.

Powdered electrodes were constructed using slurries reported in the literature.[20] For example, 50 mg $K_2La_2Ti_3O_{10}$ powder was ground in a mortar and pestle with 10 μL acetyleacetonate, 10 μL Triton X, and 250 μL water. The solution was sonicated overnight in a 4 mL scintillation vial. The slurry was spin coated onto FTO slides, 20 s at 2000 rpm, and subsequently annealed in air at 350 °C for 1 hour.

4.3 Results and discussion

4.3.1 Titania phase, TiO_2

As discussed in Chapters 2 and 3, TiO_2 co-incorporated with niobium and nitrogen is successfully employed as a photocatalyst.[21,22] Prior to our co-incorporating work, we focused on metal-doping with manganese in TiO_2, with our hypothesis being that incorporating manganese, a cation with a range of oxidation states important for multi-electron chemistry, would result in a bathochromic shift in the absorption spectrum and enhance photoelectrochemical water oxidation. A co-worker in the Bartlett Lab, Joseph Yourey, previously synthesized TiO_2:Mn (at 5 mole-percent Mn) thin films via a sol-gel route. His unpublished work shows photocurrent responses < 100 $\mu A/cm^2$ at 0.5 V vs. Ag/AgCl at pH 7 in a 0.1 M KP_i buffered solution. Photoelectrochemistry of these films suggest that Mn is not fully oxidized in the film due the presence of an oxidative peak at ~ 0.6 V vs. Ag/AgCl, similar in nature to the species observed in the $SrTiO_3$:Mn films, *vide infra*. Cyclic voltammetry shows a reversible peak with characteristic capacitance behavior. In order to overcome the presence of mixed manganese oxidation states in these films, the synthetic approach is modified by varying the annealing temperatures (500 °C and 650 °C) and atmospheres (air and N_2), targeting Mn in a 4+ oxidation state as well as trying to co-incorporate Mn/N into TiO_2. We hypothesize that the capacitive behavior observed due to the presence of Mn^{3+} could be avoided through synthesizing films with total Mn^{4+} species, which would allow for enhanced photoelectrochemical water oxidation at pH 7 and low overpotentials.

The challenge with co-incorporating thin films is in the source of nitrogen incorporation. Annealing FTO under ammonia severely decreases the conductivity and results in poor electrode performance. To avoid this challenging aspect, we alter the synthesis by incorporating an amine source in the sol precursor solution, such that, upon annealing, nitrogen would remain within the structure. The initial thin films we targeted are of the composition $Ti_{1-x}Mn_xO_{2-x}N_x$. We used monoethanolamine (MEA) in our starting solutions to incorporate nitrogen and an annealing temperature of 500 °C to target the anatase phase. This results in four samples for comparison: TiO_2, TiO_2-MEA, TiO_2:Mn, TiO_2:Mn-MEA. We employ long annealing times (12 and 24 hours) in order to crystallize the films completely and promote manganese oxidation.

Structural characterization of thin films is a major challenge, especially when using a rough substrate, such as FTO. Films annealed at 500 °C are ~ 20 nm thick (determined by profilometry, Figure B.1), which is very thin for X-ray diffraction measurements. X-ray diffraction patterns reveal peaks associated only with FTO. X-ray reflectivity was also attempted, but the surface of the underlying FTO is too rough to obtain useful data. As a result, we annealed the precursor solutions in alumina crucibles and subjected them to the same annealing schemes, resulting in powders that are anatase by powder XRD (Figure B.2a).

Surface characterization is critical in order to relate surface properties to photocatalytic activity. The surface of these films are examined by X-ray photoelectron spectroscopy. For all films, the Ti(2p) peak and Mn(2p) peaks are located at ~ 458.0 and 641.0 eV respectively, indicating the presence of Ti^{4+} and $Mn^{3+/4+}$.[23,24] Figure 4.2a shows the N(1s) binding energy for the thin films, with peaks deconvoluted ~ 400.0 eV, indicating interstitial nitrogen (N_i), with no peaks observed at a binding energy of 396.0 eV, which would correspond to substitutional nitrogen (N_S).[25–27] At 500 °C, no evidence of Sn^{4+} is observed, with no Sn(3d) peaks observed for any films, depicted in Figure 4.2b.[28] This result indicates that tin is not leaching from the substrate, which will be further discussed for annealing at 650 °C.

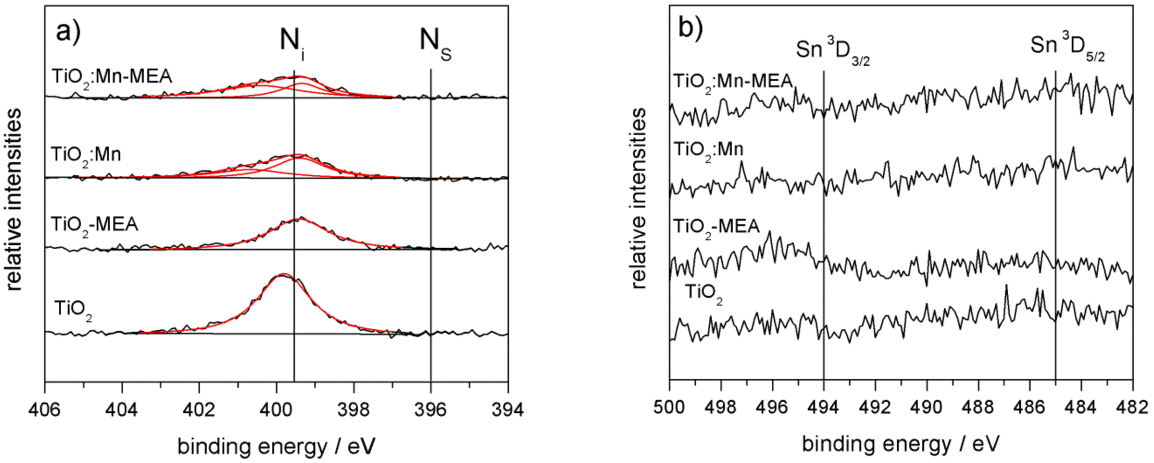

Figure 4.2 XP spectra for thin film annealed at 500 °C for 24 hours under N_2 a) N(1s) and b) Sn(3d).

The photoelectrochemistry of these films is shown in Figure 4.3. The voltammetry was performed in 0.1M KP_i buffer at pH 7 using a 150 W Xe lamp fitted with an AM1.5G filter. The power density was adjusted to 100 mW/cm^2 to simulate the solar spectrum. Despite attempts to fully oxidize the manganese within the TiO_2 structure through a longer annealing scheme, an oxidative wave at 0.6 V is still observed for the films containing manganese. TiO_2 thin films exhibit an onset potential ~ -0.4 V, similar to the TiO_2-MEA films. TiO_2-MEA films showed about a two-fold increase in photocurrent (~ 100 *vs*. 50 μA/cm^2 at 0.5 V vs. Ag/AgCl). The next step for these films would be to obtain thickness values through cross sectional SEM for all films (profilometry is not sensitive enough at this thickness to obtain exact thickness values) in order to understand the role MEA is playing in producing higher performing photoanodes compared to TiO_2 prepared without MEA.

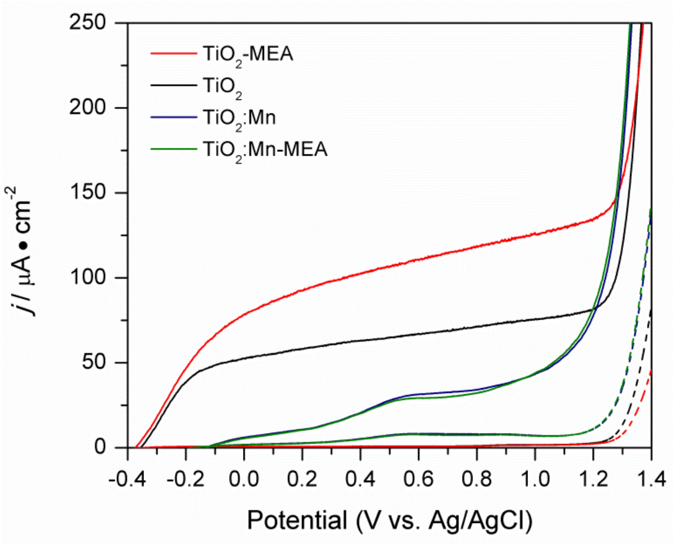

Figure 4.3 Photoelectrochemistry of films annealed at 500 °C for 24 hours under flowing N_2. Conditions: 0.1M KP_i buffer, pH 7, 150 W Xe lamp with AM1.5 filter, 100 mW/cm^2.

The rutile phase is also targeted by spin coating the original sol precursor solution onto FTO and annealing at 650 °C for 12 and 24 h under air and N_2, which results in thin films of ~ 20 nm thickness, again determined by profilometry. We anneal the precursor solutions in alumina crucibles and subject them to the same annealing schemes. TiO_2 and TiO_2-MEA powders annealed at 650 °C are mixed phase anatase/rutile, while incorporating manganese promotes the phase transition to rutile at this temperature (Figure B.2b). This phenomenon is observed in the literature for Mn incorporated in TiO_2.[29]

The chemical nature of the surface of the films annealed at 650 °C is examined using X-ray photoelectron spectroscopy, shown in Figure 4.4. Ti and Mn exist in +4 and +3/+4 oxidation states respectively for all films. The N(1s) binding energy at 400.0 eV is consistent with interstitial nitrogen (N_i) and no substitutional nitrogen (N_S) is observed at 396.0 eV, Figure 4.5a. Most important, Sn(3d) peaks at 486.0 eV binding energy is observed for the entire series, Figure 4.4b. This observation suggests that tin is leaching through the films at the high annealing temperature of 650 °C.

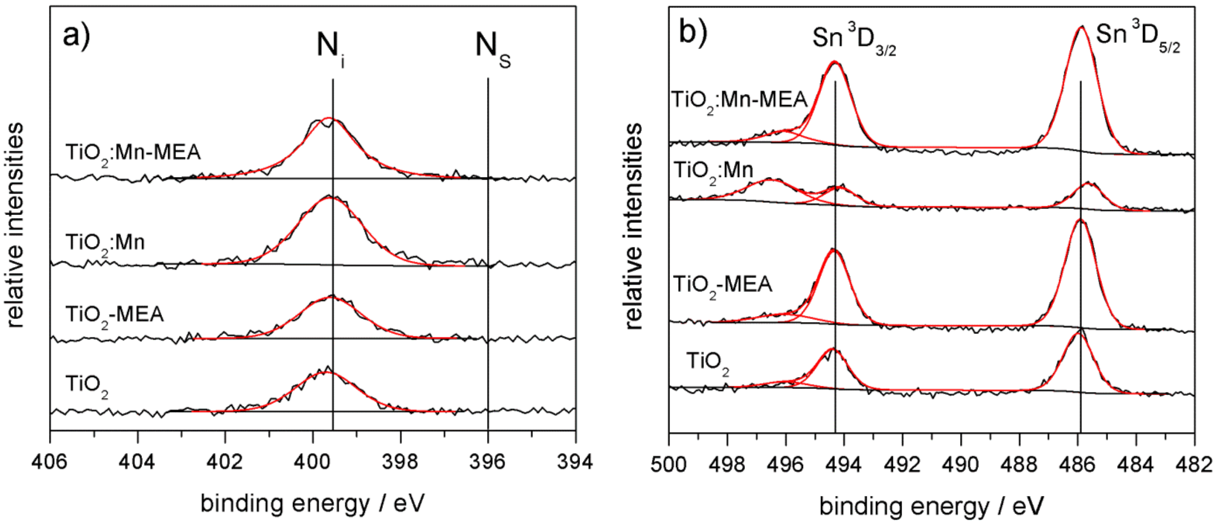

Figure 4.4 XP spectra for thin film annealed at 650 °C for 24 hours under N_2 a) N(1s) and b) Sn(3d).

In all cases for this series of films, annealing films for 24 vs. 12 hours resulted in increased photocurrent (Figure B.3), so only 24 hour annealing is discussed here. Furthermore, one layer also shows increased photocurrent compared to two layers formed by spin coating the precursor solution twice prior to annealing (Figure B.4). Annealing under air and nitrogen results in varying results. In Figure 4.5a, TiO_2 and TiO_2-MEA exhibit onset potentials ~ -0.4 V vs. Ag/AgCl. The oxidative wave ~ 0.45 V vs. Ag/AgCl for the manganese films suggests the presence of Mn^{3+}. There is a sharp take off at 0.7 V vs. Ag/AgCl, which is a ~ 500 mV shift to more negative potential compared to the electrocatalytic onset observed in the dark at ~ 1.3 V vs. Ag/AgCl. Figure 4.5b shows the linear sweep voltammetry for the N_2 annealed films, which exhibit drastically different voltammetry profiles compared to those films annealed under flowing air. TiO_2 films have ~ 500 μA/cm^2 at 0.5 V vs. Ag/AgCl, which is decent photocurrent for sol-gel films. Also noteworthy is the absence of a $Mn^{3+/4+}$ wave at ~ 0.6 V. Manganese incorporated films have ~ 150 – 75 μA/cm^2 at 0.5 V vs. Ag/AgCl for MEA and Mn only preparative routes respectively.

These films are complex in nature, for TiO_2 and TiO_2-MEA are mixed phase anatase and rutile, while TiO_2:Mn and TiO_2:Mn-MEA are rutile phase. We independently attempted to incorporate Sn^{4+} into these films through the sol-gel synthesis; however, high photocurrent density was not achieved (< 200 μA/cm^2 at 0.5 V vs. Ag/AgCl for 1 and 5 mole-percent Sn) through this method (Figure B.5). Perhaps the slow diffusion of Sn^{4+} from the substrate affords good ohmic contact between the substrate and film; whereas chemical doping (1 – 5%) of Sn^{4+} results in impurity states, aggregation, and/or modifying the surface only.

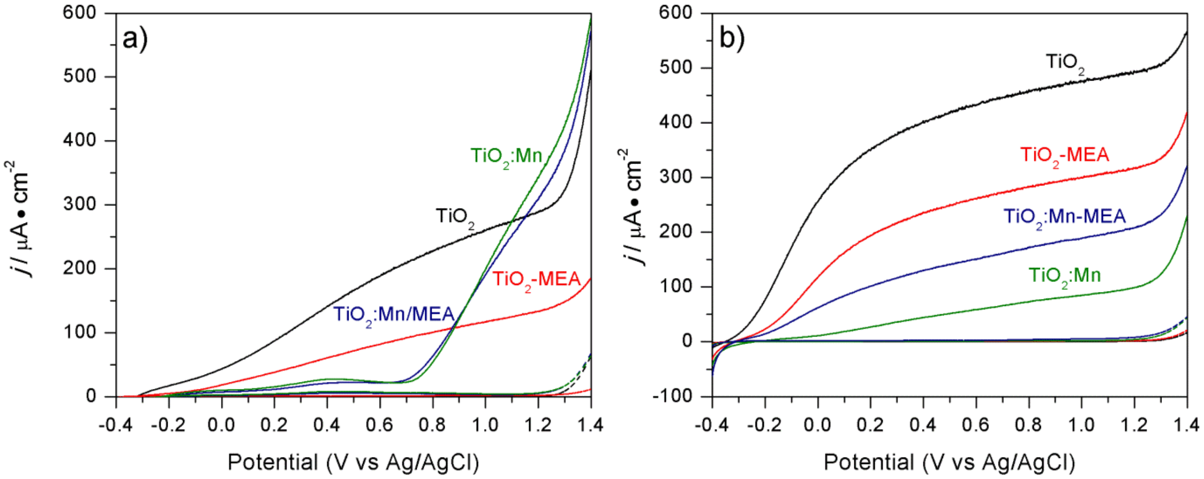

Figure 4.5 Photoelectrochemistry of films annealed at 650 °C for 24 hours under flowing a) air and b) N_2. Conditions: 0.1M KP_i buffer, pH 7, 150 W Xe lamp with AM1.5 filter, 100 mW/cm^2.

These results comparing the films annealed at 500 °C and 650 °C are important because they suggest that the upper limit of our FTO slides is less than 650 °C due to Sn^{4+} leaching from the substrate to our films at this higher temperature and long dwell time. Since anatase TiO_2 is an indirect band-gap material, we would like to target films 5–10 μm thick to better match the penetration depth of light due to small absorption coefficients. Based on our profilometry and microscopy work, our current thickness values indicate we were much too thin by our initial synthetic approach (~ 20 nm). Future work for these compositions would need to focus on eliminating the mixed valent manganese species and constructing thicker films by adding surfactants, spin coating multiple layers, and/or using higher sol concentrations. Based on our work from Chapter 2, co-incorporating a donor/acceptor pair may also prove useful in order to avoid introducing trap states within the band-gap of TiO_2. Impedance spectroscopy would be useful in order to locate trap state energy positions by constructing Mott-Schottky plots. Careful control over annealing atmosphere, such as ammonolysis, will be a better approach for incorporating substitutional nitrogen compared to our attempts using monoethanolamine (Chapter 6).

4.3.2 Perovskite phase, $SrTiO_3$

Strontium titanate, $SrTiO_3$, is a wide-band-gap perovskite structured semiconductor (E_g = 3.2 eV) that performs as a UV photocatalyst.[3,30,31] However, $SrTiO_3$ powders doped with Rh, Ir, Ru, and Mn posses absorption bands in the visible light region (400 – 800 nm).[32–34] Powdered systems have the drawback that both oxygen and hydrogen evolution must occur at the surface of a single particle. This is often difficult to achieve due to fast charge recombination rates. Moreover, as discussed in Section 4.1, many powders are prepared via high-temperature solid state syntheses, resulting in mixed-phase, large particles.[35] To overcome some of these issues, we focused on synthesizing $SrTiO_3$:Mn as thin film electrodes via the sol-gel processing. Our motivation for again targeting Mn^{4+} in this composition came from the OEC of PSII, discussed in Chapter 1, which requires a metal capable of multielectron chemistry.

A modified sol-gel process is carried out to produce thin films of $SrTi_{1-x}Mn_xO_3$, where our target compound includes isovalent Mn^{4+} substituting for Ti^{4+}. The polycrystalline X-ray diffraction patterns of FTO, $SrTiO_3$, and alloyed $SrTi_{1-x}Mn_xO_3$ (x = 0.1, 0.2, 0.3) are presented in Figure 4.6. The (*110*) Miller indices in the FTO diffraction pattern are referenced against an external standard, Al_2O_3. All samples exhibit the cubic structure of typical perovskite-type

$SrTiO_3$ (space group *Pm*3*m*) without forming any secondary phases for all manganese mole-percent ranges.[36] We did synthesize powders from the precursor solutions and use Rietveld refinement to obtain lattice parameters (Figure B.6 and Table B.1). The linear decrease in the lattice parameter is likely due to substituting Mn^{4+}, with a smaller ionic radius (0.67 Å), for the host cation Ti^{4+} (0.75 Å). Based on ionic radii, we predict that Mn^{4+} substitutes for octahedrally coordinated Ti^{4+} in the $SrTiO_3$ host lattice to form the solid solution.[37] Furthermore, we do not observe any manganese oxide phases by X-ray diffraction.

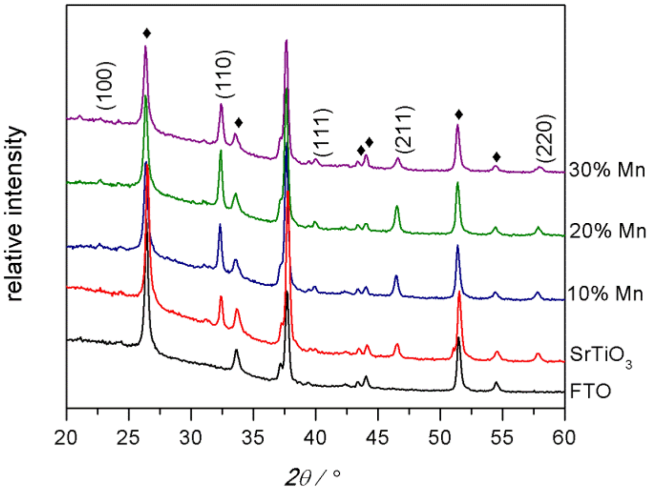

Figure 4.6 XRD pattern for various alloying levels of $SrTiO_3$. (♦) indicates FTO peaks.

ICP analysis is used to analyze the ratio of Ti/Mn present in each sample. Attempts to directly dissolve a film in aqua regia were successful; however the resulting concentration was too low to detect the manganese concentration. XRD shows the sintered powders are isostructural with annealed films, so we digested the powders in acid for chemical analysis. For the perovskite with the mole fraction of 20 mole-percent Mn, the ratio of Ti/Mn was 3.8:1, close to the targeted ratio of 4:1. SEM images show cubic like features, consistent with the perovskite crystallographic structure (Figure B.7a). Cross-Sectional SEM reveals a film thickness of ~ 200 nm (Figure B.7b), consistent with profilometry results (Figure B.8).

To probe the electronic structure of these oxides, X-ray photoelectron spectroscopy and UV-Vis spectroscopy are carried out. Figure 4.7a and b presents the Sr(3d) peak at 132.3 eV and the Ti(2p) peak located at 457.7 eV respectively, which corresponds to a Sr cation in its +2 oxidation state and the Ti cation in its +4 oxidation state at the surface of the thin film.[38] As observed in Figure 4.7c, the binding energy for Mn(2p) can be deconvoluted into Mn^{3+}, Mn^{4+} and respective hydroxo species for each oxidation state, giving rise to the four deconvoluted peaks.[39] Since $Mn^{3+/4+}$ is present in these films, we propose $SrTi_{1-x}Mn_xO_{3-\delta}$ as a more complete formula, suggesting the formation of oxygen vacancies to achieve charge compensation. Furthermore, two oxygen species are observed in the O(1s) XP spectra, Figure 4.7d. The binding energy at 529.0 eV is attributed to lattice oxygen, while the peak at 530.9 eV is characteristic of surface hydroxide.[40]

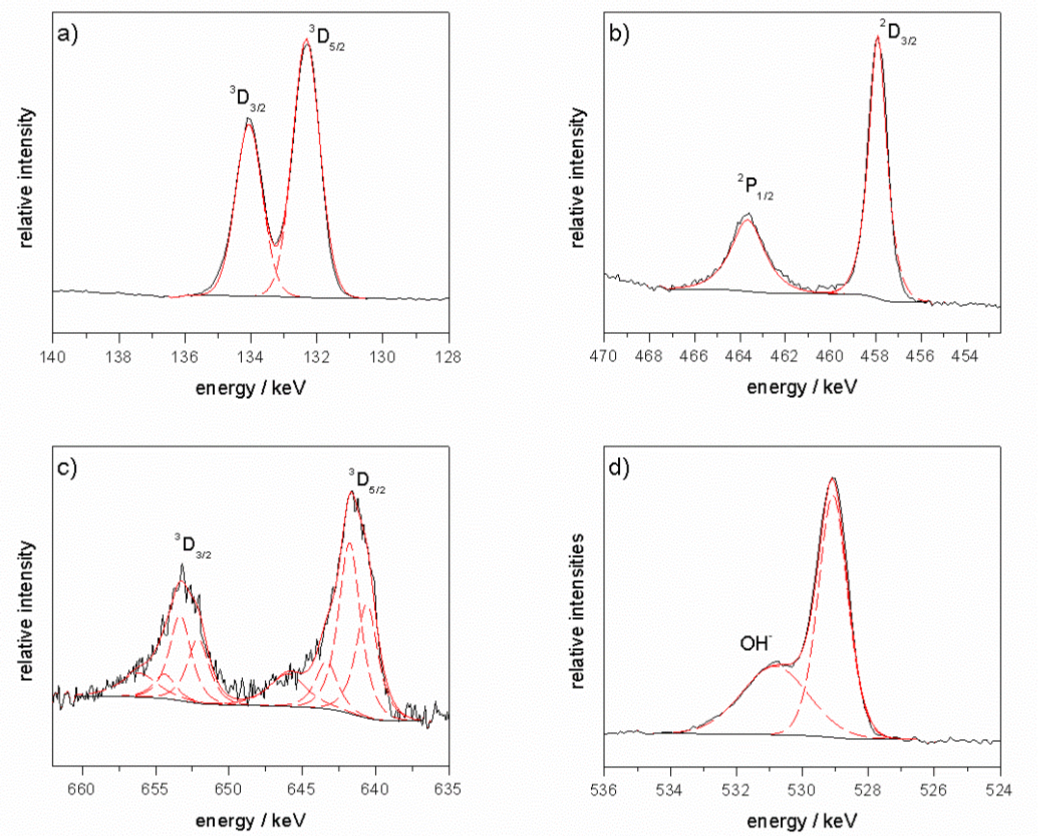

Figure 4.7 XP spectra of the deconvoluted peaks for $SrTi_{0.8}Mn_{0.2}O_{3-\delta}$ a) Sr(3d), b) Ti(2p), c) Mn(3d), and d) O(1s).

Figure 4.8 shows the UV-Vis spectra of $SrTiO_3$ and the $SrTi_{1-x}Mn_xO_{3-\delta}$ (x = 0.1, 0.2, 0.3) thin film samples. $SrTiO_3$ has an absorption band at about 400 nm, difficult to discern in this spectrum due to the thin nature of the film and resulting effects caused by the rough FTO substrate. Substituting $Mn^{4+/3+}$ cation for Ti^{4+} generates a significant effect on the absorption band compared to the host $SrTiO_3$ thin film even at the thickness of these films (~ 200-500 nm). The increase in the mole-percent of manganese leads to an increase in the UV-absorption band at 350 nm as well as the absorption band in the visible range (λ ~ 500 nm). At 30 mole-percent manganese, maximum absorption is observed at 350 nm and 500 nm.

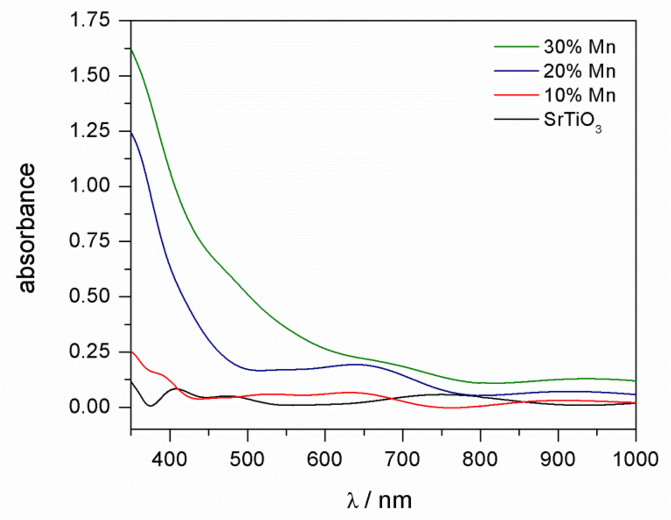

Figure 4.8 UV-Vis spectra of $SrTiO_3$:Mn thin films at various mole-percent Mn incorporation.

A STEM micrograph of the cross section of a porous $SrTi_{0.8}Mn_{0.2}O_{3-\delta}$ film on FTO is given in Figure 4.9a. Elemental mapping, which is shown in Figure 4.9b, confirms that the film includes Sr, Ti, Mn, and O, with a well-defined interface between our synthesized oxides and the FTO substrate. The film thickness determined from the STEM micrograph is ~ 530 nm. The FTO thickness measures ~ 400 nm, in excellent agreement with the value from the manufacturer.

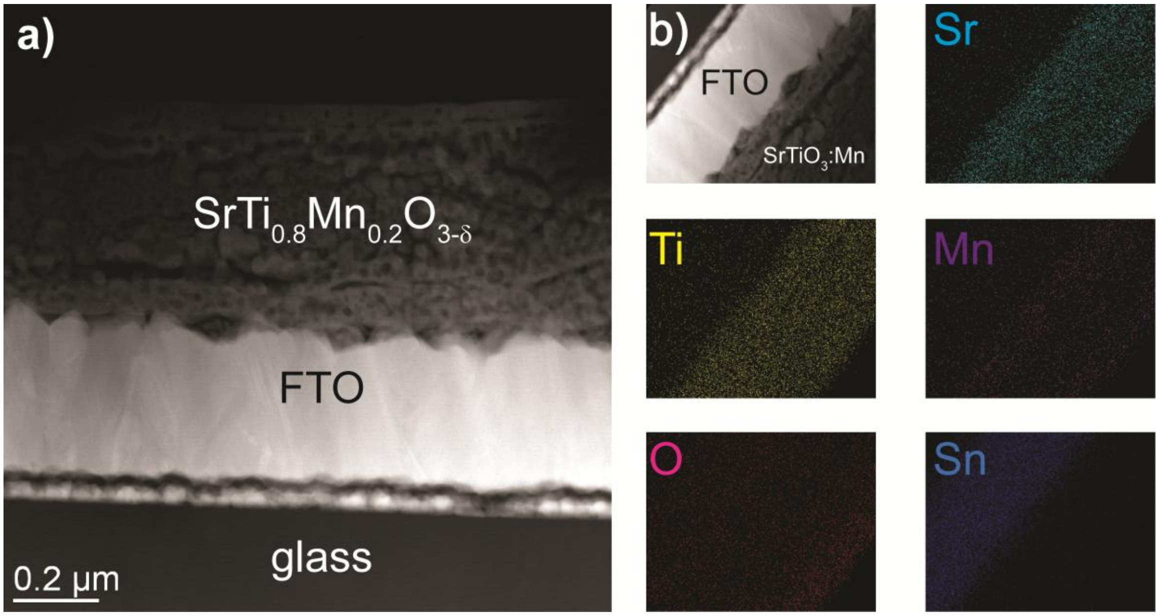

Figure 4.9 a) Cross sectional HRTEM microscopy of doped $SrTiO_3$ film and b) STEM elemental mapping images of 20 mole-percent Mn alloyed $SrTiO_3$ film (bottom right of each image) on FTO (top left of each image).

We now turn to photoelectrochemistry to examine the utility of these thin films as water oxidation photoanodes. Figure 4.10 shows a linear sweep voltammogram for a $SrTi_{0.8}Mn_{0.2}O_{3-\delta}$ thin film in 0.1M KP_i buffered pH 7 solution. For $SrTiO_3$, the dark and light linear sweeps overlay one another, indicating no photocurrent response. For the 20 mole-percent Mn film, we observe photocurrent at ~ 0.7 V vs. Ag/AgCl; however, we also observe dark current and an oxidative wave at ~ 0.58 V vs. Ag/AgCl. To investigate this oxidative wave more closely, we perform cyclic voltammetry at the same conditions, which is shown in Figure 4.10b, and correlates to the $Mn^{3+/4+}$ couple. The rectangular feature of the cyclic voltammogram is indicative of capacitance behavior, which is not favorable for photocatalytic water oxidation at low onset potentials. Photocurrent is only observed at potentials more positive than the oxidative wave, limiting the utility of this photoanodes as low overpotential water oxidation photocatalysts.

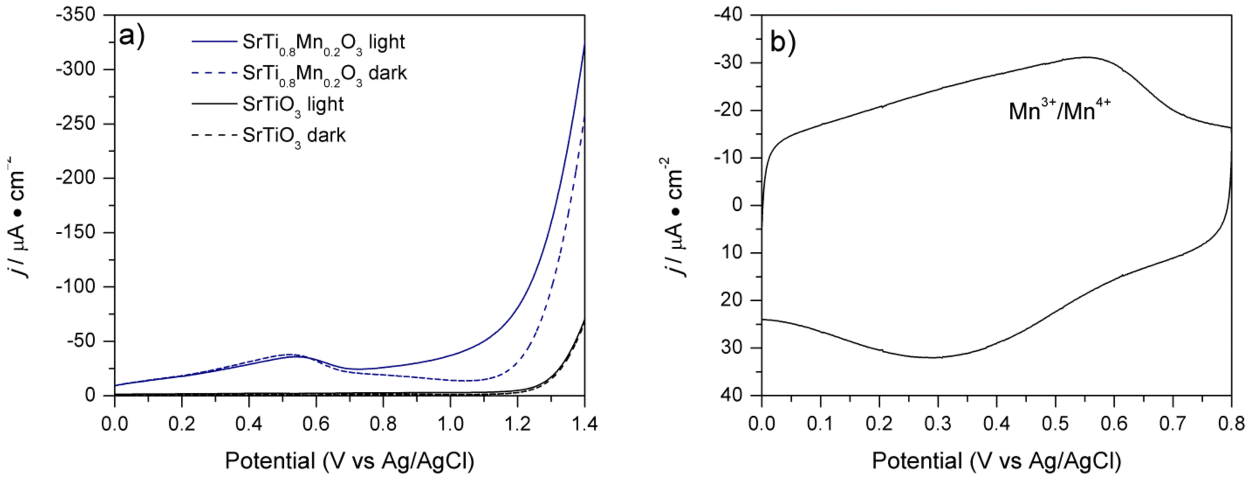

Figure 4.10 a) Linear sweep voltammetry of thin films of $SrTiO_3$ and $SrTi_{0.8}Mn_{0.2}O_{3-\delta}$. Reaction conditions: KP_i buffered pH 7 solution, 150 W Xe lamp fitted with AM1.5G filter adjusted to 100 mW/cm^{2}and b) cyclic voltammetry graph of $SrTi_{0.8}Mn_{0.2}O_{3-\delta}$ under same conditions as 4.10a.

$SrTiO_3$:Mn thin films were prepared using a facile sol-gel approach. The films absorb $\lambda \leq$ 550 nm, which was successful for our goal of targeting visible-light harvesting compounds. SEM imaging reveals cubic features, while HRTEM reveals ~200 nm thickness. These thin films also exhibited photocurrent at ~ 0.7 V vs. Ag/AgCl at pH 7; however, low current densities and dark oxidation of $Mn^{3+/4+}$ were also observed. This feature suggests the requirement for Mn to be in its 4+ oxidation state prior to generating photocurrent at lower onset potentials. Experiments to perform on these films include ICPE measurements to yield efficiency values at longer wavelengths and impedance spectroscopy to construct Mott-Schottky plots for band structure information.

4.3.3 Ruddlesden-Popper phases

Chapter 2 highlighted successful co-incorporating donor-acceptor pairs within the anatase structure. We have moved up the structural complexity ladder by targeting Ruddlesden-Popper phases (RP), with the general formula $A_2'[A_{n-1}B_nO_{3n+1}]$. These phases are of interest due to their physical properties, including ion-exchange, intercalation, and catalysis.[12] The chemistry of 2-D metal oxide compounds of the perovskite structure are well investigated for hydrogen evolution photocatalysts.[41] The attractive feature about layered perovskite materials, depicted in Figure 4.1, is derived from their large surface area, due to exfoliation of the layers with bulky cations, as compared to bulk oxides. The main issue to date with this class of oxides is that they only absorb in the UV part of the solar spectrum has a photon flux density two orders of magnitude lower than the visible portion of the solar spectrum. To overcome this limitation, we hypothesize that the absorption band edge can be shifted to longer wavelengths by incorporating metal ions (Fe^{3+}) and donor-acceptor (Nb,N) pairs into a RP structure, to enhance photoelectrochemical properties.

We use a modified Pechini method to synthesize a cation modified RP phase. For cation alloying, we incorporate various mole-percents of Fe^{3+} as $K_2La_2Ti_{3-x}Fe_xO_{10-\delta}$, where $x = 0$, 0.03, 0.06, 0.15, 0.2, 0.3, and 0.6. Since iron (3+) is not isovalent with titanium (4+), we propose the formation of oxygen vacancies, δ, to compensate for the differing charges. ICP analysis and EDX spectroscopy result in metal ion mole ratios that agree well with the targeted mole ratios. SEM microscopy shows needle-like morphology (Figure B.9). Figure 4.11 depicts the XRD pattern of the prepared powders, which includes an external standard, Al_2O_3, and shows that all compounds crystallize in the layered structure, referenced to JCPDF file 87-1167. The Miller index are indicated in Figure 4.11a, while the low angle region is shown in Figure 4.11b. Fe^{3+} (high spin Fe^{3+} in O_h symmetry, 0.64 Å) is slightly smaller in size compared to Ti^{4+} (0.75 Å), so one would expect a shift to higher 2θ values; however, at these low mole-percents of iron, we cannot definitively observe a shift in the (*002*) Miller indices for these compounds. At mole-percents > 5 %, a shift to higher 2θ value is observed. At 20 mole-percent Fe, an additional impurity peak is observed at ~ 32° 2θ, suggesting the maximum mole-percent of Fe in $K_2La_2Ti_{3-x}Fe_xO_{10-\delta}$ is < 20 mole-percent.

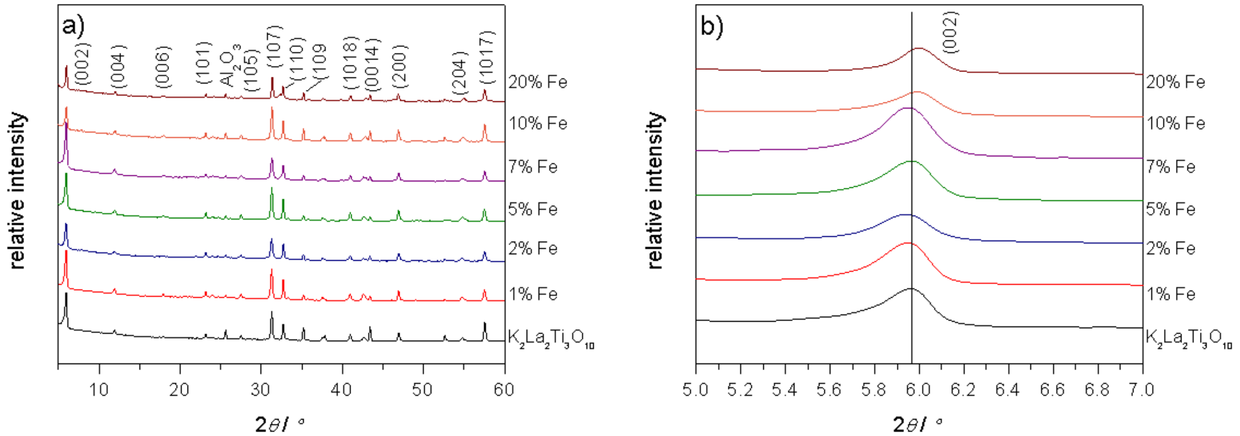

Figure 4.11 X-ray diffraction patterns for Fe alloyed $K_2La_2Ti_3O_{10-\delta}$: a) full 2θ range and b) low 2θ range to highlight the (*002*) miller indices.

The UV diffuse reflectance spectra of a series of $K_2La_2Ti_{3-x}Fe_xO_{10-\delta}$ with different alloying mole-percents of iron are shown in Figure 4.12. $K_2La_2Ti_3O_{10}$ exhibits a strong absorption in the ultraviolet region ($\lambda \leq 350$ nm), which corresponds to a 3.5 eV direct band-gap material. Through incorporating iron, however, the absorption edge shifts to longer wavelengths with increasing mole-percent iron. For example, at 1 mole-percent iron, absorption bands at ~ 450 and 585 nm are observed. The intensity of these bands increases with increasing mole-percent, with a maximum intensity at 10 % iron, which is still phase pure RP.

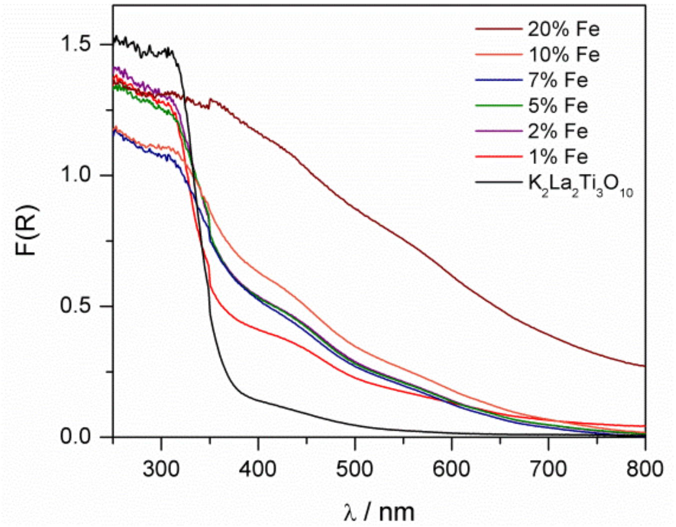

Figure 4.12 UV-vis diffuse reflectance spectra for the series $K_2La_2Ti_{3-x}Fe_xO_{10-\delta}$.

With visible light harvesting RP compounds in hand, we construct powdered electrodes in order to test the water oxidation half reaction. Electrodes are annealed at 500 °C in air for 1 hour prior to testing. No photocurrent is observed using a 150 W Xe lamp filtered with an AM 1.5G filter at pH 7 to simulate solar irradiation. Figure 4.13 shows the dark and light linear sweep voltammetry for a 10 mole-percent compound. The electrochemical onset potential for water oxidation occurs at ~ 1.3 V vs. Ag/AgCl at pH 7, and there is not any noticeable photocurrent observed for this (or any other) composition prepared by this method.

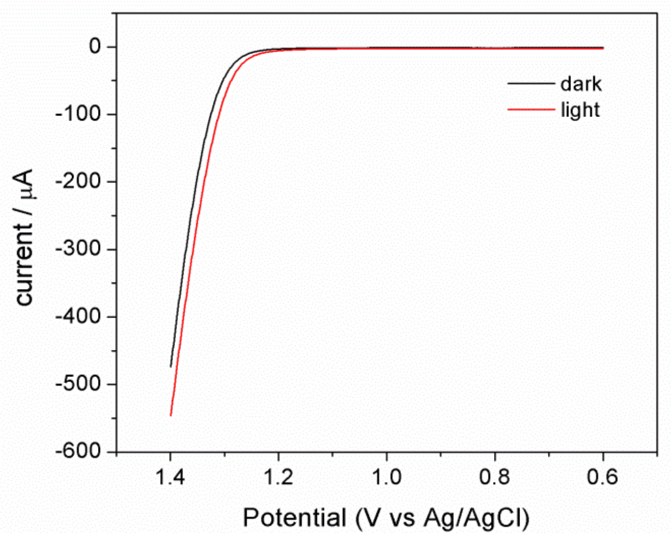

Figure 4.13 Linear sweep voltammetry of $K_2La_2Ti_{2.7}Fe_{0.3}O_{10-\delta}$. Reactions conditions: 150 W Xe lamp, AM1.5G filter, 0.1 M KP_i pH 7, Pt mesh counter electrode, Ag/AgCl reference electrode.

The are many remaining challenges from these resulting poor performing electrodes. Is the lack of photocurrent due to poor ohmic contact with the substrate through this slurry technique? Is it inherent to the compositions we synthesized? Does including a single metal ion into the compound result in trap states and a defect-rich structure, which in turn results in high recombination upon photogenerated electron/hole pairs? To answer these questions, better electrodes are necessary (Chapter 6) as well as co-incorporating to target less defective sites, which could be contributing to the decreased performance.

Chapter 2 sheds light on defect structure and corresponding function as a photocatalyst for a series of (Nb,N) co-incorporated anatase compounds. With this information in hand, we can target a new composition based off the success we observ with co-incorporated anatase and target incorporating Nb and N into the $K_2La_2Ti_3O_{10}$ structure: $K_2La_2Ti_{3-x}Nb_xO_{10-x-\delta}N_x$.

$K_2La_2Ti_{3-x}Nb_xO_{10-x-\delta}N_x$ is synthesized via the modified Pechini citrate route described above for the iron incorporated compound. The main synthetic difference in this preparation involved using $NbCl_5$ and monoethanolamine in the initial sol precursor to incorporate Nb and N respectively, and once annealed in air, gave the target composition $K_2La_2Ti_{2.4}Nb_{0.6}O_{10-x-\delta}N_x$. Powder X-ray diffraction, shown in Figure 4.14a shows the co-incorporated compound to be poorly crystalline (domain ~ 20 nm); however, the Miller indices corresponding to the RP phase are included. The poor crystallinity will prove to be a challenge for using this composition as a photocatalyst since recombination may be a dominating factor. EDX analysis confirms a metal ratio of Ti:Nb of ~ 4, consistent with our target compound. SEM microscopy is used to probe the morphology, which reveals needle like features consistent with the morphology observed for iron alloyed compositions.

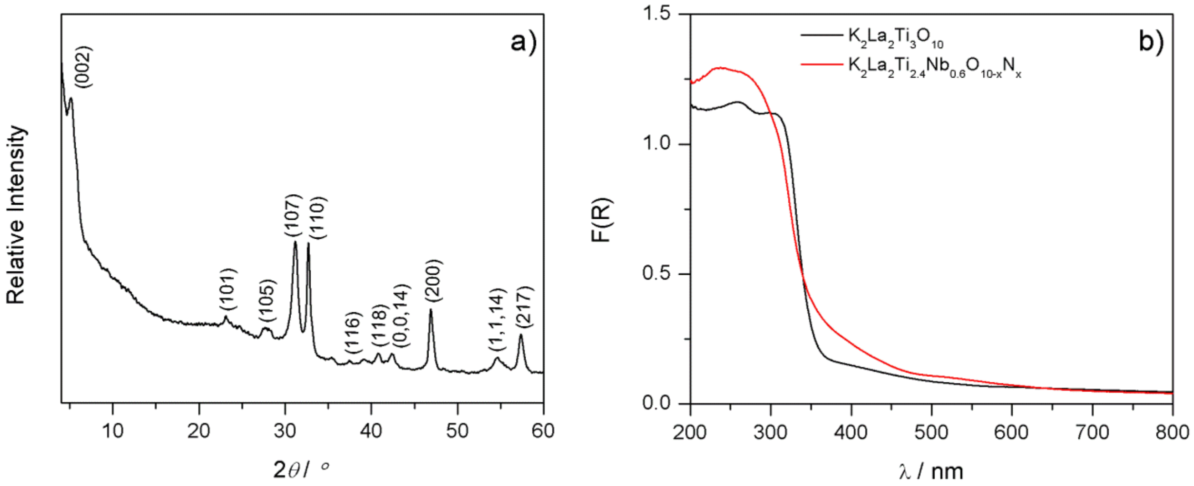

Figure 4.14 a) X-ray diffraction pattern for $K_2La_2Ti_{3-x}Nb_xO_{10-x-\delta}N_x$ at 20 mole-percent niobium and b) diffuse reflectance for $K_2La_2Ti_3O_{10}$ and $K_2La_2Ti_{2.6}Nb_{0.4}O_{10-x-\delta}N_x$.

Furthermore, the co-incorporated compound, pale yellow in color, shows increased absorption of longer wavelengths, ~ 450 nm (E_g = 2.76 eV), compared to the host compound $K_2La_2Ti_3O_{10}$, which has an absorption edge at ~ 350 nm (E_g = 3.5 eV), shown in Figure 4.14b. The pale yellow color corroborates results for similar sol-gel preparative routes for many $TiO_{2-x}N_x$ compounds.[42] RBS analysis is quite difficult, which provides an opportunity for new students to determine the mole-percent nitrogen in these compounds at the surface and in the bulk (and previously mentioned ones in this chapter), as well as determine the surface chemical environment of the nitrogen species by XPS.

We construct powder electrodes from slurries, described in Section 4.2.5, and anneal at low temperatures. Films tested at pH 7 are not photocatalytically active towards water oxidation, which was the original goal of this work. *j*-V curves performed in 1 M KOH (pH 13), shown in Figure 4.15**,** show no observable photocurrent for either of these compositions. We do however observe a difference of ~ 0.1 V in the electrochemical potential for water oxidation for the co-incorporated compound at pH 13 in the dark. This result suggests this composition is more electrocatalytically active towards water oxidation at high pH.

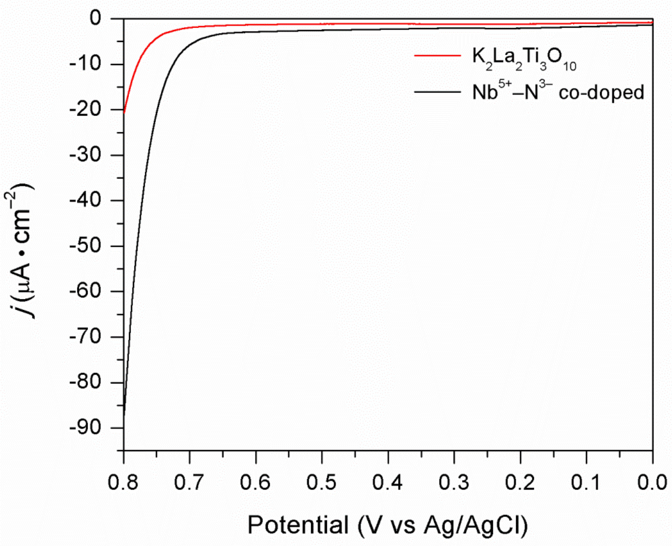

Figure 4.15 *j*-V curve at pH 13 (1 M KOH) for $K_2La_2Ti_{2.6}Nb_{0.4}O_{10-x-\delta}N_x$.

Both attempts at modifying the band-gap of $K_2La_2Ti_3O_{10}$, through Fe^{3+} and Nb/N co-incorporating, results in increased absorption to longer wavelengths of light; however, attempts to construct powder electrodes was the limiting factor. Co-incorporating RP phases is a promising area of research merely due to the lack of current research efforts for this specific type of chemistry. A new student should take what we have learned regarding (Nb,N) co-incorporated TiO_2 and apply it to the RP compound. Several key areas must be addressed: 1) improve crystallinity, through synthetic approach and/or lower alloying mole-percents, 2) include substitutional nitrogen via annealing under flowing ammonia, 3) construct good powder electrodes (Chapter 6), and 4) develop an exfoliation technique to take full advantage of a layered structure. The fourth point is quite important and would open this new field of research. Through exfoliating bulky cations into the RP layers, the surface area should increase and allow for co-catalyst loading, resulting in promising photocatalysts for water oxidation. Fundamental research with this particular composition will better guide the future of designing photocatalyst for water oxidation. We have shown that defect structure and composition dictates function as a photocatalyst; extending this knowledge to other synthetic targets is critical as we progress our research efforts in this field.

4.4 Conclusions

The focus of this chapter was to give an overview of synthesizing the three main structure types modified through alloying approaches. In all cases (titania, perovskite, and RP) metal ions were incorporated into the structure to afford compounds that absorb longer wavelengths of light than the parent structure. Our work on thin films of titania and perovskite films incorporated with manganese sheds light on several important factors to consider for future targets in the lab. Incorporating manganese into TiO_2 or $SrTiO_3$ results in mixed valent manganese, which hinders the photoelectrochemical performance of the films due to the oxidation of $Mn^{3+/4}$ occurring at ~ 0.6 V vs. Ag/AgCl. This initial oxidation of Mn^{3+} to Mn^{4+} is necessary prior to generating photocurrent to oxidize water. Our synthetic work on TiO_2:Mn thin films provided further insight that annealing atmosphere is very important; however, temperature seems to be the major contributor to producing decent photocurrent. This result could be due to several variables including mixed phase films, ohmic contact, Sn^{4+} leaching, low defect structure. Our preliminary work with RP phases shows that these compounds have promise as a water oxidation photocatalyst, with future steps outlined in Section 4.3.3. We create a solid foundation for understanding some of the obstacles in constructing powdered electrodes and sol-gel spin coated electrodes and learned valuable information regarding the temperature limits of our substrate. Additional perspective on incorporating substitutional nitrogen in these compositions and constructing powder electrodes will be addressed in Chapter 6.

4.5 References

1 Fujishima, A.; Honda, K. *Nature*, **1972**, 37-38.

2 Takata, K.; Shinohara, A.; Tanaka, M. H.; Kondo, J. N.; Domen, K. *J. Photochem. Photobiol. A* **1997**, *106*, 45-49.

3 Domen, K.; Naito, S.; Soma, M.; Onishi, T.; Tamaru, K. *J. Chem. Soc., Chem. Comm.* **1980**, 543-544.

4 Osterloh, F. E. *Chem. Mater.* **2008**, *20*, 35-54.

5 Kumar, S. G.; Devi, L. G. *J. Phys. Chem. A* **2011**, *115*, 13211-13241.

6 Takanabe, K.; Domen, K. *Chem. Cat. Chem.* **2012**, *4*, 1485-1497.

7 Liu, G.; Wang, L.; Yang, H. G.; Cheng, H. M.; Lu, G. Q. *J. Mater. Chem.* **2010**, *20*, 831-843.

8 Hangfeldt, A.; Gratzel, M. *Chem. Rev.* **1995**, *95*, 49-68.

9 Kamat, P. V. *Chem. Rev.* **1995**, *93*, 267-300.

10 Chen, X.; Shen, S.; Guo, L.; Mao, S. S. *Chem. Rev.* **2010**, *110*, 6503-6570.

11 Hu, X.; Li, G.; Yu, J. C. *Langmuir* **2010**, *26*, 3031-3039.

12 Schaak, R. E.; Mallouk, T. E. *Chem. Mater.* **2002**, *14*, 1455-1471.

13 Wright, J. D.; Sommerdjik, N.A.J.M. 'Sol-Gel Materials. Chemistry and Applications;, Gordon and Breach Science Publishers, Amsterdam, NY, 2001.

14 Livage, J.; Henry, M.; Sanchez, C. *Prog. Solid State Chem.* **1988**, *18*, 259-341.

15 Simonsen, M.; Sogaard, E. *J. Sol-Gel Sci. Technol.* **2010**, *53*, 485-497.

16 Brinker, C. J.; Scherer, G. W. 'Sol-Gel Science,' Academic Press, San Diego, CA, 1990.

17 Kessler, V. *J. Sol-Gel Sci. Technol.* **2009**, *51*, 264-271.

18 Giridharan, N. V.; Varatharajan, R.; Jayavel, R.; Ramasamy, P. *Mater. Chem. Phys.* **2000**, *65*, 261-265.

19 Pechini, M. P. Method of preparing lead and alkaline earth titanates and niobates and coating method using the same to form a capacitor. U. S. Patent No. 3, 330, 697, July 11, 1967.

20 Abe, R.; Takata, T.; Sugihara, H.; Domen, K. *Chem. Lett.* **2005**¸ *34*, 1162-1163.

21 Breault, T. M.; Bartlett, B. M. *J. Phys. Chem. C.* **2012**, *116*, 5986-5994.

22 Breault, T. M.; Bartlett, B. M. *J. Phys. Chem. C.* **2013**, *in revision*.

23 Saha, N. C.; Tompkins, H. G. *J. Appl. Phys*. **1992**, *7*, 3072–3079.

24 Sherman, D. M. *Amer. Mineral.* **1984**, *69*, 788-799.

25 Chen, X.; Burda, C. *J. Phys. Chem. B* **2004**, *108*, 15446–15449.

26 Sato, S.; Nakamura, R.; Abe, S. V. *Appl. Cat. A: Gen.* **2005**, *284*, 131–137.

27 Napoli, F. N.; Chiesa, M.; Livraghi, S.; Giamello, E.; Agnoli, S.; Granozzie, G.; Pacchioni, G. Valentin, C. D. *Chem. Phys. Lett.* **2009**, *477*, 135–138.

28 Wagner, C. D.; Riggs, W. M.; Davis, L. E.; Moulder, J. F.; Mullenberg, G. E. Handbook of X-ray Photoelectron Spectroscopy, Perkin-Elmer, Eden Prairie, **1979**.

29 Pereira, A. L. J.; Gracia, L.; Beltrán, A.; Lisboa-Filho, P. N.; da Silva, J. H. D.; Andrés, J. *J. Phys. Chem. C* **2012**, *116*, 8753-8762.

30 Townsend, T. K.; Browning, N. D.; Osterloh, F. E. *Energy Environ.* **2012**, *5*, 9543-9550.

31 Townsend, T. K.; Browning, N. D.; Osterloh, F. E. *ACS Nano* **2012**, *6*, 7420-7426.

32 Konta, R.; Ishii, T.; Kato, A.; Kudo, A. *J. Phys. Chem. B.* **2004**, *108*, 8992.

33 Iwashina, K.; Kudo, A. *J. Amer. Chem. Soc.* **2011**, *133*, 13272-13275.

34 Takata, T.; Domen, K. *J. Phys. Chem. C.* **2009**, *113*, 19386-19388.

35 Zhang, H.; Chen, G.; Bahnemann, D. W. *J. Mater. Chem.* **2009**, *19*, 5089-5121.

36 Vegard, L.; Hauge, T. *Zeitschrift für Physik* **1927**, *42*, 1-14.

37 Sun, X.; Lin, J. *J. Phys. Chem. C.* **2009**, *113*, 4970-4975.

38 Nefedov, V. I. ‘X-ray photoelectron spectroscopy of solid surfaces,’ Alden Press Ltd, Oxford, 1988.

39 Qi, G. S.; Yang, R. T. *J. Phys. Chem.* **2004**, *108*, 15738,

40 Dupin, J.; Gonbeau, D.; Vinatier, P.; Levasseur, A. *Phys. Chem. Chem. Phys.* **2000**, *2*, 1319-1324.

41 Miskei, Y.; Kato, H.; Kudo, A. *Energy Environ. Sci.* **2009**, *2*, 306-314.

42 Zhang, J.; Wu, Y.; Xing, M.; Leghari, S. A. K.; Sajjad, S. *Energy Environ.* **2010**, *3*, 715-726.

Chapter 5. Collaboration: Magnetic Interaction Between Co(II) Centers

Portions of this chapter have been published.
Maass, J. S.; Zeller, M.; Breault, T. M.; Bartlett, B. M.; Sakiyama, H.; Luck, R. L. *Inorg. Chem.* **2012**, *51*, 4903-4905. Reprinted with permission. Copyright 2012 American Chemical Society.
Figures: 5.2, 5.3; Table 5.1

5.1 Introduction

This chapter focuses on the collaborative work with Prof. Rudy Luck and co-workers at Michigan Technical University involving the magnetic interaction between cobalt (II) centers in molecular complexes. [1] The motivation for Prof. Luck's work was aimed at stabilizing molecular cobalt(III) oxides or hydroxides with bis(benzyl)phosphinate. Since phosphinates can potentially have some of the same coordination modes as phosphate, the idea was to separate out a molecular water oxidation cobalt catalyst that could be compared to Nocera's cobalt phosphate catalyst, CoP_i.[2] Furthermore, there is a manganese oxide phosphinate cluster, that acts as a water oxidation catalyst, giving additional inspiration for exploring cobalt complexes stabilized by phosphinate ligands.[3] Our contribution to this project was performing the magnetism on the complexes made by the Luck group.

A serendipitous discovery by John Maass in Prof. Luck’s group shifted the focus of the project of stabilizing molecular cobalt(III) oxides or hydroxides with bis(benzyl)phosphinate for water oxidation catalysis toward molecular magnetism and studying the magnetic interaction of octahedral and tetrahedral cobalt(II) metal centers with each other. Dinuclear cobalt complexes featuring octahedral and tetrahedral geometries with Co(III)-Co(II)[4,5] and Co(II)-Co(II)[6–8] centers have been reported. Magnetic studies have been reported for three of the Co(II)-Co(II) compounds which have very different bridging ligands. First, for the compound $[(H_2O)(dppm)_2Co(\mu\text{-}CN)CoCl_3]$, high spin isolated ($S = 3/2$) pertained but the linear nature of the data obtained (i.e., $\chi_M T$ *vs.* T was linear) could not be satisfactorily analyzed.[6] Second, for the complex $[Co_2L_2Cl_3]Cl$, L = 2,6-diamino-3-[(2-carboxymethyl)phenylazo]-pyridine (Figure 5.1), the analysis of the magnetic data resulted in the conclusion that “two low spin (1s) Co^{2+} ions pertained.”[7] Third for the compound $[(MeCN)_5Co(NCS)Co(NCS)_3]$, the magnetic analysis suggested that the data can be best fit with the Curie-Weiss expression: $\chi_M = C/(T - \Theta)$, $C = N\mu_g{}^2g^2/3k_B$, with $g_{avg} = 2.5$ and $\Theta = -15.5$ K.[5] The Co to Co distance in these compounds was 5.007, 4.800 and 5.732 Å for the first to third respectively.[8] The interest in the complexes reported in this section stems from Luck’s discovery that the dibenzylphosphinate ligand stabilizes tetrameric clusters such as $[V_4O_8]^{4+}$, $[Mo_4O_8]^{4+}$ and $[W_4O_8]^{4+}$.[9–12]

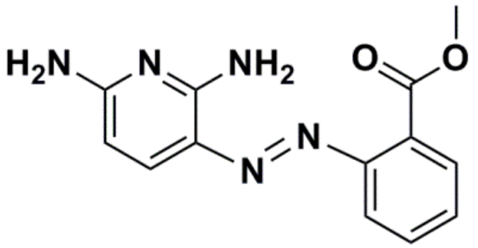

Figure 5.1 2,6-diamino-3-[(2-carboxymethyl)phenylazo]-pyridine.

5.2 Experimental

5.2.1 Materials and general procedures

Chemicals were purchased from Aldrich Chemicals and solvents were used as received. Dibenzylphosphinic acid was prepared according to the cited literature.[13] Elemental analyses were conducted by Galbraith Laboratories, Knoxville, TN. IR spectra on complexes **1** – **3** were recorded on a PerkinElmer Spectrum One spectrometer (neat). Room temperature magnetic measurements were conducted on a Johnson Matthey Auto MSB instrument. Susceptibility measurements were performed on a Quantum Design MPMS-XL7 equipped with an Evercool Dewar.

5.2.2 Synthesis

All complexes were prepared by John Maass, a graduate student in Prof. Luck's group. Previous research reacting phosphinate ligands and cobalt have resulted in polymeric species.[14–21] In an extension of this work to prepare clusters of Co(III) oxides or hydroxides,[22] this ligand affords dinuclear clusters of the form $[L_3Co(\mu_2\text{-}O_2P(CH_2C_6H_5)_2)_3CoL'][L'']$. Dark blue crystals of $[(py)_3Co(\mu_2\text{-}O_2PBn_2)_3Co(py)][ClO_4]$ **1** were isolated first from an ethanol solution consisting of a mixture of Bn_2PO_2K, $Co(ClO_4)_2{\bullet}6H_2O$, pyridine and H_2O_2.[23] It was later discovered that **1** can be made in good yield by reacting three equivalents of the potassium salt of the ligand with two equivalents of cobalt perchlorate along with excess pyridine in ethanol. The compound $[(py)_3Co(\mu_2\text{-}O_2P(Bn_2)_3Co(Cl)]$, **2**, was also first prepared unintentionally from the reaction of $Co(NO_3)_2{\bullet}6H_2O$ with pyridine and Bn_2PO_2H in methylene chloride. The addition of hexanes resulted in the formation of light pink crystals which were found to be the known compound $Co(NO_3)_2(H_2O)_2(py)_2$. The solution was filtered and the addition of more hexanes produced dark blue crystals of **2**. It is not clear how the chloride ion formed in this reaction but we have discovered that compound **2** can be produced starting with $CoCl_2$•$6H_2O$. The complex [(py)(μ_2-NO_3)Co(μ_2-O_2PBn_2)$_3$Co(py)], **3**, was obtained serendipitously in a reaction of $Co^{III}(acac)_2PyNO_2$ and Bn_2PO_2H under reflux conditions in $CHCl_3$. The addition of pentane followed by keeping the solution at 5 °C for two weeks led to the formation of dark purple crystals of **3**.

5.2.3 Magnetic susceptibility measurements

I performed the magnetic measurements on the cobalt complex for the Luck group. The sample was prepared by weighing 71.9 mg of compound **1** into a gelatin capsule. 118.6 mg of eicosane was then added to stablilize the powder in an inert waxy matrix. Susceptibility was recorded as a function of temperature from 2.0 to 300 K under a 1000 Oe measuring field. A control experiment in which only eicosane was measured was used to correct the data for the diamagnetic gram susceptibility of the eicosane. (-9.739×10^{-7} emu/g). This measurement also corrected for the constant contribution from the drinking straw and capsule with the assumption that the diamagnetic contribution from the gelatin capsule is constant (in all of the measurements, the capsule mass is 47(1) mg) and that the density of the straw is constant. After these corrections, the data were converted from gram susceptibility to molar susceptibility then corrected for the diamagnetic contribution of the sample as determined from Pascal's constants, -7.3862×10^{-4} emu/mol. The effective moment at room temperature is determined to be 6.6 Bohr magnetons, ($\mu_{eff} = 2.82\ [(\chi T)^{1/2}]$), very similar to a Guoy balance measurement at RT.

5.3 Results and discussion

A thermal ellipsoid plot of **1** is illustrated in Figure 5.2. In all structures, the two cobalt centers are bridged by three dibenzylphosphinate ligands. This ligand is very flexible and is capable of bridging at various lengths, as illustrated in the Co to Co atom distances in these compounds, which are 4.265(2), 4.278(1) and 4.0313(7) Å for **1-3**, respectively. Complexes **1** and **2** were arranged with the octahedrally coordinated Co atom arranged on a 3-fold axis and the tetrahedrally coordinated Co atom located slightly off the 3-fold axis. In **1**, three py ligands complete the octahedral geometry at one end and the other end has one py coordinated. The complex is positively charged and is balanced by a $[ClO_4]^-$ anion, as illustrated in Figure 5.2.

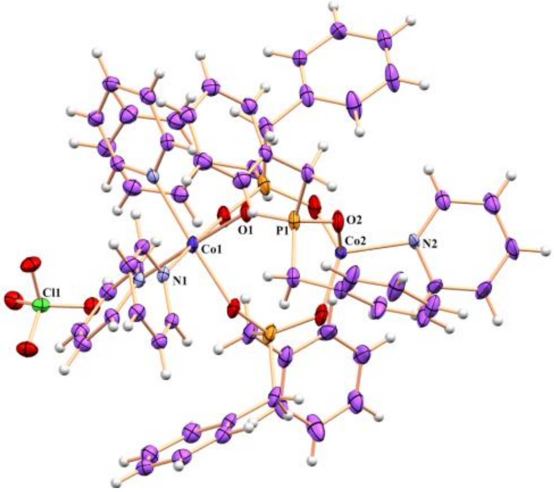

Figure 5.2 Thermal ellipsoid drawing of **1** (one orientation). Selected bond distances (Å) and angles (°) are as follows: Co(1)–O(1), 2.103(2); Co(1)–N(1), 2.192(2); Co(2)–O(2), 1.813(17); Co(2)–N(2), 2.045(4); O(1)^a–Co(1)–O(1), 91.18(8); O(1)^a–Co(1)–N(1), 86.86(9); O(1)^b–Co(1)–N(1), 177.33(8); O(1)–Co(1)–N(1), 87.04(8); N(1)–Co(1)–N(1)^a, 94.85(7); O(2)–Co(2)–O(2)^b, 125.65(13); O(2)–Co(2)–N(2), 103.6(7); O(2)–Co(2)–O(2)^a, 106.3(7); O(2)^b–Co(2)–O(2)^a, 106.0(6); O(2)^b–Co(2)–N(2), 111.3(8); N(2)–Co(2)–O(2)^a, 101.6(2): Symmetry transformation codes; ^{a} –y,x–y,z; ^{b} –x+y,–x,z. (data obtained by Luck and co-workers)

The $\chi_M T$ values for **1** and **2** were determined at room temperature using a Johnson Matthey Guoy balance to be 5.56 and 6.59 emu K mol^{-1}, respectively. These values are larger than the spin-only value for two high-spin cobalt(II) sites (3.75 emu K mol^{-1}) and suggest that there is a contribution of orbital angular momentum typical of the local $^4T_1$ term.[24] The temperature dependent magnetic susceptibility data χ_M on complex **1** was obtained over the temperature range 2 to 300 K under a 1000 Oe measuring field and this is illustrated in Figure 5.3 together with the χ_M T dependence. At 300 K, the value for χ_M T for **1** was 5.813 compared to the 5.575 emu K mol^{-1} reported for $[(MeCN)_5Co(NCS)Co(NCS)_3]$.[8] As shown in Figure 5.3, $\chi_M T$ *vs* T for **1** decreases slowly from 5.813 at 300 K to 4.575 at 50 K and then more rapidly to

2.254 emu K mol^{-1} at 2 K. We were unable to determine a satisfactory fit to the data using the Curie-Weiss equation, but this is not surprising as the analysis of high-spin cobalt(II) complexes is known to be difficult.[25–31]

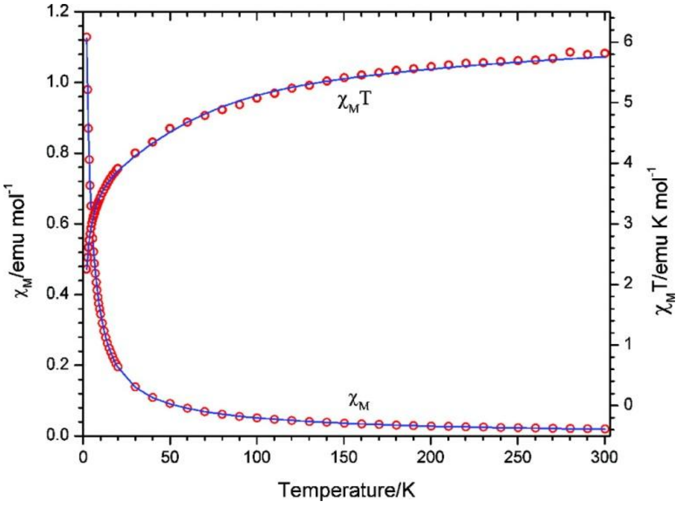

Figure 5.3 Temperature dependence of χ_M *vs T* and $\chi_M T$ *vs T* for **1** with data represented by open circles and the solid line the fit obtained using the parameters described in the text.

This analysis involved the consideration of the g factor and temperature independent paramagnetism, TIP, for the tetrahedral cobalt(II) ion; the spin-orbit coupling factor λ, the orbital reduction factor κ, and a distortion parameter ν defined as $\Delta/(\kappa\lambda)$ for the octahedral cobalt(II) ion. The intramolecular exchange interaction J and the Weiss constant Θ were considered to describe the intermolecular exchange interaction according the equation:

$$\Theta = \frac{zJS(S+1)}{3k_B} \tag{1}$$

where z is the number of nearest neighbor spins, S = 3/2 for high spin Co^{2+}, and k_B is the Boltzmann constant, 0.695 cm^{-1} K^{-1}. In general, it is difficult to separate the intramolecular interaction from the intermolecular interaction. In particular, when J is negative, it is almost impossible to determine J and Θ correctly. Table 5.1 lists the analysis of **1** and that for the complex $[Co(NCMe)_5Co(NCS)_4]$8 for comparison purposes.

Table 5.1 Magnetic parameters.[a]

Complex	g	TIP	λ, cm^{-1}	κ	v	Δ, cm^{-1}	J, cm^{-1}	Θ , K	$R_\chi{}^{b}$, 10^{-5}	R_χ T^{c}, 10^{-5}
1	2.25	0.0007	-173	0.93	-3.9	630	0.15	-1.8	2.5	5.8
$Co_2(L)_5(L')_4$[d]	2.17	0.0007	-155	0.89	-3.7	510	-2.62	-0.1	15	16

[a] Calculated as in Appendix C [b] $R_\chi=\Sigma(\chi_{M,calc}-\chi_{M,obs})^2/\Sigma(\chi_{M,obs})^2$ [c] $R_{\chi\,T}=\Sigma(\chi_M T_{,calc}-\chi_M T_{,obs})^2/\Sigma(\chi_M T_{,obs})^2$ [d] L = MeCN, L' = NCS, reference 8.

If the calculation for the fit of the low-temperature data modified J without consideration of θ, the quality of the fit was not good; however, this improved when Θ was used instead of J. Interestingly, when J and Θ were simultaneously optimized, J became positive (but small at 0.15 cm^{-1}), and the lowest R_χ value (i.e., even higher fitting quality) was obtained and in the final calculation, TIP was also considered. The value for the spin-orbit parameter λ of –173 cm^{-1} for **1** is noteworthy for the theoretical value for the free cobalt(II) ion is expected to be ~ -172 cm^{-1}.[32] That for κ at 0.93 is also close to that for the free cobalt(II) ion.[33] Both of these parameters were calculated to be slightly less for $[Co(NCMe)_5Co(NCS)_4]$. The values for Δ at 630 and 510 cm^{-1} for **1** and $[Co(NCMe)_5Co(NCS)_4]$ respectively are normal for octahedral high-spin cobalt(II) complexes (~200 – ~800 cm^{-1}).[34] For **1**, the negative v value of -3.9 and the Δ value of 627.5 suggest that the octahedral Co(II) ion is trigonally compressed, and this is also consistent with the crystal structure of **1** where O(1)^a–Co(1)–O(1) and N(1)–Co(1)–N(1)^a are larger than 90° and O(1)^a–Co(1)–N(1) and O(1)–Co(1)–N(1) are smaller than 90°.[35]

5.4 Conclusions

In conclusion, for $[Co(NCMe)_5Co(NCS)_4]$[8], if J is assumed to be 0, |Θ| becomes large and unreasonable. Therefore, the sign and magnitude of the J value at –2.62 cm^{-1} in Table 5.1 are suggestive of antiferromagnetic interactions. However, in the case of **1**, the J value at 0.15 cm^{-1}, while small, is slightly positive and thus there is a possibility that the intramolecular interaction is weakly ferromagnetic.

5.5 References

1 Maass, J. S.; Zeller, M.; Breault, T. M.; Bartlett, B. M.; Sakiyama, H.; Luck, R. L. *Inorg. Chem.* **2012**, *51*, 4903-4905.

2 Kanan, M. K.; Nocera, D. G. *Science*, **2008**, *321*, 1072-1075.

3 Brimblecome, R.; Swiegers, G. F.; Dismukes, G. C.; Spiccia, L. *Angew. Chem. Int. Ed.* **2008**, *47*, 7335-7338.

4 Chiari, B.; Cinti, A.; Crispu, O.; Demartin, F.; Pasini, A.; Piovesana, O. *J. Chem. Soc., Dalton Trans.* **2001**, 3611-3616.

5 Panja, A.; Eichhorn, D. M. *J. Coord. Chem.* **2009**, *62*, 2600-2609.

6 Li, W.; Zhan, S-. Z.; Wang, J-. G.; Yan, W-. Y.; Deng, Y-. F. *Inorg. Chem. Commun.* **2008**, *11*, 681-683.

7 Tan, X-. W.; Xie, X-. H.; Chen, J-. Y.; Zhan, S-. Z. *Inorg. Chem. Commun.* **2010**, *13*, 1455-1458.

8 Shurdha, E.; Moore, C. E.; Rheingold, A. L.; Miller, J. S. *Inorg. Chem.* **2011**, *50*, 10546-10548.

9 Feng, L.; Maass, J. S.; Luck, R. L. *Inorg. Chim. Acta* **2011**, *373*, 85-92.

10 Jimtaisong, A.; Feng, L.; Sreehari, S.; Bayse, C. A.; Luck, R. L. *J. Cluster Sci.* **2008**, *19*, 181-195.

11 Maass, J. S.; Chen, Z.; Zeller, M.; Luck, R. L. *Dalton Transactions* **2011**, *40*, 11356-11358.

12 Maass, J. S.; Zeller, M.; Holmes, D.; Bayse, C. A.; Luck, R. L. *J. Cluster Sci.* **2011**, *22*, 193-210.

13 Boyd, E. A.; Boyd, M. E. K.; Kerrigan, F. Tetrahedron Lett. **1996**, *37*, 5425-5426

14 Brechin, E. K.; Coxall, R. A.; Parkin, A.; Parsons, S.; Tasker, P. A.; Winpenny, R. E. P. *Angew. Chem., Int. Ed.* **2001**, *40*, 2700-2703.

15 Chandrasekhar, V.; Boomishankara, R.; Sasikumara, P.; Nagarajan, L.; Cordes, A. W. *Z. Anorg. Allg. Chem.* **2005**, *631*, 2727-2732.

16 Eichelberger, J. L.; Gillman, H. D. *Inorganic coordination polymers. XXI. Manganese(II), cobalt(II), nickel(II), copper(II), and zinc(II) bis(N-phenylaminomethyl) phosphinates. Effects of coordinating side groups*; Pennwalt Corp.: **1977**, 18.

17 Giancotti, V.; Ripamonti, A. *Chim. Ind. (Milan)* **1966**, *48*, 1065-70.

18 Giancotti, V.; Ripamonti, A. *J. Chem. Soc. A* **1969**, 706-13.

19 Gillman, H. D.; Eichelberger, J. L. *Inorg. Chim. Acta* **1977**, *24*, 31-4.

20 Giordano, F.; Randaccio, L.; Ripamonti, A. *Chem. Commun.* **1967**, 19-20.

21 Rose, S. H.; Block, B. P. *J. Am. Chem. Soc.* **1965**, *87*, 2076-7.

22 McAlpin, J. G.; Stich, T. A.; Ohlin, C. A.; Surendranath, Y.; Nocera, D. G.; Casey, W. H.; Britt, R. D. *J. Am. Chem. Soc.* **2011**, *133*, 15444-15452.

23 Crystal data for **1**: $C_{62}H_{62}Co_2N_4O_6P_3$•$ClO_4$, M = 1269.38, *hexagonal*, $a = b$ = 13.5260(10) Å, c = 57.341(4) Å, V = 9085.2(11) Å^3, T = 100(2) K, space group $R\overline{3}$, Z = 6, 14927 reflections measured, 5028 independent reflections (R_{int} = 0.0311). R_1 = 0.0518 ($I > 2\sigma(I)$) and $wR(F^2)$ = 0.1126 ($I > 2\sigma(I)$). Gof on F^2 =1.018.

24 Sakiyama, H.; Adams, H.; Fenton, D. E.; Cummings, L. R.; McHugh, P. E.; Okawa, H. *Open Journal of Inorganic Chemistry* **2011**, *1*, 33-38.

25 Kahn, O. *Molecular Magnetism*. VCH: **1993**, 380.

26 Lloret, F.; Julve, M.; Cano, J.; Ruiz-Garcia, R.; Pardo, E. *Inorg. Chim. Acta* **2008**, *361*, 3432-3445.

27 Sakiyama, H. *J. Chem. Software* **2001**, *7*, 171-178.

28 Sakiyama, H. *Inorg. Chim. Acta* **2006**, *359*, 2097-2100.

29 Sakiyama, H. *J. Comput. Chem., Jpn.* **2007**, *6*, 123-134.

30 Sakiyama, H. *Inorg. Chim. Acta* **2007**, *360*, 715-716.

31 Tone, K.; Sakiyama, H.; Mikuriya, M.; Yamasaki, M.; Nishida, Y. *Inorg. Chem. Commun.* **2007**, *10*, 944-947.

32 Figgis, B. N.; Hitchman, M. A. *Ligand Field Theory and its Application*. Wiley-VCH: New York, **2000**.

33 Lines, M. E. *J. Chem. Phys.* **1971**, *55*, 2977-2984.

34 Figgis, B. N.; Gerloch, M.; Lewis, J.; Mabbs, F. E.; Webb, G. A. *J. Chem. Soc. A* **1968**, 2086-2093.

35 Stiefel, E. I.; Brown, G. F. *Inorg. Chem.* **1972**, *11*, 434-436.

Chapter 6. Perspective and Conclusions

6.1 Introduction

This thesis emphasizes synthesis and characterization of compositionally complex metal oxides, specifically co-incorporated compounds. There are several unanswered questions remaining with the $Ti_{1-(5x/4)}Nb_xO_{2-y-\delta}N_y$ compounds. 1) Can we synthetically control nitrogen incorporation in order to target donor-acceptor pairs of specific mole-ratios? 2) Where are the energy levels in relation to the two half reactions of water splitting? 3) What other co-incorporated compositions should be targeted? In order to start to answer these science questions, we must think critically about each question specifically. Nitrogen incorporation may require a new synthetic approach, targeting a solution based synthesis rather than rely on nitridation via ammonolysis. Furthermore, constructing powder electrodes has been an ongoing lab challenge, so approaching this project will also require new ideas. Finally, taking what we have learned in Chapters 2 and 3 is important as we start to target new co-incorporated compounds for potential water oxidation photocatalysts.

6.2 Perspective

6.2.1 Solution-based synthesis of nitrides

As discussed throughout this thesis, synthetic control over nitrogen incorporation in metal oxide compounds is extremely difficult and complex with current synthesis methods. The most common approach to form an (oxy)nitride compound relies on a two step annealing scheme: 1) the mono-alloyed metal oxide is crystallized by annealing under air, and 2) the metal oxide undergoes a second annealing step under ammonia. This process has resulted in many nitride and (oxy)nitride compounds that have been used for water oxidation, including Ta_3N_5,[1] TaON,[2] $LaTiO_2N$,[3] $ATaO_2N$ (A: Ca, Sr, Ba),[4] and GaN:ZnO.[5] Among these, the GaN:ZnO oxynitride composed of d^{10} metal ions has realized overall water splitting under visible light irradiation when it is modified with suitable co-catalysts, such as RuO_2,[5] $Rh_xCr_{2-x}O_3$,[6] and metal/Cr_2O_3 with a core/shell structure.[7] GaN and ZnO both crystallize in the same wurtzite structure, resulting in solid solutions of the formula $(Ga_{1-x}Zn_x)(N_{1-x}O_x)$, with x ranging from 0.05 to 0.87.[8] While this field is well established, a promising research area to explore would involve a solution-based synthetic route to target compounds with very specific nitrogen mole-percents, as indicated in Chapter 2.

Non-hydrolytic sol-gel chemistry (NHSG) is an attractive route towards forming compositionally complex metal oxides. NHSG involves an oxygen donor that is not water and does not generate water *in situ*. Typically, this synthesis involves reacting precursors (chlorides, alkoxides, *etc.*) with oxygen-donors (alkoxides, alcohols, ethers, ketones, *etc.*). There are various reactions and mechanisms to consider for this type of chemistry.[9,10] One example involves alkyl chloride elimination:

$$\text{M—Cl} + \text{M—OR} \rightarrow \text{M—O—M} + \text{R—Cl} \qquad (1),$$

where the reaction of a metal chloride with a metal alkoxide directly forms metal-oxo bridges and alkyl chloride by products. Alkyl chlorides are volatile and can easily be removed at high temperatures, making this reaction attractive for forming phase pure mixed-metal oxides.[11]

NHSG methods have been used to target a variety of compounds for selective oxidation, photodegradation, alkene metathesis, and heterogeneous photocatalysis. Pertinent to this thesis, TiO_2 was prepared by Colvin and co-workers through a hot injection method (300 °C) of TiX_4

(X = halide) with a titanium alkoxide in trioctylphosphine oxide (TOPO) and heptadecane, which afforded anatase nanoparticles in ~ 5 min.[12] Colvin and co-workers reported the effects of the halide, alkoxide, and passivating agent on forming various particle sizes and phases, opening this synthetic pathway for forming metal oxide nanoparticles.

There have been no reports for forming (oxy)nitride compounds in a comparable way, but one could envision utilizing this route to afford synthetic control over compositionally complex mixed metal (oxy)nitrides. Through precise control over precursor concentrations, using amine based metal reagents in a mixture of TOPO and trioctylamine (TOA) under oxygen and moisture sensitive conditions could lend co-incorporated compounds. Ideally, one would first target N-doped and mono-alloyed TiO_2 as proof of principal before targeting the co-incorporated targets; however, under the right reaction conditions could be a promising route towards the synthesis of co-incorporated compounds. One proposed reaction to target $TiO_{1.75}N_{0.25}$ is indicated below:

$$Ti(NEt_2)_4 + 7Ti(OEt)_4 + 8TiCl_4 \rightarrow 4Ti_4O_7N + 32EtCl \qquad (2)$$

Reaction 2 was attempted several times at room temperature under nitrogen using Schlenk techniques, but did not yield the desired product that included substitutional nitrogen. Annealing the resulting brown resin in nitrogen at 500 °C for 12 hours did yield the anatase phase, shown in Figure 6.1; however substitutional nitrogen was not present by XPS, shown in Figure 6.2. Utilizing the hot injection method could lead to successful incorporation of nitrogen into anatase.

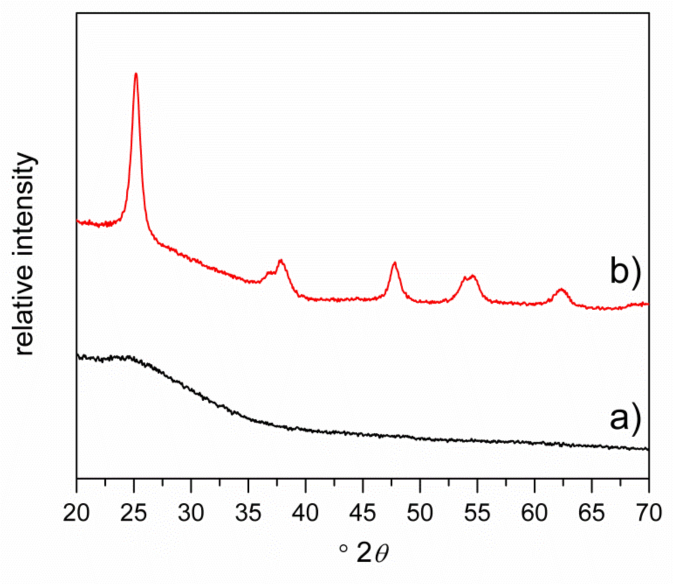

Figure 6.1 X-ray diffraction pattern of a) the dried resin and b) resin annealed at 500 °C for 12 hours under flowing N_2.

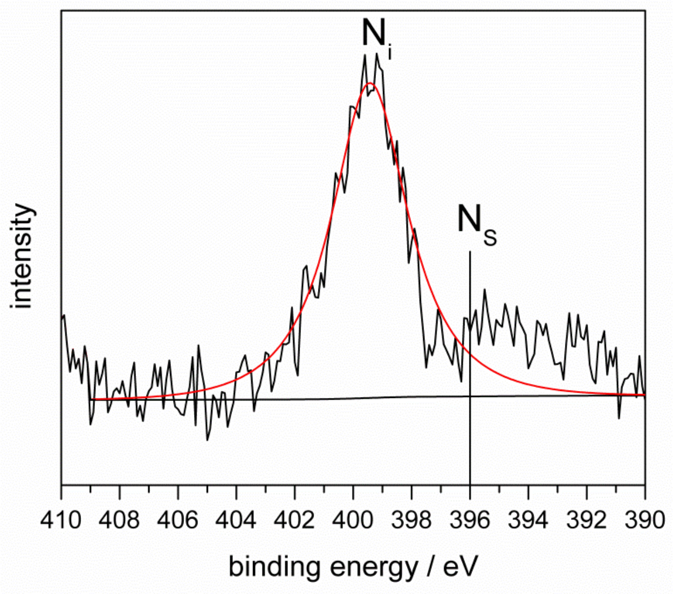

Figure 6.2 XP spectra of N(1s) core binding energy for NHSG prepared anatase compound.

There is one report of a two step preparation to make $Fe_xTi_{x-1}O_{2-y}N_y$, whereby iron(III) nitrate and titanium(IV) chloride were mixed in *tert*-butyl alcohol to form a gel, which was subsequently annealed under flowing ammonia. This resulted in mixed phases, anatase and rutile, but afforded high crystallinity and small crystallites. The composition out-performed commercial P-25 for the photodegradation of phenol.[13]

The scientific research challenge remains in the precise control over the nitrogen content in a co-incorporated compound. This type of synthesis, which will require systematically changing the precursor components, could open pathways for the synthesis of novel compounds with good control over composition, particle size, and morphology. Developing a novel one-step synthesis towards a co-incorporated compound with compositional control will significantly contribute to the field of inorganic synthesis and potentially photocatalysis.

6.2.2 Powdered electrodes

Chapter 4 introduced some of the obstacles faced for constructing powdered electrodes of Ruddlesden-Popper phase; however constructing powder electrodes in general has been a challenge. The difficulty remains in getting good adherence of the particles to the substrate (FTO) to generate an Ohmic contact with the electrolyte. We've targeted various approaches to constructing powdered electrodes based on literature preparation, mainly variations of literature adapted electrophoretic deposition approaches[14,15] and doctor blading slurries and annealing at low temperatures.[16–18] Although these approaches have formed electrodes, the powders can be easily wiped off, which results in poor photoelectrochemistry (Chapter 2).

Domen and co-workers recently developed a particle transfer method that resulted in high performing photoanodes ($LaTiO_2N$ loaded with IrO_x, > 2 mA/cm^2 at 1.2 V vs. RHE).[19] They have typically relied on slurry techniques to produce photoanodes; however, this new report is a simple alternative that results in good Ohmic contact between the photocatalyst and a conducting layer. Figure 6.3 depicts the particle transfer process: a) the photocatalyst is deposited on FTO substrate by drop casting an isopropanol suspension and allowing to dry, b) a contact layer, such as Ta, Nb, Ti, and Zr, was applied via RF sputtering, c) a thicker conductor layer, such as titanium, is applied via RF sputtering, and d) a second glass layer is applied via epoxy and removed from the initial glass layer. Loose particles are removed by ultrasonication.

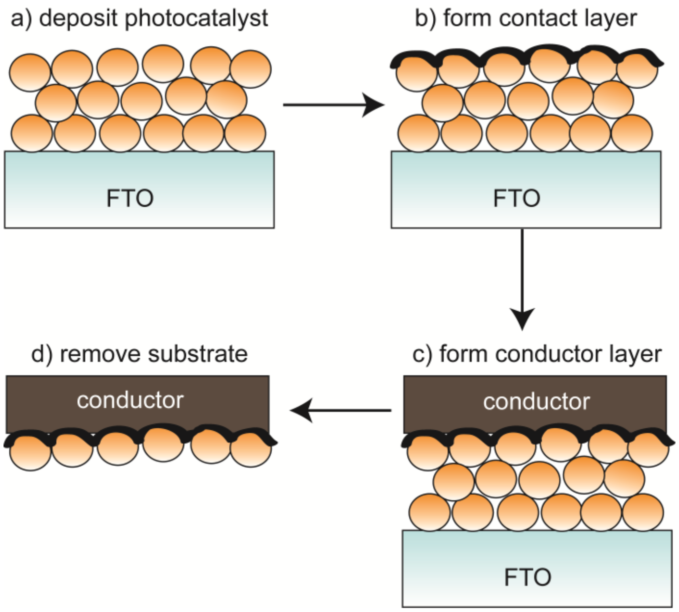

Figure 6.3 Particle transfer scheme a) deposit a photocatalyst, b) add a contact layer, c) form a conductor layer, and d) remove FTO and sonicate loose particles. Adapted from ref. 19.

The particle transfer method is an approach to try for the TiO_2:(Nb,N) powders. The next question for these powders is “what are the band-edge positions?” Constructing an electrode in the above manner would allow for impedance spectroscopy and photoelectrochemical measurements, which once coupled to our UV-Vis data, would lend insight into the energy levels of the $Ti_{1-(5x/4)}Nb_xO_{2-y-\delta}N_y$ compounds. It should be noted that Domen’s $LaTiO_2N$ electrodes were not particularly stable with this fabrication technique, so further modification would be necessary, especially for constructing co-incorporated powders.

Our lab (Charles Lhermitte) has also recently built a spray pyrolysis system, which can systematically spray precursor solutions onto an FTO substrate positioned on a hot plate. Since we have developed a sol-gel approach to form $Ti_{1-(5x/4)}Nb_xO_2$, spraying layers onto FTO to control layer thickness, followed by subsequent annealing under mixed Ar or N_2/NH_3 atmosphere could lend co-incorporated thin films. My initial attempts at nitriding materials coated onto FTO under ammonia have not been fruitful, for the conductivity of the FTO has been compromised (15 Ω/□ before *vs.* 0 Ω/□ after) following all annealing schemes; however, recent reports on short annealing schemes under NH_3 and NH_3 mixed atmospheres maintains the substrate conductivity.[20] Therefore, another approach for forming films of co-incorporated compounds would utilized spray pyrolysis for precursor composition control and layer thickness control coupled with precise control over annealing schemes and atmospheres to incorporate substitutional nitrogen.

6.2.3 Low donor-acceptor mole-percent regime targets

Chapters 2 and 3 focused on co-incorporating Nb and N into the anatase TiO_2 structure, which was partly motivated by DFT calculations by Yan and co-workers.[21] As their work points out, it is important to consider various alloying regimes because band-edge positions and band-gaps can change dramatically based on altering the alloying mole-percents. The overall goal of this theoretical study was to target donor-acceptor pairs in anatase that results in *low band-gap compounds with appropriate band edges for overall water splitting*.

At the low mole-percent regime, 3.1 or 6.25 % of O is replaced by accepters for the one donor/one accepter and one donor/two acceptors cases respectively. At the high mole-percent regime 12.5 or 25 % of O is replaced for one or two acceptors respectively. Briefly, good donor-acceptor pairs for the low mole-percent regime included (Mo, 2N) and (W, 2N), and in the high mole-percent regime include (Nb, N) and (Ta, N), with predicted band-gap values shown in Table 6.1. Based on these calculations, the results suggest that the composition-dependence of these compounds drastically influences the band-gap. For example, (Nb, N) is predicted to have a wide band-gap of 2.91 eV at low mole-percents of donor-acceptors, in contrast to a decreased band-gap of 2.68 eV at high mole-percents. We observed experimental results for (Nb, N), which despite not achieving an ideal mole-ratio of Nb:N of 1, corroborates the predicted values quite well.[22] At low mole-percents (1 mole % Nb, N), we observed a band gap of 2.37 eV, while at high mole percents (25 mole % Nb, N) we observed a band-gap of 2.2 eV. Furthermore, the defect structure at each extreme differed due to charge compensation, affecting the photocatalytic degradation of MB.

Table 6.1 Predicted band-gap energies (eV) for donor-acceptor pairs in anatase TiO_2.[21]

	low mole-percent regime	high mole-percent regime
(Mo, 2N)	2.48	1.25
(W, 2N)	2.45	1.30
(Nb, N)	2.91	2.68
(Ta, N)	2.91	2.50

With this knowledge in hand, a future direction for co-incorporating anatase would be to target the low mole-percent donor-acceptor pairs experimentally, (Mo, 2N) and (W, 2N), with predicted band offsets shown in Figure 6.4. Through our experimental approach, we observe low mole-percents of substitutional nitrogen in our co-incorporated compounds at varying mole-percents of niobium. We hypothesize that the donor (Nb) increases the mole-percent of substitutional nitrogen in these compounds through charge compensation (discussed in Chapter 2). This should hold true for other donor-acceptor pairs, suggesting that targeting good low mole-percent candidates may allow for better overall charge compensation and improved photocatalytic properties. We predict an opposite trend in photocatalytic activity for (Mo, 2N) and (W, 2N), with decreasing photocatalytic activity with increasing mole-percent donor-acceptor pairs.

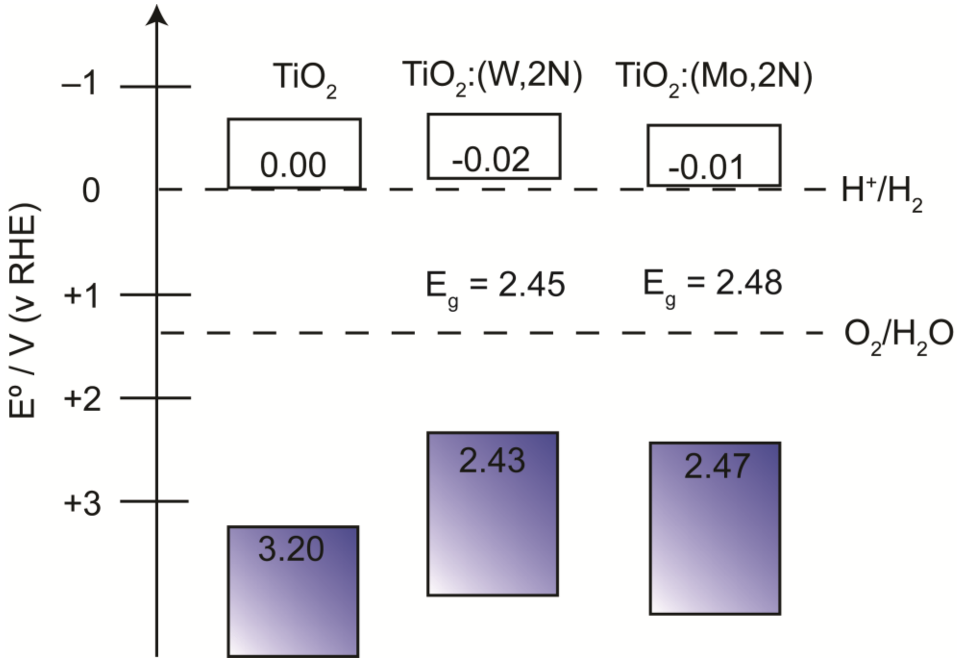

Figure 6.4 Calculated band offsets for low mole-percent donor-acceptor pairs, (Mo, 2N) and (W, 2N), adapted from ref.21.

There are some reports of co-incorporating with (Mo, 2N)[23–25] and (W, 2N)[26–29] in anatase already in the literature; however, with our studies on (Nb, N) we can perform additional experiments at this low mole-percent regime in order to contribute to the research field. For example, for (Mo, 2N), one report targeted (Mo, N) co-incorporated TiO_2; however, they did not treat dried gels under ammonia to incorporate substitutional nitrogen.[23] Furthermore, X-ray photoelectron spectroscopy results show little evidence for any nitrogen incorporation, substitutional or interstitial, which we have shown to be very important for photocatalysis. The fundamental knowledge we have acquired through completely characterizing the electronic structure of our (Nb, N) compounds can be expanded by targeting these various mole-percent compositions. Furthermore, we have only *co-incorporated* donor/acceptor pairs in TiO_2; *co-*

alloying will require new synthetic routes in order to achieve fully charge compensated donor/acceptor pairs in TiO_2.

6.3 Conclusions

A major scientific challenge facing the world today remains in developing alternative renewable energy sources, of which, photolysis is one promising pathway to exploit sunlight and water, two abundant sources, and store energy in the form of chemical bonds. Research over the past forty years has focused on using heterogeneous photocatalysts for overall water splitting; however, wide scale use of any compound has been limited due to efficiency and affordability. How do we overcome these important points? Continued fundamental research will be necessary in order to gain understanding at the basic level and expand to working systems. Our work on co-incorporated titania with (Nb,N) has provided extensive physical characterization on a complex system, which is necessary in order to understand why compositions are/are not good photocatalysts for both dye degradation and water oxidation. Continued studies exploring the electronic structure and surface properties of potential heterogeneous photocatalysts will provide a strong foundation for which further research and experimental design can build from.

6.4 References

1 Hitoki, G.; Ishikawa, A.; Takata, T.; Kondo, J. N.; Hara, M.; Domen, K. *Chem. Lett.* **2002**, *31*, 736-737.

2 Hitoki, G.; Takata, T.; Kondo, J. N.; Hara, M.; Kobayashi, H.; Domen, K. *Chem. Commun.* **2002**, *16*, 1698-1699.

3 Kasahara, A.; Nukumizu, K.; Hitoki, G.; Takata, T.; Kondo, J. N.; Hara, M.; Kobayashi, H.; Domen, K. *J. Phys. Chem. A* **2002**, *106*, 6750-6753.

4 Yamasita, D.; Takata, T.; Hara, M.; Kondo, J. N.; Domen, K. *Solid State Ionics* **2004**, *172*, 591-595.

5 Maeda, K.; Takata, T.; Hara, M.; Saito, N.; Inoue, Y.; Kobayashi, H.; Domen, K. *J. Am. Chem. Soc.* **2005**, *127*, 8286-8287.

6 Maeda, K.; Teramura, K.; Lu, D.; Takata, T.; Saito, N.; Inoue, Y.; Domen, K. *Science* **2006**, *440*, 295.

7 Maeda, K.; Teramura, K.; Lu, D.; Saito, N.; Inoue, Y.; Domen, K. *J. Phys. Chem. C* **2007**, *111*, 7554-7560.

8 Lee, K.; Tienes, B. M.; Wilker, M. B.; Schnitzenbaumer, K. J.; Dukovic, G. *Nano. Lett.* **2012**, *12*, 3268-3272.

9 Vioux, A. *Chem. Mater.* **1997**, *9*, 2292-2299.

10 Mutin, P. H.; Vioux, A. *Chem. Mater.* **2009**, *21*, 582-596.

11 Debecker, D. P.; Mutin, P. H. *Chem. Soc. Rev.* **2012**, *41*, 3642-3650.

12 Trentler, T. J.; Denler, T. E.; Bertone, J. F.; Agrawal, A.; Colvin, V. L. *J. Am. Chem. Soc.* **1999**, *121*, 1613-1614.

13 Naik, B.; Parida, K. M. *Ind. Eng. Chem. Res.* **2010**, *49*, 8339-8346.

14 Abe, R.; Higashi, M.; Domen, K. *J. Am. Chem. Soc.* **2011**, *132*, 11828-11829.

15 Zhitomirsky, I.; Petric, A. *J. Mater. Sci.* **2004**, *39*, 825-831.

16 Abe, R.; Takata, T.; Sugihara, H.; Domen, K. *Chem. Lett.* **2005**, *34*, 1162.

17 Maeda, K.; Higashi, M.; Lu, D.; Abe, R.; Domen, K. *J. Am. Chem. Soc.* **2010**, *132*, 5858.

18 Ito, S.; Chen, P.; Comte, P.; Nazeeruddin, M. K.; Liska, P.; Péchy, P.; Grätzel., M. *Prog. Photovolt: Res. Appl.* **2007**, *7*, 603-612.

19 Minegishi, T.; Nishimura, N.; Kubota, J.; Domen, K. *Chem. Sci.* **2012**, *4*, 1120-1124.

20 Hoang, S.; Berglund, S. P.; Hahn, N. T.; Bard, A. J.; Mullin, C. B. *J. Am. Chem. Soc.* **2012**, *134*, 3659-3662.

21 Yin, W-. J.; Tang, H.; Wei, S-. H.; Mowafak, M. A-. J.; Tuner, J.; Yan, Y. *Phys. Rev. B* **2010**, *82*, 045106/1-6.

22 Breault, T. M.; Bartlett, B. M. *J. Phys. Chem. C* **2013**, *in revision*.

23 Tan, K.; Zhang, H; Xie, C.; Zheng, H. Gu, Y.; Zhang, W. F. *Cat. Commun.* **2010**, *11*, 331-335.

24 Zhang, J.; Xi, J.; Ji, Z. *J. Mater. Chem.* **2012**, *22*, 17700-17708.

25 Liua, H.; Lub, Z.; Yue, l.; Liub, J.; Ganb, Z.; Shua, C.; Zhanga, T.; Shi, J.; Xiong, R. *Appl. Surf. Sci.* **2011**, *257*, 9355-9361.

26 Khan, A.; Sajjad, L.; Shamaila, S.; Zhang, J. *Mater. Res. Bull.* **2012**, *47*, 3083-3089.

27 Márquez, A. M.; Plata, J. J.; Ortega, Y.; Sanz, J. F. *J. Phys. Chem. C* **2012**, *116*, 18759-18767.

28 Thind, S. S.; Wu, G.; Chen, A. *Appl. Cat. B: Environ.* **2012**, *111-112*, 38-45.

29 Mishra, T.; Mahato, M.; Aman, M.; Patel, J. N.; Sahu, R. K. *Catal. Sci. Technol.* **2011**, *1*, 609-615.

Appendix A. Characterization Data for Co-incorporated Compounds (Chapters 2 and 3)

Portions of this appendix have been published:
Breault, T. M.; Bartlett, B. M. *J. Phys. Chem. C* **2012**, *116*, 5986-5994. Reprinted with permission. Copyright 2012 American Chemical Society.
Figures: A.1-A.22; Table A.1

Breault, T. M.; Bartlett, B. M. *J. Phys. Chem. C* **2013**, *in revision*.
Figures: A.23-A.41; Tables: A.2-A.6

Breault, T. M.; Bartlett, B. M. **2013**, *submitted*.
Figure A.43

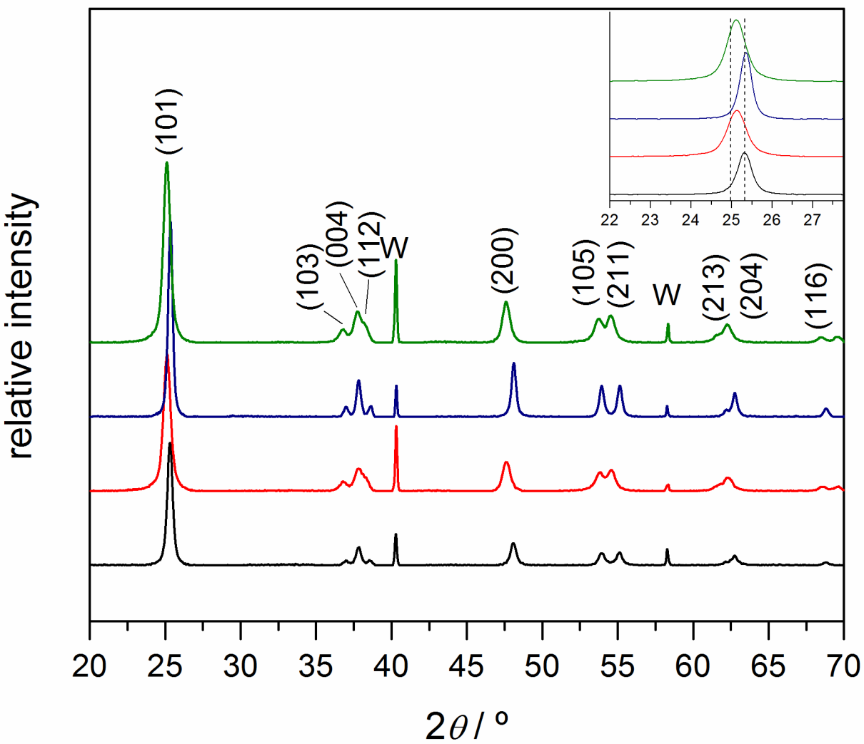

Figure A.1 X-ray diffraction patterns of the polycrystalline anatase powders after annealing at 500 °C with their corresponding Miller indices. From bottom to top: TiO_2 (black), TiO_2:Nb (red), TiO_2:N (blue), TiO_2:(Nb,N) (green). The inset highlights the (101) plane. Tungsten powder was used as an internal standard.

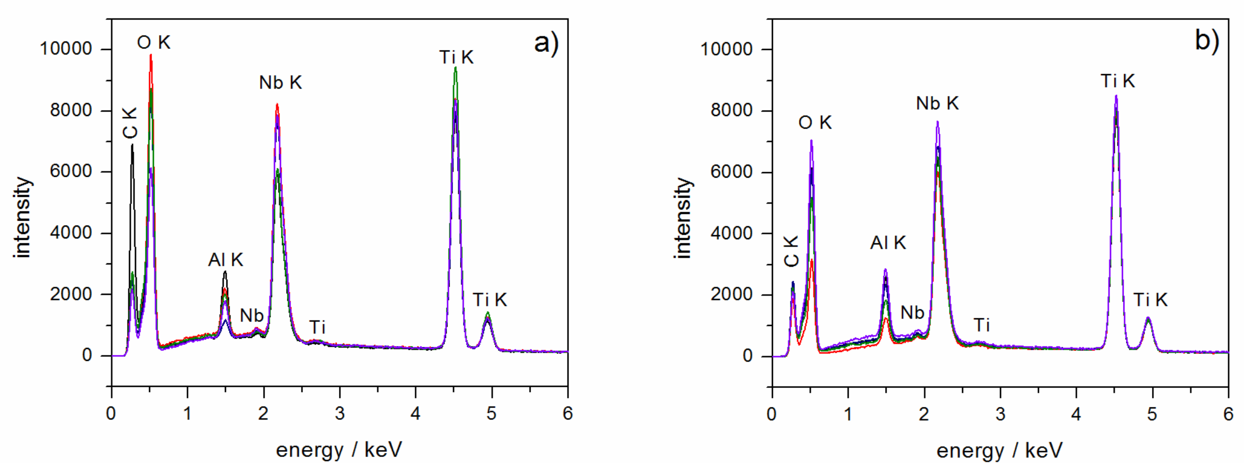

Figure A.2 EDX spectra overlaid for a) TiO_2:Nb and b) TiO_2:(Nb,N)-**1**. The Al K peak arises from the sample holder.

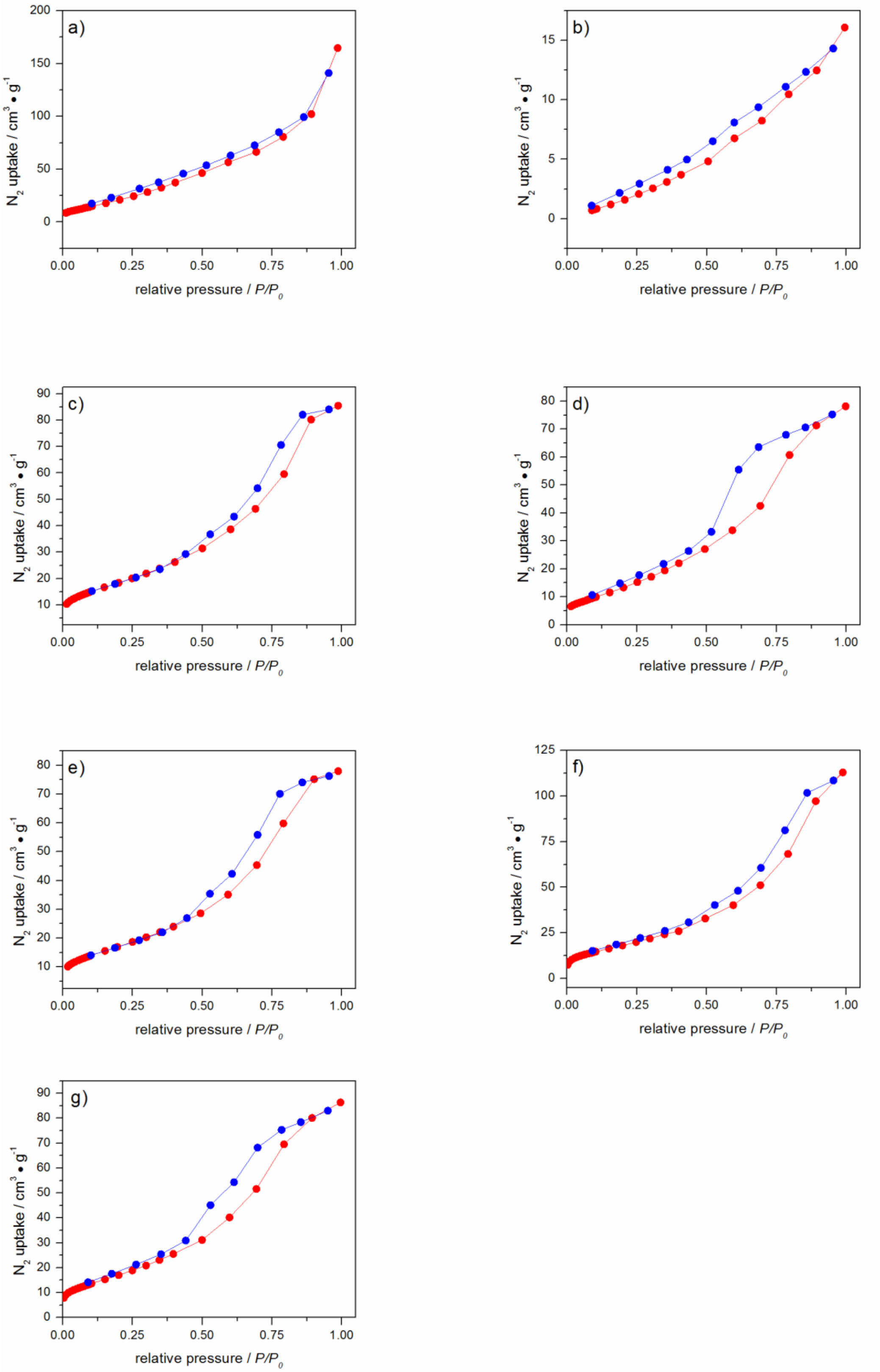

Figure A.3 N$_2$ sorption isotherms for a) Degussa P-25, b) TiO$_2$, c) TiO$_2$:Nb, d) TiO$_2$:N, e) TiO$_2$:(Nb,N)-**1**, f) TiO$_2$:(Nb,N)-**2**, and g) TiO$_2$:(Nb,N)-**3**.

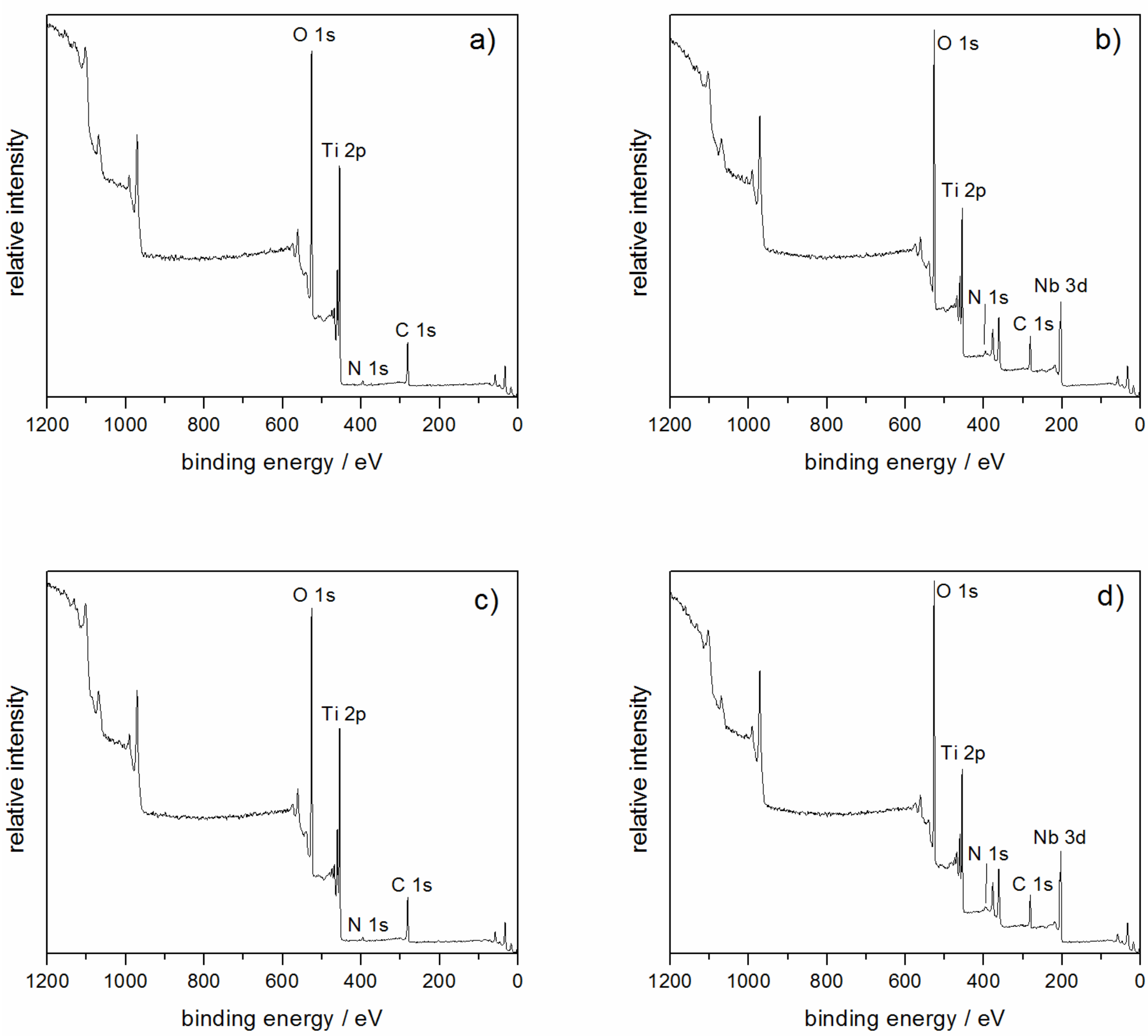

Figure A.4 XP survey scans for a) TiO_2, b) TiO_2:Nb, c) TiO_2:N, and d) TiO_2:(Nb,N)-**1**.

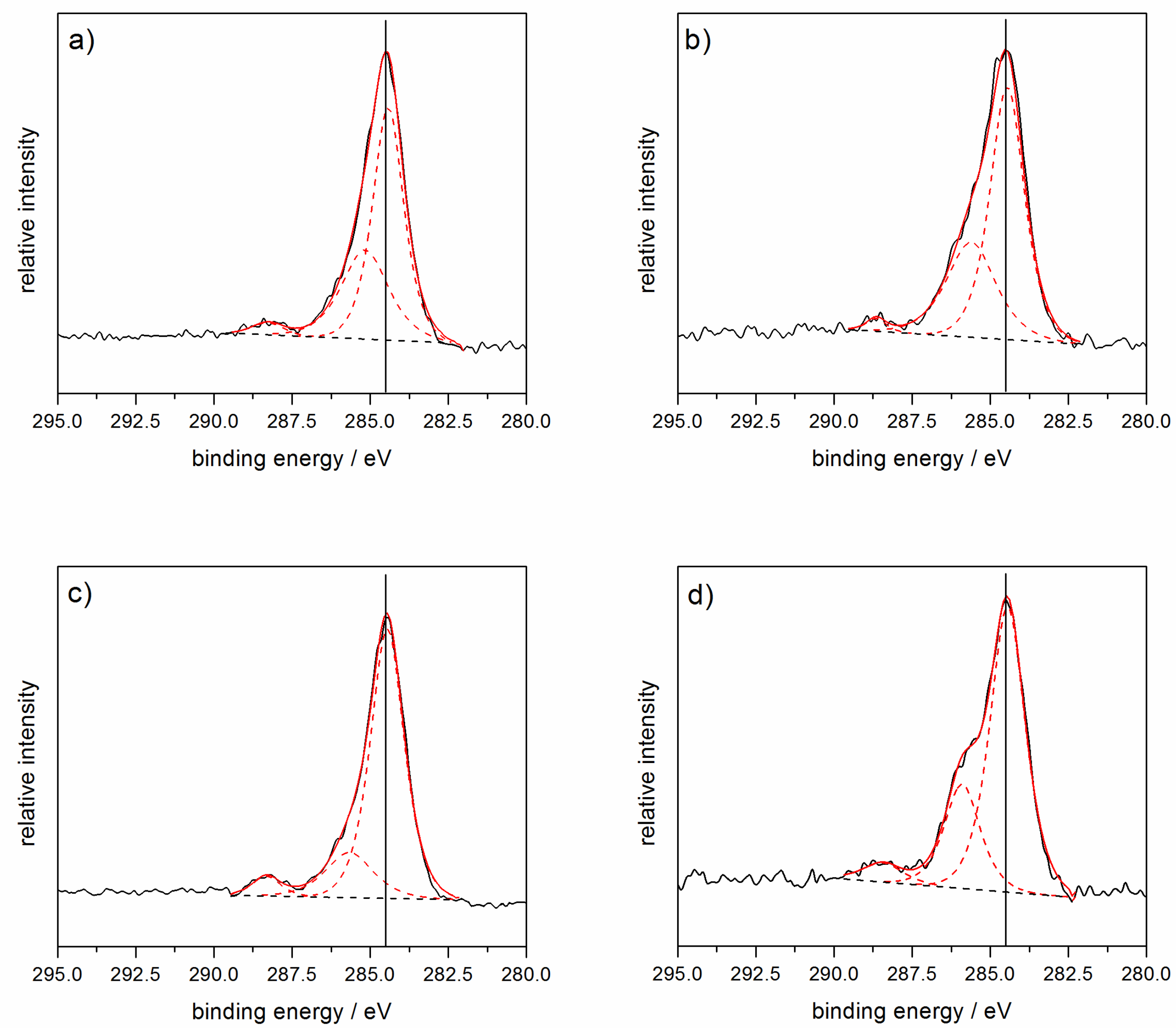

Figure A.5 XP C(1s) spectra for the samples annealed under ambient atmosphere are: a) TiO_2, b) TiO_2:Nb, c) TiO_2:N, and d) TiO_2:(Nb,N)-**1**. All samples were calibrated to 284.5 eV, denoted by the solid line.

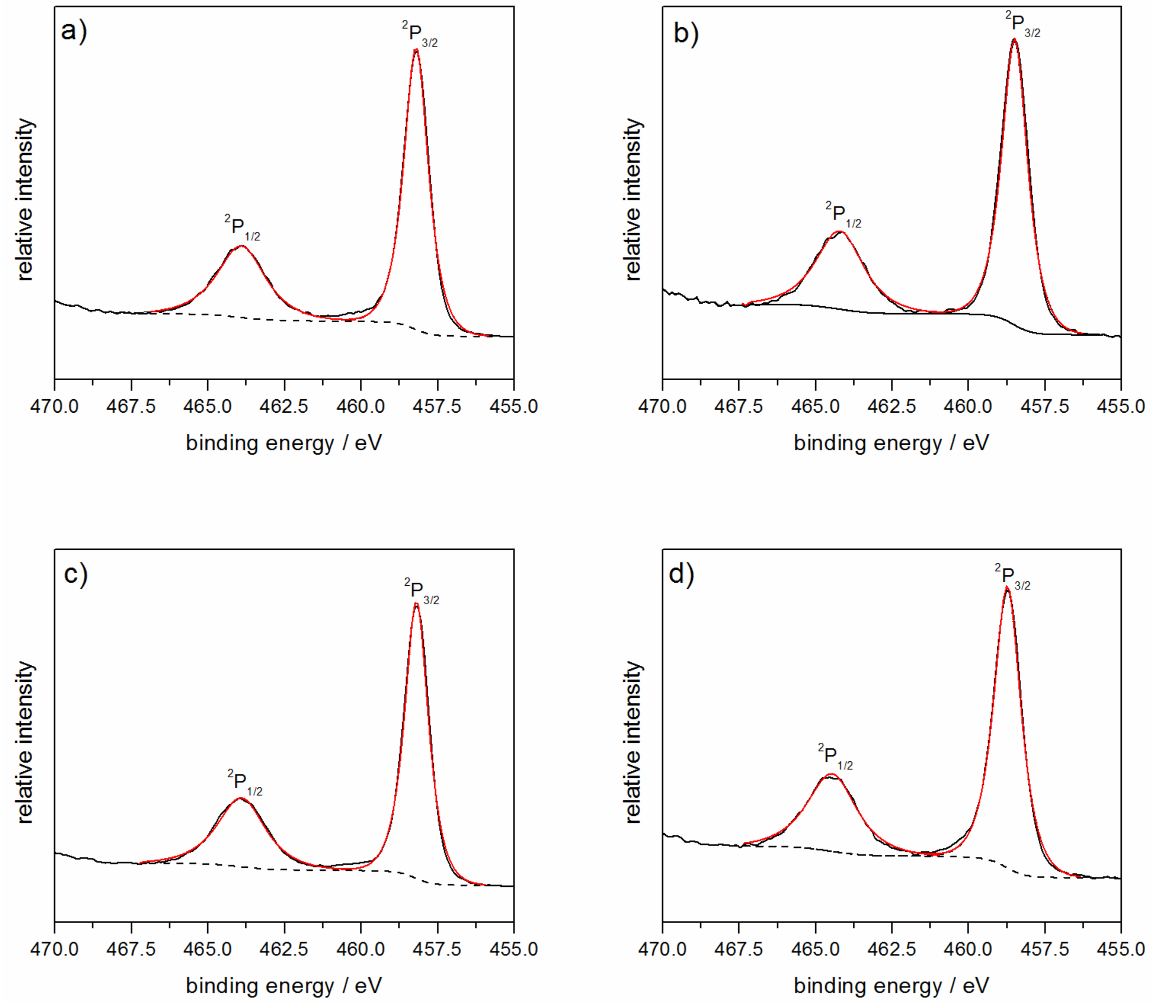

Figure A.6 Ti(2p) XP spectra for a) TiO_2, b) TiO_2:Nb, c) TiO_2:N, and d) TiO_2:(Nb,N)-**1**.

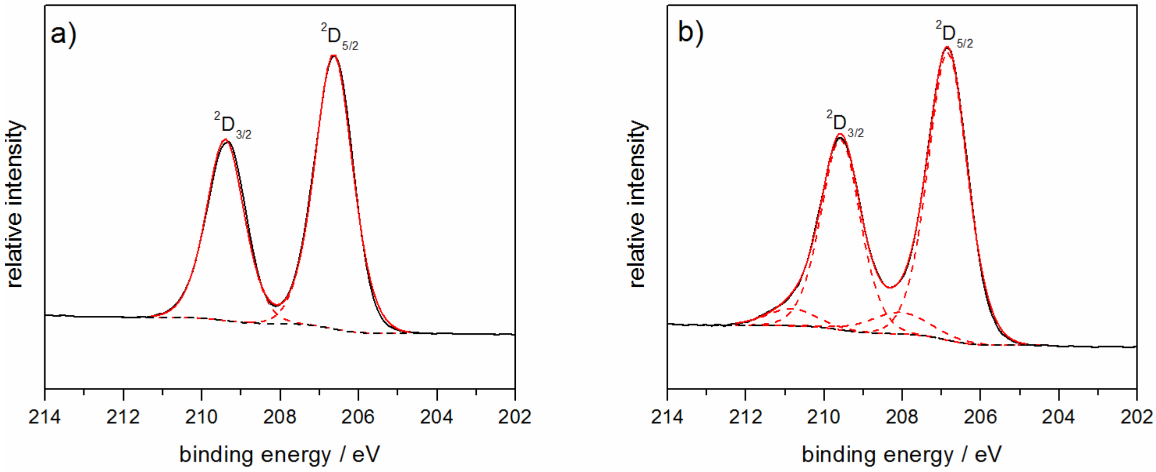

Figure A.7 Nb(3d) XP spectra for a) TiO_2:Nb, and b) TiO_2:(Nb,N)-**1**.

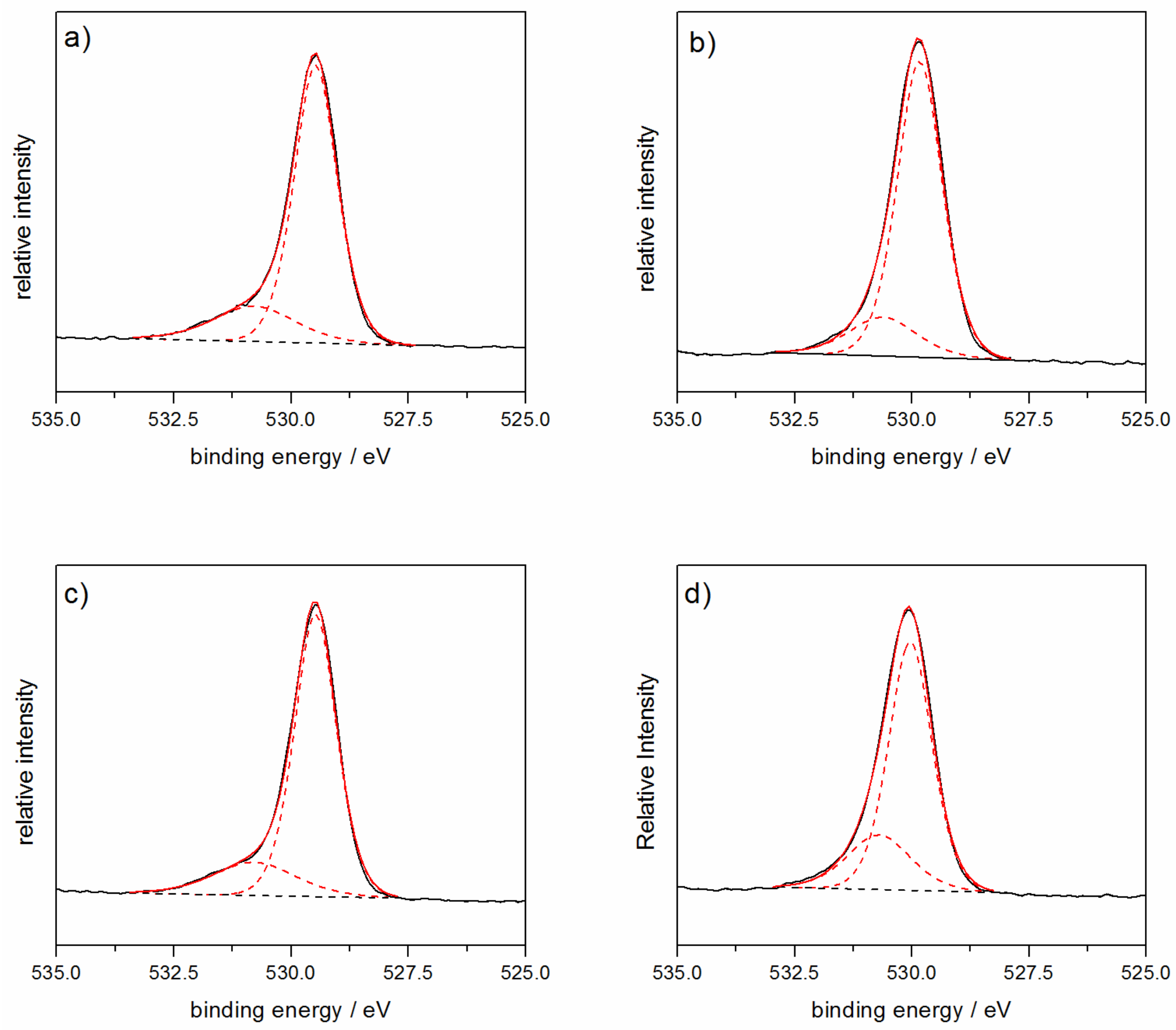

Figure A.8 O(1s) XP spectra for a) TiO_2, b) TiO_2:Nb, c) TiO_2:N, and (d) TiO_2:(Nb,N)-**1**.

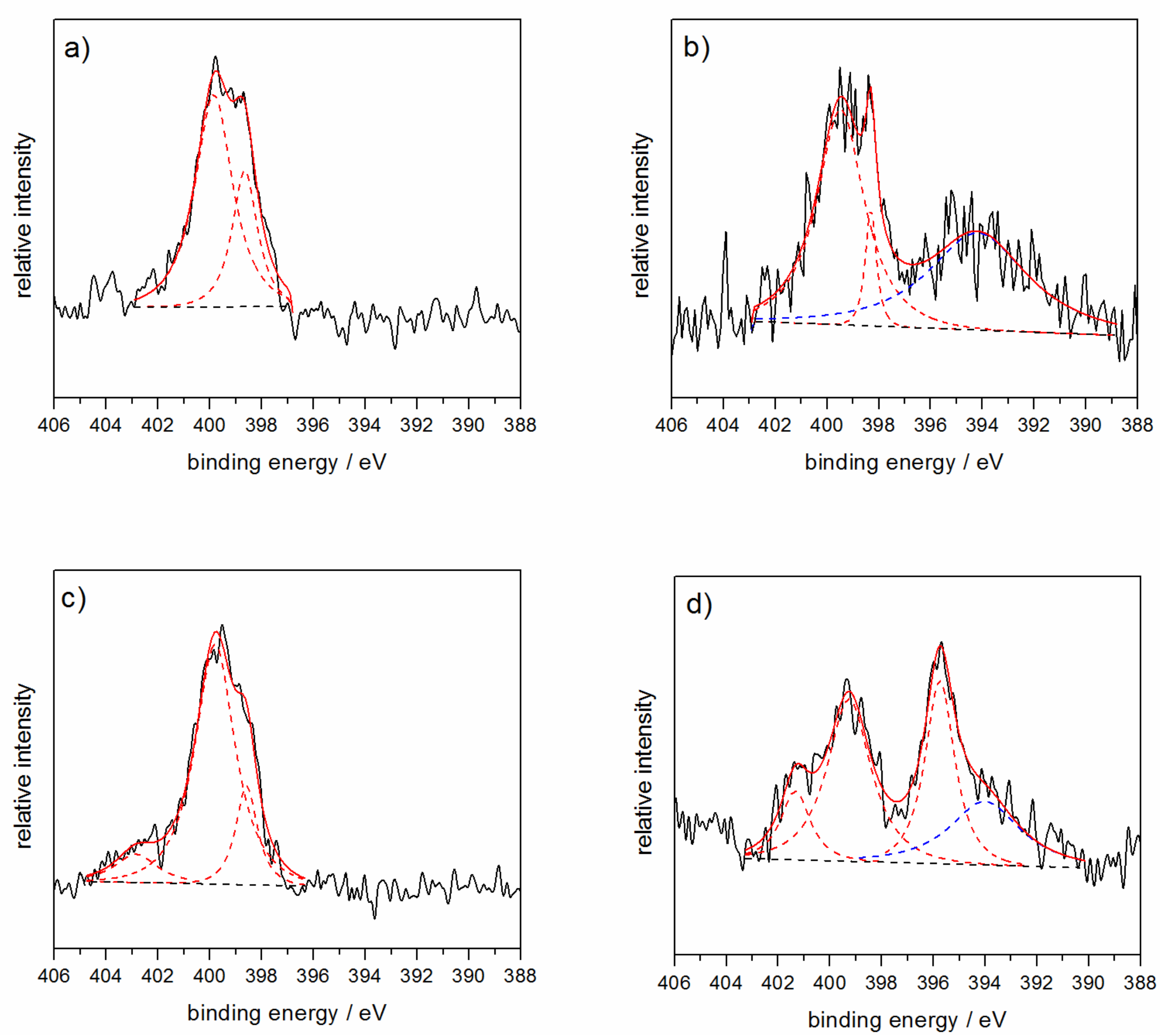

Figure A.9 N(1s) XP spectra for a) TiO_2, b) TiO_2:Nb, c) TiO_2:N, and d) TiO_2:(Nb,N)-**1**.

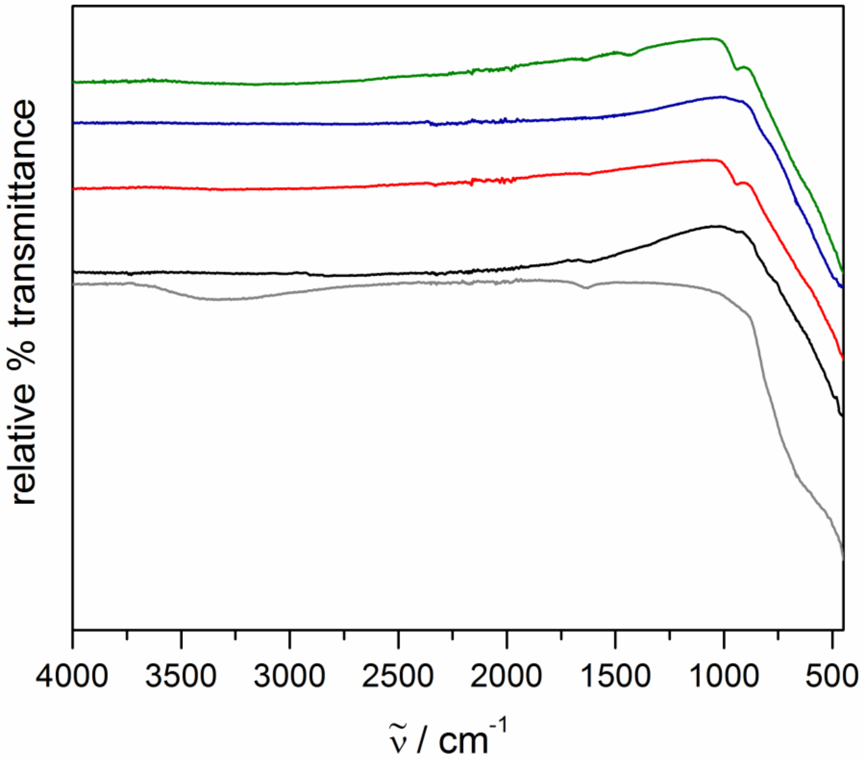

Figure A.10 From bottom to top, FTIR-ATR spectra for Degussa P-25 (gray), TiO_2 (black), TiO_2:Nb (red), TiO_2:N (blue), and TiO_2:(Nb,N)-**1** (green). Plots are offset for clarity.

Table A.1 IR spectral assignments (cm^{-1}).

	Ti-O	Nb-O	Ti-N	C=O	OH
Degussa P-25	395			1630	3300
TiO_2	418			1614	
TiO_2:Nb	404	941		1640	
TiO_2:N	457			1620	
TiO_2:(Nb,N)-**1**	398	941	1432	1640	

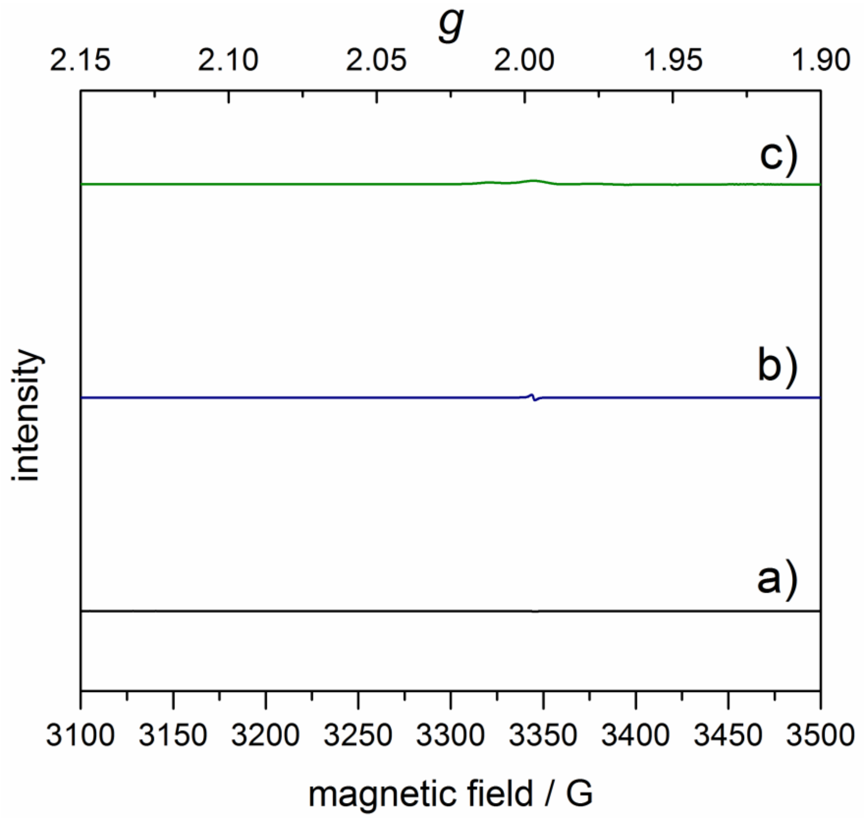

Figure A.11 EPR spectra of a) TiO_2 (black), b) TiO_2:N (blue), and c) TiO_2:(Nb,N) (green) compounds post annealed under flowing O_2 at 500 °C for 5 hours.

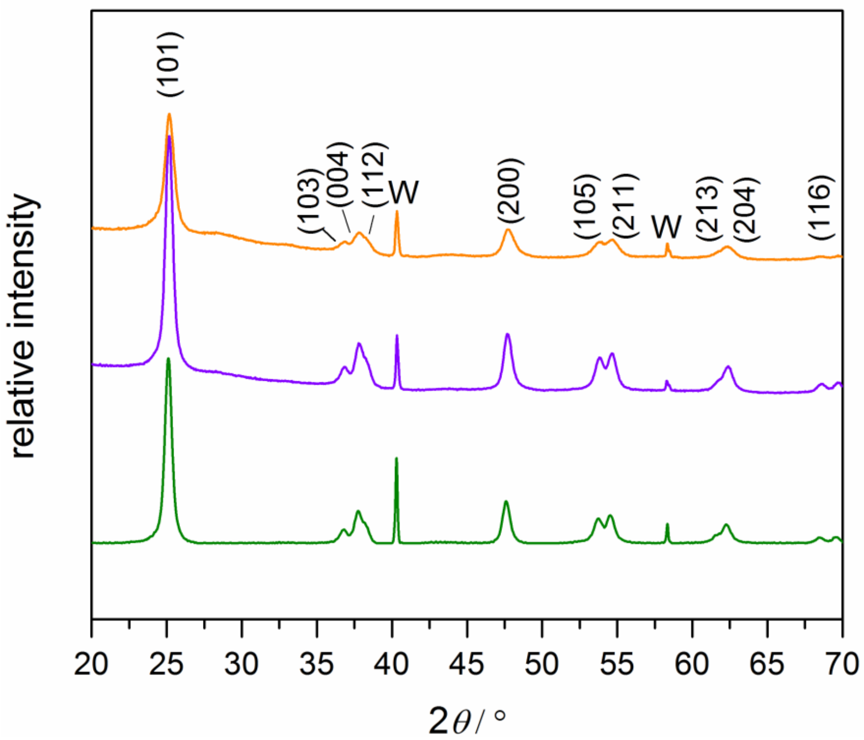

Figure A.12 From bottom to top, XRD patterns of TiO_2:(Nb,N)-**1** (green), TiO_2:(Nb,N)-**2** (violet), and TiO_2:(Nb,N)-**3** (orange).

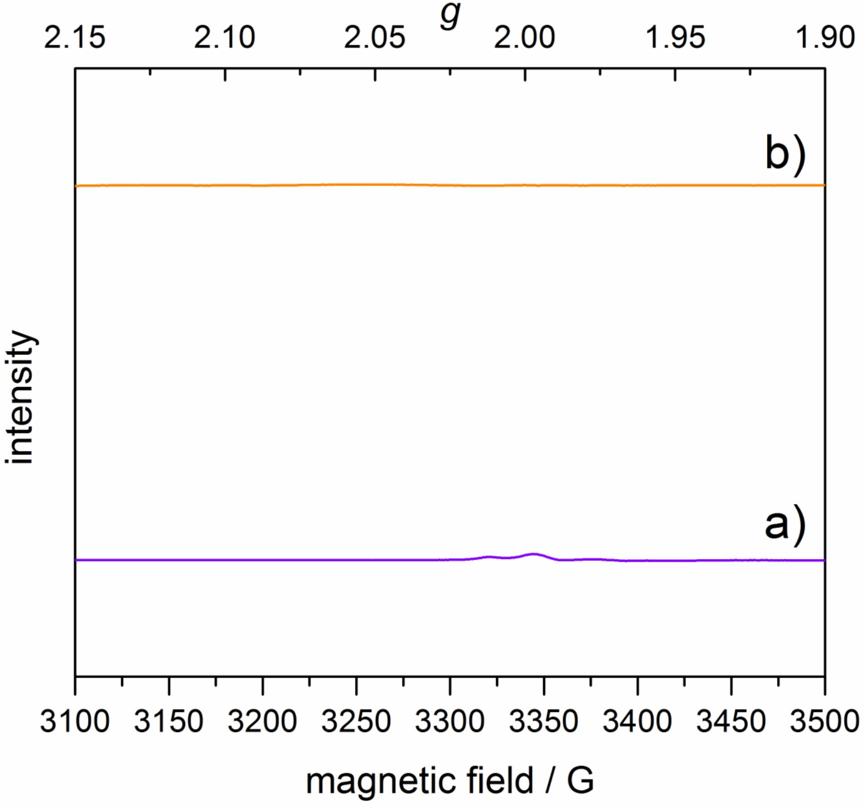

Figure A.13 EPR spectra of a) TiO_2:(Nb,N)-**2** (violet) and b) TiO_2:(Nb,N)-**3** (orange).

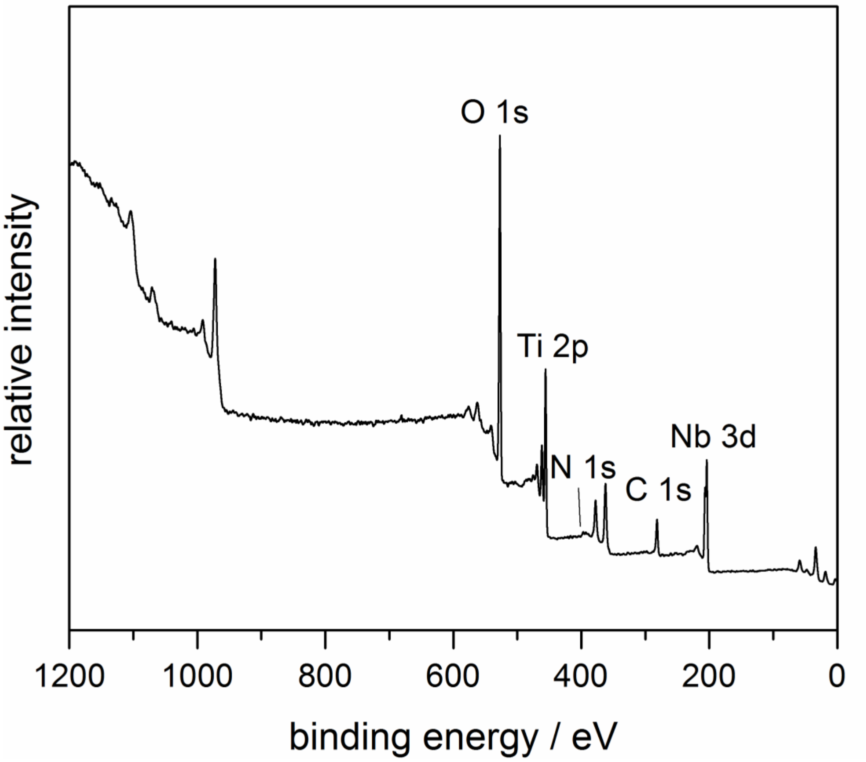

Figure A.14 XP survey scan for TiO_2:(Nb,N)-**2**.

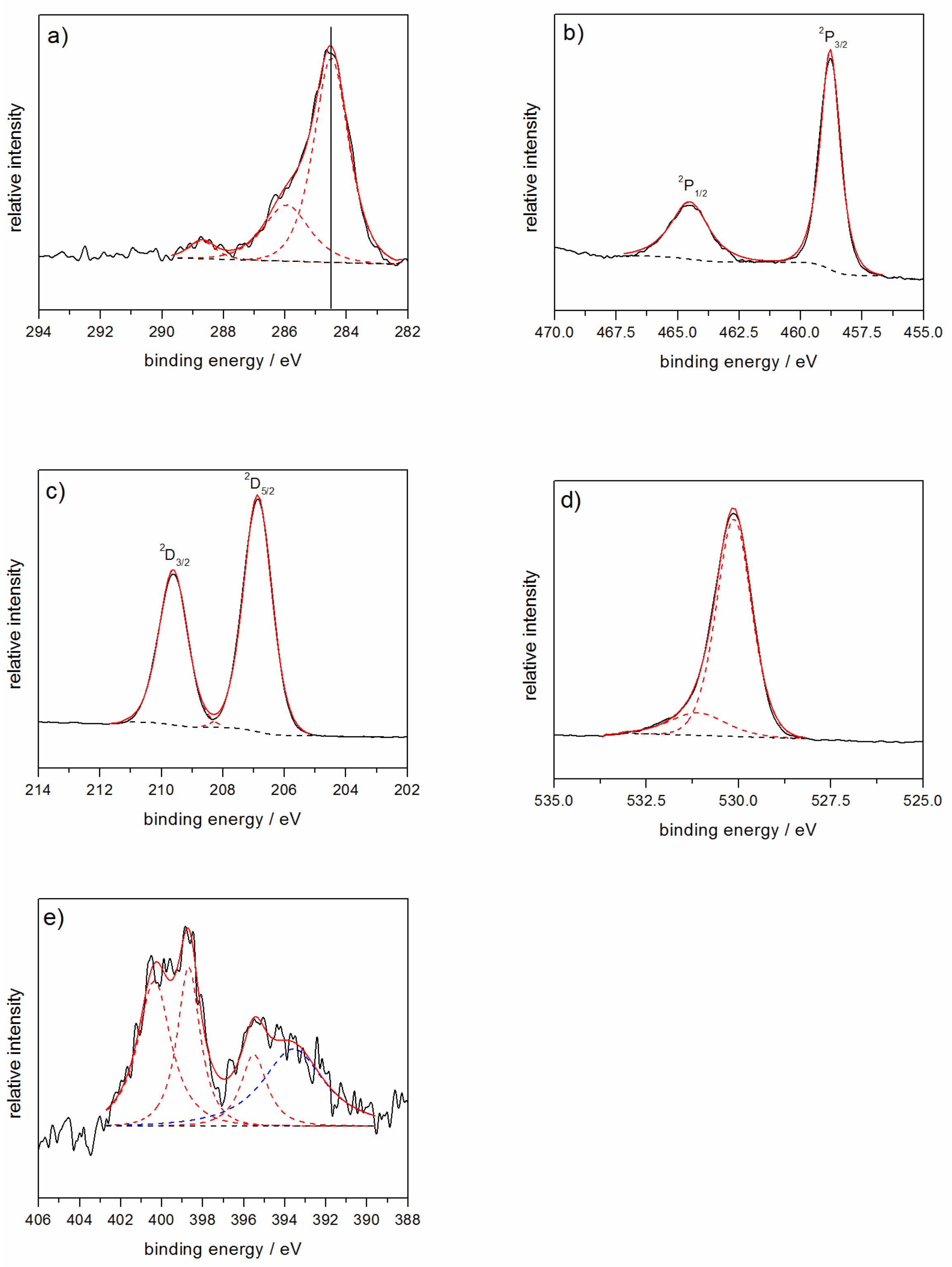

Figure A.15 TiO_2:(Nb,N)-**2** core XPS spectra for a) C(1s), b) Ti(2p), c) Nb(3d), d) O(1s), and e) N(1s).

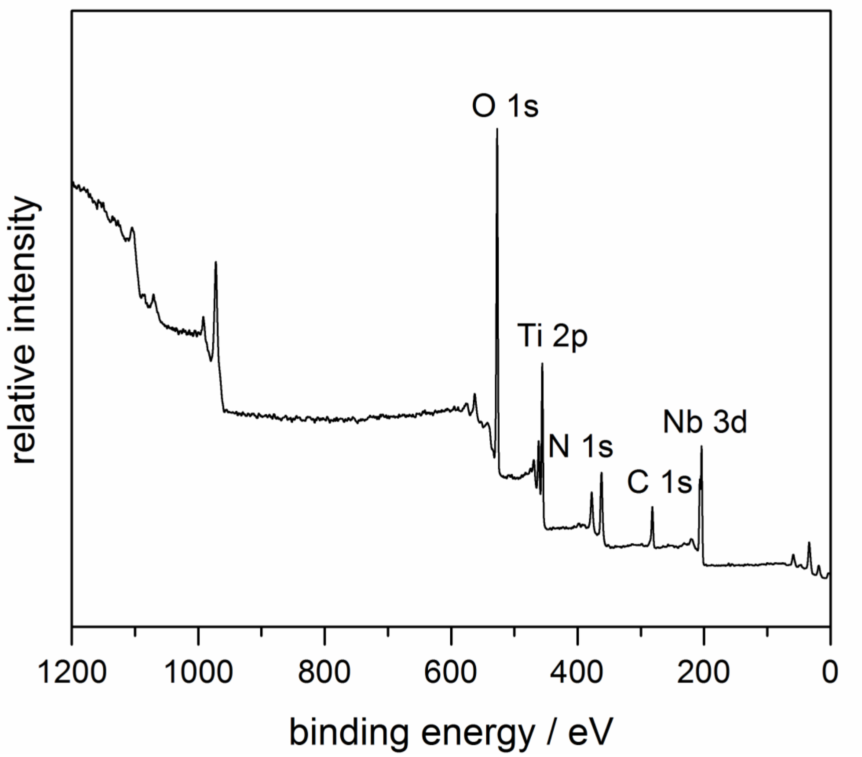

Figure A.16 XP survey scan for TiO_2:(Nb,N)-**3**.

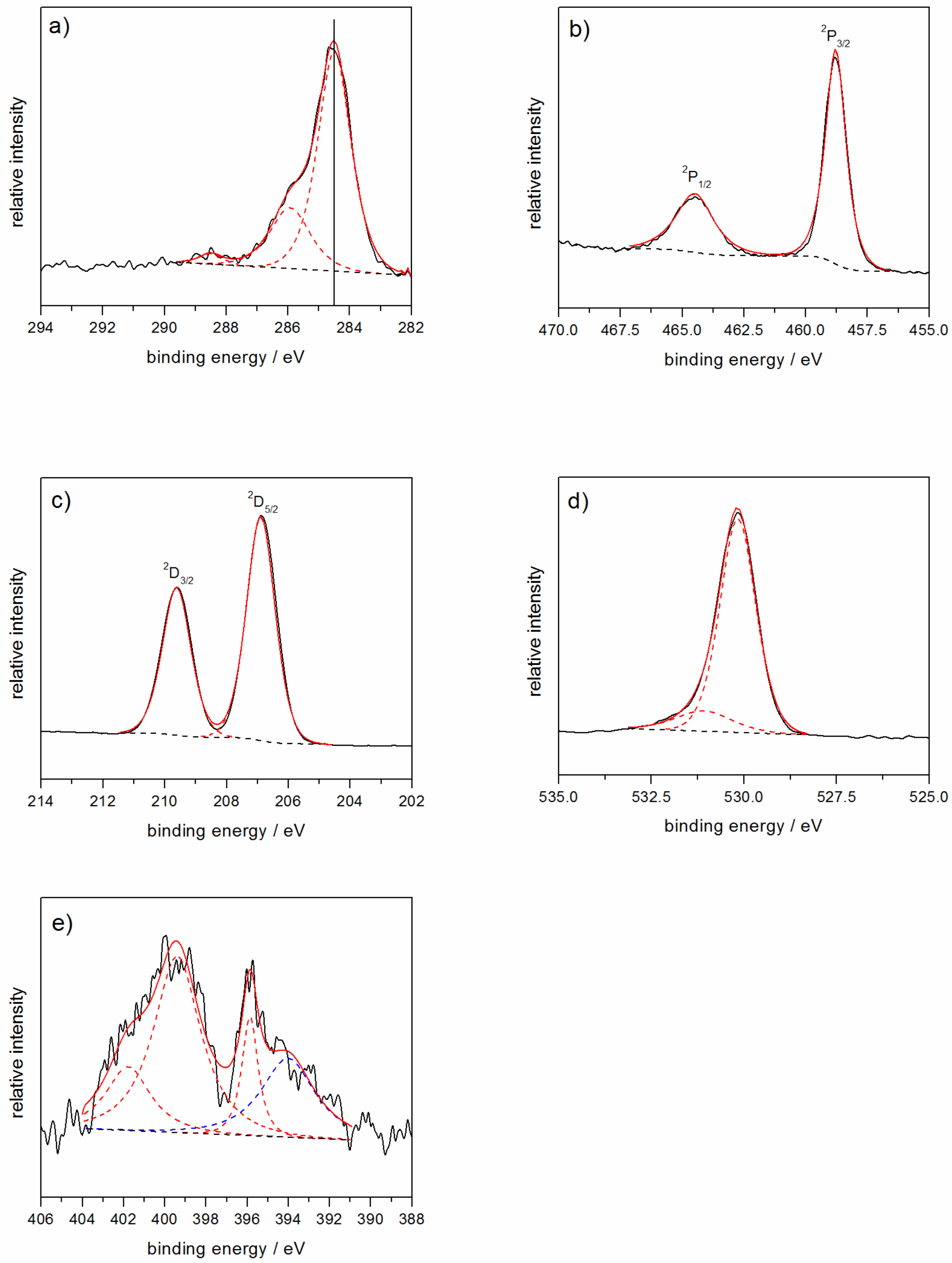

Figure A.17 TiO_2:(Nb,N)-**3** core XPS spectra for a) C(1s), b) Ti(2p), c) Nb(3d), d) O(1s), e) N(1s).

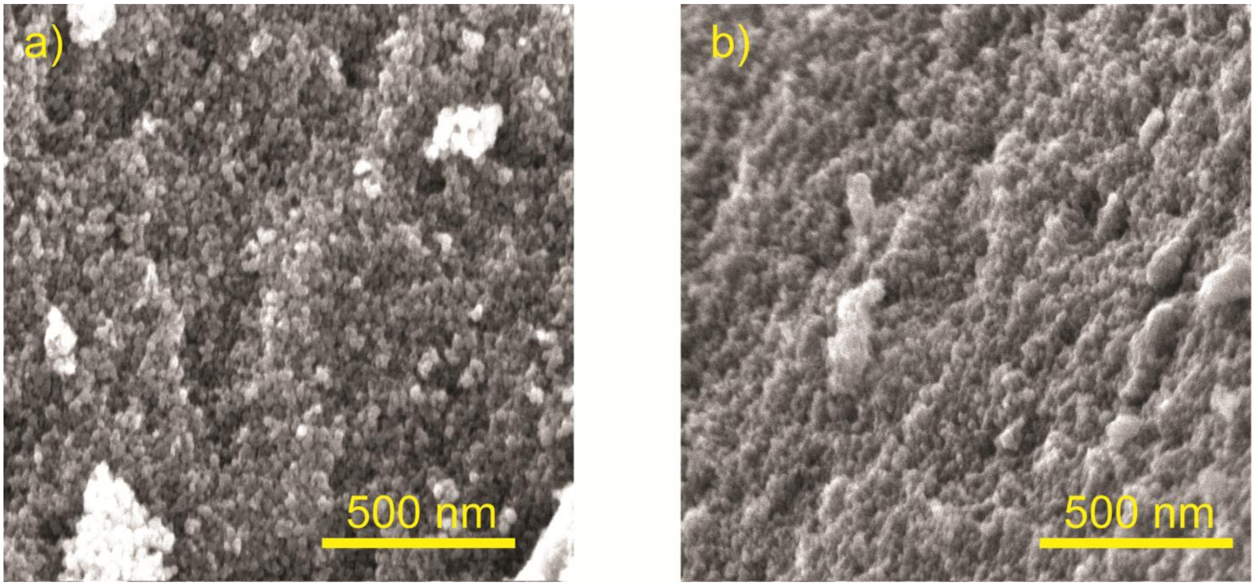

Figure A.18 SEM images of a) TiO_2:(Nb,N)-**2**, and b) TiO_2:(Nb,N)-**3**.

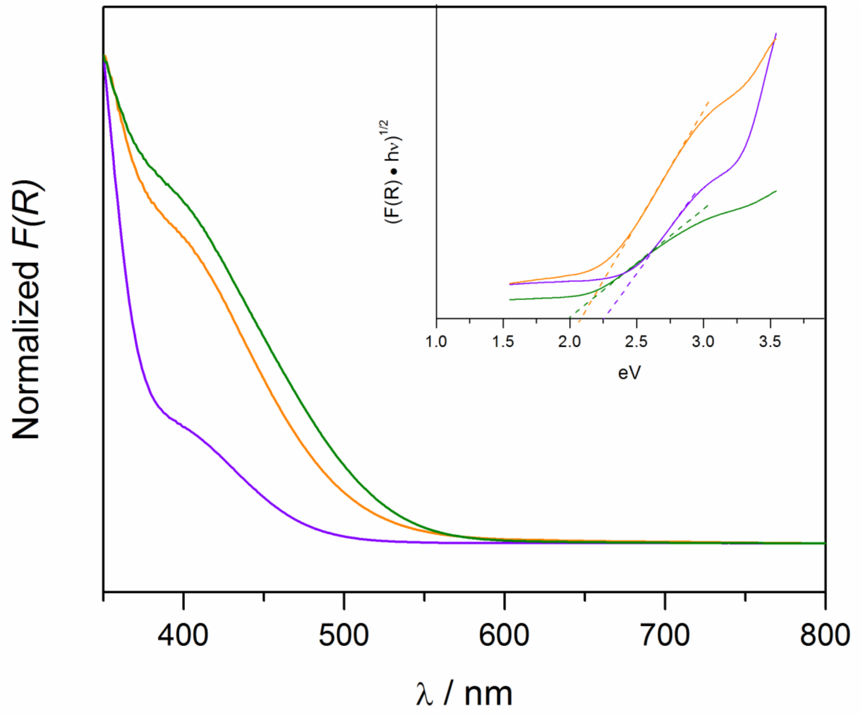

Figure A.19 UV-Vis spectra of TiO_2:(Nb,N)-**1** (green),TiO_2:(Nb,N)-**2** (violet), and TiO_2:(Nb,N)-**3** (orange). **Inset**. Tauc plots for each compound showing indirect band gaps.

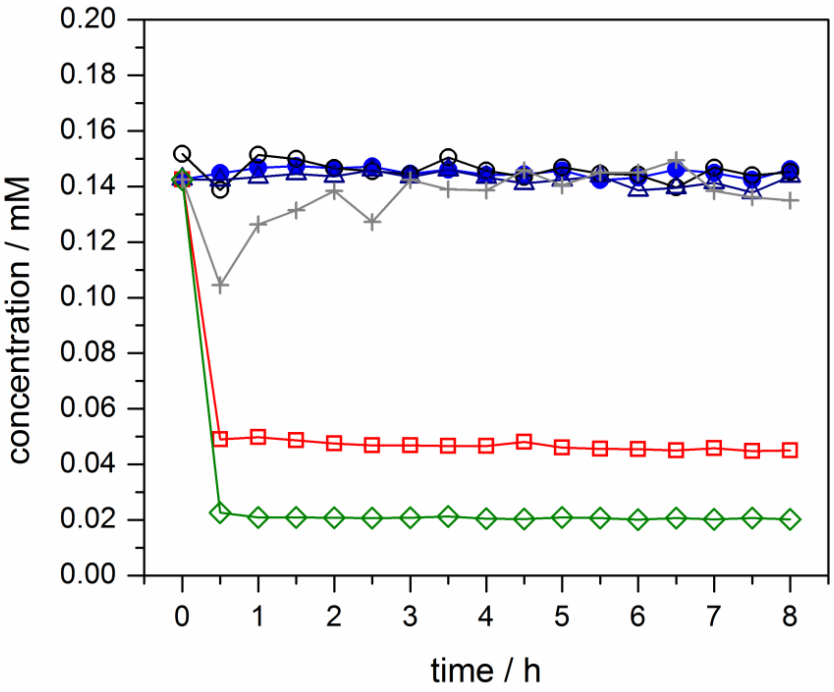

Figure A.20 Dark equilibrium adsorption isotherms of 40 ppm MB for control 40 ppm MB (●), TiO_2 (○), TiO_2:N (Δ), Degussa P-25 (+), TiO_2:Nb (□) and TiO_2:(Nb,N)-**1** (◊).

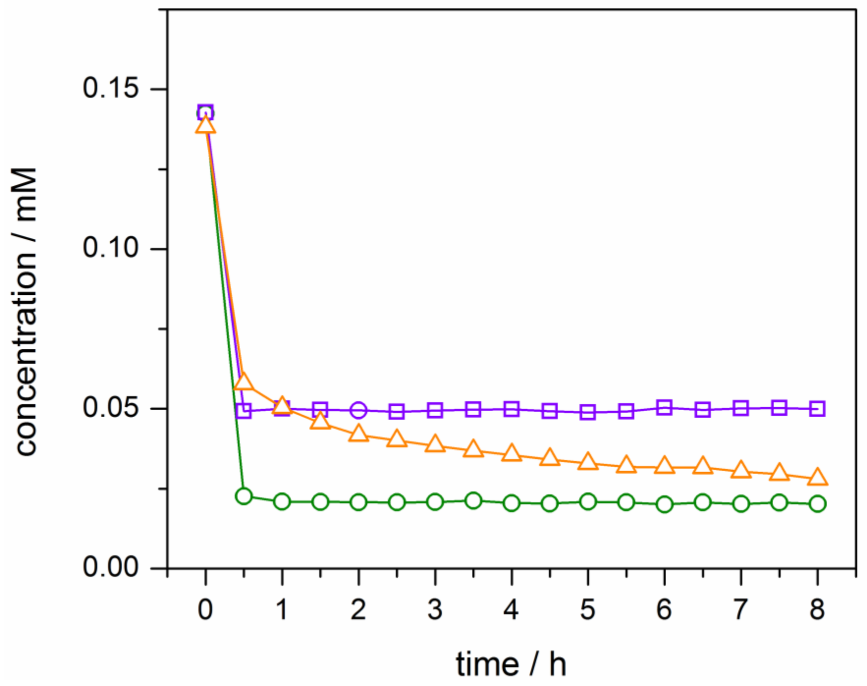

Figure A.21 Dark equilibrium adsorption isotherms of 40 ppm MB for TiO_2:(Nb,N)-**1** (○), TiO_2:(Nb,N)-**2** (□), and TiO_2:(Nb,N)-**3** (Δ).

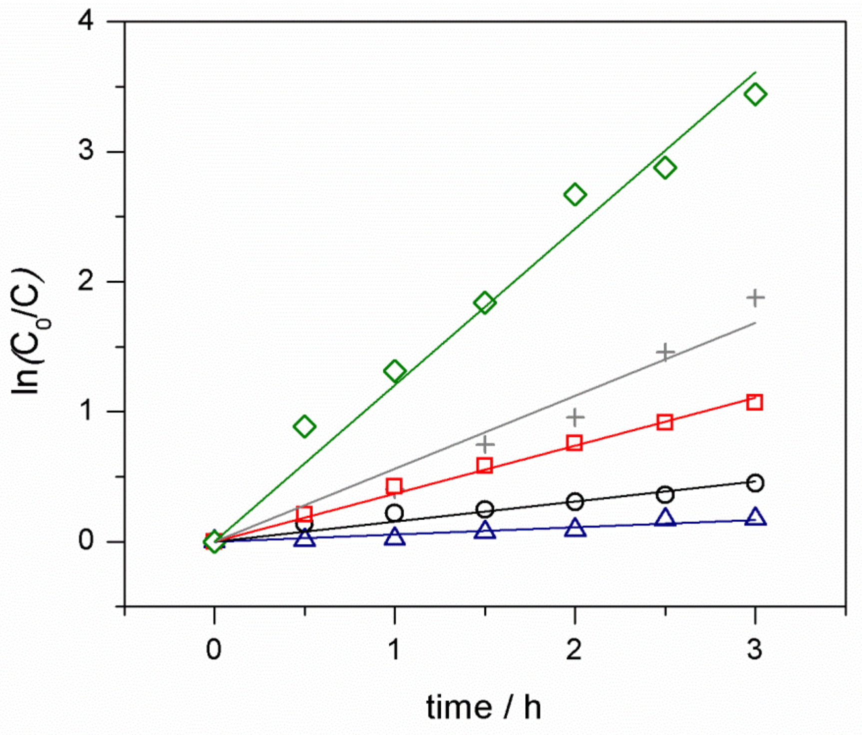

Figure A.22 Pseudo-first-order kinetics for TiO_2:(Nb,N)-**1** (◊), Degussa P-25 (+), TiO_2:Nb (□), TiO_2 (○), and TiO_2:N (Δ).

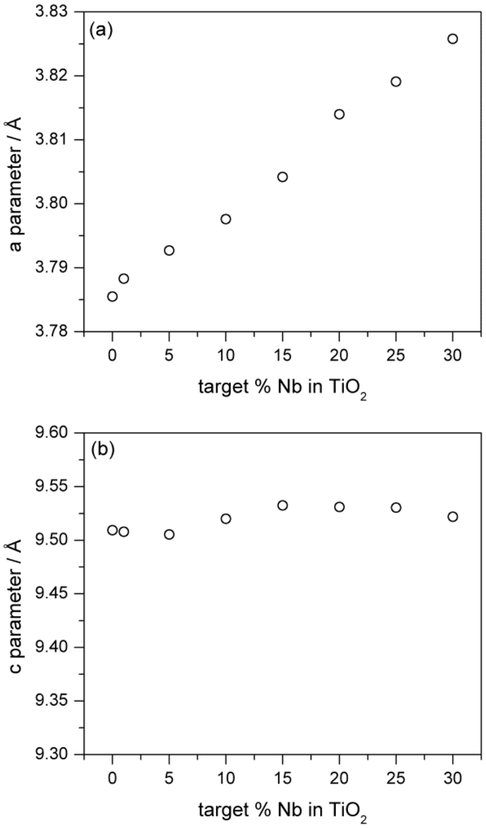

Figure A.23 X-ray diffraction refined lattice parameters for NbN-*x* compounds: a) *a* parameter and b) *c* parameter.

Table A.2 EDX ratios for NbN-*x* compounds. Spectra were recorded on five different spots within a sample. The mean and standard deviation is reported for the series.

target % Nb	target Ti:Nb	mean Ti:Nb
1	99	123.34 ± 9.11
5	19	23.94 ± 0.72
10	9	10.98 ± 0.81
15	5.67	7.01 ± 0.09
20	4	4.35 ± 0.13
25	3	3.06 ± 0.19
30	2.33	2.31 ± 0.02

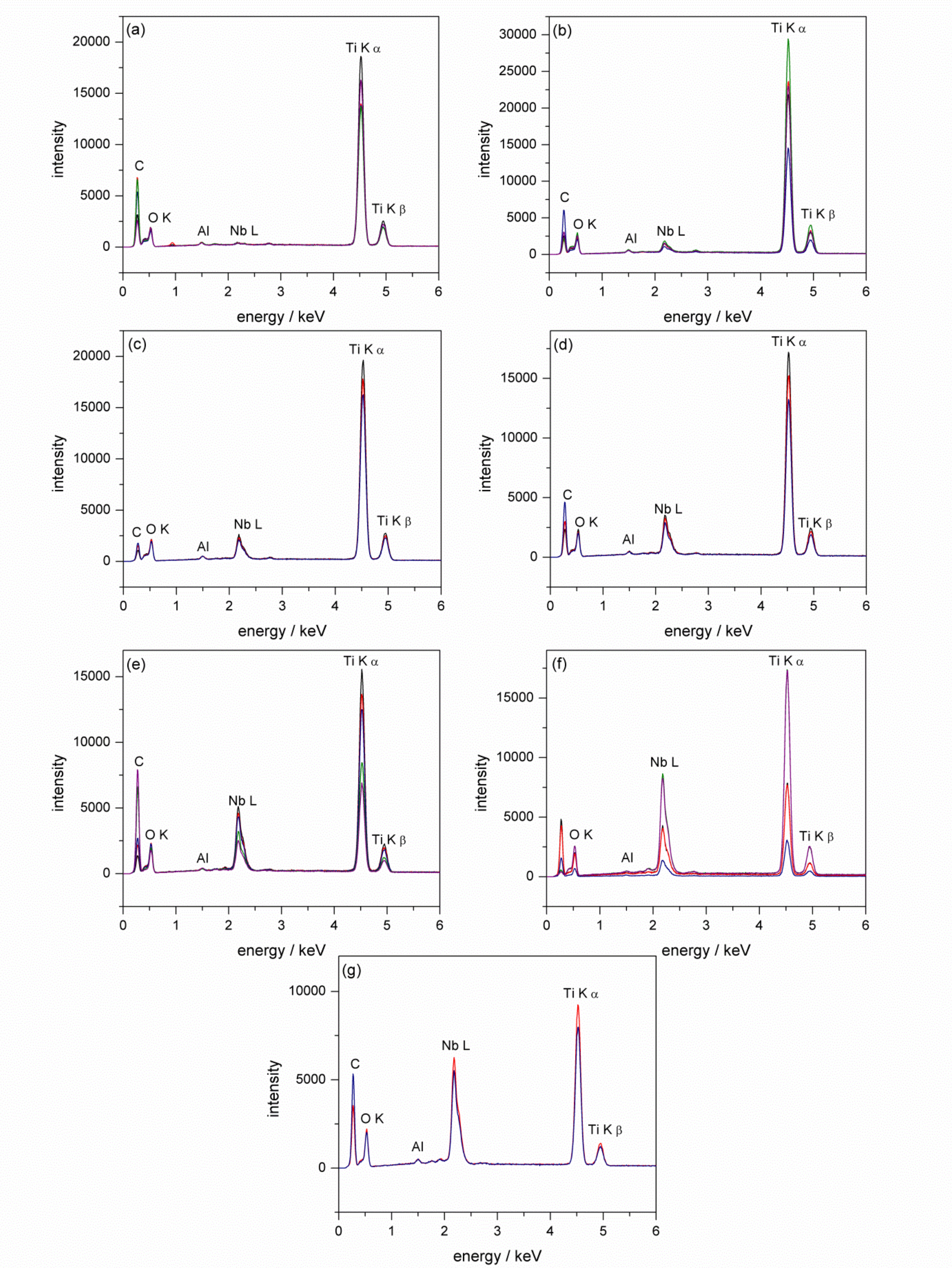

Figure A.24 EDX spectra overlaid for NbN-*x* compounds (a) NbN-1, (b) NbN-5, (c) NbN-10, (d) NbN-15, (e) NbN-20, (f) NbN-25, and (g) NbN-30. The Al peak arises from the sample holder.

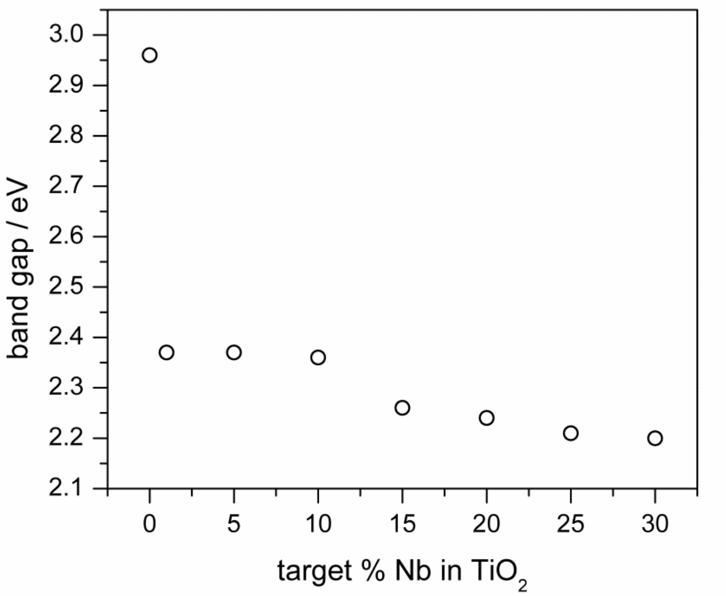

Figure A.25 Band gap vs. target % Nb in co-alloyed compounds

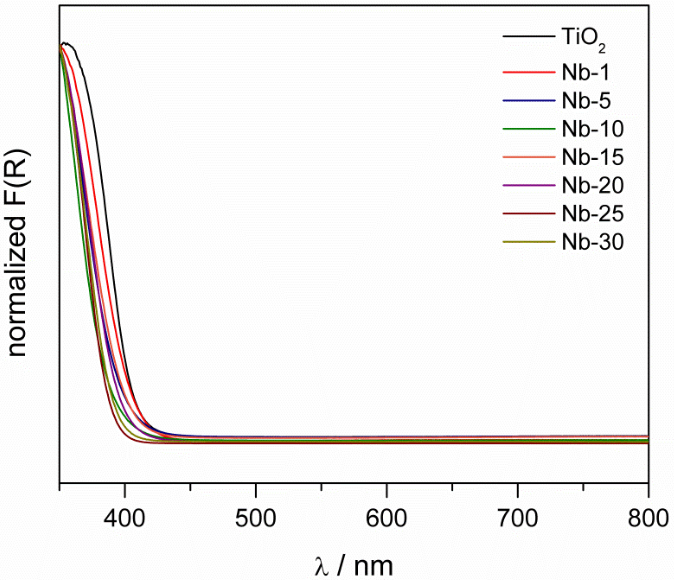

Figure A.26 Diffuse reflectance spectroscopy of mono alloyed compounds.

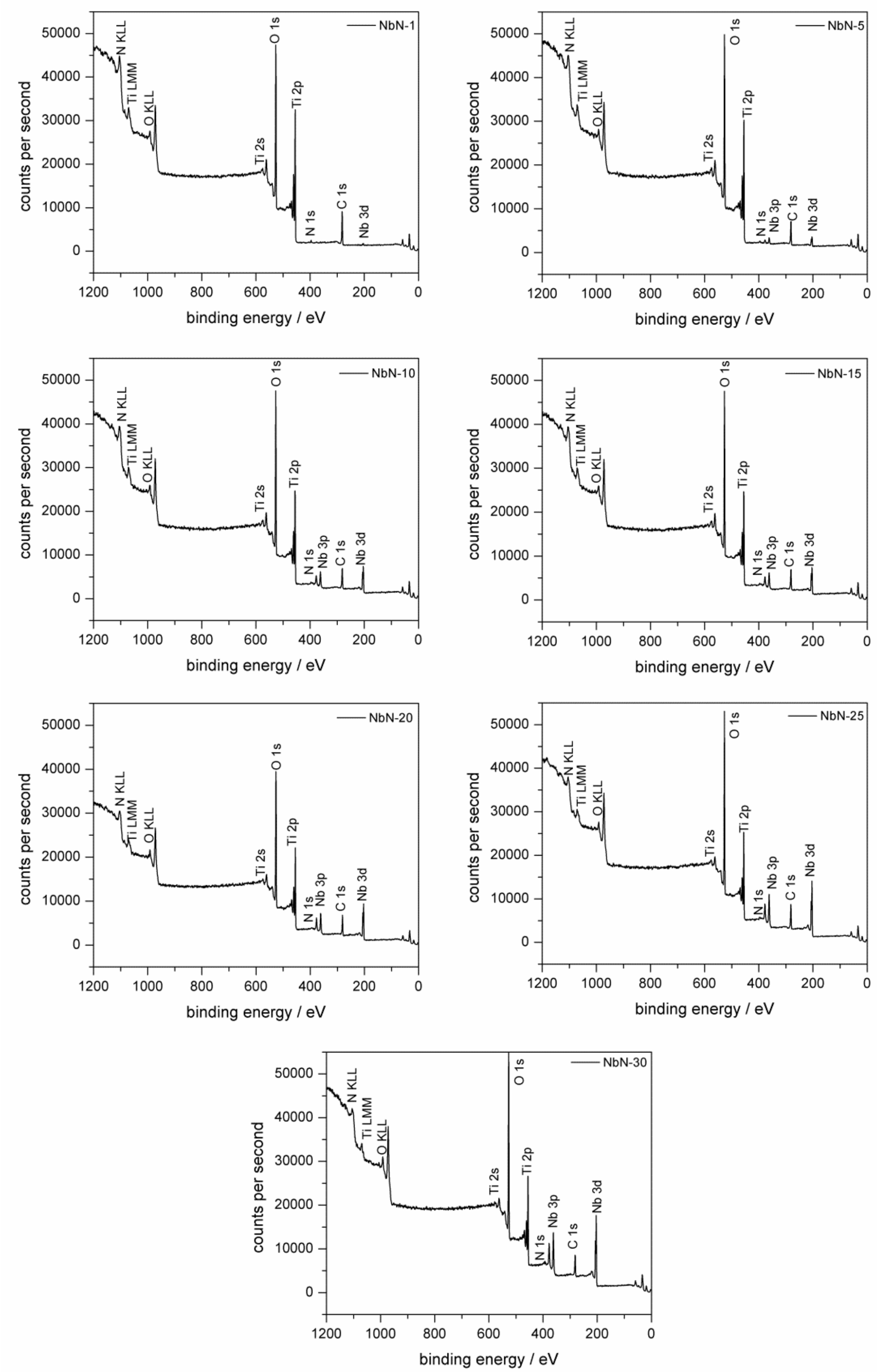

Figure A.27 XP spectra survey scans for NbN-*x* series.

Table A.3 XP binding energies (eV) for Ti(2p) and O(1s) for NbN-*x* series.

compound	Ti($2p_{3/2}$)	Ti($2p_{1/2}$)	O(1s)
Pure TiO_2[a]	459.10	*not reported*	530
NbN-1	458.34	464.05	529.63
NbN-5	458.57	464.26	529.87
NbN-10	458.64	464.35	529.95
NbN-15	458.62	464.34	529.98
NbN-20	458.68	464.36	530.03
NbN-25	458.68	464.40	530.05
NbN-30	458.75	464.47	530.13

[a] value from literature. (Saha, N.; Tompkins, H. *J. Appl. Phys*. **1992**, *7*, 3072-3079)

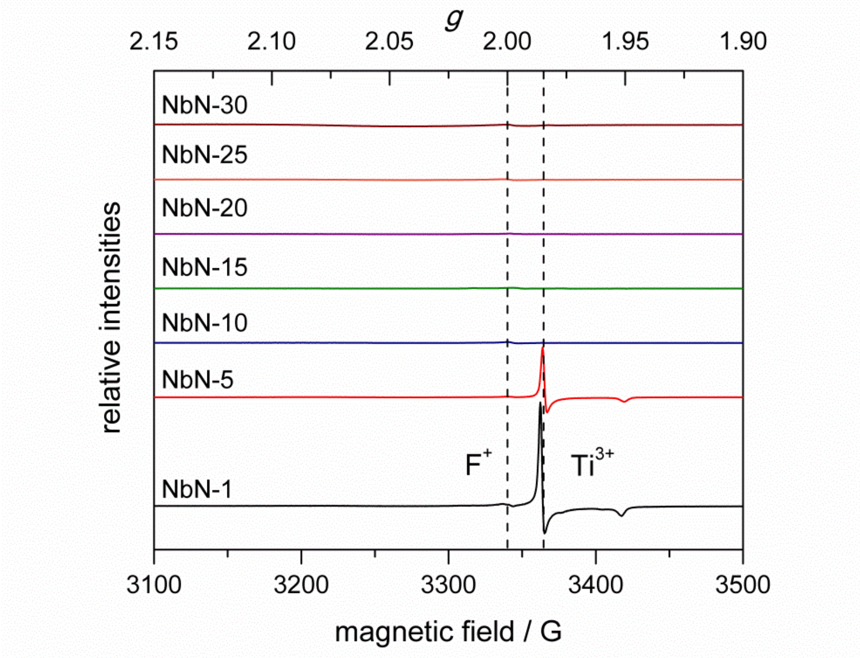

Figure A.28 Electron paramagnetic resonance spectra for NbN-*x* series (4 K).

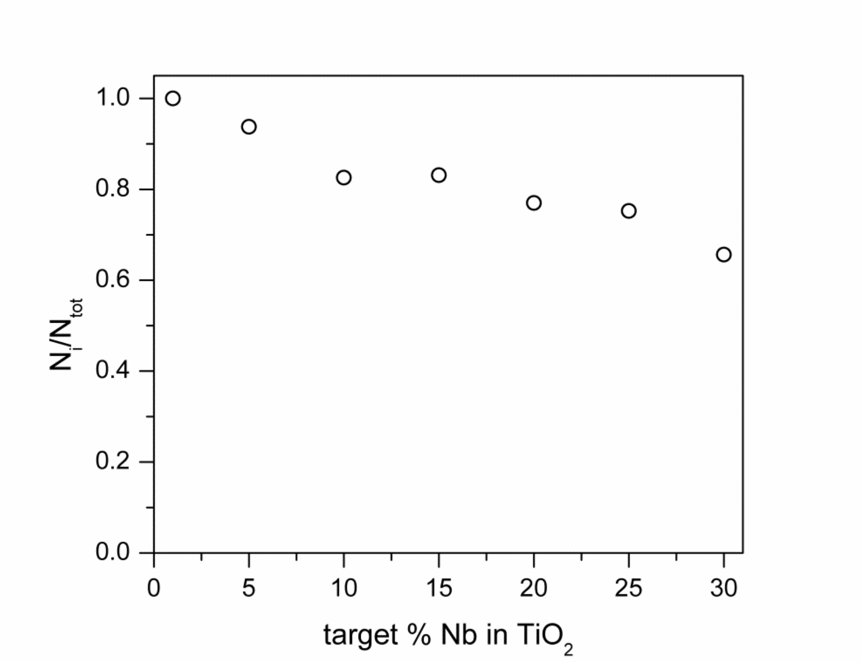

Figure A.29 N_i/N_{tot} for NbN-*x* series.

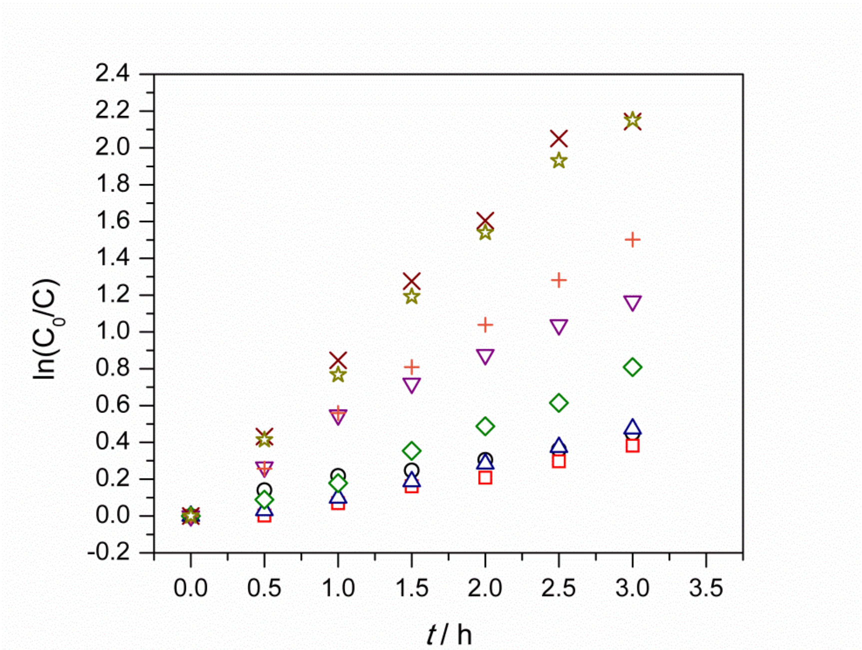

Figure A.30 Rates for NbN-*x* compounds Nb-25 (○), NbN-1 (□), NbN-5 (△), NbN-10 (◇), NbN-15 (▽), NbN-20 (+), NbN-25 (×), and NbN-30 (☆).

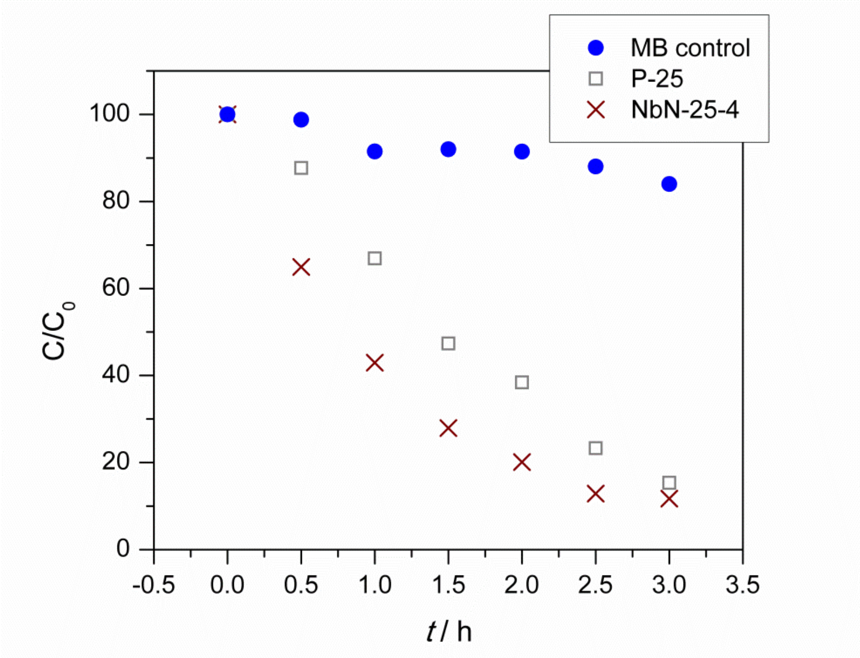

Figure A.31 Methylene blue degradation for 40 ppm MB (●), P-25 (□), and NbN-25-4 (×).

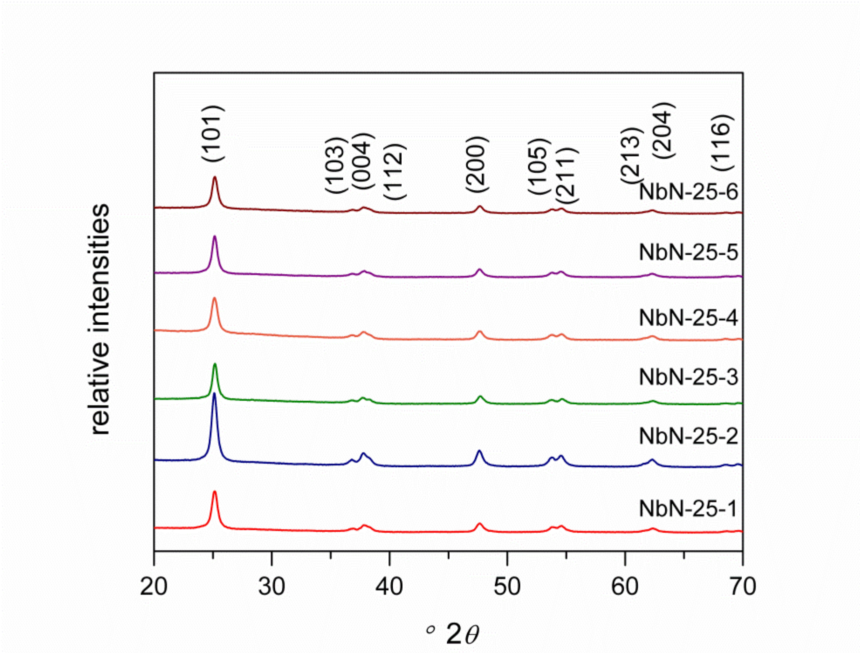

Figure A.32 X-ray diffraction patterns for NbN-25-*z* annealed under ammonia for various times.

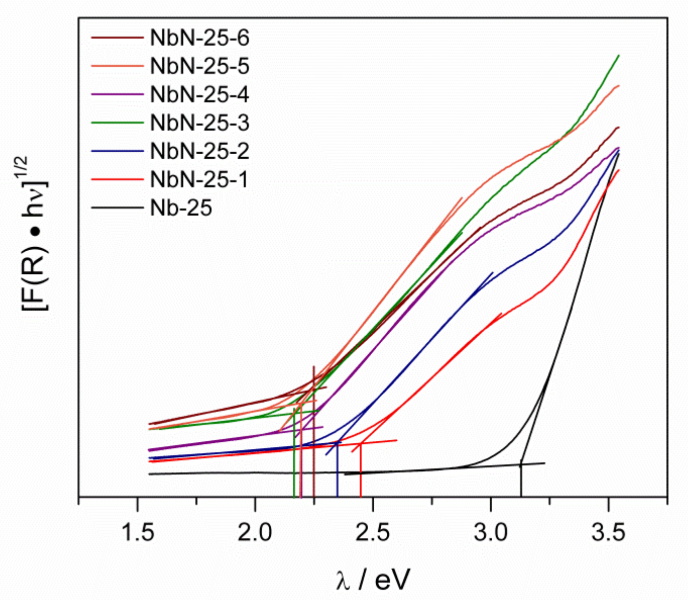

Figure A.33 Indirect tauc plots for NbN-25-*z* annealed under ammonia for various times.

Table A.4 Indirect band gap values for NbN-25-z annealed under flowing NH_3 (110 mL/ min, 2 hour ramp, 6 hour cool) for various dwell times (*z*).

Hours annealed (*z*)	Band gap / eV
Nb-25	3.13
1	2.45
2	2.35
3	2.17
4	2.19
5	2.20
6	2.25

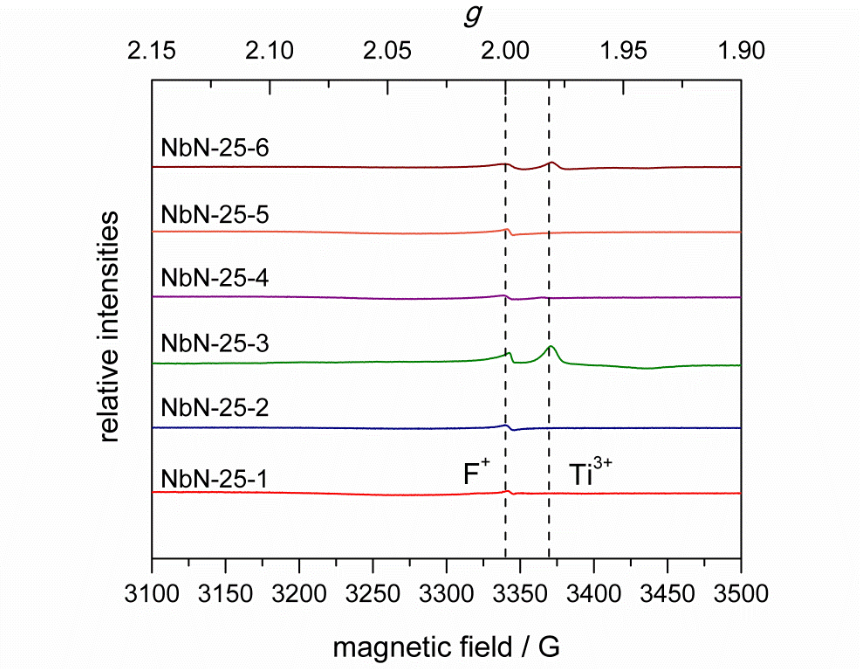

Figure A.34 EPR spectra of NbN-25-*z* series, where *z* = 1 – 6 hours, depicted from bottom to top.

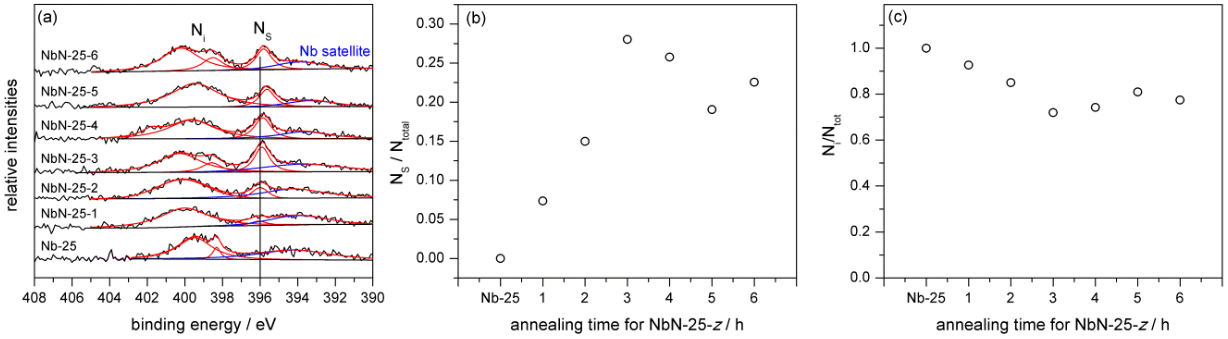

Figure A.35 (a) N(1s) spectra for NbN-25-*z* series, (b) N_S / N_{total} vs. annealing time, and (c) N_i / N_{total} vs. annealing time .

Table A.5 Ti(2p) and O(1s) deconvoluted binding energies (eV) for NbN-25-*z* compounds.

compound	Ti(2p$_{3/2}$)	Ti(2p$_{1/2}$)	O(1s)
Pure TiO_2[a]	459.10	*not reported*	530.00
NbN-25-1	458.71	464.44	530.08
NbN-25-2	458.72	464.46	530.05
NbN-25-3	458.69	464.41	530.03
NbN-25-4	458.57	464.26	529.87
NbN-25-5	458.48	464.19	529.85
NbN-25-6	458.68	464.39	530.06

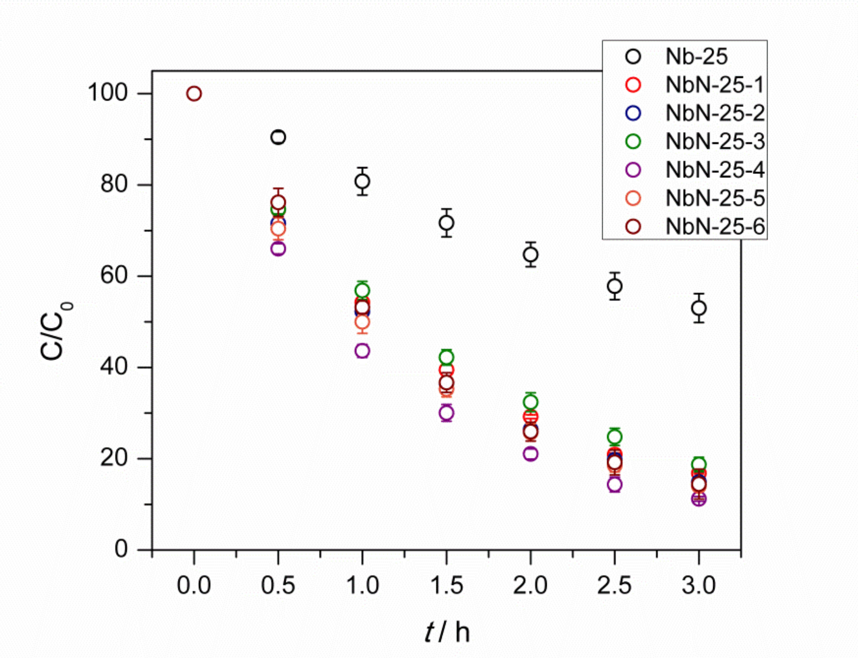

Figure A.36 Degradation profiles for NbN-25-*z* compounds. Each data point and error bar represents the mean and standard errors respectively of independent triplicates. Conditions: C_0 = 40 ppm, 50 mg photocatalyst, 3 hour dark equilibration time, 3 hour illumination by 150 W Xe lamp fitted with AM1.5G filter.

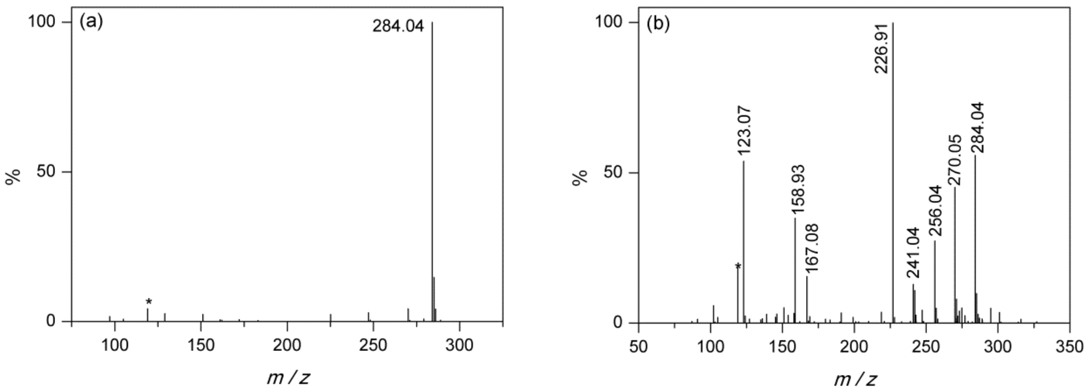

Figure A.37 Mass spectrum for (a) MB solution and (b) NbN-25-4 solution following 3 h irradiation. * *m/z* = 119 is observed in both spectra, due to an impurity or fragmentation of MB.

Table A.6 *m/z* assignments and molecular structures.

m/z	assignment	molecular structure
284.04	methylene blue	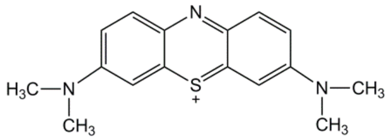
270.05	azure B	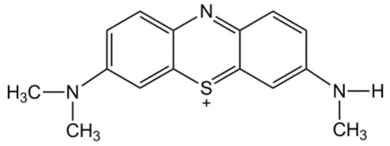
256.04	azure A	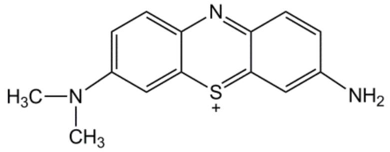
241.04	azure C	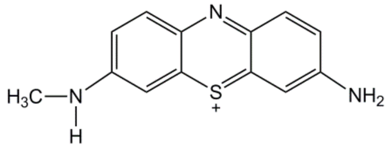
226.91	thionine	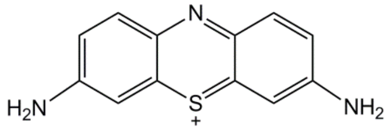
167.08	4-((hydroxymethyl)(methyl)amino) benzene-1,2-diol	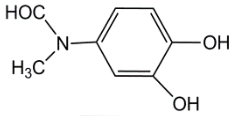
158.93	benzenesulfonic acid	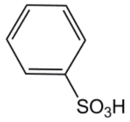
123.07	dimethylaniline	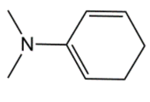

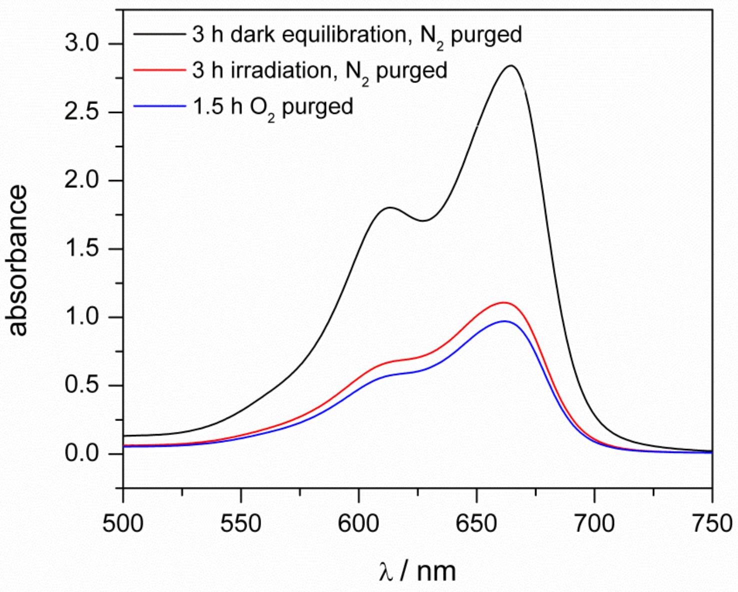

Figure A.38 Absorption spectra for NbN-25-4 in MB (C_0 = 40 ppm) purged with nitrogen for 3 h in the dark (black line), irradiated for 3 h by a 150 W Xe lamp fitted with AM1.5G filter (red line), and purged with oxygen for 1.5 h following N_2 purged reaction (blue line).

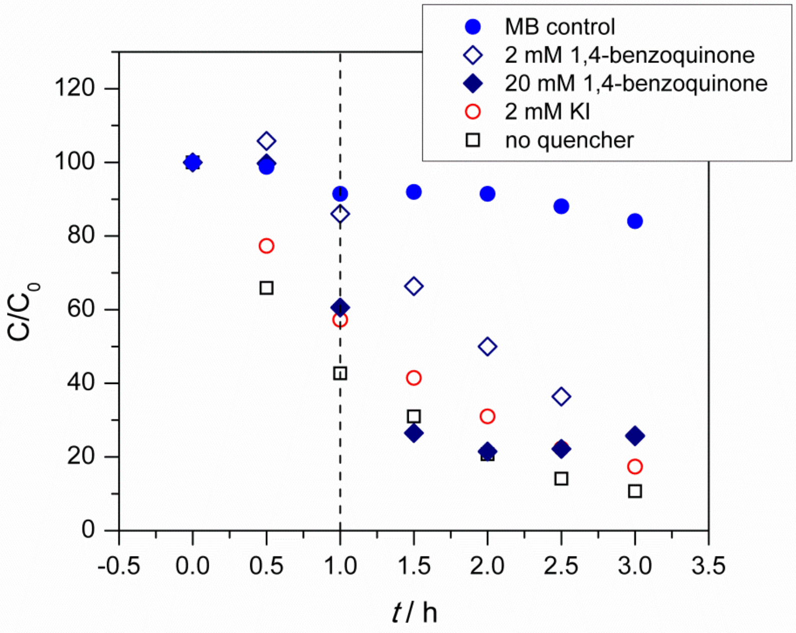

Figure A.39 Degradation profiles for MB 40 ppm AM1.5 filter (●), NbN-25-4 in the presence of: 2 mM BQ (◊), 20 mM BQ (♦), 2 mM KI (○), and no quencher (□).Conditions: C_0 = 40 ppm, 50 mg photocatalyst, 3 hour dark equilibration time, 3 hour illumination by 150 W Xe lamp fitted with AM1.5 filter.

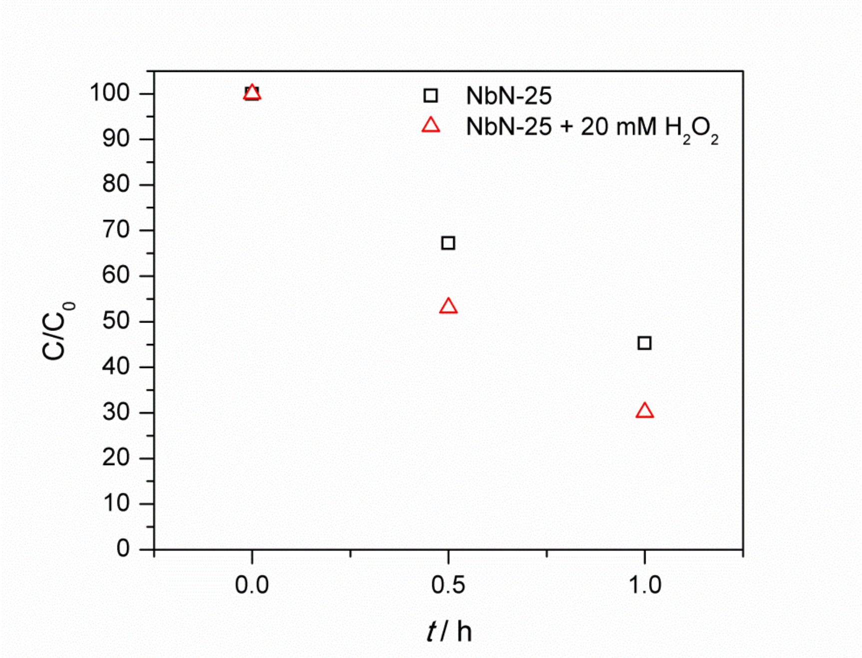

Figure A.40 Degradation profiles for MB 40 ppm with NbN-25-4 in the presence of: no additive (□) and 20 mM H_2O_2 (Δ).Conditions: C_0 = 40 ppm, 50 mg photocatalyst, 3 hour dark equilibration time, 1 hour illumination by 150 W Xe lamp fitted with AM1.5 filter.

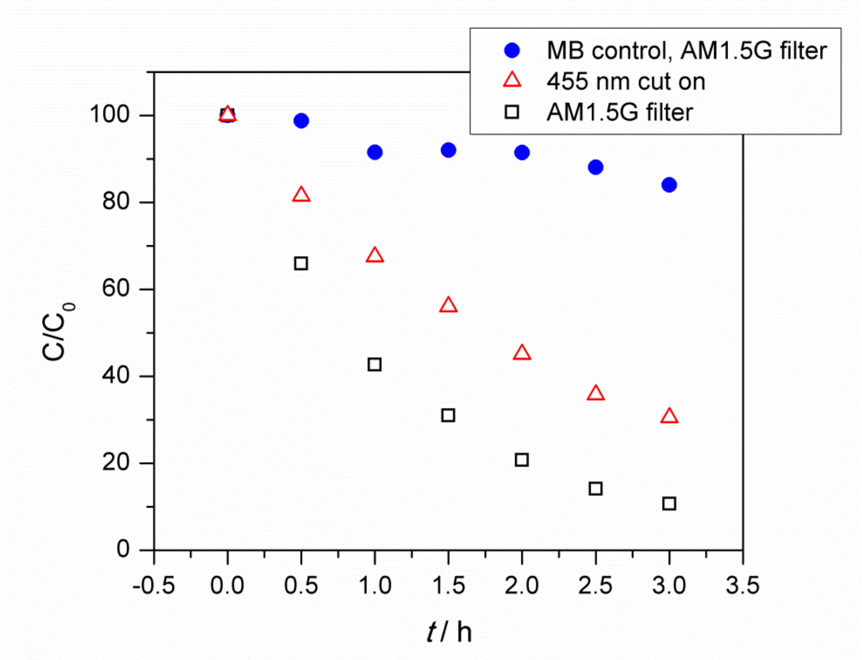

Figure A.41 Degradation profiles for MB 40 ppm AM1.5 filter (●), NbN-25-4 455 nm cut on (Δ), and NbN-25-4 AM1.5 filter (□). Conditions: C_0 = 40 ppm, 50 mg photocatalyst, 3 hour dark equilibration time, 3 hour illumination by 150 W Xe lamp fitted with appropriate filter.

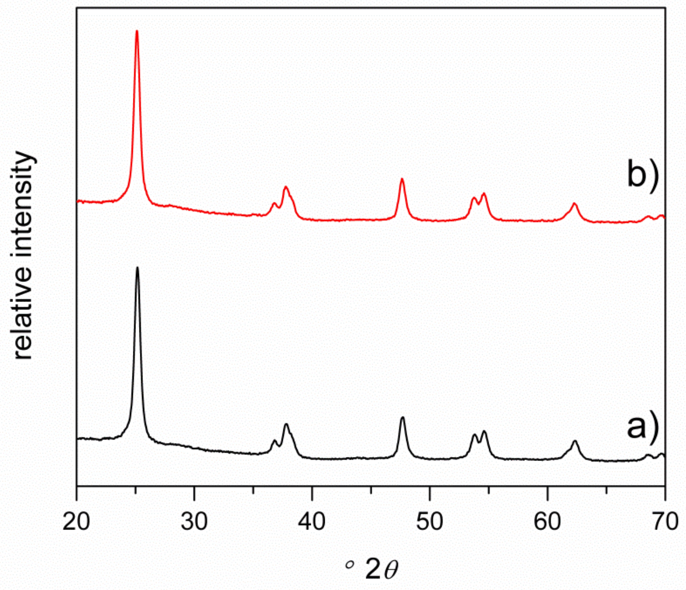

Figure A.42 XRD patterns of a) NbN-25 and b) NbN-25 loaded with 1 wt % RuO_2.

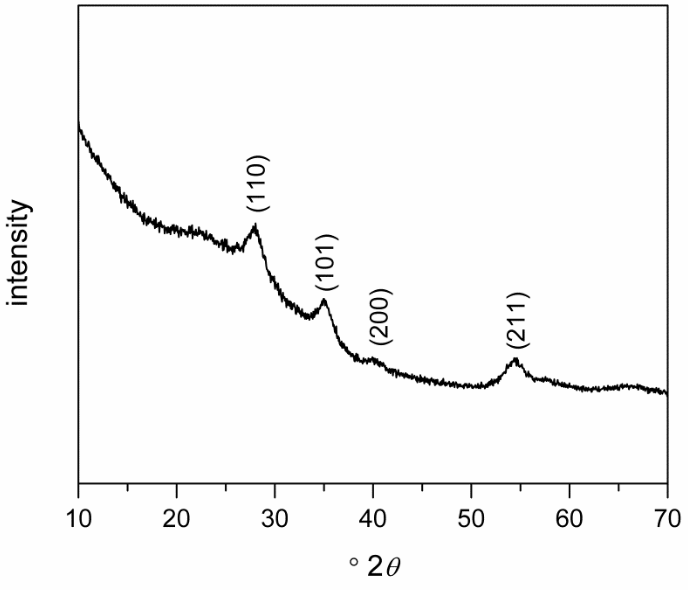

Figure A.43 XRD pattern of RuO_2 annealed at 350 °C for 1 hour (JCPDF 70-2662).

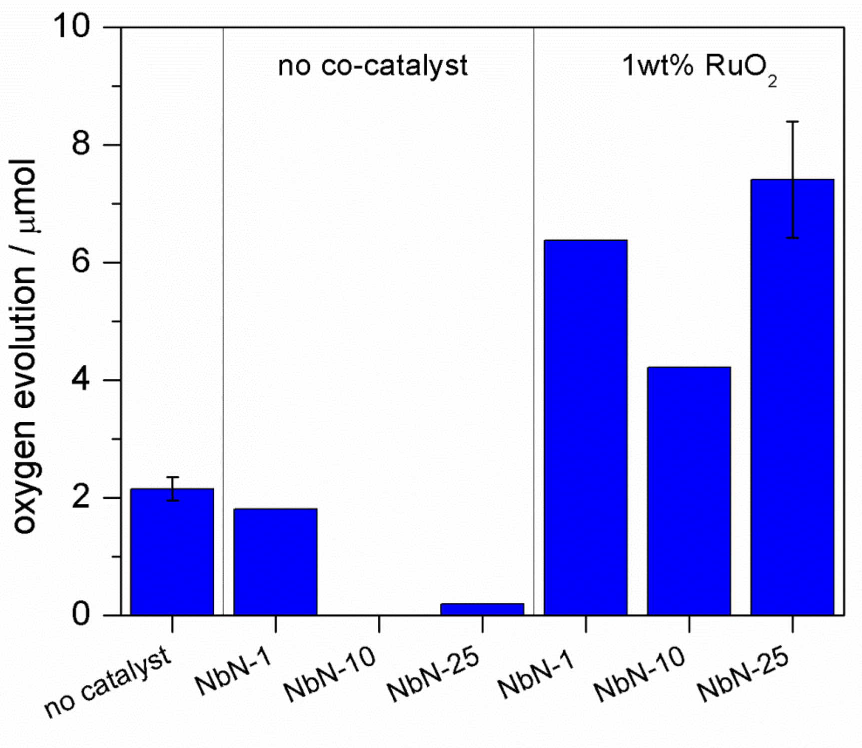

Figure A.44 Oxygen evolution after 3 hours for co-alloyed compounds loaded with and without 1 wt% RuO_2.

Appendix B. Characterization Data for Complex Metal Titanates (Chapter 4)

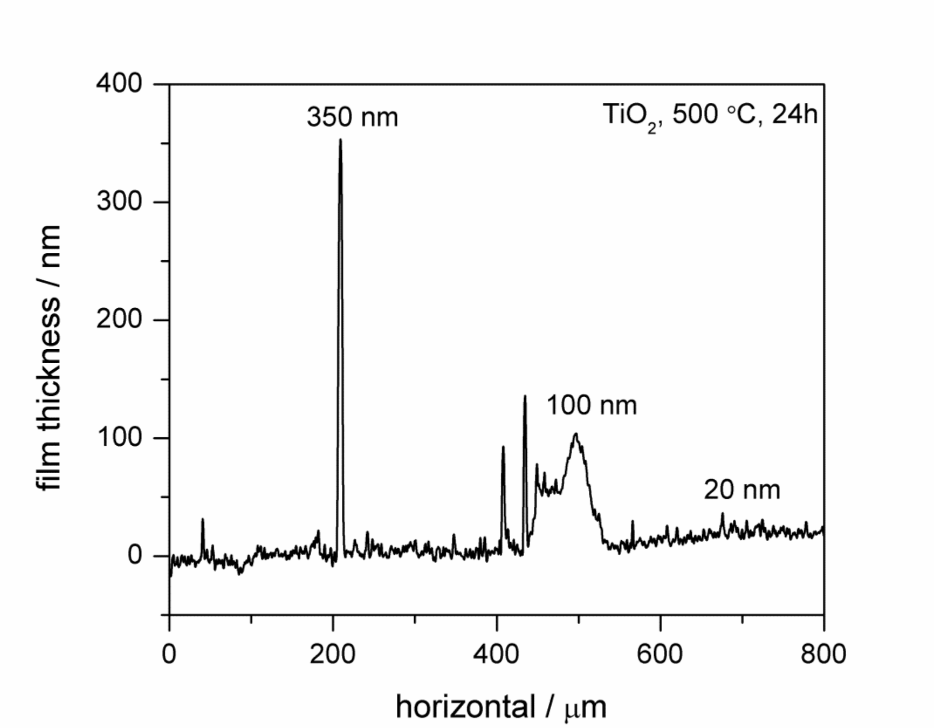

Figure B.1 Profilometry profile for TiO_2 annealed at 500 C for 24h. Film height ~ 20 nm, with thicker edges of 100- 350 nm.

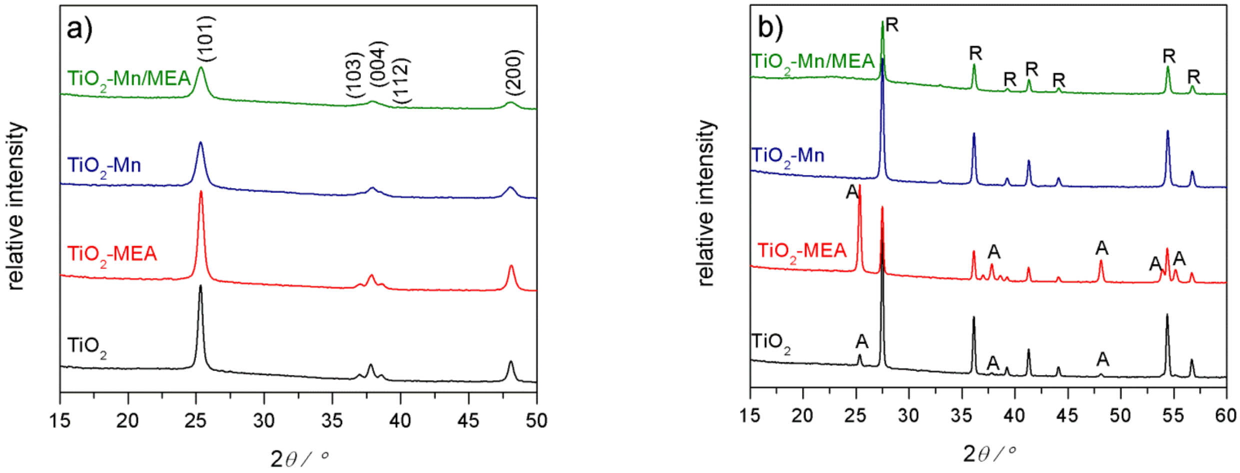

Figure B.2 X-ray diffraction patterns for various TiO_2 solutions annealed in alumina crucibles in air at a) 500 °C and b) 650 °C.

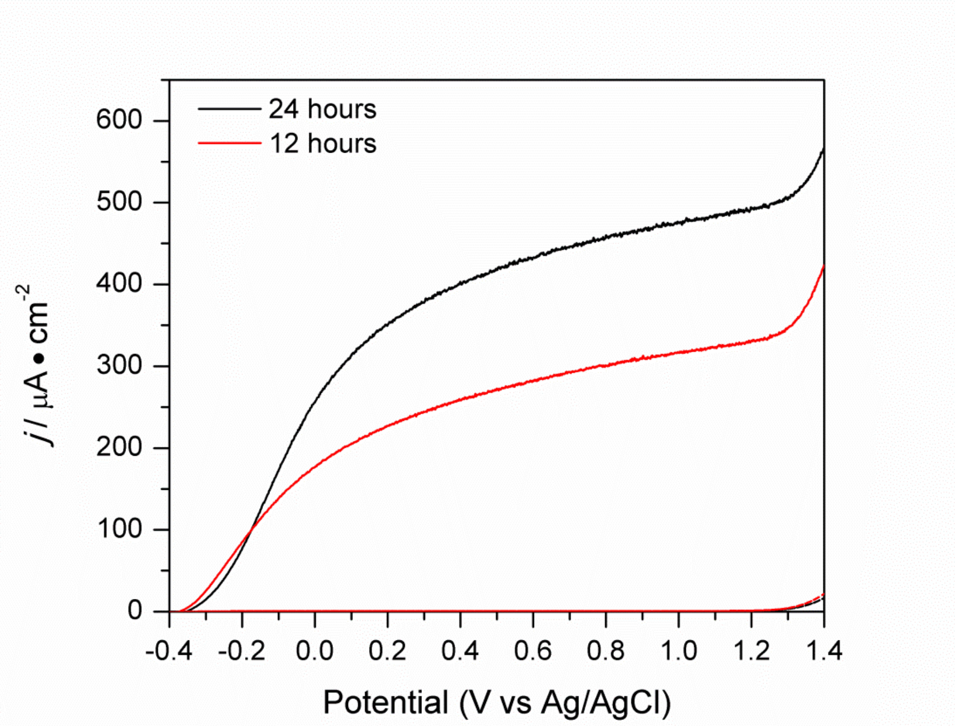

Figure B.3 LSV for TiO_2 annealed at 650 °C for 24 hours (black) and 12 hours (red). Conditions: 0.1M KP_i buffer, pH 7, 150 W Xe lamp with AM1.5 filter, 100 mW/cm^2.

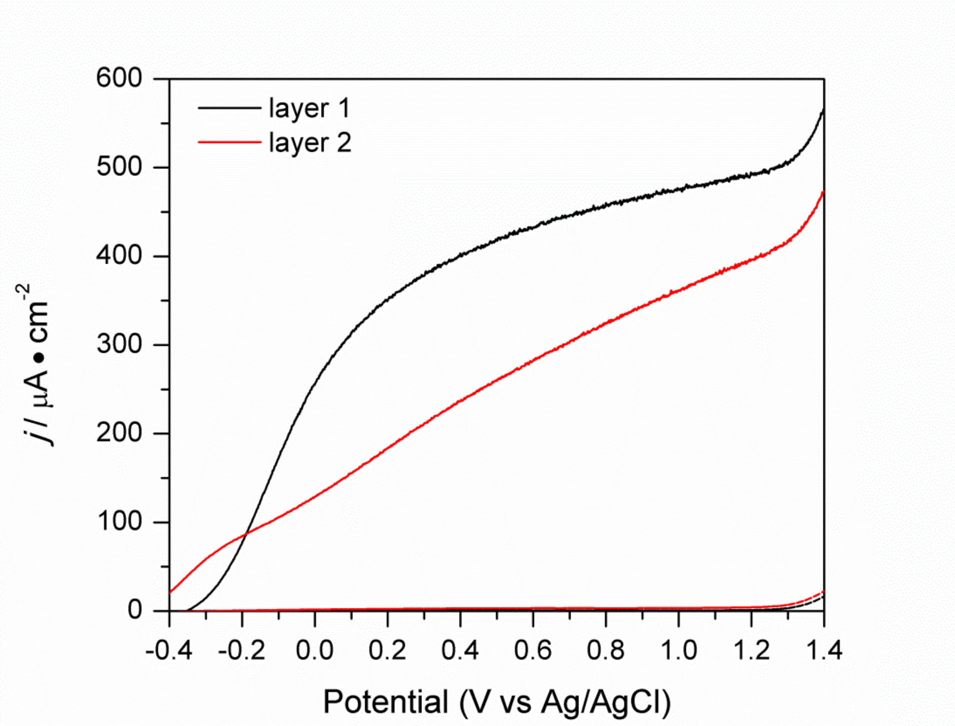

Figure B.4 LSV of TiO_2 annealed under N_2 for 24 hours at 650 °C with 1 layer (black) and 2 layers (red). Conditions: 0.1M KP_i buffer, pH 7, 150 W Xe lamp with AM1.5 filter, 100 mW/cm^2.

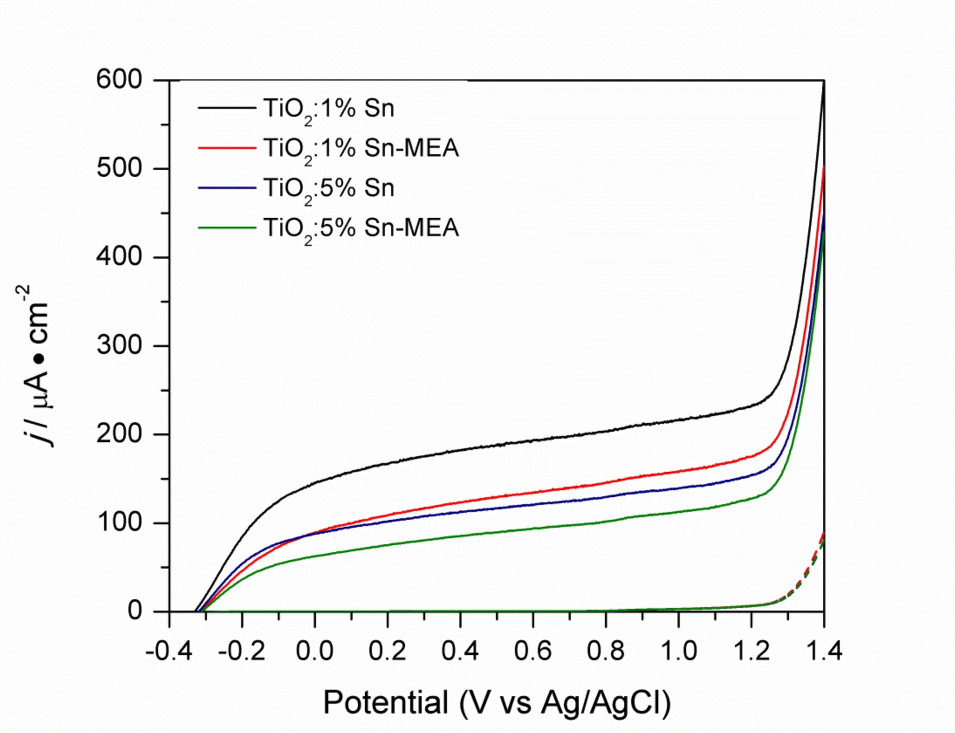

Figure B.5 LSV of TiO_2 with various mole-percent Sn^{4+} in sol-precursor solution; annealed under N_2 for 24 hours at 650 °C Conditions: 0.1M KP_i buffer, pH 7, 150 W Xe lamp with AM1.5 filter, 100 mW/cm^2.

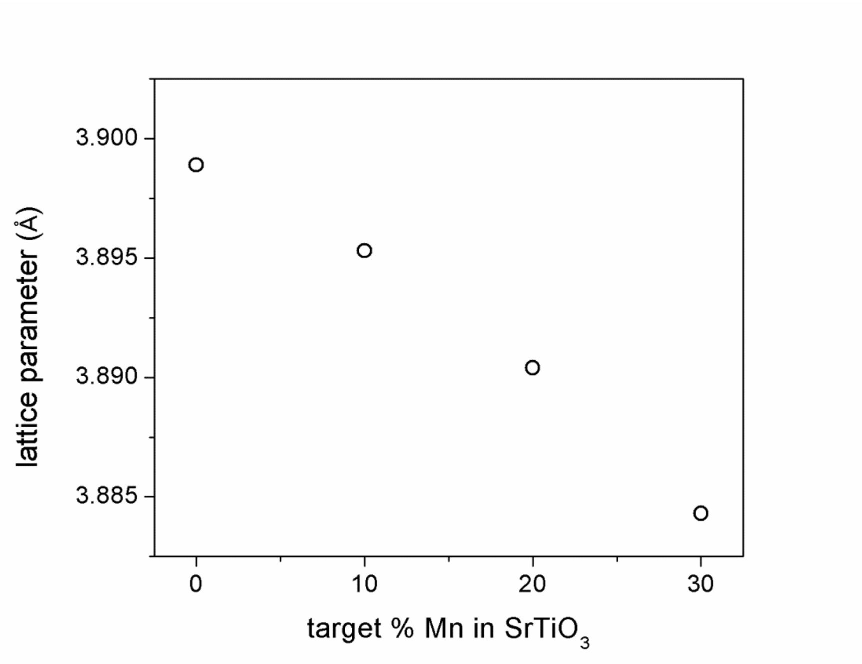

Figure B.6 Refined lattice parameters for $SrTi_{1-x}Mn_xO_3$ powders annealed from starting solution used to spin coat thin films.

Table B.1 Lattice parameters of $SrTi_{1-x}Mn_xO_3$ compounds (obtained from XRD of powders).

Compound	Lattice parameter (Å)
$SrTiO_3$	3.8989
$SrTi_{0.9}Mn_{0.1}O_3$	3.8953
$SrTi_{0.8}Mn_{0.2}O_3$	3.8904
$SrTi_{0.7}Mn_{0.3}O_3$	3.8840

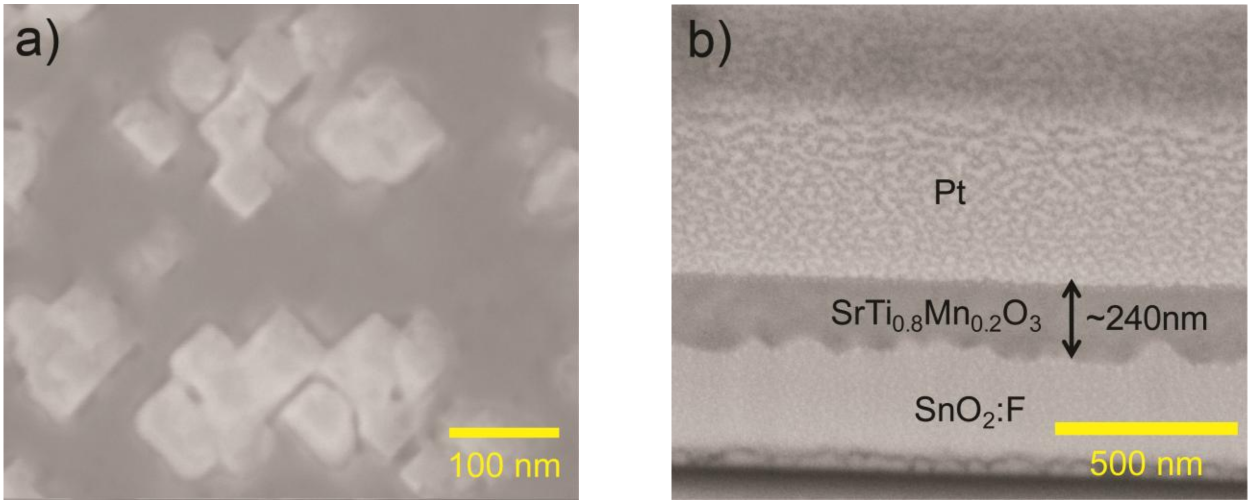

Figure B.7 SEM images of $SrTi_{0.8}Mn_{0.2}O_3$ a) top down and b) cross sectional using FIB milling.

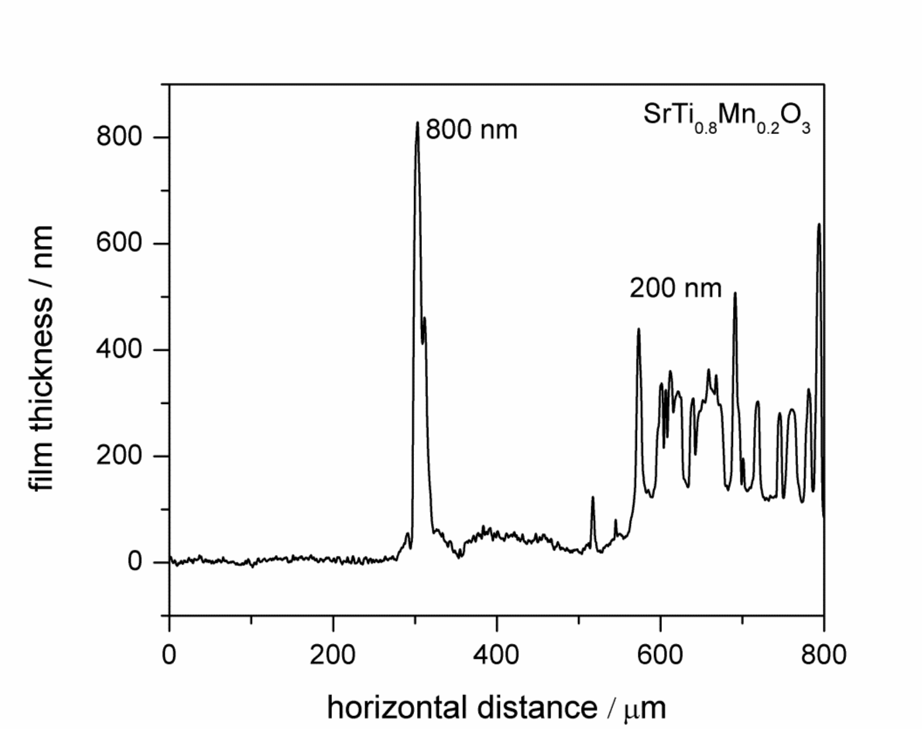

Figure B.8 Profilometry profile for one layer of $SrTi_{0.8}Mn_{0.2}O_3$ annealed on FTO, yielding ~ 200 nm film, consistent with STEM and SEM milling results. Surface is very rough, also observed through use of an optical microscope.

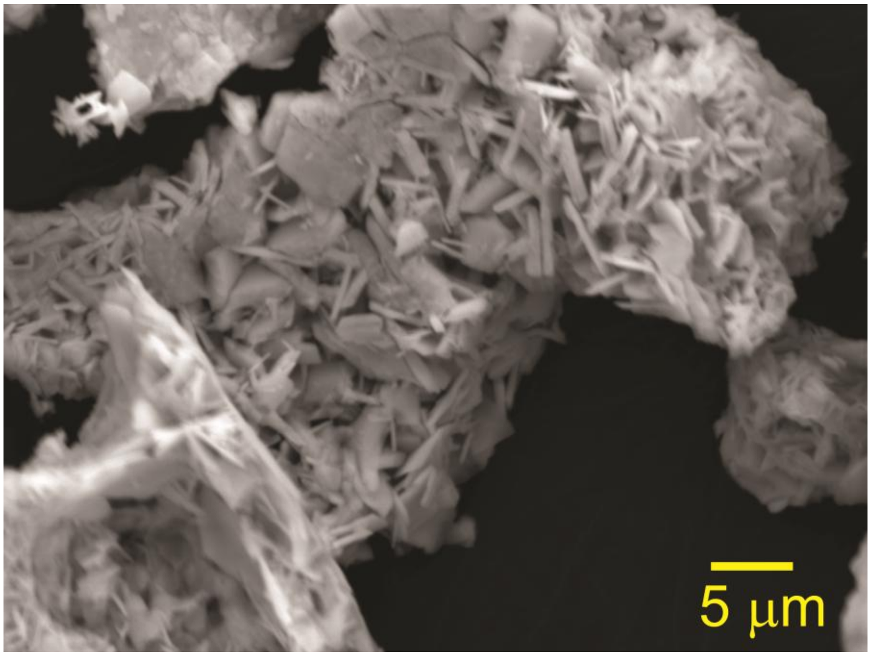

Figure B.9 Representative SEM image of $K_2La_2Ti_3O_{10}$ prepared by Pechini synthesis.